Assembly, Testing and Performance Studies of Silicon Strip Modules for CMS Tracker Phase II Upgrade

QUAID-I-AZAM UNIVERSITY
ISLAMABAD

By

Ali Awais

Department of Physics
Quaid-i-Azam University,
Islamabad-Pakistan
2024

This work is submitted as a dissertation in partial fulfillment
of the requirements for the award of the degree
of

Doctor of Philosophy

In

Physics

Department of Physics
Quaid-i-Azam University,
Islamabad-Pakistan

<u>Certificate</u>

The undersigned declare that the research work presented in this thesis titled, **"Assembly, Testing and Performance Studies of Silicon Strip Modules for CMS Tracker Phase II Upgrade"** by **Mr. Ali Awais** is carried out under my supervision in partial fulfilment of the requirements for the degree of Doctor of Philosophy in Physics.

Supervisor:

(**Dr. Ashfaq Ahmad)**
Director, EHEP
National Center for Physics
Quaid-i-Azam University,
Islamabad Pakistan.

Submitted through:

(Prof. Dr. Kashif Sabeeh)
Chairman
Department of Physics,
Quaid-i-Azam University,
Islamabad-Pakistan.

Author's Declaration

The undersigned declare that the research work presented in this thesis titled, **"Assembly, Testing and Performance Studies of Silicon Strip Modules for CMS Tracker Phase II Upgrade"** is his own work, and that, all the sources he has used or quoted have been indicated or acknowledged by means of complete references.

Ali Awais

Plagiarism Undertaking

I solemnly declare that the research work presented in this thesis titled, **"Assembly, Testing and Performance Studies of Silicon Strip Modules for CMS Tracker Phase II Upgrade"** is solely my work with no significant contribution from any other person. Small contributions/help wherever taken has been dully acknowledged and that complete thesis has been written by me.

I understand the zero tolerance policy of HEC and Quiad-i-Azam University towards plagiarism. Therefore, I as an author of above titled thesis declare that no portion of my thesis has been plagiarized and any material used as reference is properly referred/cited.

I undertake that if I am found guilty of any formal plagiarism in the above titled thesis ever after my Ph.D. degree and that HEC and the University has right to publish my name on HEC/University website on which names of students are placed who submitted plagiarized thesis.

Ali Awais

Abstract

The Large Hadron Collider (LHC) is gearing up for an upgrade to transform into the High Luminosity LHC (HL-LHC) by 2028. This upgrade will create a more intense radiation environment within the detection systems. To cope with this, the CMS detector, a key part of the LHC, will undergo the Phase-2 upgrade which includes replacing the current Tracker with a new Silicon tracking system, split into two parts: the Outer Tracker and the Inner Tracker. The Outer Tracker will feature two types of modules, 2S (Strip-Strip) and PS (Pixel-Strip), which are based on a novel transverse momentum (pT) discrimination concept.

The thesis work aims to establish assembly sites from scratch for producing 2S modules for the Outer Tracker. The development of assembly setups demonstrates positive outcomes in module assembly, from mechanical modules to functional silicon modules. The sensor-to-sensor mechanical tolerance limits are achieved well within 400 μrad rotationally, and 50 μm and 100 μm translationally, perpendicular and parallel to the strip direction, respectively. Additionally, successful development of IV and noise measurement setups for testing the modules' functionality post-assembly is achieved. Testing of functional prototype modules using these setups confirms the effectiveness of the assembly processes.

Furthermore, the performance of a 2S module in a beam environment is evaluated by reconstructing and analyzing data from a DESY test beam using the Corryvreckan an offline reconstruction framework. The study explores the potential of the user-friendly Corryvreckan framework for future test beam analysis, focusing on hit detection efficiency and stub efficiency for 2S modules. The obtained results show agreement within 1% with previously established results using the EUTelescope offline reconstruction framework.

Dedication

This thesis is dedicated to my loving family, whose unwavering support, encouragement, and sacrifices have been the foundation of my academic journey.

Acknowledgements

This thesis would not have been possible without the support and inspiration from a group of people. I would like to express special gratitude to my supervisor, Dr. Ashfaq Ahmad, for his invaluable guidance and encouragement throughout this research project. Right from the start, he provided me with the freedom to explore and offered respectful, honest, and fair guidance. His expertise, patience, and constructive feedback played a crucial role in shaping this work.

I would like to thank NCP management for granting access to resources and facilities crucial for this research. Special thanks go to the CMS Outer Tracker working group, for their assistance and support throughout the research.

I would also like to thank my lab colleagues: Dr. Malik Imran Awan, Dr. Irfan Asghar, Dr. Imdad Ali, Dr Saleh Muhammad and many others. The time that I have spent working with you was very interesting, pleasant and entertaining.

I am indebted to my family for their unwavering love, understanding, and encouragement, without which this endeavor would not have been possible.

Finally, I extend my heartfelt appreciation to all my friends and colleagues who have supported me during this journey.

Contents

1

Introduction

The Standard Model of particle physics stands as the cornerstone of our comprehension of fundamental particles and their interactions. It effectively accounts for the electromagnetic, weak, and strong nuclear forces, along with the constituent particles of matter. Nonetheless, pivotal questions surrounding the nature of dark matter, neutrino masses, and the unification of forces remain unanswered within its framework. Addressing these questions, physicists have delved into theories beyond the Standard Model (BSM), including Supersymmetry and extra dimensions. Playing a central role in this pursuit is the Large Hadron Collider (LHC), the world's premier particle accelerator. Through collisions at unprecedented energies, the LHC strives to uncover new particles and phenomena that could unlock the enigmas that transcend the Standard Model. This endeavor charts the course for the future of particle physics research.

The High-Luminosity Large Hadron Collider (HL-LHC) upgrade [1] is fueled by ambitious physics objectives aimed at unveiling new dimensions in particle physics understanding. By elevating luminosity, the HL-LHC aims to refine measurement precision, unveil rare processes, and cast light on fundamental inquiries. The exploration of particle properties, combined with the quest for new physics beyond the Standard Model, promises to chart new territories in the subatomic realm. With the potential to illuminate mysteries like dark matter, Higgs boson properties, and potential signs of new physics, the HL-LHC stands to redefine the frontiers of knowledge.

Within this context, the CMS detector undergoes the Phase-2 upgrade [2] to tackle the higher radiation environment of HL-LHC. This comprehensive upgrade includes various enhancements, particularly a substantial upgrade to the tracker detector. New technologies, including high-density pixel sensors and advanced readout electronics, are employed to meet the challenges posed by elevated collision rates and radiation levels. As part of this upgrade, the outer tracker system will incorporate innovative p_T modules [3], directly contributing to the Level 1 (L1) trigger and aiding in handling high rates at HL-LHC. As part of CMS Tracker collaboration, our institute is dedicated to assembling one of these p_T module types, the 2S module, for the CMS Outer Tracker upgrade.

This thesis focuses on the assembly and testing procedures developed for the 2S module. It covers a range of techniques, including precise glue dispensing studies, metrology methods to calculate sensor misalignment, and a test box for noise measurements at low temperature conditions. Mechanical, dummy, and prototype functional modules have been assembled to enhance assembly precision, accompanied by an array of testing procedures under various conditions.

The performance of prototype 2S modules was assessed during a test beam at DESY, focusing on sensor spatial resolution and module's p_T discrimination capability. The data generated for one of the test beams were reconstructed and analyzed using Corryvreckan, test beam reconstruction software [4] for hit detection efficiency and stub efficiency. Finally, the results were compared with previous outcomes obtained using the EUTelescope offline reconstruction framework.

The thesis comprises various chapters, starting with an introduction to the standard model, motivations for exploring beyond the Standard Model Physics, a detailed look at the LHC and the CMS detector. It then proceeds to discuss the present perspective of the CMS Tracker, its Phase-2 upgrade, the development of assembly and testing setups at National Center for Physics (NCP), details of 2S module assembly and testing, and the analysis of DESY test beam data using the Corryvreckan framework, concluding with a comparison of the results with those obtained through the EUTelescope framework.

2

Particle Physics and CMS Experiment

The chapter begins by discussing the field of high-energy physics and it aims at describing the Standard Model. Additionally, an overview of the world's largest accelerator, the Large Hadron Collider (LHC) [5], is provided. The Compact Muon Solenoid (CMS) detector [6] is also introduced, which is composed of several sub-detector systems that collect information about the particles produced during proton-proton or heavy ions collisions at the LHC. This information is then analyzed to identify any new particles that may have been created.

2.1 An Overview of the Standard Model

The Standard Model (SM) of Particle Physics is an all-encompassing theoretical framework that explains the fundamental constituents of matter and their interactions. This comprehensive model has evolved over several decades, owing to a wealth of experimental observations and theoretical advancements by numerous scientists [7 - 12]. At its core, the SM incorporates three fundamental forces that govern the behavior of particles and their interactions. These forces are the strong, electromagnetic, and weak forces (with the latter two unified as the electroweak force). Here, some of the key components of SM, including fundamental particles, forces, and interactions, are presented. However, for a more thorough understanding specialized textbooks are available as references [13], [14].

The theoretical foundation of the Standard Model is based on the deep principles of Quantum Field Theory (QFT) [15]. Within this framework, quantum mechanics merges with classical fields and special relativity, giving rise to the notion of quantum fields. Notably, the idea of gauge symmetry is employed to ensure that the Lagrangian density ($\mathcal{L}$), a functional describing the fields ψ(x) and their space-time derivatives $\partial_\mu\psi$(x), remains invariant under local gauge and global symmetries, as well as invariance with respect to groups of internal symmetry. This elegant construction accounts for the conservation laws as a profound consequence of Noether's theorem [16].

2.1.1 Classifications of Particles

In the Standard Model, the excitation of quantum fields gives rise to particles that carry intrinsic spin angular momentum. These fundamental particles are categorized based on their intrinsic spin into two groups: fermions and gauge bosons. Fermions, characterized by half-integer spin, obey Fermi-Dirac statistics, while gauge bosons, with integer spin, adhere to Bose-Einstein statistics. Figure 2.1 illustrates the classifications of particles in the SM.

According to the SM theory, fermions act as the building blocks of matter. They are further organized into three generations and consist of two types of particles: quarks and leptons. Quarks possess an electric charge of either +2/3 or -1/3 (in terms of electronic charge) and come in six flavors: up (u), down (d), charm (c), strange (s), top (t), and bottom (b). Quarks also carry color charges (red, blue, and green) and a baryon number of 1/3. All the quantum numbers associated with quarks are conserved during interactions, except for flavor, which can change during weak interactions.

Leptons, also arranged in three generations, include the electron (e), muon (μ), and tau (τ), each carrying a negative unit of electric charge. Associated with these charged leptons are their corresponding neutrinos: electron-neutrino (ν_e), muon-neutrino (ν_μ), and tau-neutrino (ν_τ), all electrically neutral. The lepton numbers (L_e, L_μ, and L_τ) associated with each lepton and its respective neutrino are conserved during interactions. Additionally, in the framework of the SM, every fermion has an antimatter counterpart, which is identical in all respects except for having opposite charge and quantum numbers.

The gauge bosons play a crucial role by mediating interactions between fermions. For instance, the photon (γ) mediates electromagnetic interactions, gluons (g) mediate strong interactions, and the $W^{\pm}$ and Z^0 bosons mediate weak interactions. These interactions, governed by the exchange of gauge bosons, are central to understanding the dynamics and behavior of particles within the Standard Model.

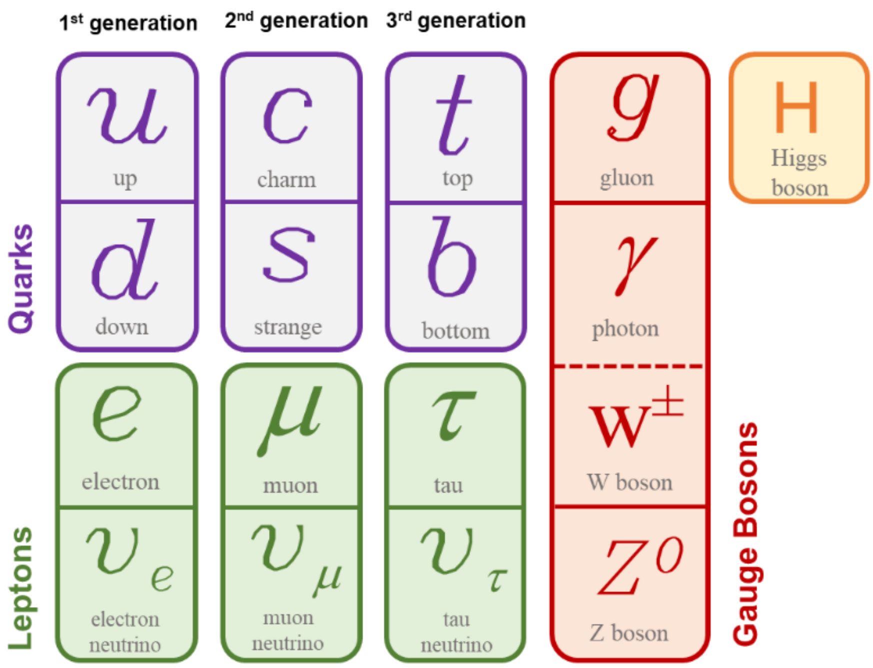

Figure 2.1: The Standard Model encompasses a diverse array of particles, comprising quarks, leptons, gauge bosons, and the Higgs boson.

2.1.2 Fundamental Interactions

The formulation of the Standard Model is founded upon the framework of three local gauge symmetry groups, namely $SU(3)_C \otimes SU(2)_L \otimes U(1)_Y$, where the subscripts C, L, and Y correspond to the quantum numbers color, weak isospin (associated with left-handed chiral fields), and hypercharge, respectively.

i. Electromagnetic Interaction

The origin of gauge invariance in the electromagnetic (EM) theory is closely tied to the non-uniqueness of the vector potential $\vec{A}$ and scalar potential φ for a given set of physical electric (E) and magnetic (B) fields. The transformations carried out to preserve E and B fields are termed gauge transformations, and the invariance of Maxwell's equations under these transformations is known as gauge invariance. In four-vector notation, the gauge transformation is expressed as

$$A_\mu \rightarrow A'_\mu = A_\mu + \frac{1}{e}\partial_\mu \alpha \tag{2.1}$$

where $A_\mu = (\varphi, -\overrightarrow{A})$ and $\partial_\mu = (\partial_t, -\overrightarrow{\nabla})$. The free Maxwell EM field equation, which do not include any source term can be written as

$$\partial_\mu F_{\mu\upsilon} = 0 \tag{2.2}$$

where $$F_{\mu\upsilon} = \partial_\mu A_\upsilon - \partial_\upsilon A_\mu \tag{2.3}$$

is the electromagnetic field strength tensor and it is invariant under the gauge transformation defined in equation (2.1), implying that Maxwell's equations are gauge field invariant equations. The Lagrangian density of Maxwell field is given as

$$\mathcal{L}_{EM} = -\frac{1}{4}F_{\mu\upsilon}F^{\mu\nu} \tag{2.4}$$

The gauge invariance can be thought as an internal space rotational invariance. The set of all such transformation forms group, which is *U(1)* Abelian symmetry group in this case. The Dirac Lagrangian density for fermions is given as

$$\mathcal{L}_{Dirac} = \bar{\psi}(i\gamma^\mu \partial_\mu - m)\psi \tag{2.5}$$

where ψ is the fermion spinor γ^μ are the Dirac matrices and $\overline{\psi} = \psi^\dagger \gamma^0$. The Lagrangian in equation (2.5) is invariant under *U(1)* global transformation given as

$$\psi(x) \rightarrow \psi'(x) = \psi(x)e^{i\alpha} \tag{2.6}$$

where α is a constant. However, under *U(1)* local gauge transformation, α is replaced by α(*x*) dependent on space time coordinate *x* with

$$\psi(x) \rightarrow \psi'(x) = \psi(x)e^{i\alpha(x)} \tag{2.7}$$

Under the local gauge transformation of (2.7), the Lagrangian density in equation (2.5) does not remain invariant. To maintain the Dirac equation invariant under *U(1)* local gauge transformation, the partial derivate is replaced with gauge covariant derivative defined as

$$\partial_\mu \rightarrow D_\mu = \partial_\mu - ieA_\mu \tag{2.8}$$

and by making above replacement the equation (2.5) becomes

$$\mathcal{L}_{Dirac} = \bar{\psi}(i\gamma^{\mu}\partial_{\mu} - m)\psi + e\bar{\psi}\gamma^{\mu}A_{\mu}\psi \qquad (2.9)$$

The last term can be interpreted as the interaction of the Dirac field with the electromagnetic field. Combining the EM Lagrangian density in equation (2.9), the Quantum Electrodynamics (QED) Lagrangian is obtained, which is invariant under *U(1)* gauge transformation.

$$\mathcal{L}_{QED} = -\frac{1}{4}F_{\mu\upsilon}F^{\mu\nu} + \bar{\psi}(i\gamma^{\mu}\partial_{\mu} - m)\psi + e\bar{\psi}\gamma^{\mu}A_{\mu}\psi \qquad (2.10)$$

$$\Rightarrow \qquad \mathcal{L}_{QED} = \mathcal{L}_{EM} + \mathcal{L}_{Dirac} + \mathcal{L}_{int}$$

The field A_{μ} is massless since it lacks an associated mass term, and consequently, its associated vector boson, the photon, is also massless.

ii. Strong Interaction

The strong interaction within the Standard Model is effectively described by Quantum Chromodynamics (QCD) and falls under the $SU(3)_c$ non-abelian gauge symmetry group. The conservation of color charge within this group is denoted by the subscript *C*. The field tensor for QCD is represented as:

$$G_a^{\mu\upsilon} = \partial^{\mu}G_a^{\upsilon} - \partial^{\upsilon}G_a^{\mu} + g_s f_{abc}G_b^{\mu}G_c^{\nu} \qquad (2.11)$$

Here, G_a corresponds to the gluon gauge field with an index "a" ranging from 1 to 8, g_s represents the strong coupling constant, and f_{abc} are the structure constants of the *SU(3)* group. The gauge symmetry of *SU(3)* implies the existence of eight massless generators, which are the gluons themselves. These gluons assume a crucial role in facilitating the color interaction between quarks. Given that the gluon themselves carry color charge, they could interact among each other as well. The QCD Lagrangian can be constructed as follows:

$$\mathcal{L}_{QCD} = -\frac{1}{4}G_{a\mu\nu}G_a^{\mu\nu} + \sum_{k=1}^{6}\bar{\psi}_k\,(i\gamma^{\mu}D_{\mu} - m_k)\psi_k \qquad (2.12)$$

Here, ψ_k denotes the spinor for quarks, and the covariant derivative is given by:

$$D_{\mu} = \partial_{\mu} - ig_s T_a G_a^{\mu} \qquad (2.13)$$

In the above expression, T_a represents the *SU(3)* generators, and $T_a = \frac{1}{2}\lambda_a$, with λ_a being the Gell-Mann matrices. The QCD Lagrangian can be decomposed into three components as shown below:

$$\mathcal{L}_{QCD} = -\frac{1}{4}G_{a\mu\nu}G_a^{\mu\nu} + \sum_{k=1}^{6}\bar{\psi}_k\,(i\gamma^{\mu}\partial_{\mu} - m_k)\psi_k + \sum_{k=1}^{6} g_s\,T_a\bar{\psi}_k\gamma^{\mu}G_a^{\mu}\psi_k \qquad (2.14)$$

$$\Rightarrow \qquad \mathcal{L}_{QCD} = \mathcal{L}_G + \mathcal{L}_q + \mathcal{L}_{int}$$

An important consequence of the gluon self-interaction within the QCD field is the phenomenon of color confinement. As quarks move apart, the strong force between them remains constant, leading to an increase in the potential energy of the quark system. At a distance of approximately 1 fm, the system's energy becomes sufficient to produce a quark-antiquark pair, resulting in new quark combinations rather than isolated quarks. Additionally, a particular feature is observed at small distances where the strength of the strong force decreases rapidly, causing quarks to behave almost as free particles. This behaviour is known as "asymptotic freedom."

iii. Electroweak Theory

The electroweak theory unifies the $SU(2)_L \otimes U(1)_Y$ group based on the same principles of gauge invariance as Quantum Electrodynamics (QED). It suggests that both electromagnetic (EM) and weak interactions are distinct manifestations of the same force. The $U(1)_Y$ group represents the EM interactions while the $SU(2)_L$ group embodies the isospin group of weak interactions. Within the $SU(2)_L$ group, both charged and neutral currents exist, where charged currents change the flavor of left-handed fermion fields, while neutral currents conserve flavor. The subscript "L" in $SU(2)_L$ signifies the non-conservation of parity and indicates that the weak isospin current primarily couples with left-handed fermions. Left-handed and right-handed spinors are defined as follows:

$$\psi_R = P_R\psi = \frac{1}{2}(1+\gamma^5)\psi \qquad (2.15)$$

$$\psi_L = P_L\psi = \frac{1}{2}(1-\gamma^5)\psi \qquad (2.16)$$

Here, $P_{R,L}$ are the chirality operators and $\gamma^5 = i\gamma^0\gamma^1\gamma^2\gamma^3$. In SM, fermions can be expressed as left-handed weak isospin doublets ($T_3 = \pm 1/2$) with families of quarks (Q_i) and leptons (L_L^i),

$$Q_i = \begin{pmatrix} u \\ d \end{pmatrix}_L \begin{pmatrix} c \\ s \end{pmatrix}_L \begin{pmatrix} t \\ b \end{pmatrix}_L$$

$$L_L^i = \begin{pmatrix} \nu_e \\ e \end{pmatrix}_L \begin{pmatrix} \nu_\mu \\ \mu \end{pmatrix}_L \begin{pmatrix} \nu_\tau \\ \tau \end{pmatrix}_L$$

or right-handed weak isospin singlets ($T_3 = 0$) given as

$$u_i = (u_R), (c_R), (t_R) \quad \& \quad d_i = (d_R), (s_R), (b_R)$$

$$L_R^i = (e_R), (\mu_R), (\tau_R)$$

In this prescription of weak isospin, the right-handed neutrinos do not accommodate. The electroweak Lagrangian can be constructed as follows:

$$\mathcal{L}_{EW} = -\frac{1}{4} W_{a\mu\nu} W_a^{\mu\nu} - \frac{1}{4} B_{\mu\nu} B^{\mu\nu} + \sum_{f=\psi_L,\psi_R} \bar{f}\, i\gamma^{\mu} D_{\mu} f \qquad (2.17)$$

where *f* represents the left- or right-handed fermion spinor. The field tensors are given by:

$$W_a^{\mu\upsilon} = \partial^{\mu} W_a^{\upsilon} - \partial^{\upsilon} W_a^{\mu} + g_2 f_{abc} W_b^{\mu} W_c^{\nu} \qquad (2.18)$$

$$B^{\mu\nu} = \partial^{\mu} B^{\nu} - \partial^{\nu} B^{\mu} \qquad (2.19)$$

W_a^{μ} and B^{μ} are the gauge fields with index a = 0,1,2, f_{abc} represents the structure constant of the *SU(2)* group. The covariant derivative in equation (2.17) is given as:

$$D_{\mu} = \partial_{\mu} - i\frac{g_1}{2} Y B_{\mu} - i\frac{g_2}{2} T_i W_{\mu}^{a} \qquad (2.20)$$

where g_1 and g_2 are the coupling strengths between fermions and gauge fields, and Y and T_i are the generators for the *U(1)* and *SU(2)* groups, respectively. The combined symmetry $SU(2)_L \otimes U(1)_Y$ enforces the conservation of weak hypercharge, given by:

$$\frac{Y}{2} = Q - T_3 \qquad (2.21)$$

where Q represents the electric charge, and T_3 is the weak isospin.

The electroweak theory necessitates the existence of four massless particles, two charged and two neutral, but the short range of weak interaction indicates that the carrier particles are massive. This implies that the underlying symmetry is broken by some mechanism that imparts mass to the exchange particles ($W^{\pm}$ and Z^0) involved in weak interactions but leaves the photons (exchanged in EM interactions) massless.

iv. Spontaneous Symmetry Breaking

A scalar field, recognized as the Higgs field, was incorporated into the framework of the Standard Model by F. Englert, R. Brout, and P. Higgs [17 - 18]. In the Brout-Englert-Higgs (BEH) mechanism, the introduction of the Higgs field leads to the spontaneous breaking of the electroweak symmetry, and its interactions are responsible for imparting masses to both bosons and fermions.

In the BEH mechanism, the Lagrangian can be formulated in terms of a vector field interacting with a complex scalar field (ϕ). The Lagrangian for the scalar field is given by:

$$\mathcal{L}_{Higgs} = (\partial_\mu \phi)^\dagger (\partial^\mu \phi) - V(\phi) \tag{2.22}$$

Within the electroweak model, there are two neutral and two oppositely charged gauge bosons. Consequently, the scalar field encompasses a weak isospin doublet, consisting of two complex scalar fields:

$$\phi = \frac{1}{\sqrt{2}} \begin{pmatrix} \phi_1 + i\phi_2 \\ \phi_3 + i\phi_4 \end{pmatrix} \tag{2.23}$$

Here, ϕ_1, ϕ_2, ϕ_3, and ϕ_4 represent the real scalar fields. The Higgs potential is formulated as:

$$V(\phi, \phi^\dagger) = \mu^2 \phi^\dagger \phi + \lambda (\phi^\dagger \phi)^2 \tag{2.24}$$

The interaction Lagrangian of the scalar field with the electroweak model ($SU(2)_L \otimes U(1)_Y$ symmetry) can be expressed by replacing ∂_μ with D_μ as defined in equation (2.20). Thus, equation (2.22) can be rewritten as:

$$\mathcal{L} = \left(D_\mu \phi\right)^\dagger (D^\mu \phi) - \mu^2 \phi^\dagger \phi - \lambda (\phi^\dagger \phi)^2 \tag{2.25}$$

For $\mu^2 < 0$, the Higgs potential in equation (2.24) exhibits an infinite set of degenerate minima at:

$$\phi^\dagger \phi = \frac{\phi_1 + \phi_2 + \phi_3 + \phi_4}{2} = -\frac{\mu^2}{2\lambda} \equiv \frac{v^2}{2} \tag{2.26}$$

A possible ground state can be chosen as:

$$\phi_{vac} = \frac{1}{\sqrt{2}} \begin{pmatrix} 0 \\ v \end{pmatrix} \tag{2.27}$$

Here,
$$v = \sqrt{\frac{-\mu^2}{\lambda}} \tag{2.28}$$

Excitations above this ground state can be studied by introducing quantum fluctuation *h(x)* in ϕ_{vac} and expanding around the minima:

$$\phi_{vac} = \frac{1}{\sqrt{2}} \begin{pmatrix} 0 \\ v + h(x) \end{pmatrix} \tag{2.29}$$

Substituting this into equation (2.24) yields:

$$V(\phi, \phi^{\dagger}) = -\frac{\mu^4}{4\lambda} - \mu^2 h^2 + \lambda \upsilon h^3 + \frac{\lambda}{4} h^4 \quad (2.30)$$

This equation can be interpreted in terms of a real scalar field h with a corresponding scalar boson, known as the Higgs boson. The Higgs boson exhibits self-interactions through cubic and fourth-power terms. The Higgs boson's mass can be deduced from the quadratic term as:

$$m_H = \sqrt{-2\mu^2} = \sqrt{2\lambda\nu} \quad (2.31)$$

Similarly, substituting ϕ_{vac} from equation (2.29) into the kinetic term of equation (2.25) results in:

$$\left(D_\mu \phi\right)^{\dagger}(D^\mu \phi) = \frac{1}{2}\left(\partial_\mu h\right)(\partial^\mu h) + \frac{g_1^2}{8}\left(W_\mu^1 + iW_\mu^2\right)(W^{1\mu} - iW^{2\mu})(\upsilon + h)^2 +$$
$$\frac{1}{8}(g_1 W_\mu^3 - g_2 B_\mu)(g_1 W^{3\mu} - g_2 B^\mu)(\upsilon + h)^2 \quad (2.32)$$

Through a linear combination of W_μ^a and B_μ, the gauge fields can be defined as:

$$W_\mu^{\pm} = \frac{1}{\sqrt{2}}(W_\mu^1 \mp iW_\mu^2) \quad (2.33)$$

$$A_\mu = \frac{g_2 W_\mu^3 + g_1 B_\mu}{\sqrt{g_1^2 + g_2^2}} \quad (2.34)$$

$$Z_\mu = \frac{g_1 W_\mu^3 - g_2 B_\mu}{\sqrt{g_1^2 + g_2^2}} \quad (2.35)$$

Equation (2.32) can be expressed as:

$$\left(D_\mu \phi\right)^{\dagger}(D^\mu \phi) = \frac{1}{2}\left(\partial_\mu h\right)(\partial^\mu h) + m_w^2 W^{+\mu} W_\mu^- + \frac{2m_w^2}{\nu^2} W^{+\mu} W_\mu^- h + \frac{1}{2} m_z^2 Z^\mu Z_\mu +$$
$$\frac{m_z^2}{\nu^2} Z^\mu Z_\mu h + \frac{m_z^2}{2\nu^2} Z^\mu Z_\mu h^2 \quad (2.36)$$

Where $$m_w = \frac{g_2 \upsilon}{2} \quad (2.37)$$

and $$m_z = \frac{\upsilon\sqrt{g_1^2 + g_2^2}}{2} \quad (2.38)$$

Hence, from equations (2.30) and (2.36), it can be inferred that the Lagrangian portrays a scalar field h with a mass m_H, a massive complex vector field $W_\mu^{\pm}$ with a mass m_w and a massive real vector field Z_μ with a mass m_z. With the introduction of weak mixing angle θ_w defined as

$$\cos\theta_w = \frac{g_2}{\sqrt{g_1^2+g_2^2}} \tag{2.39}$$

the mass of the weak gauge bosons can be found by using equation (2.37), (2.38), and (2.39),

$$m_z = \frac{m_w}{\cos\theta_w} \tag{2.40}$$

v. Fermion Masses

The SM encapsulates the left-handed doublet and right-handed singlet quark and lepton families, as described in the section on Electroweak theory. The mass term for a Dirac fermion is given as:

$$-m(\bar{\psi}_L\psi_R + \bar{\psi}_R\psi_L)$$

This term couples both with the right- and left-handed components. However, while the $SU(2)_L$ group only acts on left-handed fermions, this coupling renders mass non-invariant. An alternative approach to impart fermion masses is through Yukawa couplings with the scalar field. In this scenario, the Higgs field couples with the massless quark or lepton field through the coupling strength g_i.

For instance, consider the coupling of the electron doublet, L_L^e, the Higgs doublet φ , and the right-component of the electron field:

$$\mathcal{L}_{Yukawa}^e = -g_e(\bar{L}_L^e\varphi e_R + \bar{e}_R\varphi^\dagger L_L^e) \tag{2.41}$$

This interaction maintains $SU(2)_L$ invariance. When spontaneous symmetry breaking occurs and excitations above the ground state are considered, the Lagrangian transforms into:

$$\mathcal{L}_{Yukawa}^e = -\frac{g_e v}{\sqrt{2}}(\bar{e}_L e_R + \bar{e}_R e_R) - \frac{g_e}{\sqrt{2}}(\bar{e}_L e_R + \bar{e}_R e_R)h \tag{2.42}$$

Alternatively:

$$\mathcal{L}_{Yukawa}^e = -m_e(\bar{e}e) - \frac{m_e}{v}(\bar{e}e)h \tag{2.43}$$

In the first term, the electron mass ($m_e = \frac{g_e v}{\sqrt{2}}$) emerges, illustrating the coupling of the electron to the Higgs field through its non-zero vacuum expectation values. The second term underscores the coupling between the electron and the Higgs boson itself.

In summary, the Lagrangian of the SM encompasses all the Lagrangians of fermion and boson, along with their interactions:

$$\Rightarrow \qquad \mathcal{L}_{SM} = \mathcal{L}_{gauge} + \mathcal{L}_{fermions} + \mathcal{L}_{Higgs} + \mathcal{L}_{Yukawa} \qquad (2.44)$$

The SM, founded on the $SU(3)_c \otimes SU(2)_L \otimes U(1)_Y$ gauge symmetry, stands as a cornerstone in particle physics. Nonetheless, despite its accomplishments, there remain substantial gaps in our comprehension.

2.1.3 Unsolved Queries within the Standard Model

Several questions remain to be addressed to understand physical phenomena, some of which are outlined below. These inquiries have motivated scientists to delve into theories that extend beyond the Standard Model (BSM), such as Supersymmetry, Large-scale extra dimensions, sterile neutrinos, and even string theory.

i. Dark Matter

The challenge of dark matter in the context of the Standard Model centers on its inability to explain the presence of non-luminous matter that significantly influences the universe through gravity but does not interact electromagnetically. The known particles and forces in the Standard Model do not account for dark matter's properties. Astronomical observations highlight this discrepancy, motivating the exploration of theories BSM to potentially explain the nature of dark matter and its gravitational effects.

ii. Hierarchy Problem

The Hierarchy Problem within the Standard Model refers to the challenge of explaining the significant disparity between the electroweak scale (characterized by particle masses) and the Planck scale (associated with gravity). Quantum corrections to the Higgs boson's mass, influenced by virtual particles, create an apparent fine-tuning issue due to the vast energy gap.

iii. Neutrinos as Majorana Particles

The investigation whether neutrinos are Majorana particles is an important question in particle physics. While the Standard Model assumes neutrinos are Dirac particles with distinct antiparticles, the possibility that neutrinos might be their own antiparticles, known as Majorana particles, has gained attention. This could have implications for understanding neutrino masses and neutrinoless double-beta decay, a process that, if observed, would confirm neutrinos as Majorana particles and provide insights into their properties and lepton number violation. Investigating neutrinos as Majorana particles is a focal point of current research efforts in particle physics.

iv. Unification of Forces

The Standard Model successfully describes three fundamental forces but leaves out gravity, posing the challenge of unifying all forces in a single framework. Efforts to achieve this, such as the pursuit of a Theory of Everything, aim to integrate gravity with the other forces. However, the significant differences in behavior and energy scales between these forces present obstacles to their unification. Unifying forces remains a central goal in theoretical physics, holding the promise of a more complete understanding of the universe's fundamental nature.

2.2 Experimental High Energy Physics

The collaboration between theory and experiment has played a significant role in the development of the Standard Model. Table 2.1 highlights the labs and experiments that uncovered various particles.

Progress in experimental methods, powered by advanced particle accelerators, has played a vital role in these remarkable achievements. A particle accelerator generates a beam of high-energy particles with controlled timing and specific distribution. This beam can be directed at a stationary target or collide with another beam moving in the opposite direction to study physics processes. The machine produces latter type of collision is called a collider. During collisions, the total energy and momentum of the colliding particles in the initial state lead to a Lorentz quantity given as

$$s = \left(\sum_{i=1}^{2} E_i\right)^2 - \left(\sum_{i=1}^{2} p_i\right)^2 \qquad (2.45)$$

This equation uses natural units (c = 1). To create heavy particles, the center-of-mass energy $(\sqrt{s})$ must surpass the combined mass of particles produced in the collision. While fixed target setups have low $\sqrt{s}$ values, collider machines can achieve much higher energies. Additionally, the collision point within the particle beams is surrounded by a complex detection system that identifies collision products and reconstructs the physics processes. Table 2.2 provides the $\sqrt{s}$ values for some colliders.

Table 2.1: Experimentally measured particles, and their discovery year and lab.

Particle	Type	Lab/ Experiment	Discovery Year
e^{-}	Lepton	Cathode Ray Tube	1897 [19]
γ	Gauge boson	Photoelectric Effect	1905 [20]
μ^{-}	Lepton	Cosmic Ray Experiments	1936 [21]
v_e	Lepton	Nuclear Rector	1953 [22]
v_μ	Lepton	BNL	1962 [23]
u	Quark	SLAC	1968 [24], [25]
d	Quark	SLAC	1968 [24], [25]
s	Quark	SLAC	1968 [24], [25]
c	Quark	SLAC, BNL	1974 [26], [27]
τ^{-}	Lepton	SLAC	1975 [28]
b	Quark	Fermilab	1977 [29]
Gluons	Gauge boson	PLUTO, TASSO (DESY)	1979 [30], [31]
$W^{\pm}, Z^{0}$	Gauge bosons	UA1, UA2 (CERN)	1983 [32 - 35]
t	Quark	CDF, D0 (Fermilab)	1995 [36], [37]
v_τ	Lepton	DONUT (Fermilab)	2000 [38]
H	Boson	CMS, ATLAS (CERN)	2012 [39], [40]

2.3 The Large Hadron Collider

The world's most powerful collider in operation today is the Large Hadron Collider (LHC) [5]. It is capable of colliding proton beams with $\sqrt{s}$ of up to 14 TeV. The LHC is located in a 26.7 km circumference tunnel that spans the Switzerland-France border. The European

Organization for Nuclear Research (CERN) in Geneva, Switzerland, oversees its activities. In addition to protons, the LHC is also capable of producing and colliding heavy ion beams.

Table 2.2: Some particle colliders and their center of mass energy

Collider	Type	√s	Laboratory
PEP-II	$e^+ e^-$	10.5 GeV	SLAC
HERA	$e^- p / e^+ p$	320 GeV	DESY
Tevatron	$p\bar{p}$	1.96 TeV	Fermilab
LHC	$p\bar{p}$	13 – 14 TeV	CERN

In LHC two adjacent beams travel parallel but in opposite directions around the ring. There are four intersection points where particle collisions take place. There are nearly 10,000 superconducting magnets installed at LHC which are used for different purposes, these include dipoles, quadrupoles, and higher poles. The superconducting resonating cavities are used to accelerate the beam. When the alternating electric field inside the cavity is in the direction of the beam it gives a kick to the beam, thus producing the beam in the form of bunches. These large numbers of superconducting magnets and cavities are operated by superfluid He-4 at 1.9 K temperature.

Figure 2.2 depicts CERN's accelerator complex, where beam energy progressively increases. Linear Accelerator 4 (LINAC 4) generates a 160 MeV energy H^- beam. Then, the Booster (PSB) strips electrons from H^- ions, converting them into proton ions, which are then accelerated to 2 GeV. The Proton Synchrotron (PS) and Super Proton Synchrotron (SPS) incrementally elevate the beam energy to 26 GeV and 450 GeV, respectively. The final step is the LHC, where the proton beam energy is boosted to 7 TeV. In the LHC, proton bunches circulate for 5 to 24 hours after accumulation and acceleration. The LHC ring houses 2808 bunches, each containing 1.2×10^{34} protons. Collisions occur at a frequency of 40 MHz, corresponding to collisions every 25 ns.

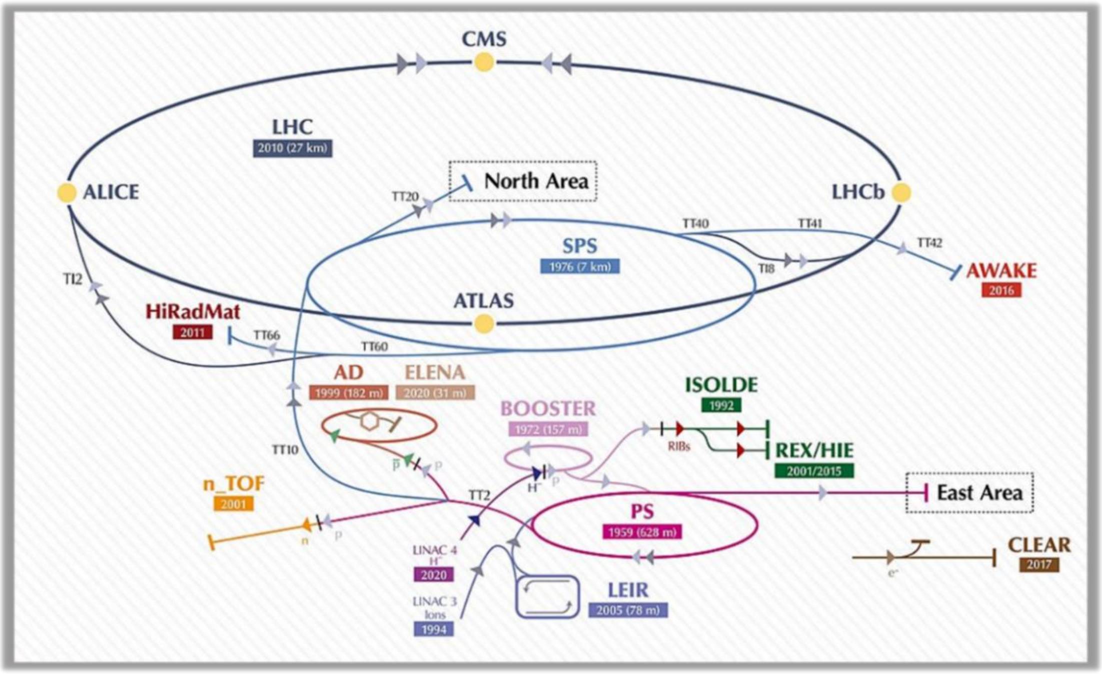

Figure 2.2: Schematic showing different accelerators at CERN [5].

2.3.1 Luminosity

Luminosity ($\mathcal{L}$) refers to the number of collisions that occur between particles per unit time per unit cross-sectional area. It is a crucial parameter used to describe the event rate and is determined by factors such as the number of particles present in each bunch (n_p), the number of bunches (n_b), the bunch cross-sectional area (A), and the revolution frequency (f). The instantaneous luminosity can be calculated using the formula

$$\mathcal{L} = \frac{n_b\, n_p^2\, f}{A} \tag{2.46}$$

The particle generation rate during collision time is related to $\mathcal{L}$ and its cross-section σ (the measure of likelihood of a collision occurring) and is given as

$$\frac{dN}{dt} = \sigma\mathcal{L} \tag{2.47}$$

From the perspective of luminosity and center-of-mass energy, the LHC began operating at an instantaneous luminosity value of twice its intended value ($\mathcal{L} = 2 \times 10^{34}$ cm^{-2} s^{-1}) after the conclusion of Run-2, while as of 2022, during LHC Run-3, it operates in a stable mode at $\sqrt{s}$ = 13.6 TeV.

In 2012, the Large Hadron Collider (LHC) accomplished its primary goal of discovering the Higgs boson through the independent effort of two main experiments at CERN, CMS [39] and ATLAS [40]. The initial observation was made at center of mass energy ($\sqrt{s}$) 7 TeV and 8 TeV with integrated luminosity approximately 20 fb^{-1} data (2×10^{15} pp-collisions). At this energy, the σ of Higgs boson (m_H = 125 GeV) is estimated to be around 20 pb, resulting in roughly 400,000 Higgs bosons produced according to equation (2.47).

2.3.2 Experiments at LHC

There are four main points at LHC where the beams collide and large detectors are installed for experiments. These include CMS [6], ATLAS [41], LHCb [42], and ALICE [43] (Figure 2.2). Both CMS and ATLAS are general purpose experiments and are used to study physics in the TeV range. These experiments are performing measurements for the standard model with high precisions and also exploring physics beyond the standard model. The LHCb experiment is specialized for heavy flavor physics involving the quarks of the 2^{nd} and 3^{rd} generation. One of the major goals of this experiment is to study the decays that involve B mesons. The detector is optimized for the low transverse momentum collision products which decay in the detector forward region. The ALICE experiment is focused to investigate quark-gluon plasma through high-energy heavy ion collisions.

The term pile-up is used to describe the phenomenon of multiple proton-proton collisions taking place within the same bunch crossing in a particle accelerator. This can result in a significant amount of data that may be challenging to separate and analyze, often leading to an increased uncertainty in the analysis of collision data. The LHC is particularly susceptible to pile-up due to the high number of particles in its proton beams. Advanced algorithms for event reconstruction and real-time trigger systems have been developed to mitigate the impact of pile-up on data analysis.

2.4 The CMS Experiment

The particle physics detectors are built with the motivation to reconstruct the primary particles produced as a result of colliding beams. One of the largest and most significant detectors at the LHC is the Compact Muon Solenoid (CMS), depicted in Figure 2.3. The length and diameter of the detector are 21 m and 15 m respectively, while its weight is about 14,000 tons. The CMS detector combines various measurements to reconstruct the particles produced in high-energy collisions with high precision. The superconducting solenoid is a critical component of the Compact Muon Solenoid (CMS) detector, producing a uniform magnetic field of 3.8 T. The solenoid is 12.9 m in length and 5.9 m in bore diameter, and it is enclosed within an iron yoke structure, that weighs 12,500 tons, used to contain the magnetic field.

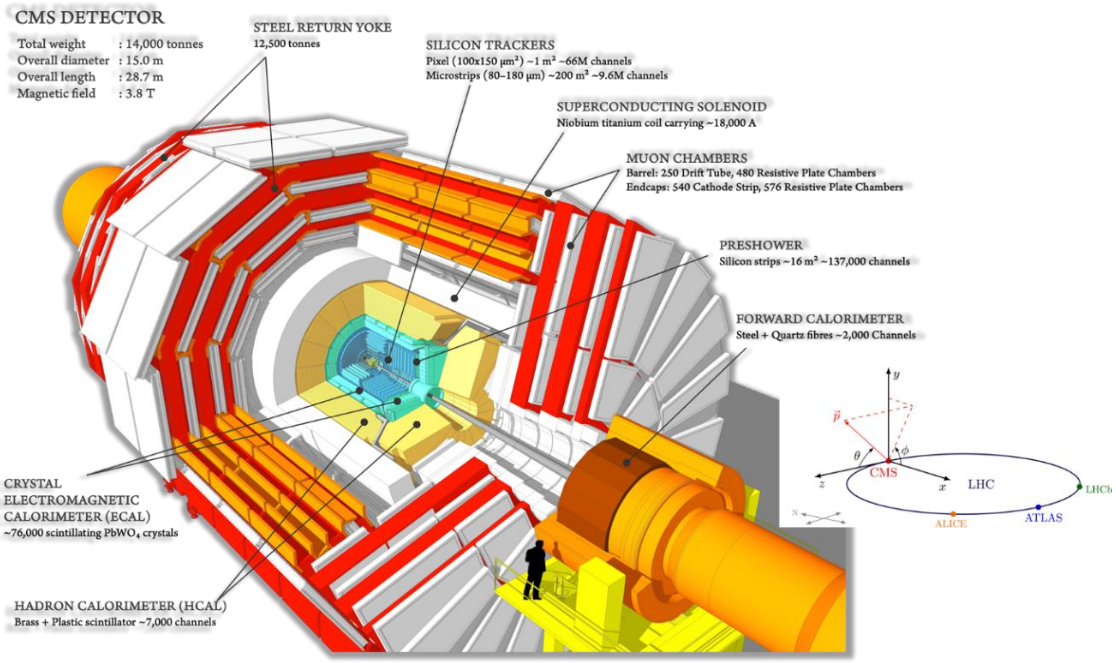

Figure 2.3: The CMS detector at LHC [44]. The right side displays the choice of coordinates system used at CMS.

The coordinate of the CMS detector (Figure 2.3) is defined by choosing the origin at the collision point. The center of the LHC is defined as the direction of the *x*-axis, and the *y*-axis points vertically upward. As a result, the *z*-axis is established in the anticlockwise direction of the LHC beam line. An important quantity is rapidity, which is related to the angle between the *xy* plane and the direction of emission of a collision product, and it is defined as:

$$y = \frac{1}{2}\ln(\frac{E + p_z c}{E - p_z c})$$

where E represents the energy of the collision product and p_z is the momentum along the beam axis. For highly relativistic particles perpendicular to the beam direction, p_z will be small, resulting in a rapidity value zero. On the other hand, if the particle is in the direction of the beam, E will be approximately equal to p_z, resulting in a rapidity of ∞. Calculating rapidity, especially near the beam pipe region, is challenging in reality due to the unknown mass of particles in that area. Therefore, another quantity called pseudorapidity, which is almost equal to rapidity for highly relativistic particles, is defined. Pseudorapidity, calculated from the polar angle (θ), is used to define the momentum coverage of the detector and is given as:

$$\eta = -\ln \tan(\theta/2) \tag{2.48}$$

CMS has various sub-detectors installed to measure the energy and momentum of different particles, such as photons, electrons, hadrons, and muons.

2.4.1 Sub-detectors at CMS

The different sub-detectors are optimized in the form of layers to give a specific type of information about a traversing particle. In order to optimally cover the maximum pseudorapidity range, equation (2.48), the sub-detectors consist of cylindrical layers referred to as barrels and flat disk layers known as end-caps. The schematic view of the slice of the CMS, Figure 2.4, shows the barrel segment of different sub-detectors. It also depicts different particles traversing the detector.

i. Silicon Tracking Detector

The Silicon Tracker [45] serves as the foremost sub-detector, positioned closest to the beam pipe, and records the trajectory of charged particles as they pass through its layers. The solenoid magnetic field causes these particles to bend, making it possible to measure their momentum by tracking their trajectories with this sub-detector. The CMS tracker is entirely composed of silicon, with its innermost layers utilizing pixel detectors surrounded by micro-strip detectors. As particles traverse through the pixel or micro-strip, they produce signals that are then detected and amplified. Since this sub-detector is exposed to the highest concentration of particles, a radiation-hard material is used in its construction.

ii. Electromagnetic Calorimeter (ECAL)

The ECAL [46], serving as the second sub-detector, accurately estimates the energy of electrons, positrons, and photons. The ECAL is constructed using radiation-hard lead tungstate ($PbWO_4$) scintillating crystals, which have a radiation length (X_o) of only 0.89 cm and a Moliere radius (R_M) of 2.2 cm, with the ability to withstand high radiation levels up to 10 Mrad.

Approximately 61,200 crystals are employed in the barrel, while 15,000 crystals are utilized in the endcap. These crystals emit up to 80% of the light during bunch crossing time (Bx) of 25 ns. Although the $PbWO_4$ crystals possess a low light yield of 30 γ/MeV, this limitation is overcome with the utilization of silicon vacuum phototriodes (VPTs) and avalanche photodiodes (APDs). In terms of radiation lengths, the ECAL sub-detector's total depth exceeds 25 X_o.

iii. Hadron Calorimeter (HCAL)

The HCAL [47] forms the third layer of the CMS detector, and is situated around the ECAL. This sub-detector is utilized for direct measurement of the energy of hadrons and for indirect measurement of non-interacting neutrinos. The HCAL is constructed in a sandwich-like structure, where dense materials and plastic scintillator tiles are arranged in alternating layers. Because of the high interaction length (λ_I), dense materials like steel or brass are used in the HCAL sub-detector, while the scintillators are equipped with embedded wavelength-shifting fibers for readout purposes. The thickness of HCAL in interaction length varies between 7 – 11 λ_I depending on η (equation (2.48)).

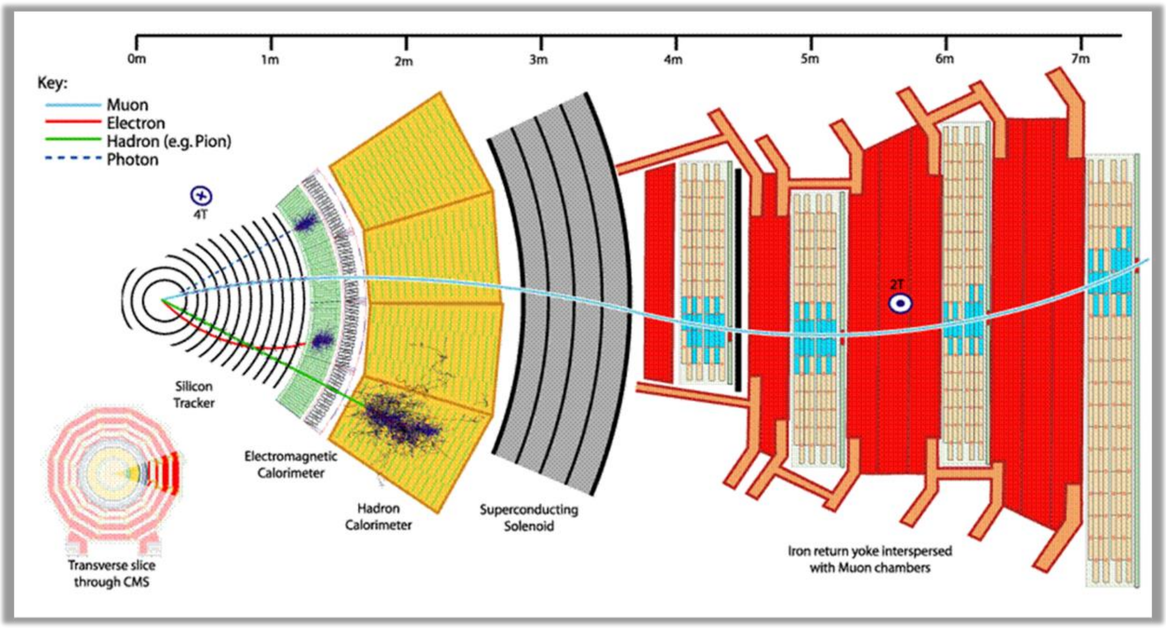

Figure 2.4: The slice of CMS detector is depicted schematically [48]. The detection of particles is carried out using one or more sub-detectors, depending on the particle type.

iv. Solenoid Magnet

The large solenoid magnet, around which the whole CMS experiment is built, makes the fourth layer. The magnet operates with a current of 18.2 kA flowing in superconducting niobium-titanium, producing a magnetic field of 3.8 T along the z-axis (see Figure 2.3) and stores the energy of 2.3 GJ. The main purpose of this massive magnet is to deflect the paths of charged particles produced in collisions.

v. Muon Chambers and Iron yoke

The muon chambers and iron yoke form the last layer of CMS. The muon chambers utilize gaseous detectors based on various types of technologies. Since all particles, apart from high-energy muons and neutrinos, are absorbed in HCAL, the muon chamber located at the furthest end of the CMS detector is used to detect muons. The iron yoke is used to control the magnetic field outside the solenoid and the field strength in it is about 2 T.

2.4.2 CMS Trigger System

The information collected from collisions generates about 1 megabyte of raw data per bunch crossing, potentially leading to data volumes of 40 TB/s. For studying rare particle production, a large number of collisions are needed, resulting in a vast amount of data that experiments cannot store entirely. To manage this, a trigger system is used to save only the relevant events.

The CMS trigger system consists of two parts: the Level-1 trigger (L1) and the High-Level Trigger (HLT) [45, 46]. The L1 trigger is the initial stage and makes quick decisions within 3.2 μs using information from the calorimeters and muon system. It employs hardware-based collision reconstruction algorithms, utilizing technology like Field Programmable Gate Arrays (FPGAs) and Application-Specific Integrated Circuits (ASICs). By applying basic selection criteria, the L1 trigger reduces the readout rate to 100 kHz, and the chosen events move to the HLT stage. The HLT can access all sub-detectors and uses substantial computing power to perform event reconstruction based on interesting physics events.

3

Silicon Tracking Detector at CMS

To determine the position and momentum of charged particles, tracking detectors employ silicon detector technology. This chapter begins with an overview of the basics of semiconductor technology, including the pn junction, as well as strip and pixel detectors. Subsequently, the current CMS tracking detector, which consists of a pixel and strip sub-detection system, is discussed. Furthermore, performance results of the tracking detector are presented. Finally, the chapter concludes with a discussion of radiation damage in semiconductor detectors.

3.1 Silicon Detectors Technology

The technology of silicon detectors is widely used in particle physics experiments. These detectors are more sensitive to passing particles due to their lower ionization energy as compared to the gaseous detectors. In addition, the high density of silicon material produces strong signals even with thin sensors. Furthermore, the low diffusion rate of induced charged particles results in high position resolution, making these detectors ideal for use in tracking detectors to measure the position of charged particles passing through them. The following sections cover some basics of silicon detectors, while more comprehensive discussions of semiconductor detectors can be found in textbooks [51 - 53].

3.1.1 Introduction to Semiconductors

The electrons of an individual atom occupy specific energy levels, known as atomic orbitals. When a large number of identical atoms (~ 10^{22}) come together to form a crystal lattice in a macroscopic solid piece, the atomic orbitals of the nearby atoms overlap. The discrete energy levels then combine into a large number of orbitals that are so closely spaced in energy that they can be considered a continuum, or an energy band. In materials, there are several band gaps present throughout the band structure. The filling of energy states with electrons follows the Fermi-Dirac distribution, which is expressed as:

$$f(\varepsilon) = \frac{1}{e^{(\varepsilon - \mu)/kT} + 1} \tag{3.1}$$

where k, μ, and T denotes the Boltzmann constant, Fermi level, and temperature. At T = 0 K, all the energy states up to μ are filled. The last band that is completely filled with electrons is known as the valence band, while the band above it, which may only be partially filled with electrons, is called the conduction band. These two bands are particularly important, as the Fermi level is typically located near them. Figure 3.1 illustrates the position of the Fermi level for conductors, semiconductors, and insulators. For conductors, the valence band and conduction band have an overlapping region, and the Fermi level is positioned within the conduction band. As a result, there are always free electrons available for conduction. In contrast, in insulators and semiconductors, the Fermi level lies in the bandgap between the valence and conduction bands.

The semiconductor elements, such as Si and Ge, have four electrons in their valence shell, and they form covalent bonds by sharing their electrons with other atoms in a crystal lattice. At T > 0 K, due to presence of thermal vibrations some of the electrons jump from valance to conduction band after breaking the covalent bonds, thus making the material conductive. The leaving electron produces a vacancy in the valence band, known as hole. The hole can be filled by the neighboring atom and, thereby, can move through the lattice, producing a positive charge current. The thermally excited electrons and holes are the intrinsic charge carriers, making a pure semiconductor material referred to as an intrinsic semiconductor.

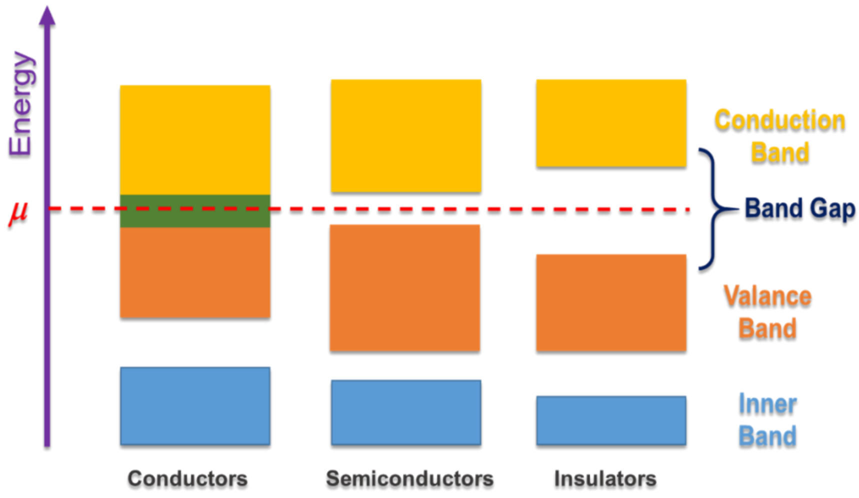

Figure 3.1: The energy band diagram of conductors, semiconductors and insulators at T = 0K. In case of conductors, there is an overlap between the valance and conduction bands and the Fermi level (μ) is also present in this overlap.

The addition of impurities to a semiconductor alters its conduction properties, resulting in the creation of an extrinsic semiconductor. This technique is commonly referred to as doping. If the doping element belongs to group V in periodic table, which contains five valence electrons, four of these electrons will form covalent bonds with atoms in the semiconductor lattice, while the remaining electron will be unbound. The free electron could jump into the conduction band making the semiconductor conductivity dominated by electrons. Such type is known as n-type semiconductor and the dopant atoms are called donors. On the other hand, if the impurity atom belongs to group III of periodic table, elements having three electrons in their valance shell, a vacancy in the valance band is created thus increasing the number of holes in semiconductor. This type is known as p-type semiconductor where the conduction is dominated by the holes. The dopant atoms in this case are called acceptors. Figure 3.2 explains the phenomenon of doping. The doping concentration and thus the charge carrier concentration is typically increased to 10^{12} cm^{-3} - 10^{18} cm^{-3}. The movement of electrons and holes through the semiconductor can be attributed to either an externally applied electric field or a gradient in carrier concentration. These phenomena are known as drift and diffusion, respectively. According to reference [54], the mobility of charge carriers is influenced by the doping concentration, temperature, and effective mass. Typically, electrons exhibit higher mobility than holes.

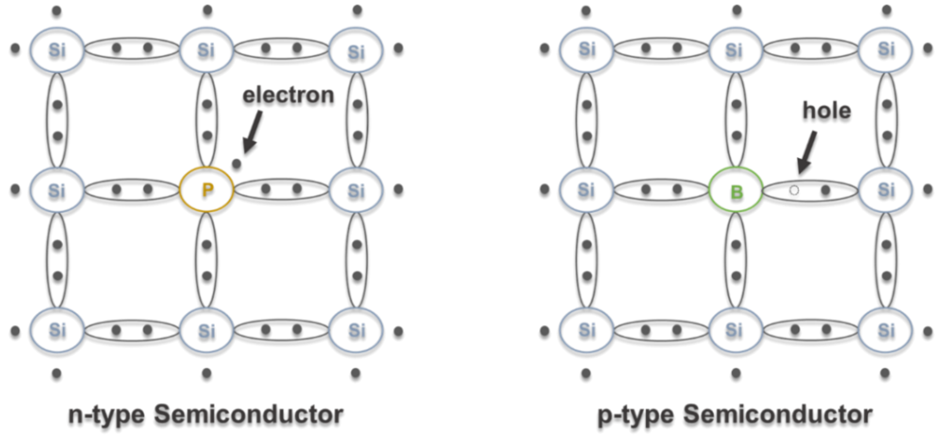

Figure 3.2: Composition of extrinsic silicon semiconductors doped with n-type and p-type impurities.

3.1.2 p-n Junction Diode and Detectors

Doping in intrinsic semiconductors causes a shift in the Fermi level due to an excess of electrons or holes (see Figure 3.3). When a p-type semiconductor is combined with an n-type semiconductor, a p-n junction diode is created at their interface. The resulting charge carrier concentration gradient drives a diffusion process, in which electrons flow from the n-type region to occupy the holes in p-type region. This diffusion process leads to an accumulation of positive space charge in n-type region and negative space charge in p-type region. At the junction, the electric field generated by the space charge accumulation produces drift which acts against additional diffusion, thus resulting in a balance between drift and diffusion processes. In thermal equilibrium, a space charge region or depleted region, free of charge carriers, is formed.

The depletion region can be manipulated by applying the external bias voltages across the pn-junction. In forward bias configuration, the positive and negative electrodes are connected to p-type and n-type regions, respectively. The depletion region is squeezed in this configuration and pn-junction conducts. In reverse bias configuration on the other hand, the positive and negative electrodes are attached to the n-type and p-type regions respectively. In reverse bias configuration, the depletion region widens and prevents conduction. However, a leakage current is still present in this state, comprising a diffusion component caused by minority carriers and a generation component due to thermally generated electron-hole pairs.

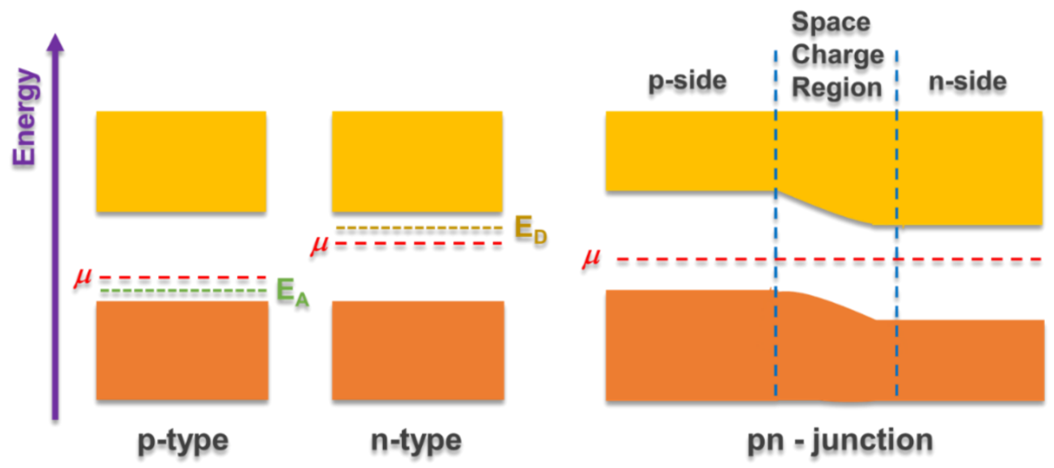

Figure 3.3: Energy band diagram of p-type, n-type, and pn-junction diode. E_A and E_D shows the energy levels of acceptor and donor atoms respectively.

3.1.3 Semiconductor Sensors for High Energy Physics

A typical semiconductor sensor used in high energy application is described in Figure 3.4. The p+ and n+ implants have a higher doping concentration than the p-bulk to improve the electrical junction between Aluminium and semiconductor material. The pn-junction is formed in section between the n+ implant and p-bulk. The top electrode is segmented into one or two dimension to make a strip or pixel sensor to increase the granularity of the sensor and improves the position resolution. Each segment of the strip (pixel) sensor is wire (ball) bonded to read-out application specific integrated circuit (ASIC). Further details on strip and pixel detectors can be found in [55].

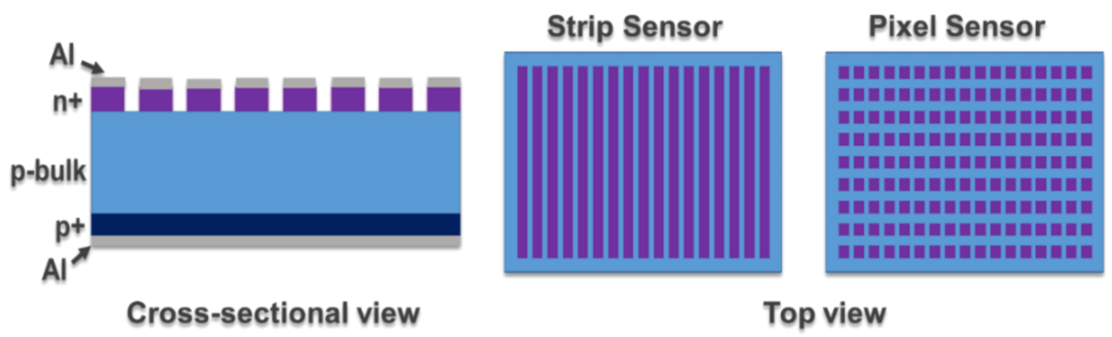

Figure 3.4: A simplified structure of semiconductor sensors used in high energy physics.

The operation of silicon sensors are carried out in a reverse bias condition, where the space charge region (SCR) widens as the reverse biasing voltage (V_b) increases. The relationship between the width (W) of the SCR and V_b can be described using the following equation [55]:

$$W = \sqrt{2\varepsilon\mu\rho V_b} \tag{3.2}$$

where ε, μ are the permittivity and permeability while ρ is base resistivity of the silicon sensor. The depletion region grows with V_b and only a small leakage current flows. This leakage current is present due to a diffusion component and a thermal generation component from outside and inside the space-charge region respectively. Additionally, the voltage at which the SCR becomes equal to the sensor thickness (D) is referred to as the full depletion voltage (V_{FD}), and it can be calculated using the equation (3.2) by inserting $W = D$:

$$V_{FD} = \frac{D^2}{2\varepsilon\mu\rho} \tag{3.3}$$

At the V_{FD}, the diffusion current due to minority carriers becomes negligible due to their large diffusion lengths within the SCR. However, thermal generation of electron-hole pairs within the SCR contributes to the leakage current (I_L), which can be expressed as [55]:

$$I_L = \frac{1}{2} eAw\sigma N_t v_{th} n_i \tag{3.4}$$

Here, A represents the area of the sensor, σ signifies the charge carrier cross-section, N_t denotes the impurity state concentration at the middle of the band gap, and v_{th} represents the thermal velocity. Notably, the presence of the term n_i (intrinsic carrier concentration) makes I_L temperature-dependent, as n_i varies with temperature

$$n_i \propto T^2 e^{\frac{-E_b}{k_B T}} \tag{3.5}$$

where E_b is the bandgap energy and k_B is the Boltzmann constant.

A charged particle traveling at relativistic speeds when traverses a medium causing the ionisation of atoms, due to its electromagnetic interaction with electrons of the medium, and resulting in energy loss. The mean ionisation energy of silicon is 3.6 eV. The Bethe-Bloch curve, as shown in Figure 3.5, describes the average amount of energy that particles lose with

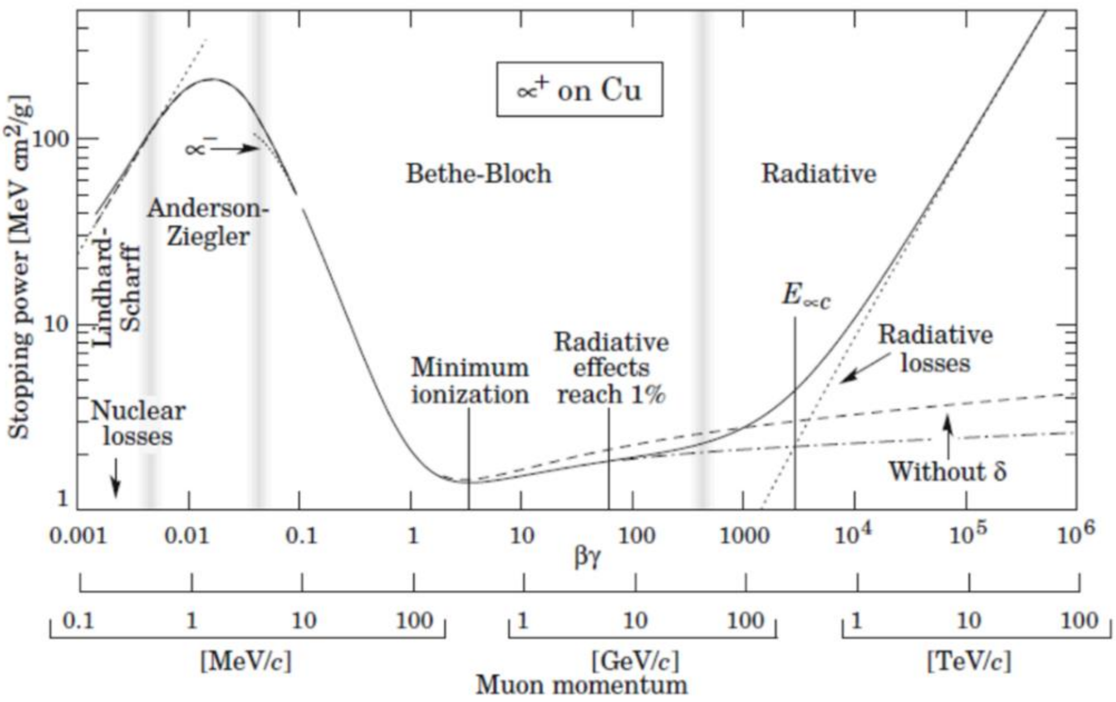

Figure 3.5: Stopping power of copper for muon traversal [55]. The sensor design should be capable of detecting minimum ionizing particles (MIPs). Here $\beta = \frac{v}{c}$ and $\gamma = \frac{1}{\sqrt{1-\beta^2}}$.

increasing momentum when traversing through copper. The most notable aspect of the curve is the minimum, representing the minimum deposited energy, at value $\beta\gamma = 3$. To detect Minimum Ionizing Particles (MIPs), every detector must maintain its noise well below this energy level.

Reverse-biased silicon sensors can operate as a semiconductor detector, as charged particles passing through its depleted region lose some of their kinetic energy and produce electron-hole pairs. The electrons and holes start to drift under the influence of the applied bias voltage and produces an electric current pulse on the electrodes, following the principles of the Schockley-Ramo theorem [56]. The amplitude of the pulse is proportional to the number of particles drifting in the electric field. The time taken from the start of drift to the final collection of particles is referred to as the charge collection time, which is used to characterize a sensor. The collection time is typically of the order of O(10 ns) and is smaller in case of electrons.

3.1.4 Read-out Electronics

The ASICs attached to sensors are known as front-end electronics and contain multiple channels, each with an amplifier and discriminator. Each segment of the sensor is connected to a channel in the ASIC, and thus the collected current in a segment of the sensor is integrated, and the resulting charge is compared with a reference voltage known as the threshold voltage. If the collected charge is greater than the threshold voltage, then an information bit is formed, known as a hit. In the next stage of front-end electronics, the information collected by all channels is combined, and this stage is referred to as digital sampling. Further understanding about the front-end module can be found in [55].

Once the front-end electronics collect the data, it is sent to the Data Acquisition (DAQ) system, which aggregates and stores the information. This system is also known as the back-end electronics. Together, the semiconductor sensor, readout electronics, and mechanical support make up the silicon tracking detector.

The Silicon tracking detector at CMS has a granularity of approximately O(10^8) channels, and its detector subsystem has a sampling rate of 40 MHz.

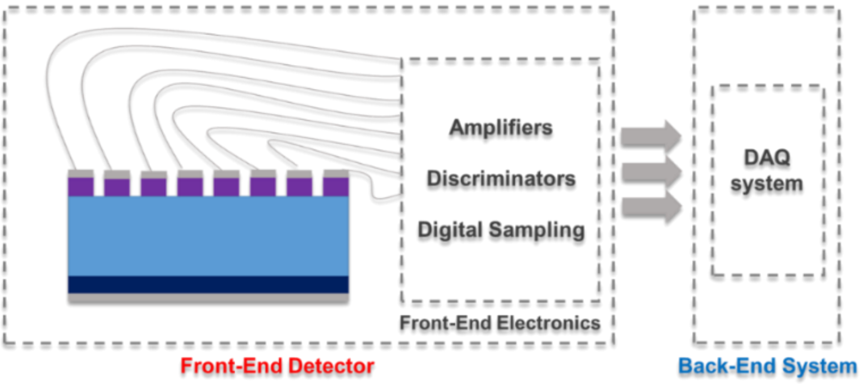

Figure 3.6: Read-out chain of a silicon detection system.

3.2 Tracking Detector

The basic idea behind the tracking detector is that the charged particles, bent by the magnetic field due to the Lorentz force ($\vec{v} \times \vec{B}$), produce electrical signals in silicon sensors arranged in cylindrical layers. The sensors provide positional information about the charged particle. Combining data from different layers helps to recreate the particle's path, known as a 'track'. Figure 3.7(a) illustrates that when moving through the axial magnetic field, a charged particle follows a curved path with a radius of curvature *R*. The transverse momentum p_T of a singly charged particle can be computed as follows

$$\frac{mv^2}{R} = evB$$

$$\Rightarrow \qquad p_T = 0.3\,BR \tag{3.6}$$

The units for *p*, *B*, and *R* are expressed in GeV/c, Tesla, and meters, respectively. The curvature radius (*R*) can be found using the sagitta (*s*) and the path length (*L*), as illustrated in Figure 2.7(b). The relationship between these quantities is given by:

$$s = R - R\cos\frac{\varphi}{2} \approx R\frac{\varphi^2}{8}$$

$$\Rightarrow \qquad R = \frac{L^2}{8s} \qquad where\ \ \varphi = \frac{L}{R}$$

substituting the value of '*R*' in equation (3.6)

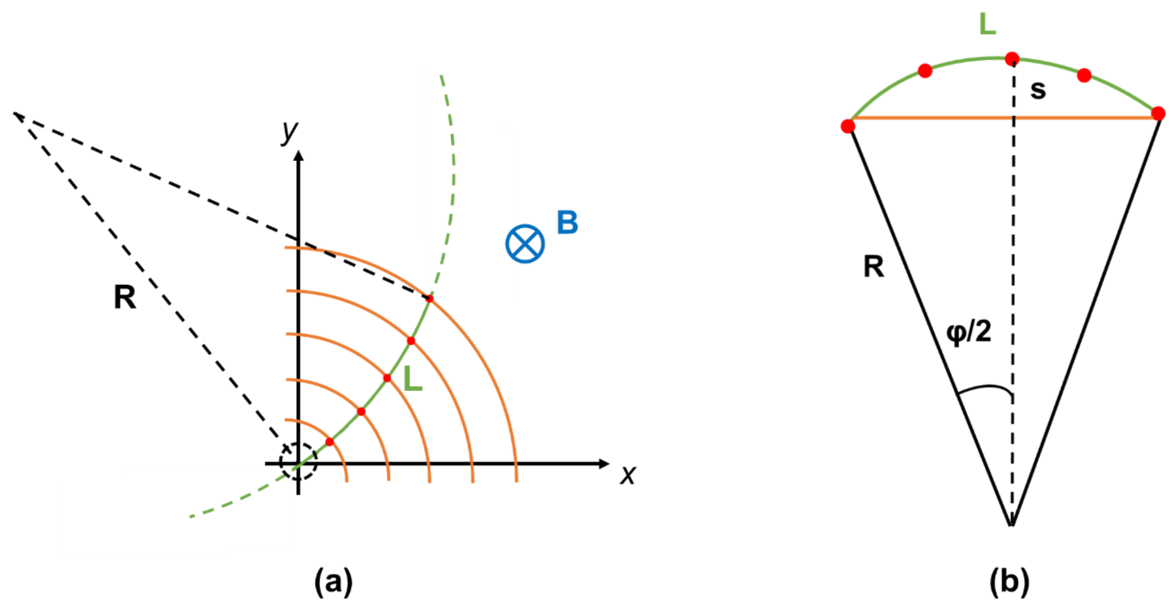

Figure 3.7: Principle of silicon tracking detector for track reconstruction. (a) Charged particle passing through detector layers. (b) Parameters: curvature radius *R*, sagitta (*s*), and path length (*L*) used for momentum calculation.

$$p_T = \frac{0.3BL^2}{8s} \qquad (3.7)$$

therefore, the momentum resolution "σ (p_T)" depends on resolution of sagitta "σ (s)" as

$$\frac{\sigma(p_T)}{p_T} = \frac{\sigma(s)}{s} = \frac{8p_T}{0.3BL^2}\sigma(s) \qquad (3.8)$$

In case of 'N' points σ (s) depends on position resolution "$\sigma_{r\varphi}$" of measurement points as provided in reference [57]

$$\sigma(s) = \sqrt{\frac{720}{N+4}}\frac{\sigma_{r\varphi}}{8} \qquad (3.9)$$

$\sigma_{r\varphi}$ has contributions from intrinsic factors and multiple scattering. Thus, it is evident from equations (3.7) and (3.9) that the momentum resolution depends on the position resolution of individual measurement points, magnetic field **B**, and path length (L) of the tracks.

3.3 CMS Tracking Detector

The CMS features a silicon tracking detector, situated at its innermost region. It comprises of both silicon pixel and strip sensors. Figure 3.8, depicts the one-quarter view in the r-z plane (with r in the x-y plane) of the current CMS silicon Tracker. The detector has dimensions of 5.6 meters in length and 2.5 meters in diameter. It is designed to provide coverage in pseudorapidity range $-2.5 < \eta < 2.5$ (η as specified in equation 2.48). The silicon pixel section is positioned closest to the interaction point, surrounded by the silicon strip section. The tracking detector's total active area is approximately 200 m^2, with the strip detector accounting for 198 m^2 and the pixel detector contributing about 1.75 m^2 of active area.

Currently, the silicon pixel section consists of the Phase-1 pixel detector, comprising 124 million pixels, each measuring 100 x 150 μm^2. These pixels are distributed across 1856 pixel modules, spanning 4 barrel layers and 3 end-cap disks. The barrel layers are situated at distances of 29 mm, 68 mm, 109 mm, and 160 mm from the center, while the end-cap disks are positioned at z = ± 291 mm, ± 396 mm, and ± 516 mm.

On the other hand, the silicon strip detector section spans radially from 200 mm to 1160 mm and up to ± 2820 mm in the z-direction (refer to Figure 3.8). It comprises 15148 modules, housing a total of 9.6 million micro-strips ranging from 80 µm to 205 µm in width and 10 cm to 20 cm in length. By utilizing various types of strip modules with differences in thickness, strip length, and pitch, modules can be placed where they best fit. The strip detector is composed of 10 barrel layers, consisting of Tracker Inner Barrel (TIB) and Tracker Outer Barrel (TOB), and 12 disks formed by Tracker Inner Disks (TID) and Tracker End-Caps (TEC).

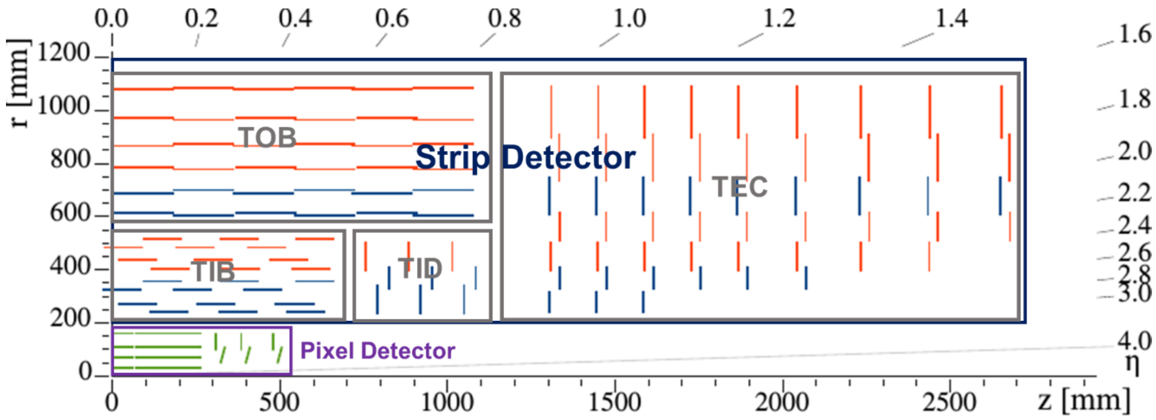

Figure 3.8: A one-quarter view of current CMS Tracker is presented in the r-z orientation for visualization [58]. The innermost section is composed of a pixel modules, while the outer section is made of strip modules and segmented into inner barrel (TIB), inner disk (TID), outer barrel (TOB), and end-caps (TEC).

3.4 Performance of the CMS Tracker

Figure 3.9 illustrates the hit efficiency of the Phase-1 pixel detector, which remains above 98% even at an instantaneous luminosity of 1.5 x 10^{34} $cm^{-2}s^{-1}$. In Figure 3.10, it is shown that the hit efficiency exceeds 99% and 98% at luminosity 1.8 x 10^{34} $cm^{-2}s^{-1}$ for the strip detectors TIB and TOB, respectively. Overall, both pixel and strip detectors exhibit very high hit efficiency, except for Layer 1 in the pixel detector, which is designed for an instantaneous luminosity of 1.5 x 10^{34} $cm^{-2}s^{-1}$ and demonstrates an efficiency of approximately 98% at this level.

Figure 3.11 depicts the track reconstruction efficiency simulation for the Phase-1 Tracker under different pile-up (PU) conditions as a function of η. An efficiency of 98% is attained in the barrel region, up to $|\eta| < 1$, with a slight drop observed in efficiency in the transition region from the barrel to the end-caps (the values of η in barrel and endcap regions are more clearly visible in Figure 3.8). There is a noticeable decrease in efficiency in the forward region, possibly attributed to the absence of a detection system.

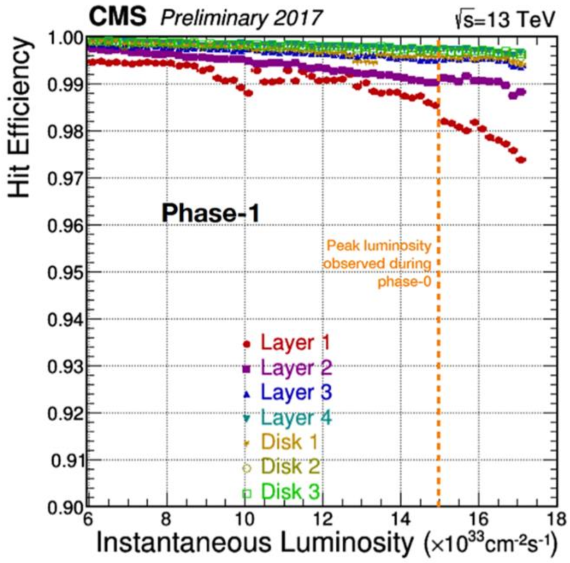

Figure 3.9: The hit efficiency of CMS Phase-1 pixel detectors versus the instantaneous luminosity of the LHC [59].

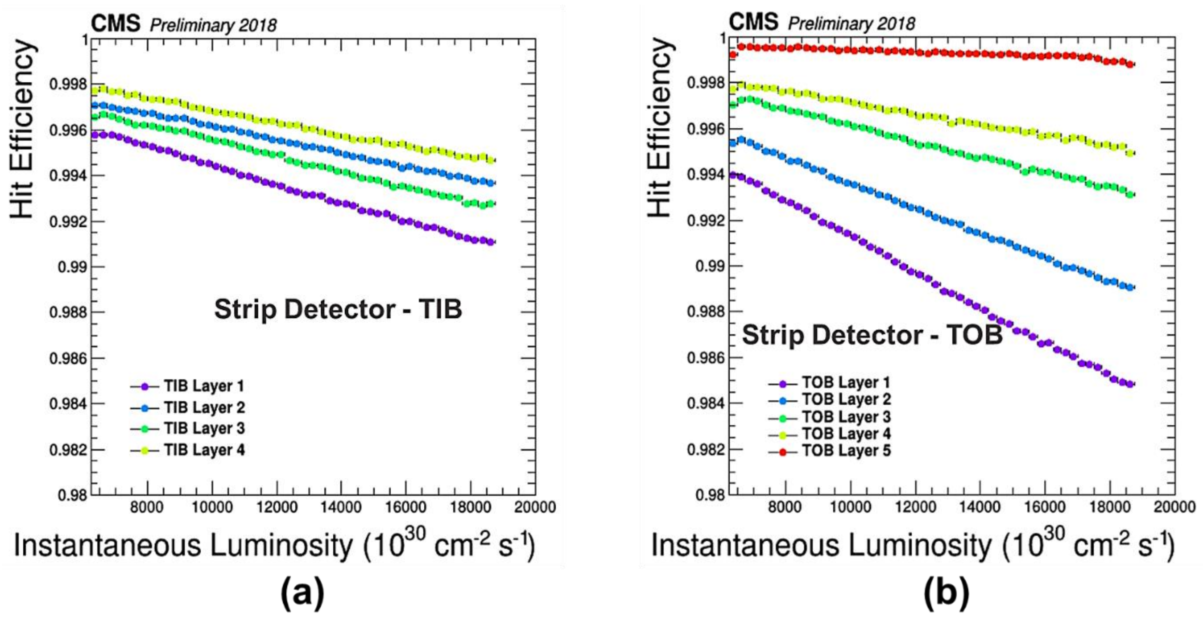

Figure 3.10: The hit efficiency versus instantaneous luminosity of LHC for CMS Tracker strip detector (a) TIB part and (b) TOB part [60].

Figure 3.12 (a) presents a comparison of the simulated track p_T resolution of the Phase-1 Tracker with that of the initial Phase-0 Tracker. The Phase-1 tracker exhibits improved p_T resolution in the region $\pm1.2 < |\eta| < \pm1.6$. This enhancement is attributed to the incorporation of a fourth layer into the Phase-1 pixel detector [61]. Additionally, Figure 3.12 (b) shows a comparison of the rate of falsely reconstructed tracks in Phase-0 and Phase-1 Trackers, highlighting the better performance of the Phase-1 Tracker.

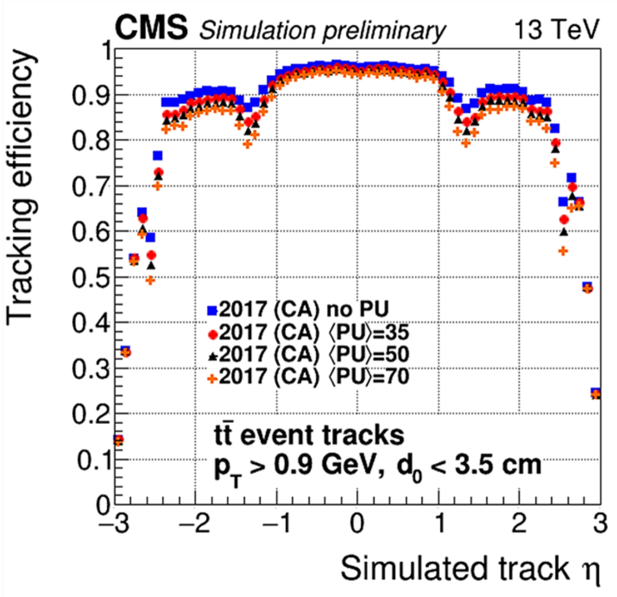

Figure 3.11: Simulated track reconstruction efficiency for the Phase-1 tracker at different pileup conditions [62].

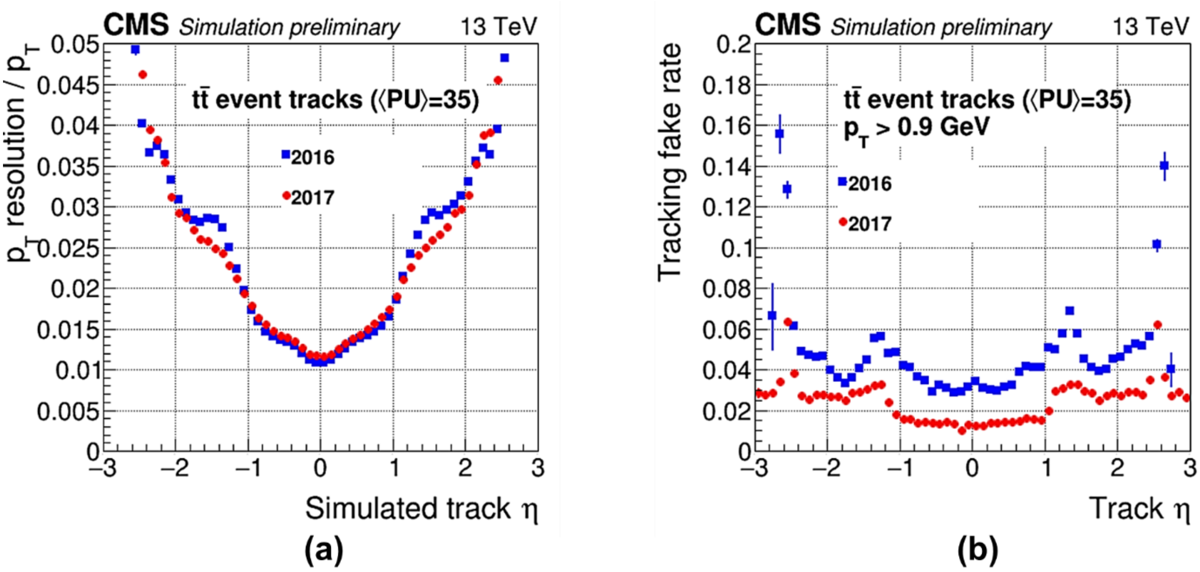

Figure 3.12: Comparison of the (a) simulated track p_T resolution and (b) simulated tracking fake rate for Phase-0 (2016) and Phase 1 (2017) Trackers [62].

3.5 Radiation Damage

When particles traverse a silicon detector, collisions with atomic electrons cause energy loss, leading to ionization in silicon, which forms the basis of detection. Energetic charged and neutral particles passing through the silicon detector are not only detected but also induce permanent damage, consequently degrading detector performance. The damage can be classified as surface or Ionizing Energy Loss (IEL) and bulk damage or Non-Ionizing Energy Loss (NIEL).

i. Ionizing Energy Loss

Surface damage in silicon sensors is mainly caused by ionizing radiation, and it mostly affects the thin insulating silicon oxide layer between the sensor channels. The excess of charge carriers produced by ionizing radiation inside the semiconductor cannot cause permanent damage since they can recombine or get attracted towards the electrodes. However, in the case of an oxide layer on top of the sensors, ionization increases the fixed oxide charges and interface traps. The positive oxide charges attract minority electrons from the p-bulk and affect the isolation between the sensor channels. This, in turn, increases bulk current and cross-talk between the read-out channels, leading to additional noise in the detector channels and degraded detector resolution.

ii. Non-Ionizing Energy Loss

Non-ionizing radiation is the main cause of bulk damage in silicon sensors. When heavy charged particles undergo elastic collisions with atomic nuclei in the crystal lattice, it can dislocate individual atoms or Cluster defects are formed based on the energy of the dislocated atom. The semiconductor experiences new energy levels due to the presence of these defects, which can cause parasitic current through the detector and trap charge carriers in the defective zones. This affects the charge collection time and detector efficiency, ultimately degrading the sensor. Further details on sensor radiation damage can be found in [58, 59].

iii. Single Event Upset

Ionizing radiation can also induce charge in the detector integrated circuit, which is known as a single event upset (SEU) [65]. This can corrupt digital information temporarily, but it does not cause permanent damage, and the information can be recovered after the electronic circuit is reconfigured.

iv. Radiation Effects on the Current CMS Tracker

A front-end module operated in an environment with high radiation can be recalibrated, operated at low temperature, and high bias voltage to compensate for permanent damage. However, at some point, the noise level becomes so high that the signal cannot be distinguished. The current strip detector in CMS Tracker is capable of operating with full efficiency up to an integrated luminosity of 500 fb^{-1} and an average pileup (PU) of fewer than 50 collisions per bunch crossing. As shown in Figure 3.13, after operation up to 1000 fb^{-1}, many layers of the strip detector will no longer remain operational due to high leakage current or full depletion voltage limitations. These non-functional layers in the TEC, TOB, and TIB are indicated in blue.

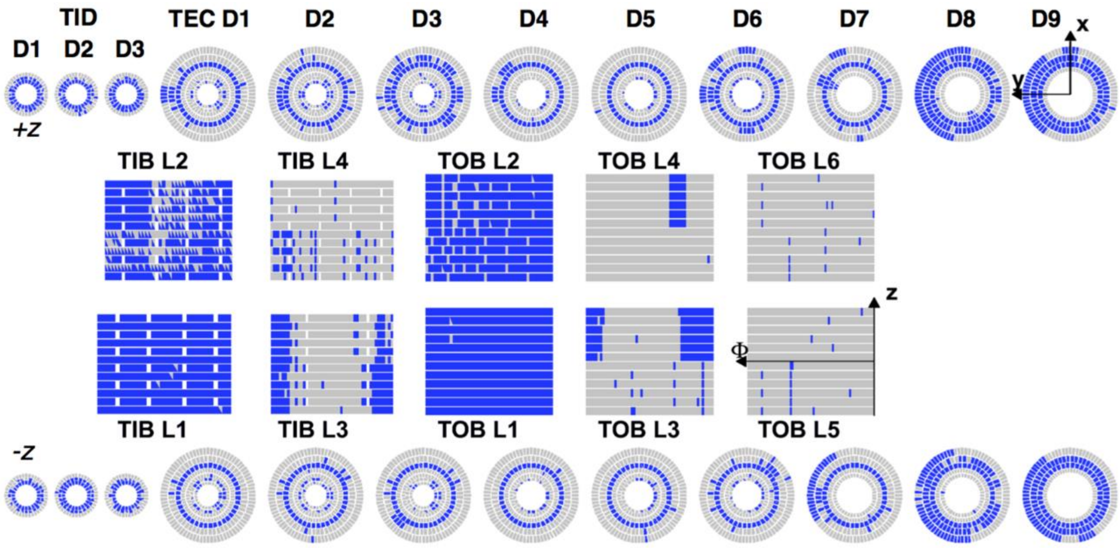

Figure 3.13: A map indicating the non-functional modules, highlighted in blue, after an integrated luminosity of 1000 fb^{-1}, given that the minimum achievable coolant temperature is -20 ºC. [2].

4

The CMS Tracker Phase-2 Upgrade

The LHC is undergoing an upgrade to the High-Luminosity LHC (HL-LHC), with the goal of increasing luminosity, which consequently raises the radiation environment within the detection systems. To address this, the CMS detector will undergo a Phase-2 upgrade. This chapter focuses specifically on the CMS Tracker Phase-2 upgrade. The information in this section is primarily originates from references [58].

During CMS Phase-2 upgrade, two types of modules, namely Strip-Strip (2S) and Pixel-Strip (PS), will be implemented in the Outer Tracker. These modules utilize a new concept of p_T discrimination and enhance the detection capabilities of the CMS detector. At the end of this chapter, there will be a comprehensive discussion about the 2S module, covering its features, functionalities, and its role in improving the detection capabilities of the CMS detector.

4.1 The High Luminosity LHC Upgrade

4.1.1 Physics Objective

The LHC is presently in RUN 3 and has a notable history of physics programs. One of its most significant achievements was the discovery of the SM Higgs Boson in 2012 by the CMS and ATLAS collaborations [39 - 40]. Following this discovery, both CMS and ATLAS have confirmed the decay of the Higgs boson into the standard model (SM) gauge bosons (W and Z) and photons with over 5σ significance. Furthermore, investigations into the Higgs decay into fermions such as $\tau^+\tau^-$ [66, 67] and $b\bar{b}$ [68, 69] have reached over 5 sigma statistical significance, fully aligning with Standard Model expectations for their corresponding couplings. Additional statistical data gathering is necessary to enhance the precision of SM measurements. Another idea to expand the Standard Model for higher energy levels is by using Super Symmetry (SUSY) and other theoretical models, which introduce new particles (refer to section 2.1.3). Experimental studies at the LHC indicate that physics processes in these models are associated with small cross-sections, posing challenges in their detection. Achieving the large data samples are required to detect these very rare events could be feasible only through extended operation of the LHC, which is currently impractical.

The LHC accelerator will be upgraded to high luminosity LHC (HL-LHC) [1] to run at the instantaneous luminosity of 5 x 10^{34} $cm^{-2}s^{-1}$ which is five times higher compared to the current LHC design. This upgrade will imply that up to 200 pileup collisions, leading to an annual luminosity of 300 fb^{-1} and integrated luminosity of approximately 3000 fb^{-1} over 10 years, an accumulation that would take 60 years under nominal LHC conditions.

CMS will be able to attain precision at the per cent level for multiple Higgs couplings through the HL-LHC, and this significant improvement can be visualized by referring to Figure 4.1. Additionally, despite the Higgs boson pair production cross-section being approximately 1000 times smaller than that of single Higgs boson production, it is still anticipated that the measurement of the trilinear Higgs boson coupling will be possible at the HL-LHC. Moreover, by increasing the integrated luminosity, indirect searches for physics beyond the standard model can be carried out through the measurement of rare decays. Figure 4.2 illustrates the mass fit projection of $B_{s,d}$ to di-muons decay. In this decay, B_s to di-muons is expected to become a precision measurement, while the B_d to di-muons is anticipated to achieve a significance of 6.8σ. The HL-LHC has the potential to uncover novel channels with low production cross-sections or feeble coupling strengths, leading to potential breakthroughs in various beyond standard model research areas like SUSY exploration, extra dimension analysis, and more. Further insights into the physics motivations of the HL-LHC can be found in references [2], [70].

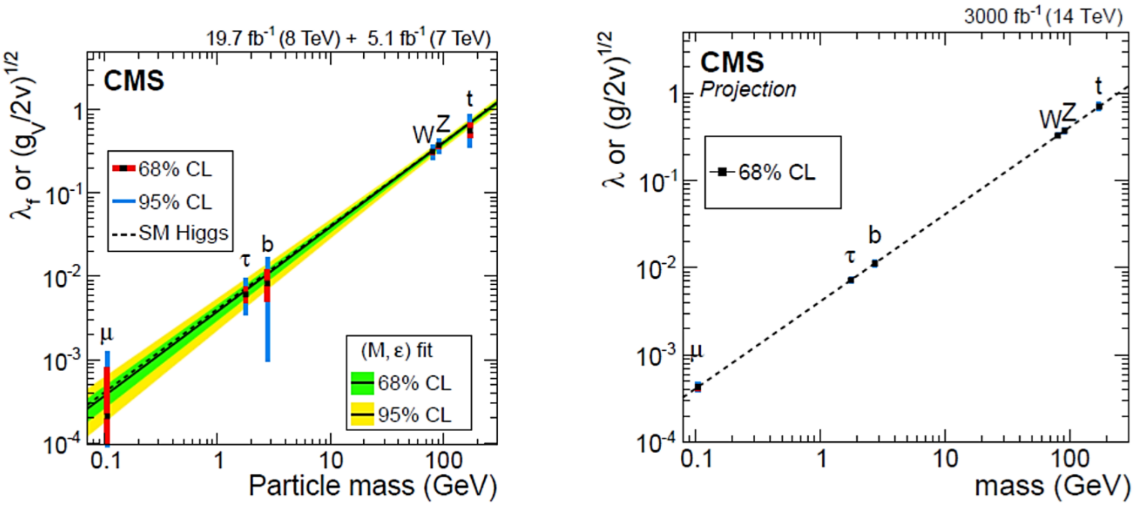

Figure 4.1: On the left side, the LHC results show the precision on the couplings of the Higgs boson, observed with 24.8 fb^{-1} data. On the right side, the same precision is projected from HL-LHC results, as a function of the masses of the bosons or fermions involved. [70].

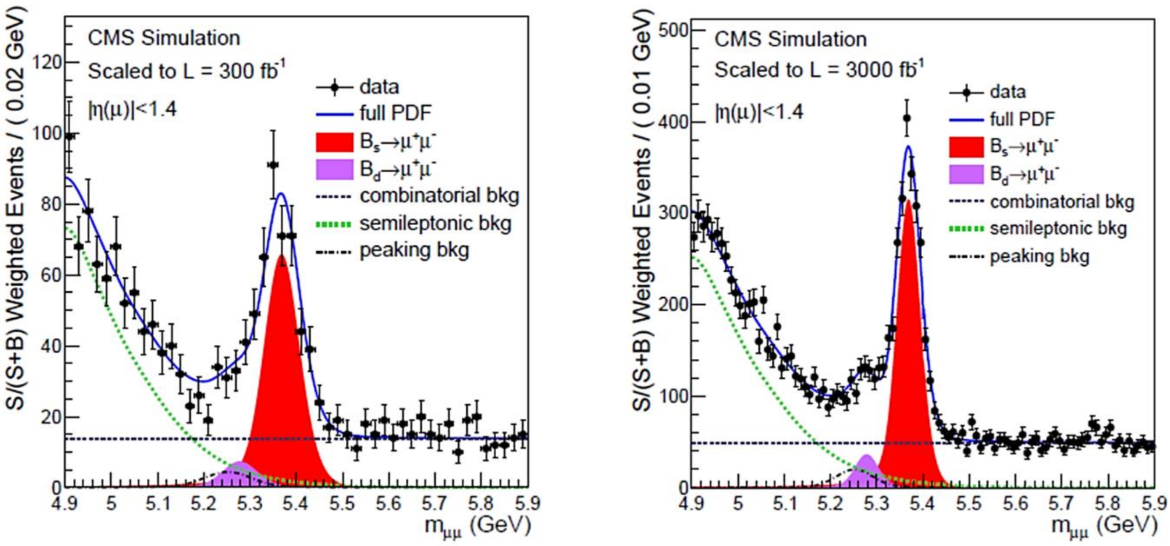

Figure 4.2: Projections of mass fits for the $B_{s,d} \rightarrow \mu^{+}\mu^{-}$ measurement with expected performances of Phase-I and Phase-II CMS detectors, for 300 fb^{-1} (left) and 3000 fb^{-1} (right) of integrated luminosity (adapted from [70]]).

4.1.2 HL-LHC Upgrade Project

The HL-LHC project is scheduled to commence in three years from 2026 to 2028 (Figure 4.3). As part of upgrade project, the installation of new cryogenic system and powerful bending magnets have already been performed during the long shutdown 2 (LS-2) [71]. The upgrade project of the injection system, LIU, has also been completed during LS-2 [72].

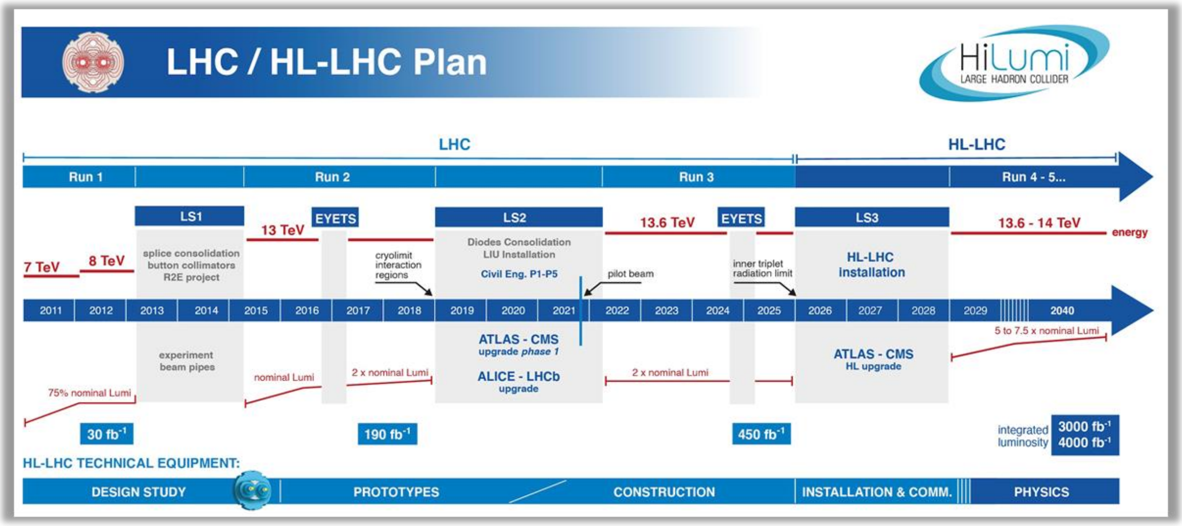

Figure 4.3: The LHC current scenario and HL-LHC upgrade plan*.

During the long shutdown 3 (LS-3), the LHC accelerator will be upgraded to reduce beam sizes in the interaction regions and increase luminosity. This will be achieved through the use of Nb_3Sn insertion magnets, which are capable of producing peak magnetic fields of 12 T. Superconducting radio-frequency crab cavities will also be implemented in both the CMS and ATLAS experiments, with the aim of further increasing luminosity.

The current collision process inside the experiment is demonstrated in the left panel of Figure 4.4, in which elliptical bunches cross each other at a certain angle, resulting in a low interaction rate and limited overlap. However, the use of crab cavities will turn bunches before collision as illustrated in the right panel of Figure 4.4, thus increasing luminosity. The crab cavities located at the beam exit position will return bunches to their original orbits. For further detailed information about the LHC upgrade to HL-LHC, please refer to [1].

* The plan has been replicated from https://hilumilhc.web.cern.ch/article/ls3-schedule-change

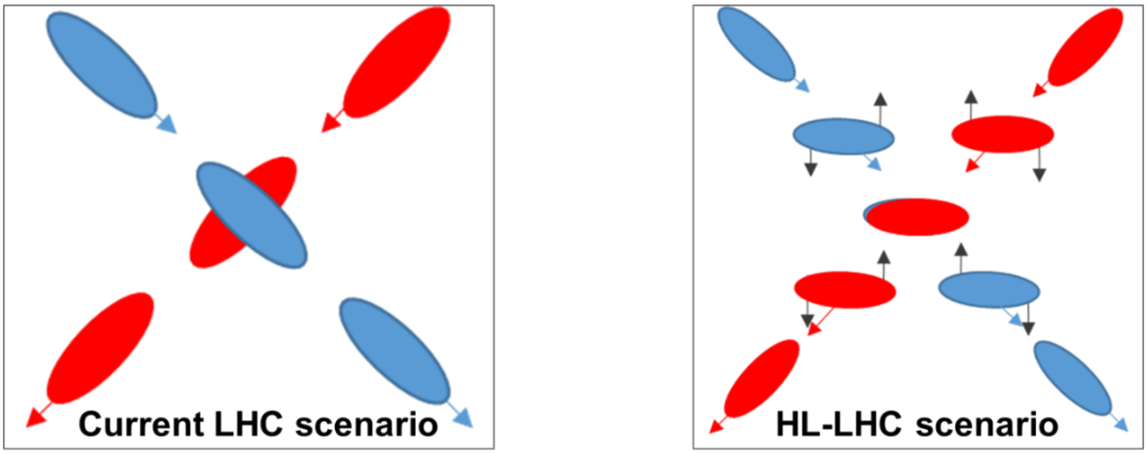

Figure 4.4: The influence of crab cavities on particle beams is depicted by showcasing a side-by-side comparison of the current LHC collision (on the left) and a collision involving crab cavities (on the right).

The HL-LHC is planned to operate at a center-of-mass energy of 13.6 – 14 TeV, with a particle beam bunch spacing of 25 ns. Upon completing the installation and commissioning phase, the HL-LHC is projected to operate for the next decade and achieve peak luminosity of 5 x 10^{34} cm^{-2} s^{-1}, with the potential to reach 7.5 x 10^{34} cm^{-2} s^{-1} [73]. These improvements will enable the CMS and ATLAS detectors to collect integrated luminosities of up to 3000 fb^{-1} over the expected lifespan of the HL-LHC.

4.2 CMS Phase-2 Upgrade

The higher luminosity of HL-LHC is expected to cause a significant increase in the number of pile-up interactions, which could reach up to 140 – 200. Figure 4.5 depicts a comparison between collisions during RUN-2 and those expected in HL-LHC conditions. The increase in pile-up interactions may create difficulties for the current detectors to operate consistently and effectively. To address this issue, upgrades for experiments such as CMS and ATLAS are currently under development for HL-LHC. The CMS detector is scheduled for a Phase-2 upgrade that involves improving its detection system, front-end electronics, and DAQ system. A brief overview of the CMS Phase-2 upgrade is presented in the following paragraphs, while detailed information can be found in [2].

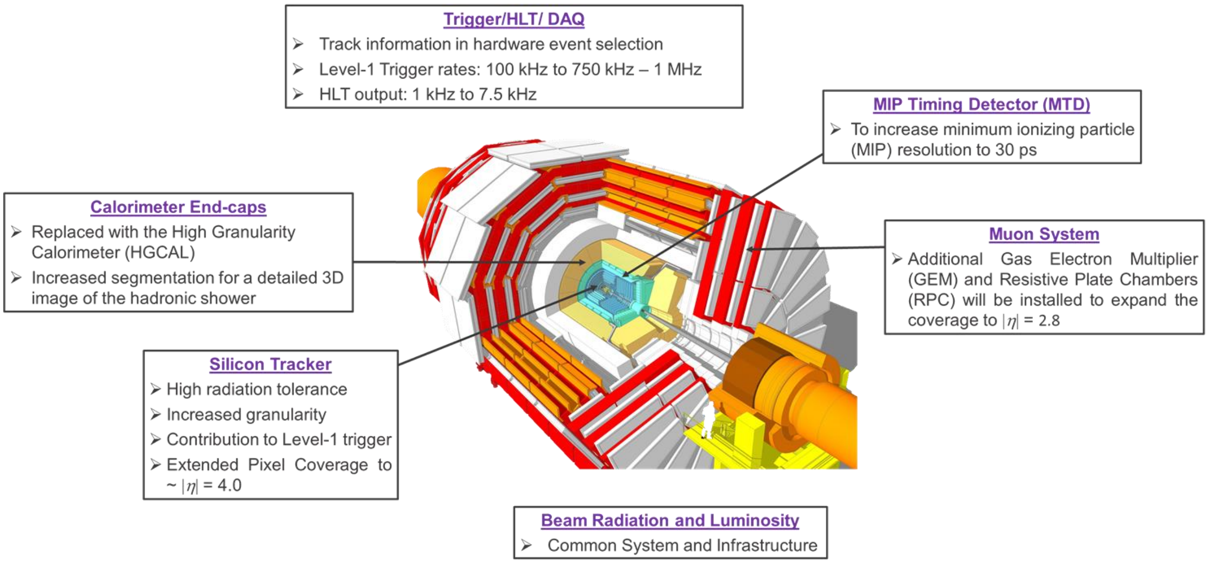

Figure 4.5: The upgrade details of different CMS sub-detectors for Phase-2 upgrade. (Image credit: CMS)

As part of the CMS Phase-2 upgrade, the Silicon Tracker will be replaced completely by a new system to meet challenging demands such as high radiation tolerances and increased granularity. A detailed discussion about the Silicon Tracker upgrade will be presented in next section.

The MIP Timing Detector (MTD) will be added between the Tracker and ECAL to enhance timing resolution for Minimum Ionising Particles (MIPs) to 30 ps [74]. The detector part in barrel section will use Silicon Photomultipliers (SiPMs) and scintillating crystals, while Low Gain Avalanche Detectors (LGADs) will be used in the end-cap region.

The Calorimeter will undergo several upgrades during the CMS Phase-2 upgrade. The front-end electronics in calorimeter's barrel section will be upgraded to eliminate the current 3.2 μs latency constraint [75]. The upgraded electronics will transfer data from each bunch crossing with reduced signal shaping times. This will improve timing precision and lead to a timing resolution of approximately 30 ps of high-energy photons and hadrons. The end-caps of ECAL and HCAL will be replaced with the High Granularity Calorimeter (HGCAL) [76]. The new HGCAL feature tungsten absorbing plates interleaved with silicon sensors for ECAL end-cap layers. The HCAL end-caps near the beam-pipe will use silicon as the detecting material and brass as the absorbing material, while a combination of brass and plastic scintillator will be used in the outer region. The new system will have significantly increased segmentation, resulting in a detailed three-dimensional image of the hadronic shower.

For increased muon trigger acceptance, additional Gas Electron Multiplier (GEM) and Resistive Plate Chambers (RPC) chambers will be installed to expand the coverage (η) up to 2.8 [77]. The current muon system electronics will also be upgraded to handle high data rates.

As part of the CMS Phase-2 upgrade, the CMS DAQ and control system will be enhanced with extended bandwidth capabilities. Additionally, there will be improvements and upgrades made to various other areas including data reconstruction, storage, analysis, access algorithms, luminosity measurement systems, and beam radiation protection. These upgrades will ensure that the CMS detector is equipped to handle the higher luminosity and increased number of pile-up interactions expected during HL-LHC operations.

4.3 Phase-2 Upgrade of CMS Tracker

The current Silicon Tracker will be replaced by a new system as part of CMS Phase-2 upgrade [58] to cope with the challenging demands of high radiation tolerances. The CMS Phase-2 Tracker will feature increased forward acceptance (up to $\eta \sim 4$), increased radiation hardness, higher granularity, contribution to L1 trigger, compatibility with higher data rates and a longer trigger latency.

Figure 4.6 depicts the sketch of one quarter of the CMS Phase-2 Tracker in the *r-z* plane. The new tracker will be composed of two main parts: an Inner Tracker (IT) and an Outer Tracker (OT) shown inside the blue and red boxes, respectively. In order to maintain the occupancy at levels below per million in IT and below a few percent in OT, an increase in granularity is necessary. Where, occupancy refers to the probability of a channel being hit by a particle per bunch crossing. The upgrade also aims at ensuring a better particle tracking performance. Extensive studies on performance degradation have been carried out and are documented in the Technical Proposal for the CMS Phase-2 Upgrade [2].

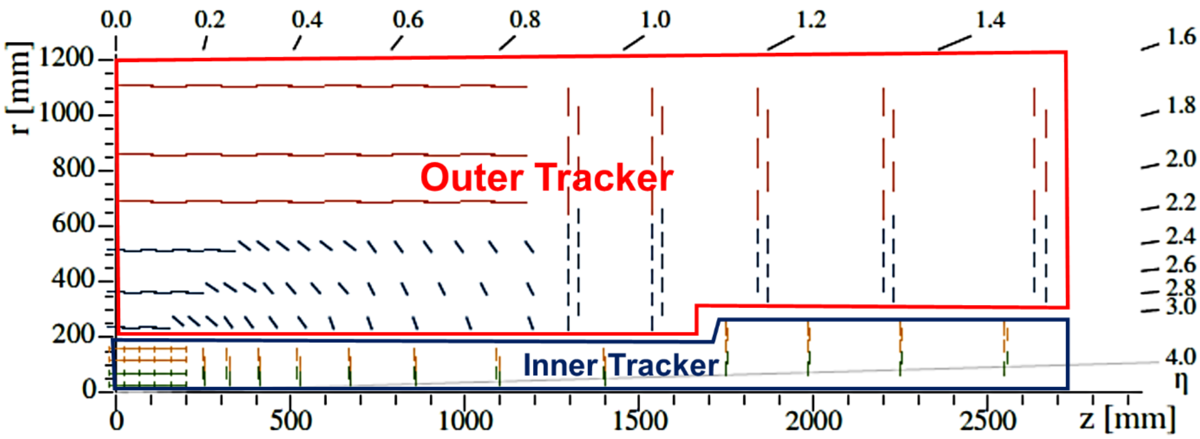

Figure 4.6: A quarter view of the CMS Phase-2 Tracker in the *r*-*z* plane. The tracker is divided into two main components, namely the Inner Tracker (enclosed within the blue box) and the Outer Tracker (enclosed within the red box) [58].

4.3.1 Inner Tracker (IT)

The IT will cover the region up to r ≤ 250 mm and |z| ≤ 2500 mm, as shown in Figure 4.6. The design of IT contains four barrel layers (TBPX), eight small endcap disks (TFPX) and four endcap extension disks (TEPX) on each side along the beam axis which would allow to cover a range of pseudo-rapidity up to $|\eta| = 4.0$ (Figure 4.7). Two types of micro-pixel detector modules will be used in IT [78]: two-chip design (2x1) modules and four-chip design (2x2) indicated as green and orange respectively in Figure 4.7. In IT, pixel sensors with increased granularity, 25 x 100 μm^2 pitch, will be used. The 3D pixel sensors [79], because of their better radiation resistance properties, due to shorter charge drift length, and a reduced heat dissipation associated to the leakage current, will be used in the innermost barrel layer. The micro-pixel readout chip, known as CMS Readout Chip (CROC), will be bump bonded to pixelated silicon sensors. The chip has been developed for both CMS and ATLAS by the RD53 collaboration [80].

4.3.2 Outer Tracker (OT)

The OT will cover the region from 250 ≤ r ≤ 1100 mm and |z| ≤ 2700 mm, as shown in Figure 4.7. It will provide coverage in pseudo-rapidity up to $|\eta| = 2.4$ with its six barrel layers, TB2S and TBPS, and five endcap disks, TEDD, on each of its sides, as depicted in Figure 4.8.

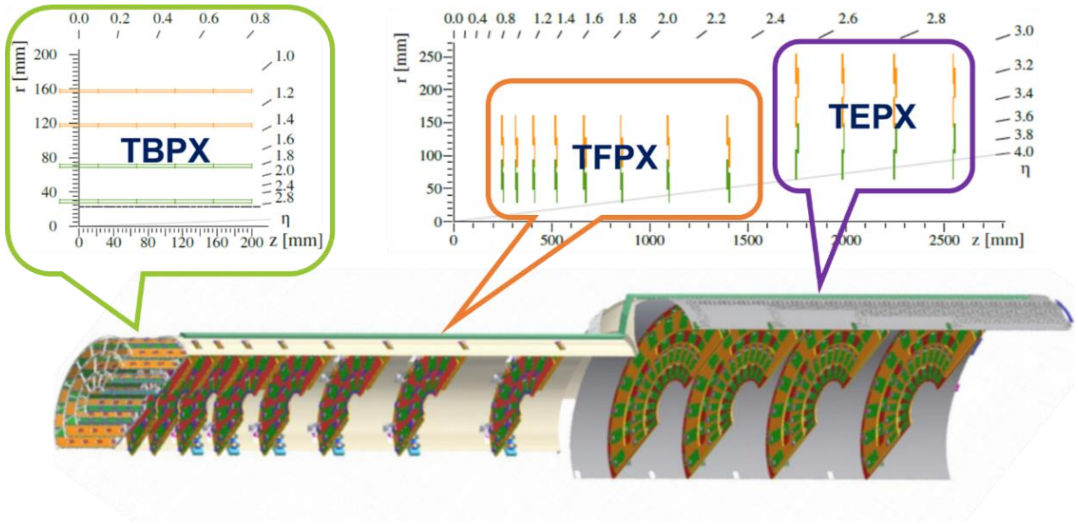

Figure 4.7: A quarter view of the Phase-2 Inner Tracker in the *r*-*z* plane, where the CAD drawing is shown in lower part [58]. The IT is divided into three regions: TBPX, TFPX, and TEPX. The green and orange lines in the upper view indicate the two-chip (2x1) and four-chip design (2x2) modules, respectively.

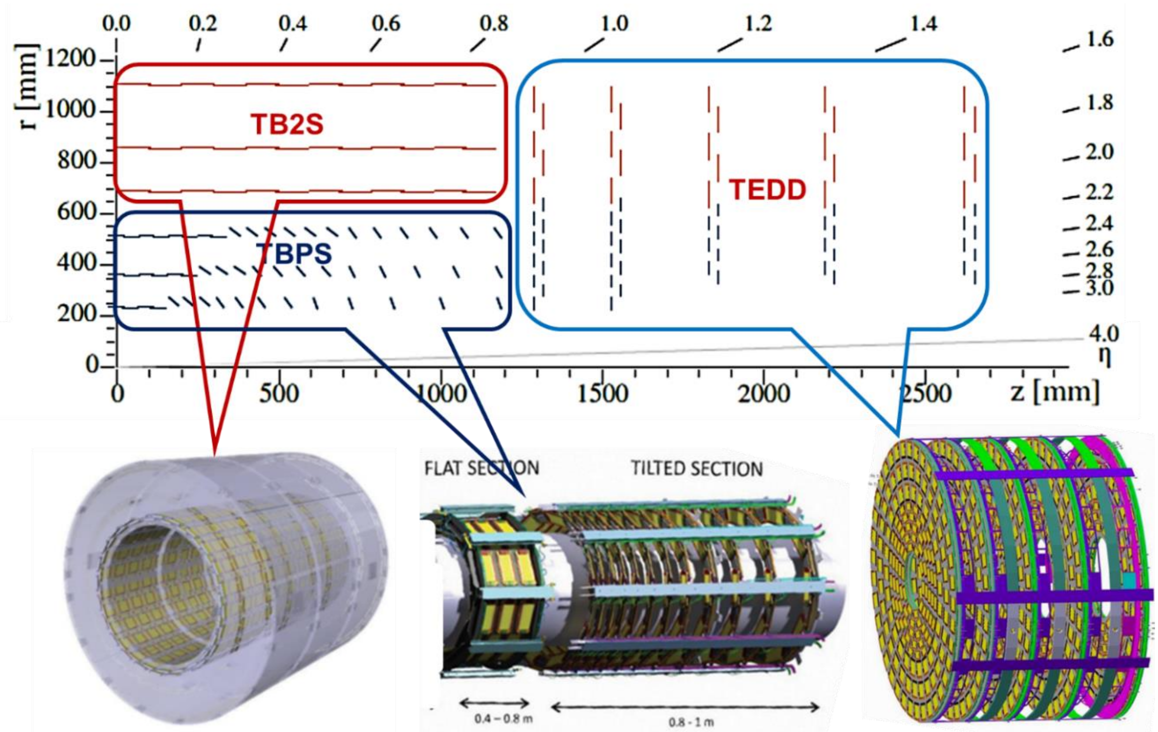

Figure 4.8: A quarter view of the Phase-2 Outer Tracker (OT) in the r-z plane, where the CAD drawings of different portions of detector are shown in lower part [58]. The OT is divided into three regions: TBPS, TB2S, and TEDD. The blue and red lines in the upper view indicate the two-type of pT modules PS and 2S respectively.

The Outer Tracker (OT) will incorporate two types of p_T modules [3], namely 2S and PS, for implementing L1 trigger functionality. Section 4.4 will provide detailed information about these p_T modules. PS modules, featuring a macro-pixel sensor, will be installed in the inner barrel region, TBPS, and at lower radii, up to 700 mm, in TEDD. Conversely, the outermost regions in the barrel section, TB2S, and TEDD will utilize 2S modules. CMS has devised an innovative geometry layout titled TPBS to enhance efficiency in the $|\eta| > 1.5$ region, as demonstrated in simulations shown in Figure 4.9 (further details can be found in reference [58]).

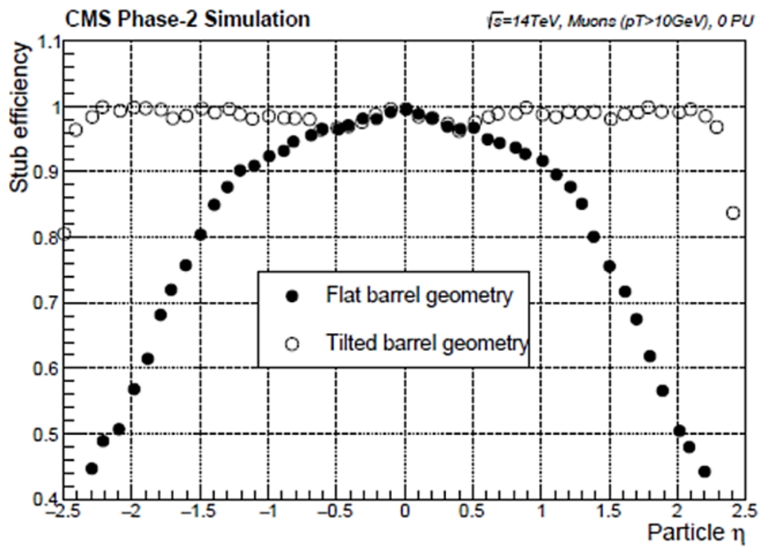

Figure 4.9: Comparison of stub reconstruction efficiency for flat and tilted geometry in TBPS layer 1 in Figure 4.8 (adapted from [58]).

4.3.3 Radiation Environment Modeling

Detailed FLUKA [81, 82] simulations were conducted to assess the radiation levels in different regions of the detector. The simulation results are presented in Figure 4.10, which illustrates the expected maximum fluence levels in 1 MeV n_{eq}/cm^2 (neutron equivalent per cm^2) for various parts of the Tracker. These estimates are based on a total integrated luminosity of 3000 fb^{-1} for pp collisions at a center-of-mass energy of 14 TeV. The fluence in layer 1 in IT is estimated to be 2.3 $x10^{16}$ n_{eq}/cm^2, whereas its values are expected to be 9.6 x 10^{14} n_{eq}/cm^2 and 3.0 x 10^{14} n_{eq}/cm^2 for PS and 2S modules respectively in OT [58]. It is also observed that the fluence levels are primarily dependent on r, with moderate variations in the z-axis.

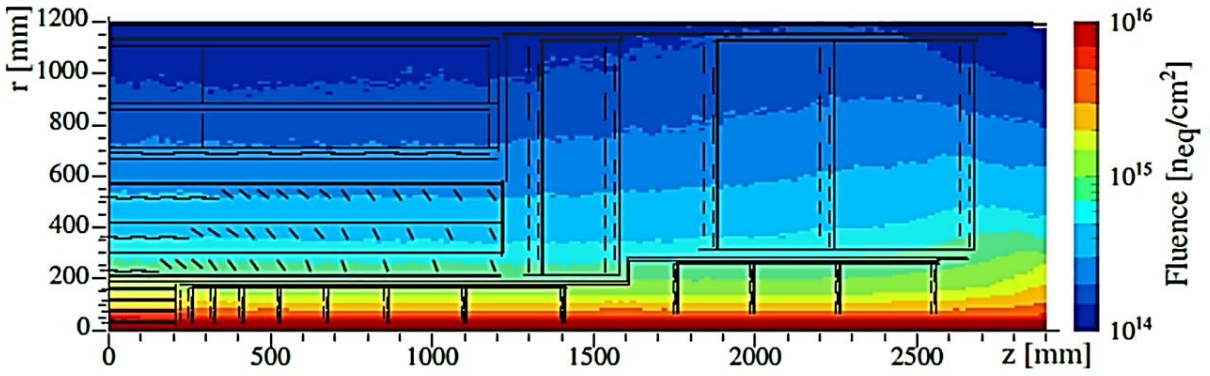

Figure 4.10: The expected maximum fluence values for various parts of the Phase-2 Tracker, were estimated for total integrated luminosity of 3000 fb^{-1} using FLUKA simulations (referenced from[58])

4.3.4 Material Budget Comparison

Material budget measures the amount of material particles encounter in a detector, influencing their trajectory and energy loss. Reducing it is vital for efficient high-energy physics detector design. Figure 4.11 shows that the Phase-2 Tracker, despite having more channels, has a much lower material budget within the tracking volume compared to the Phase-1 Tracker.

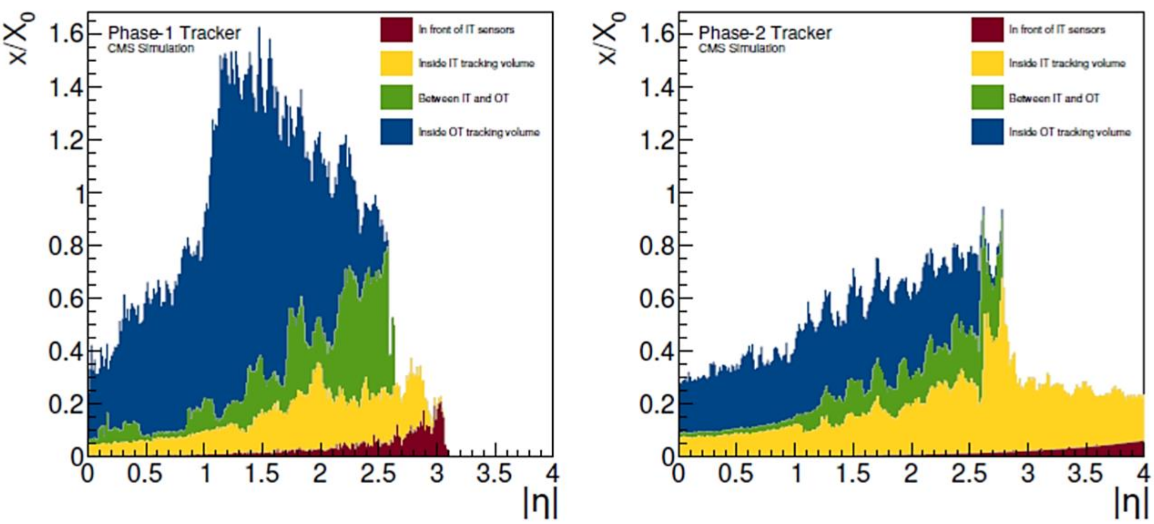

Figure 4.11: Comparison of material budget, estimated in units of radiation lengths, for different regions inside the tracking volume of CMS Trackers, (left) Phase-1 and (right) Phase-2. (adapted from [58])

4.3.5 Projected Performance

Figure 4.12 shows a comparison of the transverse momentum resolutions for single muons with a p_T of 10 GeV at different pseudorapidity values between the Phase-1 and Phase-2 Trackers. The Phase-2 tracker is expected to perform better than Phase-1 system despite of increased event occupancy.

Figure illustrates the simulation results of the tracking efficiency and fake rate for tracks for CMS Phase-2 Tracker. The simulations results are originated for tracks with pT greater than 0.9 GeV, from $t\bar{t}$ events, under 140 and 200 pileup scenarios. The tracking efficiency remains similar under both scenarios. On the other hand, the fake rate remains below 2% across the entire range of η for 140 pileup events, while for 200 pileup events, the fake rate is consistent with the expected performance of the Phase-1 Tracker, as described in Figure 3.12.

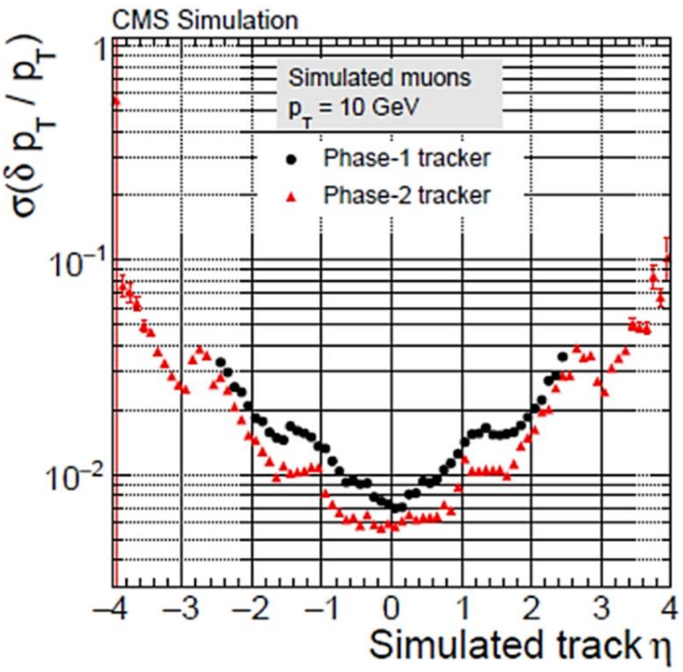

Figure 4.12: The resolutions of the transverse momentum (left) and transverse impact parameter (right) for single muons with a pT of 10 GeV, as a function of pseudorapidity, are compared between the Phase-1 and Phase-2 trackers (adapted from [58]).

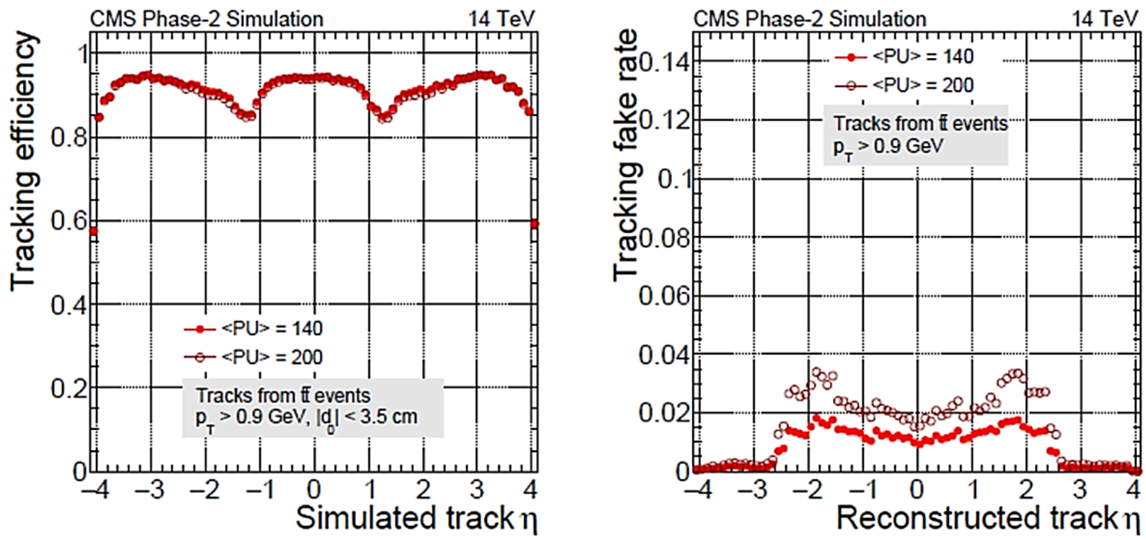

Figure 4.13: A comparison of the track efficiency and fake rate for tracks with a pT greater than 0.9 GeV, originating from $t\bar{t}$ events, as a function of pseudorapidity, under pileup scenarios of 140 and 200 (adapted from [58]).

4.4 pT Modules and Input to L1 Trigger

The high pile-up conditions of HL-LHC make it necessary to enhance the CMS L1 trigger system. To improve the L1 trigger system, two key factors need to be addressed: the selection rate of interesting events needs to be increased, and the discrimination power of the event selection process needs to be improved. To achieve the goal of increasing the selection rate, the CMS collaboration aims to increase the L1 trigger rate from the current 100 kHz to 750 kHz, while extending the latency time from 3.2 μs to 12.5 μs. To accomplish the improvement in event discrimination, the trigger decision information obtained from the modules located in the OT will be utilized. This approach can improve the capacity for discrimination and enable the acquisition of necessary information required for precise detection of interesting events. For this purpose, the modules in OT are based on novel p_T discrimination concept.

The p_T modules function by reducing local data in the front-end electronics of each module, helping to limit the data volume transmitted at the bunch crossing rate of 40 MHz. Equipped to reject charged particles with low transverse momentum (p_T), they utilize the CMS strong magnetic field (3.8 T). Figure 4.14 illustrates this concept, where two silicon sensors in a module act as seed and correlation layers, with the seed layer facing towards the interaction point. As charged particles bend due to the magnetic field, they hit both sensor layers at different positions. Particles with low p_T experience more bending, enabling on-module discrimination of their transverse momentum. Hits on both layers can be matched to form a "stub" by defining a correlation window on the correlation layer. Setting a threshold, such as rejecting particles below 2 GeV, achieves a data volume reduction of approximately ten times, allowing stub transmission at the bunch crossing rate while storing other signals in the module's front-end pipeline until a trigger signal is received. Figure 4.15 shows different sensor spacing values implemented across the OT for equivalent data filtration.

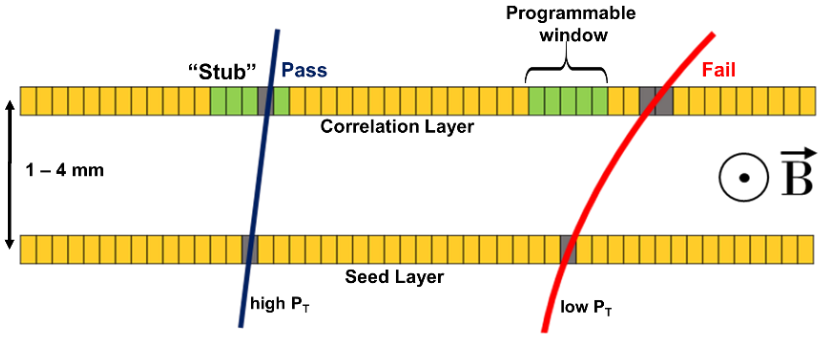

Figure 4.14: The pT discriminating concept that will be used in Phase-2 outer tracker modules to reduce the data volume for L1 trigger. The p_T threshold is determined by the size of the programmable window in the correlation layer. (sourced form [58])

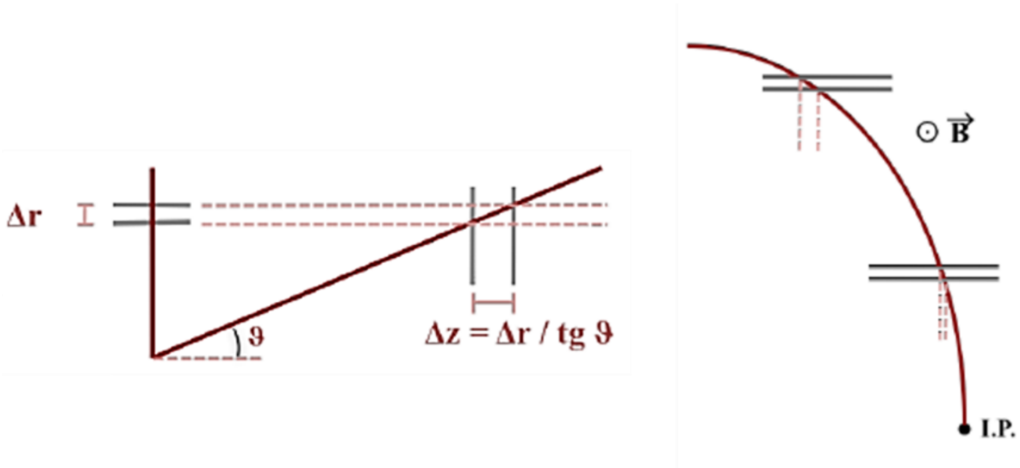

Figure 4.15: Sensor spacing in p_T modules vary to achieve the same discriminating power. The left side shows two modules at the same radius level but in different positions - one in the barrel and the other in the endcap. The right side of figure illustrates that module with the same spacing exhibit larger correlation window at larger radii for the same transverse momentum. (sourced form [58])

The OT will incorporate two types of p_T modules, PS and 2S, as shown in Figure 4.16. The PS modules will feature a macro-pixel sensor (PS-p) with 30720 macro-pixels measuring 100 μm x 1.5 mm, and a strip sensor (PS-s) with 1920 strips having a strip length of 2.5 mm and pitch of 100 μm. To facilitate data readout, the Macro-Pixel Sub-Assembly (MaPSA) will be utilized, which involves bump bonding the PS-p sensor to the Macro Pixel ASICs (MPA) [83]. The strip sensor will be wire-bonded to FEH consisting of the Short Strip ASICs (SSA) [84]. After processing, the SSA sends the cluster data to the MPA, where it is correlated with cluster data of hits on the macro-pixel to construct stubs. The power hybrid (POH) connected to the PS module provides both high voltage for sensor biasing and low voltage for on-module power to SSAs and MPA through a DC-DC converter. The readout hybrid (ROH) is equipped with the LpGBT chip, which serializes the module's data, and VTRx+, the opto-transceiver module, used to connect the module to the back-end electronics.

The 2S module, on the other hand, employs two strip sensors with a strip length of 5 cm and pitch of 90 μm. These strip sensors are wire-bonded to FEH, which consists of the CMS Binary Chip (CBC) [85] for readout purposes. The CBC clusters the hits from both top and bottom sensors and correlates them over a configurable window to generate stubs at Bx rate. Additional details on the 2S module are provided in the following section.

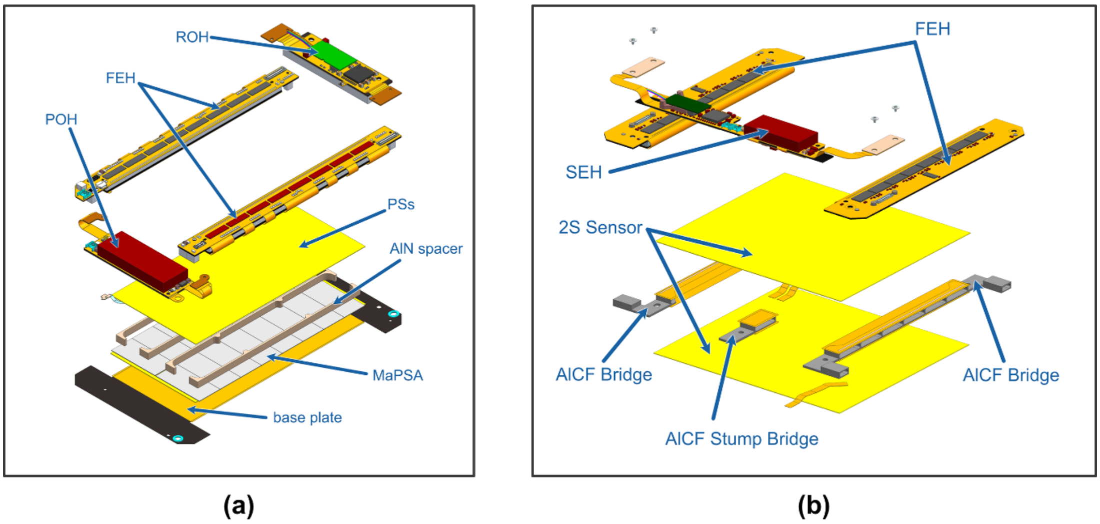

Figure 4.16: 3D sketch illustrating the components of (a) PS module and (b) 2S module.†

† The sketch is provided in [58] but latest designs are copied from https://espace.cern.ch/Tracker-Upgrade/SitePages/Home

4.5 Silicon Strip or 2S Module

The silicon strip-strip or 2S module will be constructed with two distinct sensor spacing: 1.8 mm and 4.0 mm. This section provides at brief insights into the strip silicon sensors, front-end electronics, and mechanics of the 2S module.

4.5.1 Silicon Strip Sensors

A thorough research and development process was conducted to select the appropriate silicon material for OT sensors [86 - 88]. The deep diffuse float zone (ddFZ) has been chosen as wafer material due to its ability to limit the active thickness of the sensor which contributes to the signal, as opposed to the physical thickness. Different sensors and test structures were extensively analyzed for their noise behavior, charge collection, and strip isolation, both before and after being exposed to neutron and proton irradiation. In addition to these parameters, the ability to extract sufficient signal with a leakage current for the bias voltage is also crucial. For OT sensors, those with n-in-p (n-type implants in p-type bulk) polarity were determined to be the best option since the signal is predominantly induced by drifting electrons and the fake hit rate contribution is reduced. The sensor with an active thickness of 290 μm, while a physical thickness of 320 μm, has been finalized [88]. More detailed information regarding the sensors can be found in the specified reference [58].

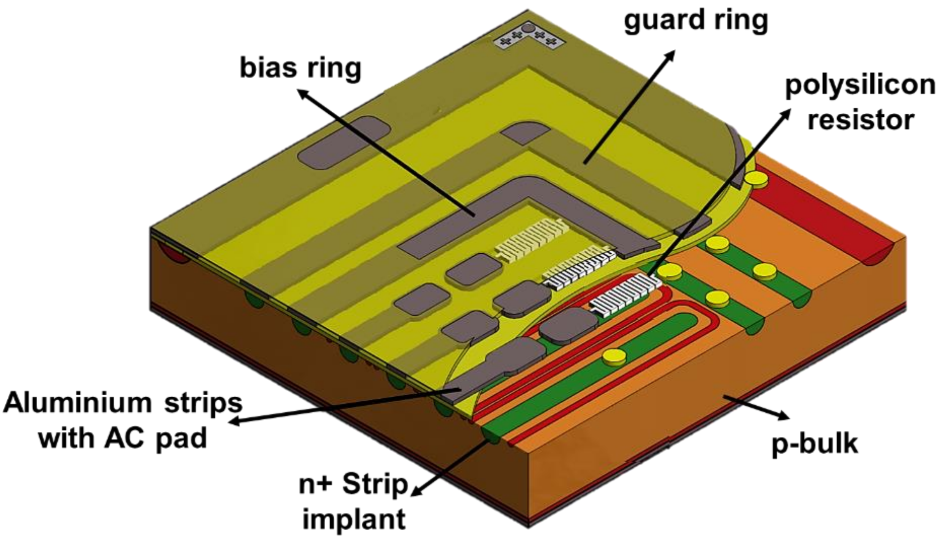

Figure 4.17: This 3D model depicts an AC-coupled silicon strip sensor with n-in-p doping, which shares similarities with the sensors utilized in the Phase-2 Outer Tracker of the CMS experiment. (Figure adapted from reference [55])

Figure 4.17 depicts a segment of the strip sensor schematic, similar to the one that will be used for the strip sensor in the 2S module. The active region of the sensor is encircled by a bias ring, which evenly distributes ground potential to all strips (n+ implants) via a polysilicon resistor (1.5 MΩ). The guard ring guarantees stable sensor operation up to a reverse bias voltage of -800 V. The 2S module will incorporate two identical strip sensors measuring 10 x 10 cm^2, each consisting of 2032 identical strips segmented into two columns of 5 cm length. The sensor is also equipped with proper alignment marks and labels to ensure accurate usage.

4.5.2 Front End Hybrid (FEH)

The Front End Hybrid (FEH) [89, 90] is a crucial component of the module electronics, designed with a high-density interconnect to facilitate efficient wire-bond pad alignment of input channels with both sensors in 2S modules. The FEH is composed of a four-layer polyimide circuit, which is folded over an aluminum nitride and carbon fiber stiffener. Each FEH, designed for 2S module, is equipped with eight CMS Binary Chips (CBC) and one Concentrator Integrated Circuit (CIC). Figure 4.18 depicts three variants of the FEH developed during the prototyping phase. The one on the left, called 8CBC2, had only 08 x CBC2 chips and could be read electrically only. The middle version had 08 x CBC3 chips and an extra Mezzanine card with the CIC chip, allowing for both electrical and optical reading. The rightmost prototype, named fully functional 2S FEH, combined both 08 x CBC3 and CIC chips.

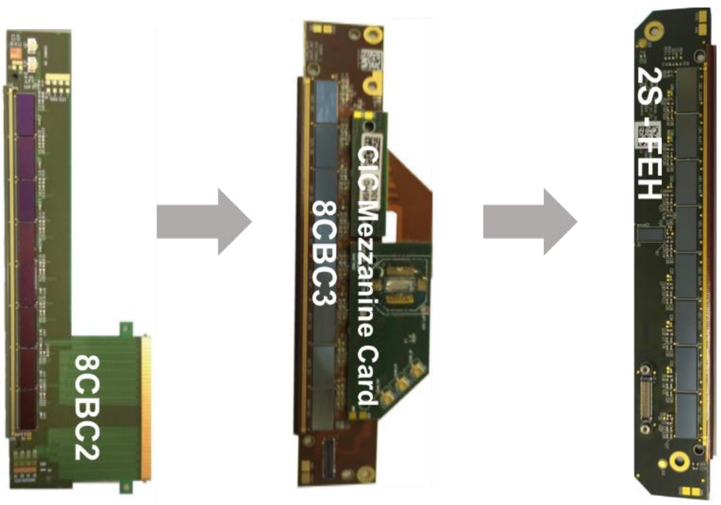

Figure 4.18: The FEH versions developed during the prototyping phase for 2S modules. The left most version, is known as 8CBC2. The version in the middle is referred to as 8CBC3, while the version on the right is known as fully functional 2S FEH.

i. CMS Binary Chips (CBC)

The CBC chip [85] is designed using 130 nm CMOS technology, and CBC3 serves as the final prototype of the chip [91]. The CBC chip has been engineered with a focus on radiation hardening and resistance to single event upset (SEU). It is capable of processing data from 254 strips, with 127 top and 127 bottom sensor strips in a 2S module. The CBC3 chip encompasses all the necessary functions to identify clusters of programmable maximum width, perform top-to-bottom correlations over configurable windows, and generate high pT stubs. Running at a frequency of 320 MHz, it can provide both triggering information and triggered readout data at a rate of 320 Mb/s. The chip can sustain an average L1 trigger rate of up to 1 MHz and has a pipeline depth of 512 buffers. This depth enables the chip to achieve a L1 trigger latency as low as 12.8 μs.

a. Front-end channel

The analogue front-end of a single CBC channel is depicted in Figure 4.19. The input signal first undergoes two-stage pre-amplification before passing through a programmable offset adjustment controller, which uses an 8-bit register to compensate for any amplifier and comparator mismatches between channels. The comparator stage produces a binary output, with a digital "1" being outputted when the signal passing through it is above a defined threshold. With a load capacitance of around 9 pF per strip in a 2S module, the front-end noise is roughly 1000 e^{-}. To measure the performance of the front-end channel, it is possible to use a test pulse calibration by injecting charge directly from a capacitance. This method allows for precise calibration of the front-end and the quantification of its response. Digital Analogue Counts (DAC), also referred to as V_{cth}, can be used in steps to adjust the comparator voltage. It's important to note that lower DAC values result in higher thresholds due to electronic readout or negative signal.

b. Block diagram

The CBC3 chip functional block diagram, shown in Figure 4.20, features various blocks that perform different functions. To prevent dead time caused by pileup and match the Bx rate of 40 MHz, the front-end analog produces a brief pulse that rises within 20 ns and falls back to the baseline within 50 ns. The chip includes a test circuit to inject charge into each analog front-end channel, and a low-dropout regulator (LDO) generates a stable voltage supply at around 1V from a single 1.25V supply. The Channel Mask block is programmable and serves to

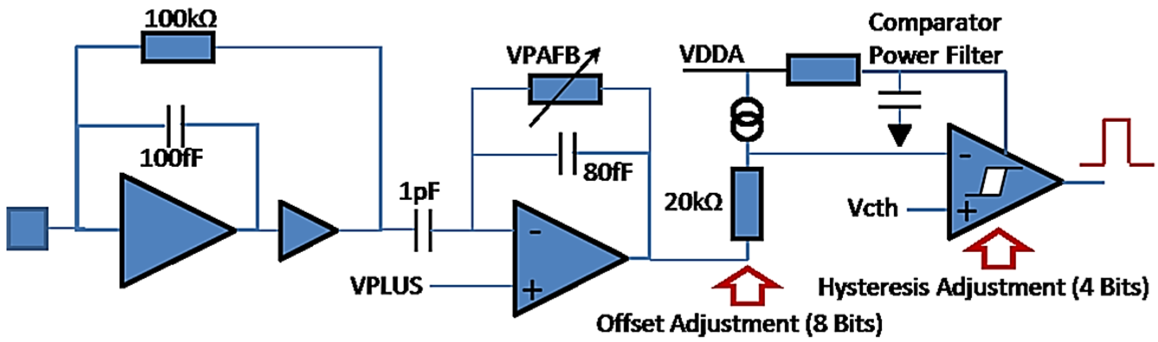

Figure 4.19: The front-end of a single input channel of the CBC3. It comprises two staged amplifiers that process the incoming analogue signal. The amplified signal is then offset-adjusted and directed to the comparator stage, where it is compared against the threshold voltage (V_{cth}). Only signals that surpass V_{cth} are considered valid 'hits' and recorded in binary format. (Figure adapted from [92])

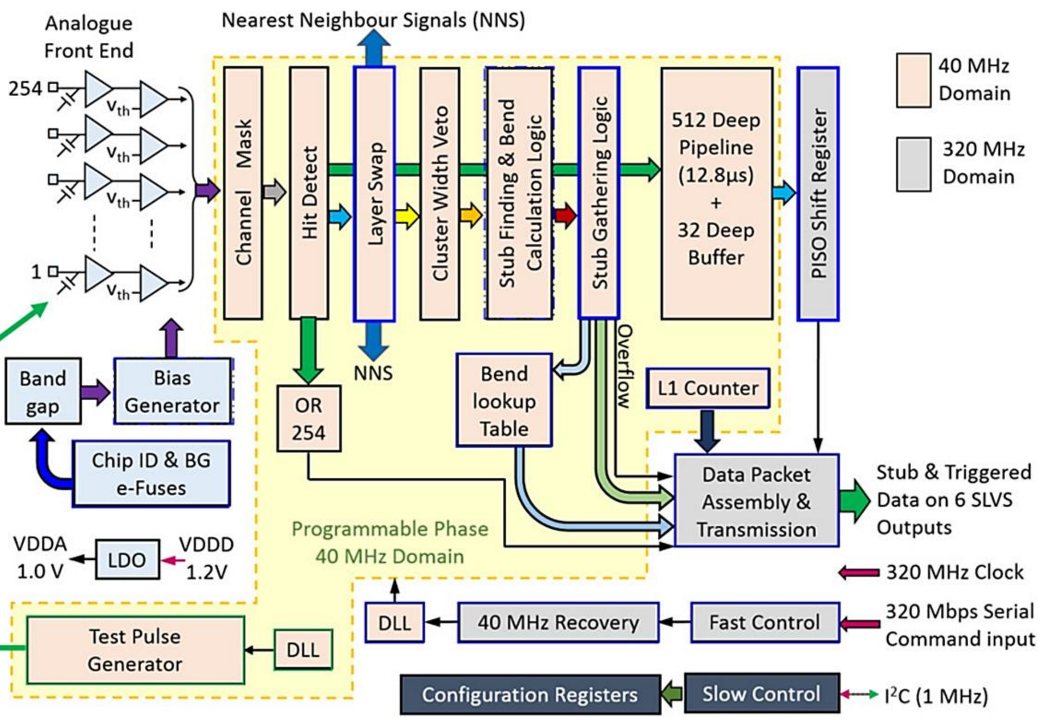

Figure 4.20: The functional block architecture of the CBC3. (Figure adapted from [91])

prevent noisy signals from passing to the succeeding logic blocks. The Hit Detect circuit samples the outputs of the comparators and generates a 25 ns pulse at a rate of 40 MHz if a hit is detected. It also includes a Highly Ionizing Particle suppression circuit that can be configured to suppress long duration outputs. The circuitry operating in the 40 MHz clock domain is provided with a clock signal through a programmable Delay-Locked Loop circuit (DLL). The OR254 block can be disabled from normal operations, and it generates an output signal only if a hit is present at any of the CBC channels. The Top & Bottom Channel Swap block ensures that the seed layer always faces the beam, and the Cluster Width Discrimination block filters out clusters wider than four strips to prevent them from passing to the next block. The Offset Correction & Correlation block performs the p_T stub finding operation, where the width and center of the window (in correlation layer) can be programmed up to 7 and 3 strips, respectively. The Stub Gathering Logic block produces the address of the seed cluster and bend information, indicating the cluster location in the window layer, to determine the stub direction. The bend Lookup Formatting block features a programmable lookup table to optimize bend resolution, and the Stub Gathering Logic can transmit bend information and up to three stub addresses per bunch crossing to the CIC chip.

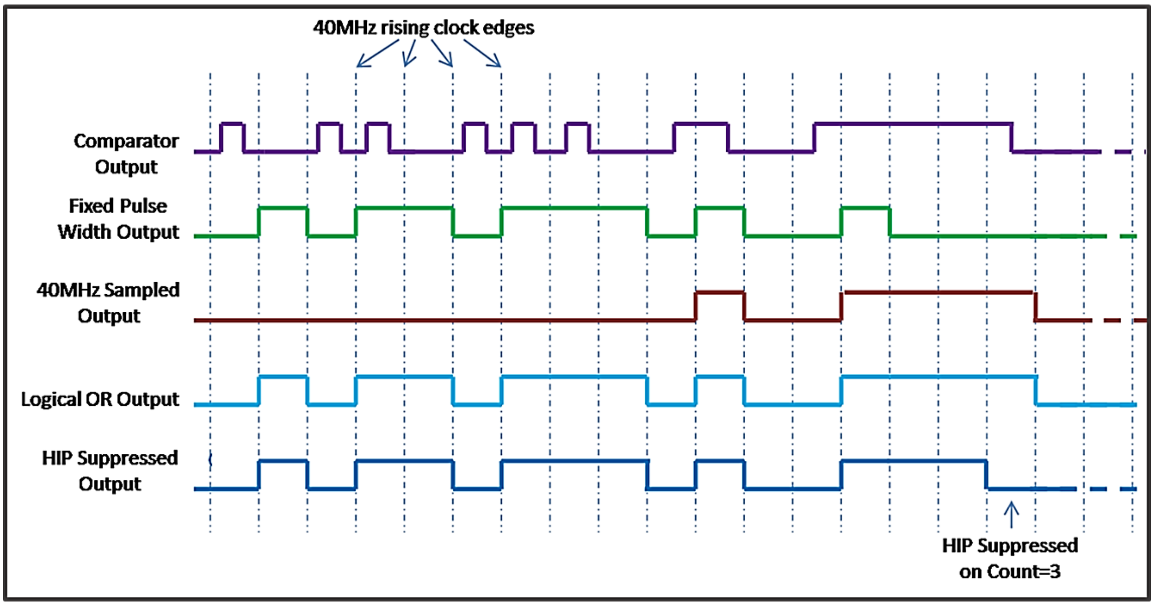

Figure 4.21: The operational modes for hit detection in the CBC3: Fixed Pulse Width, 40 MHz Sampled, Logical OR, and HIP Suppressed. This figure is adapted from reference [92].

Figure 4.21 illustrates the various hit detection modes available in Hit Detect block. In the fixed pulse width mode, the output consists of a constant 25 ns pulse, irrespective of the comparator output width. In the 40 MHz sampled mode, only comparator outputs corresponding to the rising clock edge are captured, and the output returns to zero only at the first rising clock edge following the comparator's return to zero. The Logical OR mode combines the outputs of both fixed pulse and 40 MHz sampled modes. In HIP suppressed mode, a highly ionizing particle circuit can be chosen, utilizing the 40 MHz sampled mode output, which enforces the pulse to return to zero if it exceeds the preprogrammed pulse width.

ii. Concentrator Integrated Chip (CIC)

The radiation hard CIC chip, fabricated with 65 nm CMOS technology, serves as data aggregator. It collects data from eight CBCs using six differential lines operating at 320 Mb/s between each CBC, and formats it into data packets containing information about triggers and raw data from events that pass the L1 trigger. The data packets are then transmitted via seven differential lines at 320 or 640 Mb/s to the LpGBT in the SEH. The references [58, 93, 94] can be consulted for more details about the CIC chip.

4.5.3 Service Hybrid (SEH)

The primary functions of the SEH [95, 96] in a 2S module is to distribute power, serialize data, and convert between optical and electrical signals. It is a flex circuit that is adhered to a carbon fiber stiffener, with a portion of the circuit folded around the stiffener (Figure 4.22). The SEH can be connected to FE hybrids on both ends using fine-pitch connectors via flexible tails. The flex circuit is equipped with three active components, including a DC-DC converter, LpGBT, and VTRx+, as well as a high voltage (HV) filter circuit. The HV filter circuit is located on the back side of the SEH (folded portion) and small kapton tails, which are glued onto the sensor's back side, are connected to this circuit to provide biasing voltage to the sensors.

The Low-power Gigabit Transceiver (LpGBT) [97] receives data at a rate of 320 Mb/s from two CICs located on both Front-End Hybrids (FEHs) through six differential lines. Out of these six lines, five are responsible for delivering stub data and the sixth line is used for transmitting full readout data. After serializing and formatting the data, LpGBT transmits it to Versatile Transceiver plus (VTRx+) [98], which is a pluggable device used for opto-electrical conversion, at a speed of 5.12 Gb/s. Additionally, LpGBT uses the I^2C protocol to configure the CBCs, CICs, and VTRx+. The DC-DC converter [99] serves the purpose of powering the electronics on the module. For a 2S module, it employs a two-step DC-DC conversion scheme. The first stage, bPOL12V, receives 11 volts from the feed line and converts it into a stable 2.55 V for VTRx+ to drive the VCSELs. The second stage, bPOL2V5, converts the 2.55 V into 1.25 V, which is supplied to the CBCs and CICs present on both FEHs, as well as to LpGBT and VTRx+. An electromagnetic shield is utilized to cover the DC-DC converter since to safeguard the silicon sensors and FE electronics from any stray electromagnetic radiations generated by inductor inside the DC-DC converter. More information on the SEH can be found in the references [58, 95, 96].

4.5.4 Mechanics

In Figure 4.22, the assembled and exploded view of a 2S module is displayed. Two types of sensor spacing will be utilized in the construction of 2S modules, as previously mentioned. These two types are comparable in all operational aspects, with the only distinction being the spacers between the sensors, known as bridges. The bridges have holes that are employed to secure them to the support structure of the Tracker and to attach them to cooling lines to dissipate heat generated by the module during operation. The bridges are composed of carbon-fibre reinforced aluminium (Al-CF), which has a high thermal conductivity and a CTE (Coefficient Thermal Expansion) value of 4 ppm/^{o}C, which is very close to that of silicon sensors 3 ppm/^{o}C. This will help minimize the mechanical stress inside the module induced by cooling the detector from +20 ^{o}C to -33 ^{o}C (the detector cooling will be discussed in next section). Two long Al-CF bridges will be used to provide cooling to the module, and an extra short bridge will be used to reduce the asymmetric heat dissipation created by the service hybrid. Some 2S modules will be attached to six cooling points on the support structure, and for those modules, a second short bridge will be attached at the position opposite to the short bridge under the service hybrid.

To apply high voltage to the sensors, a high voltage tail (HV-tail) is connected to the sensor backside using wire-bonds while it is plugged into the SEH. The sensor backside is attached with polyimide (PI) strips to provide electrical isolation between the bridges and the sensors. The bridges are at ground potential while the sensors are at biasing potentials. Kapton MT foil, which has a thickness of 25 µm and a dielectric strength of approximately 0.2 kV/µm, is used for this purpose. The hybrids, FEHs, and SEH are all affixed to the AlCF bridges, and wire-bonds are applied between AC pads on strip and FEH bond pads to connect all the sensor strips to CBC channels.

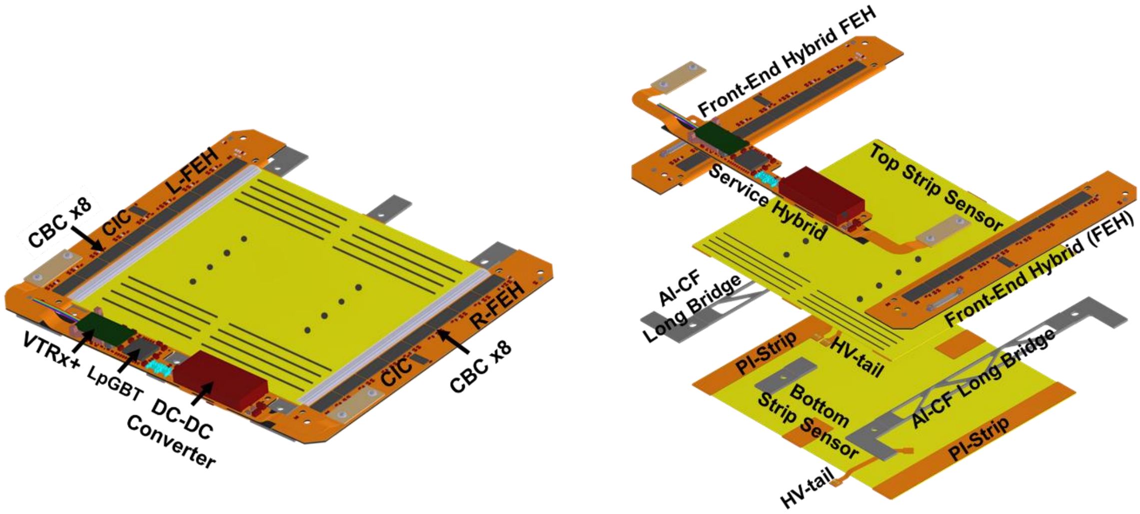

Figure 4.22: The assembled (left) and exploded (right) view of a 2S module are depicted, showing all the constituent parts used in its assembly in an exploded view [58].

4.6 Thermal Studies for 2S Module

The information presented in this section draws heavily from the reference [58]. The CMS phase 2 tracker will incorporate a two-phase CO2 cooling system to address the significant power dissipation in the tracking volume. With an estimated dissipation of 100 kW for the OT and 50 kW for IT, the cooling system aims to maintain a consistent temperature of -35°C. This temperature regulation is critical for achieving and sustaining low temperatures within the detector components, enhancing operational stability, reducing thermal noise, and improving measurement precision. Additionally, the cooling system plays a vital role in keeping the temperature of the silicon sensors below -20°C. This protects the sensors from radiation damage and prevents thermal runaway, a self-reinforcing temperature increase caused by leakage current. By ensuring the reliability and optimal performance of the sensors, the cooling system enhances the overall effectiveness of the tracker system in detecting charged particles.

Figure 4.23 shows the results of thermal performance studies conducted on 2S modules in the TB2S under three different scenarios. The investigations were carried out using finite element analyses (FEA) by integrating the module's CAD model into ANSYS. The worst-case fluence value, obtained through FLUKA simulation, was used, and the power consumption values of the front-end ASICs were determined through prototypes and simulations (5.4 W for the 2S module). The coefficient of heat transfer from the inner wall of the cooling pipe to CO_2 was assumed to be 5000 $W/m^2/K$. The heat generated by the silicon sensors due to leakage current was calculated using the formula $P^{RT} = \alpha\Phi VU$, where α is the damage constant, and Φ, V, and U are anticipated fluence, sensor volume, and biasing voltages. For more details on the analysis methodology, please refer to Reference [58].

The dotted line in Figure 4.23 represents the operational temperature of the coolant, while thermal runaway is found to occur well below this temperature for all three scenarios.

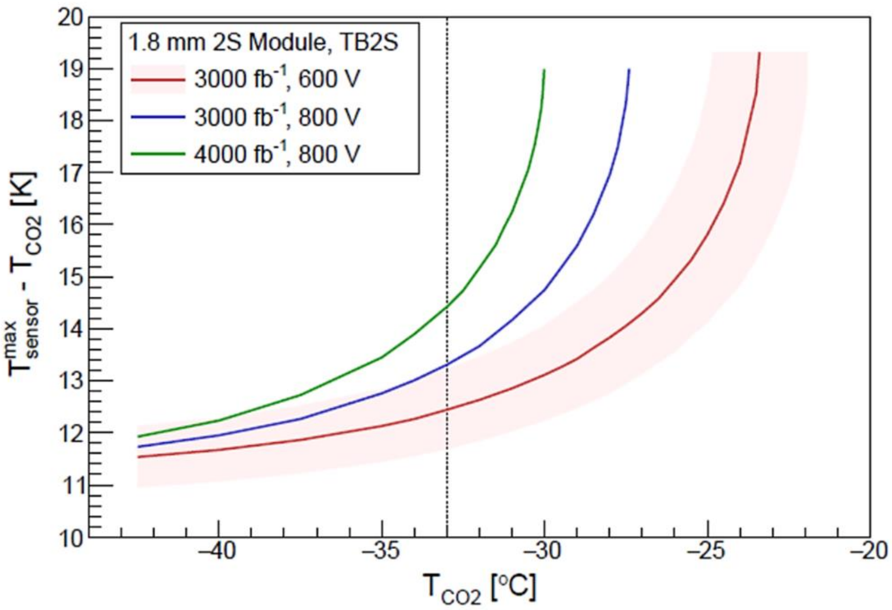

Figure 4.23: The FEA simulation outcomes for a 1.8 mm 2S module in TB2S, demonstrating the maximum sensor temperature difference with coolant (CO_2) temperature against the coolant temperature [58].

5

Prototyping of 2S Module Assembly and Testing Procedures

This chapter delves into the extensive research and development carried out at NCP for assembly and testing of the 2S module for the CMS Phase-2 upgrade. NCP plays a crucial role in the CMS Phase-2 Outer Tracker production line, which will utilize a total of 7,680 2S modules and 5,616 PS modules. The chapter begins by examining the assembly setup used during the prototyping phase, with a focus on module metrology and sensor current-voltage (IV) analysis to ensure compliance with specifications. The effectiveness of the assembly process is demonstrated through the presentation of results from assembled modules.

Furthermore, the chapter discusses the prototyping of test procedures aimed to evaluate module performance. Various tests conducted on prototype modules yield valuable insights into their functionality and performance characteristics. The chapter also covers the development of a cold test box designed to assess module behavior under low-temperature conditions. The design and construction of the cold test box are explained, with emphasize on its importance for Phase-2 upgrade.

5.1 Module Assembly Procedure

The assembly procedure for the 2S module at the National Center for Physics (NCP) follows a series of carefully executed steps, facilitated by custom built jigs. These jigs were made by a local company using drawings from the CERN share folder. Figure 5.1 provides a detailed illustration of the assembly process, depicting the various steps involved in module construction.

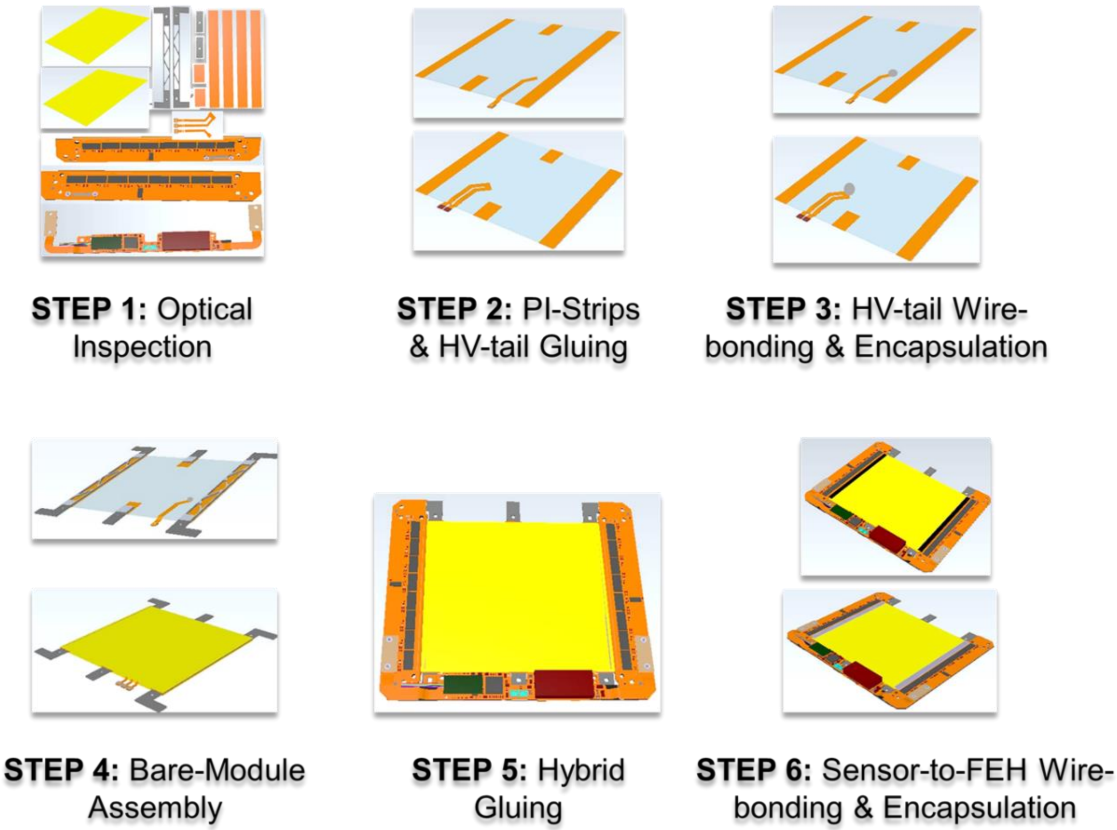

Figure 5.1: Different steps followed during the module assembly. Step 1: Visual inspection of all the components to check for mechanical damage. Step 2: Gluing of kapton strips and HV-tail on the sensor back-plane. Step 3: Wire-bonding and encapsulation of HV-tail to ensure secure connections. Step 4: Assembly of the bare module by gluing the sensors together and utilizing AlCF spacers. Step 5: Attachment of hybrids (FEH and SEH) through adhesive. Step 6: Placement of wire-bonds between sensor strip AC-pads and FEH bond-pads, followed by encapsulation for protection.

The assembly process commences with a visual inspection of the components received from CERN, which include silicon strip sensors, Al-CF bridges, module hybrids (FEHs and SEH), high-voltage tails for sensor biasing, and kapton (polyimide) strips. In the second step, the kapton strips and HV tails are glued to the backside of each sensor. Wire-bonding of the HV tails followed by encapsulation, using silicone elastomer to ensure secure connections, are then performed.

The subsequent step focuses on assembling the bare module by carefully gluing the two sensors together, with their respective back-planes facing each other, while utilizing Al-CF bridges as spacers. Glue is applied to both sides of the Al-CF bridges during this process. Once assembled, the bare module undergoes metrology to evaluate any potential misalignments between the sensors in terms of translation or angular orientation.

Next, the hybrids (two FEH and one SEH) are affixed to the bare module using adhesive. In the fifth step, wire bonding is performed between the FEH bond pads and the sensor strip AC pads. To ensure additional protection, these wire bonds are encapsulated with silicon elastomer in the final step of the assembly.

Throughout the assembly process, IV (current-voltage) measurements are performed at different stages to monitor the functionality of the sensors. These measurements play a crucial role in verifying that the sensors are operating correctly within the desired parameters. The subsequent section will explore the specific details of each assembly step, during prototyping, in the context of this study, encompassing any required adjustments or corrections undertaken to achieve precise assembly within the specified tolerance limits using the jigs.

5.2 Assembly Prototyping

5.2.1 Optical Inspection

The module components are developed after extensive research and development conducted by various groups within the CMS Silicon Tracker upgrade collaboration. After the R&D phase, these components are manufactured by different vendors for series production. Upon completion, the components are sent to CERN from the respective vendors. Before reaching the assembly center, the components undergo a series of quality tests at different institutes to ensure their compliance with the required standards.

The essential components needed for constructing a 2S module include two silicon strip sensors, polyimide (PI) strips of varying lengths (long and short), a set of HV-tail with both one-leg and two-leg configurations, a set of AlCF bridges consisting of two long bridges and one or two short bridges, two FEH (left and right), and one SEH.

The initial step in the assembly process involves conducting meticulous visual inspections of all the components under a microscope. This detailed examination aims to identify any potential mechanical damage or defects that may have occurred during transportation or handling. By carefully inspecting each component, the overall quality and integrity of the components is ensured before proceeding with the subsequent assembly steps.

5.2.2 PI Strips and HV-tail Gluing

PI Strips Placement Tolerance Limits

In the operational condition, when referring to the functioning state of the module, both sensors' back-planes are maintained at a biasing potential, a predetermined voltage level necessary for their proper operation. Simultaneously, the bridges, which are integral components of the module, are maintained at ground potential. This grounding is essential, as the bridges will be physically connected to the mounting structure in the Tracker. To ensure effective electrical isolation between the bridges and the sensor backside, kapton MT (polyimide) foil of thickness 25 μm and dielectric strength ~ 0.2 kV/mm is used. The PI strips, or Polyimide strips, are utilized to create a barrier or insulating layer between the bridges and the sensor backside. This insulation is necessary to prevent any electrical short-circuiting that could occur if the bridges directly contacted the sensor backside. Figure 5.2 displays the measurement of PI strips from Al-CF bridges and the sensor corner as depicted in the 2S module CAD file.

To guarantee a stable electrical operation of the module, especially when subjected to high voltages of up to 1000 V, it is crucial to adhere to a minimum distance of 500 μm between the Al-CF bridge and any point on the sensor backside [100]. This stipulation serves as a vital safety measure aimed at mitigating the risk of electrical breakdown or arcing between the bridge and the sensor backside. Failure to maintain this distance could potentially lead to detrimental consequences such as damage to the module or a compromise in its overall performance. From Figure 5.2, the PI strip placement tolerance limits can be calculated as ±150 μm horizontally and ±200 μm vertically, ensuring a distance of 500 μm between the Al-CF bridge and any point on the sensor backside.

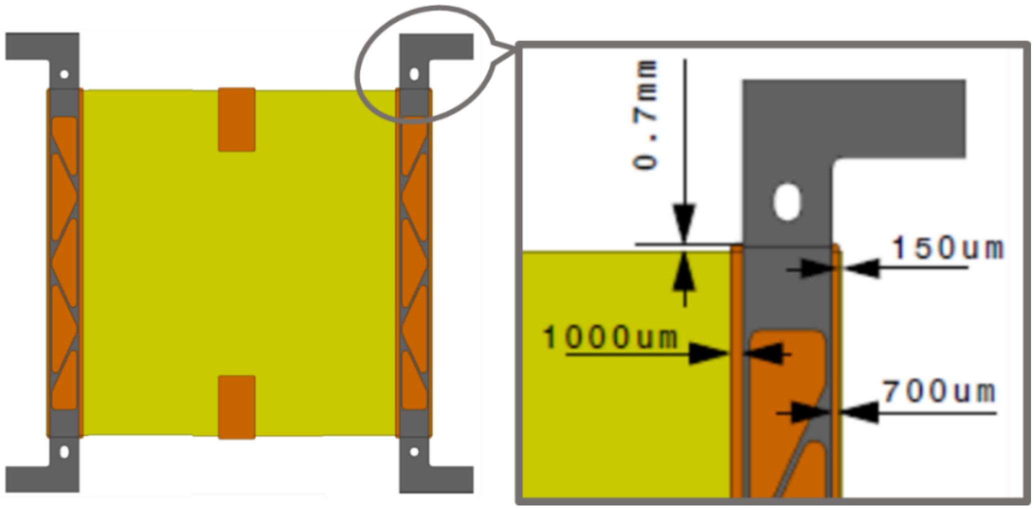

Figure 5.2: Zoomed view displaying the dimensions of PI strips and AlCF bridges from one corner of the sensor, as obtained from the CAD file of the 2S module. These identical dimensions are applied to all four corners. (Credit: CMS)

PI Gluing Jig Correction

The process of placing PI strips on the sensor backplane involves the use of the PI Gluing Jig, depicted in Figure 5.3. This jig consists of two main parts: the PI strips placement jig and the sensor holding jig.

The initial step of the process involves the placement of the sensor into the sensor holding jig. It is crucial to ensure that the sensor's backplane is positioned facing upwards and aligned precisely against the provided alignment stoppers, clearly illustrated by the circles in Figure 5.3 (b). After this, a specific quantity of the *Polytech LV 601* [101] glue is carefully applied using glue dispensing system, which will be explained in detail later in section 5.3. *Polytech LV 601* is a two-component glue that combines a hardener and resin in a precise ratio of 100:35. After the glue application, the PI placement jig is positioned on top of the sensor holding jig, utilizing alignment pins as indicated in Figure 5.3 (c). The jigs are then held together for a brief period of 5 to 10 seconds before being lifted, ensuring proper adhesion between the sensor and the strip. However, after the reception of jig, it was found that the PI Gluing jig did not yield accurate results for placing PI strips on glass plates with dimensions similar to those of the sensor. To rectify this issue, the alignment stoppers on the sensor gluing jig were gradually adjusted. They were meticulously ground in small increments using fine emery paper while closely monitoring the accuracy of strip placement.

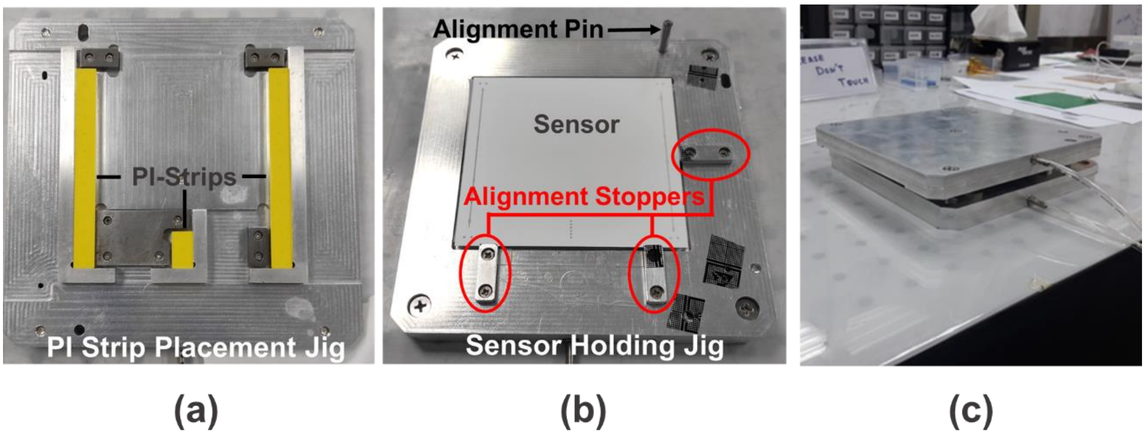

Figure 5.3: (a) PI strip placement Jig. (b) Sensor holding Jig, showing alignment stoppers inside the red circle and an alignment pin used to guide the PI strip placement jig. (c) The PI strip placement jig placed on the sensor holding jig for strip transfer.

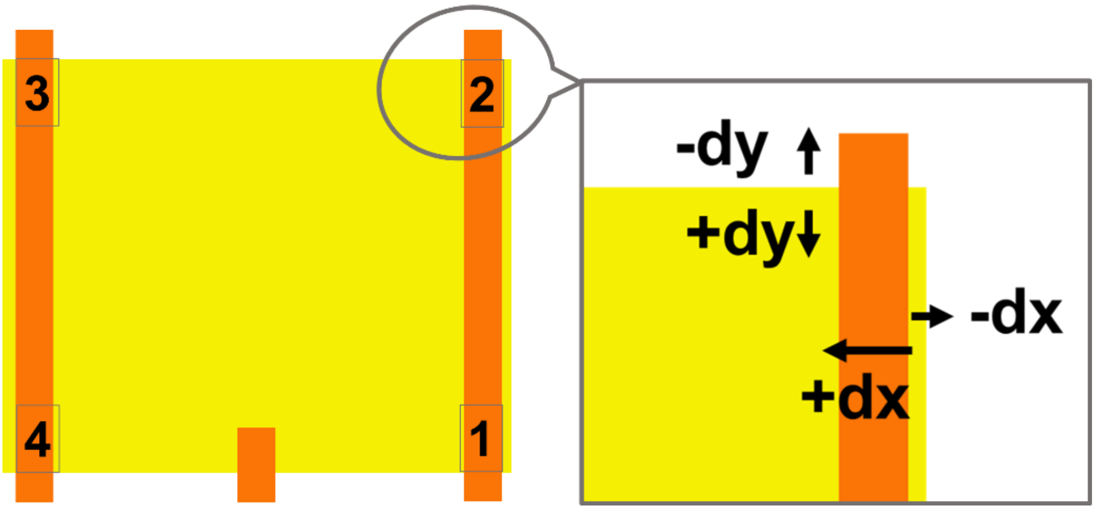

Figure 5.4: Deviation, dx and dy, in strip placement position from actual values as indicated in Figure 5.2. The maximum allowable deviation is $dx_{max} = \pm 150$ µm (horizontal) and $dy_{max} = \pm 200$ µm (vertical). Positive deviations indicate placement away from the sensor corner, while negative deviations indicate placement towards the sensor corner. The calculations were performed for measurements near the four corners, labeled 1, 2, 3, and 4, following a similar scheme.

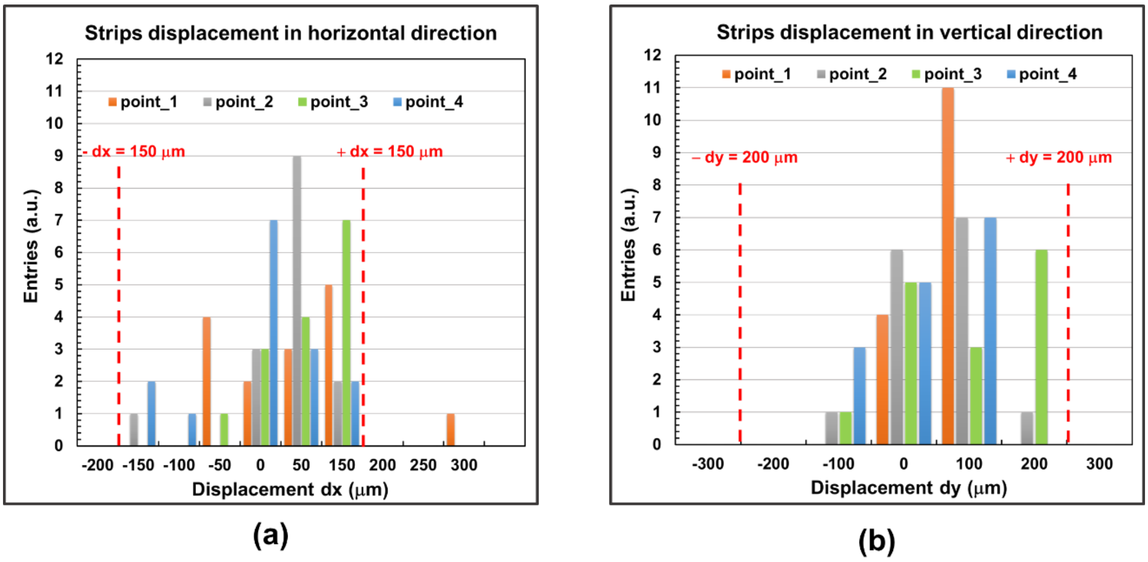

Figure 5.5: Histograms depicting strip placement deviations in horizontal and vertical directions for points 1, 2, 3, and 4 (labeled in Figure 5.4). The measurements were taken after the jig correction, and red dashed lines represent the maximum tolerance limits.

Figure 5.5 depicts a histogram that provides insight into the precision of strip placement at various points, as mentioned in Figure 5.4, in both the horizontal and vertical directions. The strip displacement values, represented as dx and dy, remain consistent in both Figure 5.4 and Figure 5.5, staying well within the tolerance limits of ±150 μm horizontally and ±200 μm vertically. By examining Figure 5.5, it becomes evident that, following the implementation of necessary corrections to the PI Gluing jig, all attempts at PI strip placement were successfully accomplished within the tolerance limits in both the horizontal and vertical directions. This outcome indicates the effectiveness of the corrective measures taken to ensure accurate and precise strip placement for the Silicon module.

HV-tail Gluing

High Voltage (HV) tails are essential components used to supply biasing voltage to the sensor through the service hybrid in a 2S module. These HV-tails, namely one leg and two leg tails, are attached to the sensor's backplane using glue. The one leg tail is positioned at the bottom of the sensor, while the two leg tail is placed on the top sensor. It's worth noting that the two leg HV-tail incorporates a thermistor for measuring the sensor's temperature. Figure

5.6 depicts the specific placement positions of the HV-tails, on top and bottom sensor, extracted from the CAD file.

To simplify the gluing process of HV-tails, a specially designed 3D printed extension‡ is added to the PI Gluing Jig. This extension serves the purpose of precisely attaching the HV-tails to their respective position. The procedure for placing the HV-tails is demonstrated in Figure 5.7. Initially, the HV-tails are fixed into the corresponding grooves on the jig, with a smaller groove for the one leg tail and a larger groove for the two leg tail. A precise amount of glue, *Polytech LV 601*, is then applied on the tail. Subsequently, the HV-tail jig is positioned onto the PI Gluing Jig, and a weight bar is applied onto the tail to ensure sufficient pressure. Finally, the HV-tail jig is slid to complete the placement process.

After the process of gluing, the PI strips and HV-tail onto the sensors' backplane, the assembled components are carefully placed inside a dry cabinet within the controlled humidity and temperature environment. They remain in this environment for a period of 20 to 24 hours to allow the glue to dry thoroughly.

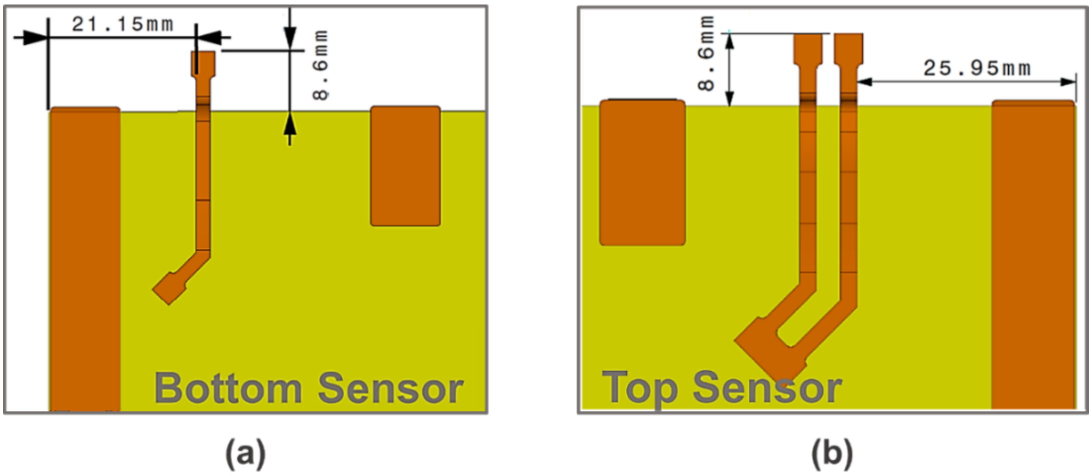

Figure 5.6: Placement positions of HV-tails for (a) top and (b) bottom sensor corners, as extracted from the 2S module CAD file. (Credit: CMS)

‡ The drawing of 3D extension jig is shared by the Belgian module assembly group.

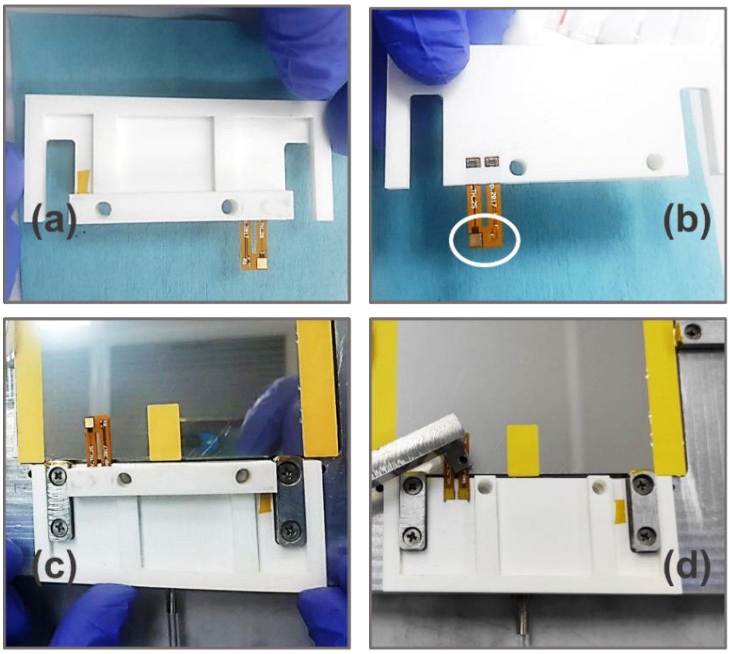

Figure 5.7: HV-tail gluing process: (a) HV-tail is held inside the groove of the extension jig. (b) Glue is applied to the tail. (c) The extension jig is landed on the PI gluing Sensor holding jig. (d) A weight bar is applied on the glue joint to hold the tail firmly.

5.2.3 HV-tail Wire-bonding and Encapsulation

The process of establishing a high voltage connection involves wire-bonding the HV-tails to the sensor backplane. This intricate procedure is executed using the advanced *Delvotec G5 64000* wire-bonder, which employs a 25µm diameter Aluminum wire mixed with 1% Si obtained from *Heraeus* [102]. It requires the precise application of 10 to 20 wire-bonds between the HV-tail bond pad and the sensor backplane, as illustrated in Figure 5.8. To ensure the longevity and protection of these wire-bonds, a silicon elastomer, *Sylgard 186* [103], is meticulously utilized. *Sylgard 186* is a two-component glue that combines a hardener and resin in a specific ratio of 100:10. Only a minuscule drop of Sylgard is manually dispensed, employing a regular syringe equipped with a conical plastic needle, whose inner diameter typically ranges from 0.81-1.194 mm. As the backplanes of both sensors face each other when assembled in a bare module, the available space between them imposes a constraint on the height of the applied Sylgard, which must remain less than 1 mm. The height of the dry Sylgard measures below 0.7 mm in multiple measurements, thus validating the precision of the process.

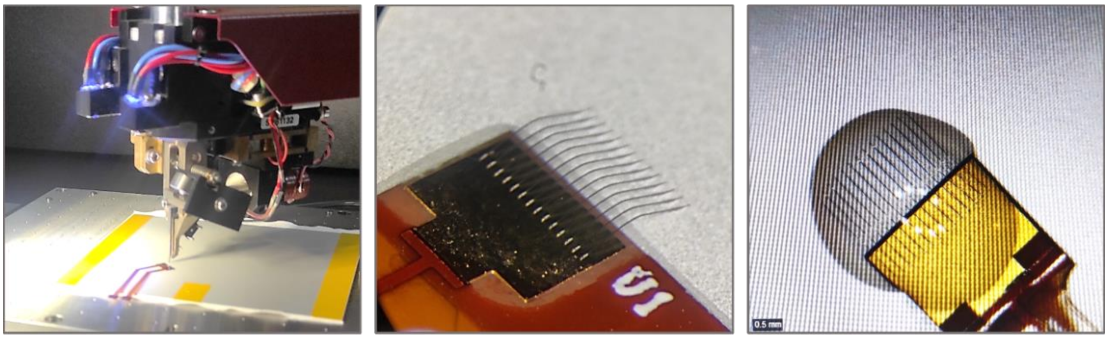

(a) (b) (c)

Figure 5.8: Wire-bonding and encapsulation process. (a) Wire-bonding process using the bond head of the *Delvotec G5 64000* wire-bonder for bonding the HV tail. (b) Microscopic view of wire-bonds between HV-tail bond pads and sensor backplane. (c) Encapsulation of wire-bonds using *Sylgard 186*.

5.2.4 Bare Module Assembly

The term "bare module" refers to a module that does not include the front-end and service hybrids. The assembly of the bare module involves the use of sensor gluing and a glue transfer jig, as illustrated in Figure 5.9.

The process of assembling the bare module is outlined in Figure 5.10. In this process, the bottom sensor, which has one leg HV-tail, is placed on the sensor gluing jig with its backplane facing upwards. The sensor is then pressed against the alignment stoppers, marked within the black circle, using spring pushers and vacuum is turned on to hold the sensor in position. The *Polytec TC437* [104] glue, a two-component adhesive consisting of a hardener and resin mixed in a ratio of 100:10, is applied to the AlCF bridges using the glue transfer jig (Figure 5.9 (b)). The bridges are then placed on the sensor, as depicted in Figure 5.10(a), using guiding pins mentioned in Figure 5.9 and subsequently, the spring pushers are released. The top sensor, with two legs HV-tail, is placed on the sensor-bridge assembly with the strip side facing upwards and is pushed against the alignment stoppers using spring pushers (Figure 5.10(b)). Finally, a weight plate is applied (Figure 5.10(c)) to ensure a proper glue joint and a thin layer of glue. The bare module assembly remains on the sensor gluing jig for 16 to 20 hours to allow the glue to dry.

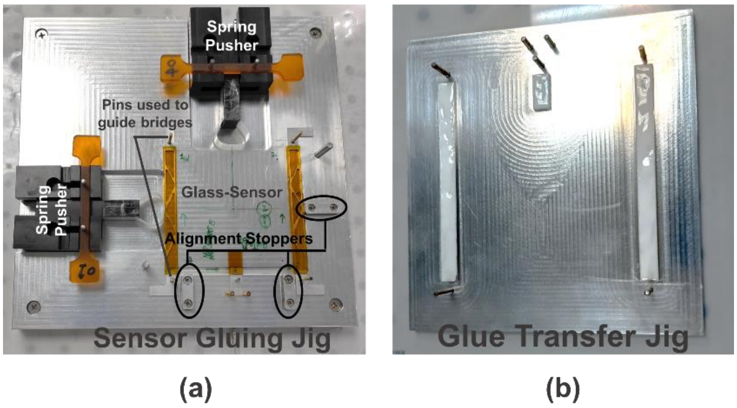

Figure 5.9: Jigs used in bare module assembly. (a) Sensor gluing jig. (b) Glue transfer jig.

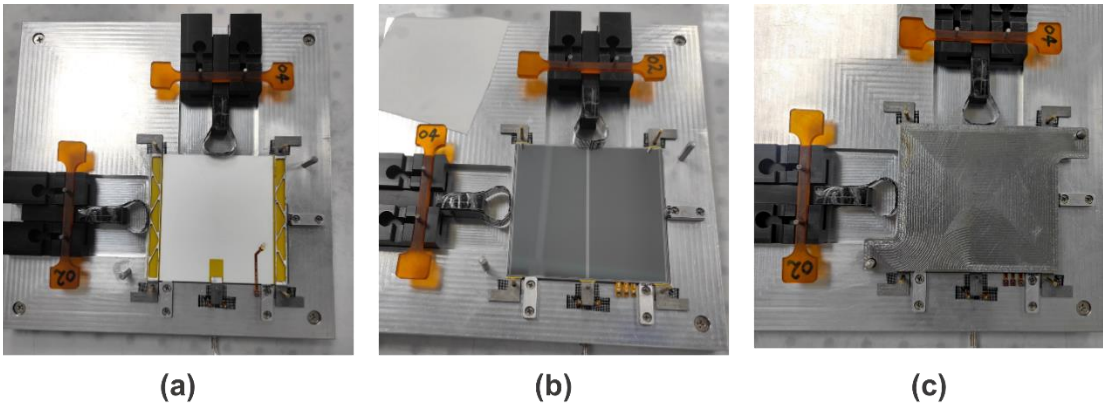

Figure 5.10: Bare module assembly steps. (a) Placement of bottom sensor, glue application, and bridge placement. (b) Placement of top sensor. (c) Application of weight plate for glue joint.

Once the drying procedure is completed, the bare module is removed from the sensor gluing jig, and metrology is performed to determine any misalignment between the sensors. The details of the metrology method will be described in Section 5.4. During the module assembly, it is crucial to ensure proper alignment between the two sensors. The assembly tolerance includes a limit of 400 μrad ($\Delta\theta$) for the angle between the sensors and translations of 50 μm and 100 μm in the directions parallel (Δx) and perpendicular (Δy) to the strips, respectively [58].

The tolerance values are derived from the intrinsic resolution of the 2S module. The front-end electronics of the module provide a binary readout, which introduces an intrinsic offset that cannot be corrected beyond the sensor half-pitch. These known offsets are accounted for in the stub finding logic through a programmable parameter. A tilt of one sensor with respect to the other sensor can introduce a variation in the intrinsic offset that cannot be corrected during online stub finding. Therefore, the tilt between the sensors must be smaller than the sensor half-pitch to minimize its contribution to the resolution. As depicted in Figure 5.11, a small tilt of less than 20 μm over the strip length is targeted for module assembly, which corresponds to an angular tilt limit of less than 400 μrad for 2S modules [58].

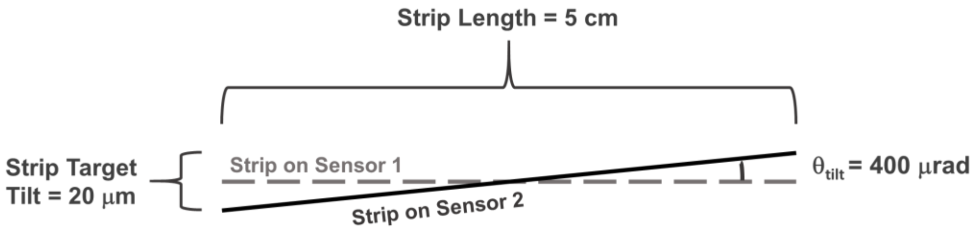

Figure 5.11: Illustration of the tilt angle between two sensors with a single strip shown for each sensor. The tilt angle corresponds to a target tilt of 20 μm, which translates to 400 μrad for a 5 cm strip.

Upon receiving the jig, a test is conducted by assembling a mechanical module, which consists of glass plates of sensor dimensions and aluminum bridges as spacers. Significant errors in the nominal positions of the bridges from the sensor corner (as indicated in Figure 5.2) and sensors misalignment are observed. To address these errors, the alignment stoppers are initially ground using abrasive paper to achieve the proper position of the bridges. Subsequently, fine grinding of the alignment stoppers is performed in steps to correct the sensor-to-sensor misalignment within the specified limits. After each iteration, a mechanical module is assembled for evaluation. Table 5.1 shows the metrology measurements of different modules during the iteration process. Once the assembly of the mechanical and non-functional (dummy) silicon module is achieved within the tolerance limits, functional modules are assembled. The metrology results of the functional modules are presented in next chapter.

5.2.5 Hybrid Gluing

Figure 5.12 provides a visual representation of the two variants of the hybrid gluing jig utilized for attaching the hybrids. The left-side variant showcases the initial design of the jig, which was conceived by CERN during the prototyping phase. Recognizing the need for improvements and addressing the challenges encountered during the process, the right-side variant was subsequently developed by the Karlsruhe assembly center, KIT.

The correct placement of wire bonds between the sensor and hybrid, while meeting the required pull strength, relies on minimizing the skew angle. Achieving this objective entails maintaining a precise alignment between the FEH bond pads and the sensor strip AC pads, with a margin of 90 μm. The hybrid gluing jig facilitates the alignment between the bond pads and AC pads, ensuring that the wire bonds are positioned accurately and securely.

Table 5.1: 2S Modules' metrology results during Sensor Gluing Jig correction.

Module Name	Δθ (μrad)	Δx (μm)	Δy (μm)
NCP-M01	452	60	6
NCP-M02	435	38	10
NCP - D01	1753	38	55
NCP-M03	342	-14	20
NCP-M04	-33	89	-4

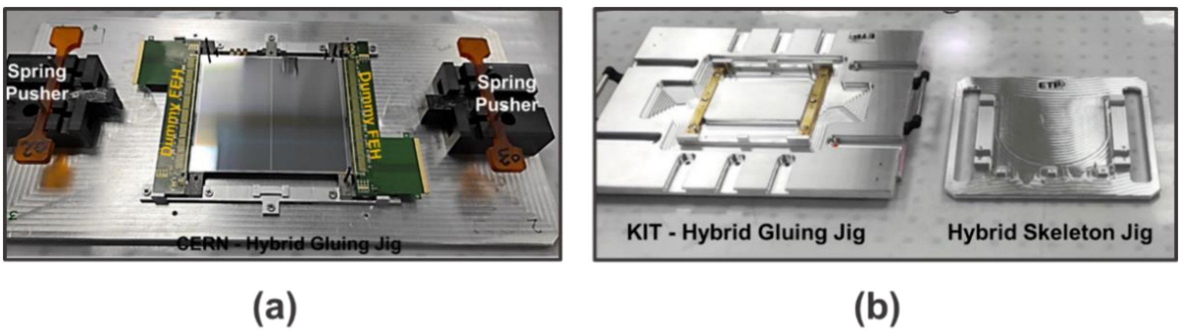

Figure 5.12: Hybrid Gluing Jig variants designed by (a) CERN and (b) KIT Assembly Center.

When utilizing the CERN hybrid gluing jig for assembly procedure, the first step involves attaching the Front-End Hybrids (FEHs). The bare module is positioned on the hybrid gluing jig, and a small drops of TC437 glue are manually applied to each of the four corners of the bridges, as shown in Figure 5.13(a). The FEHs are then carefully placed, and a 100 μm kapton spacer is inserted between the FEH and the sensor. The FEH is gently pushed towards the sensor using a spring pusher (Figure 5.13(b)). Under a microscope, the hybrids are adjusted to align their bond pads with the sensor strip AC pads. Each bond pad on the FEH is connected to a channel in the CBC. Finally, weight bars are placed to evenly distribute the glue and ensure a proper glue joint (Figure 5.13(c)). The glue requires 16 to 20 hours to dry. In the second step, the Sensor Hybrid (SEH) is glued by applying small drops of the same glue on the bridges and carefully placing the hybrid using guiding pins. Weight bars are employed once again to achieve a proper glue joint (Figure 5.13(d)).

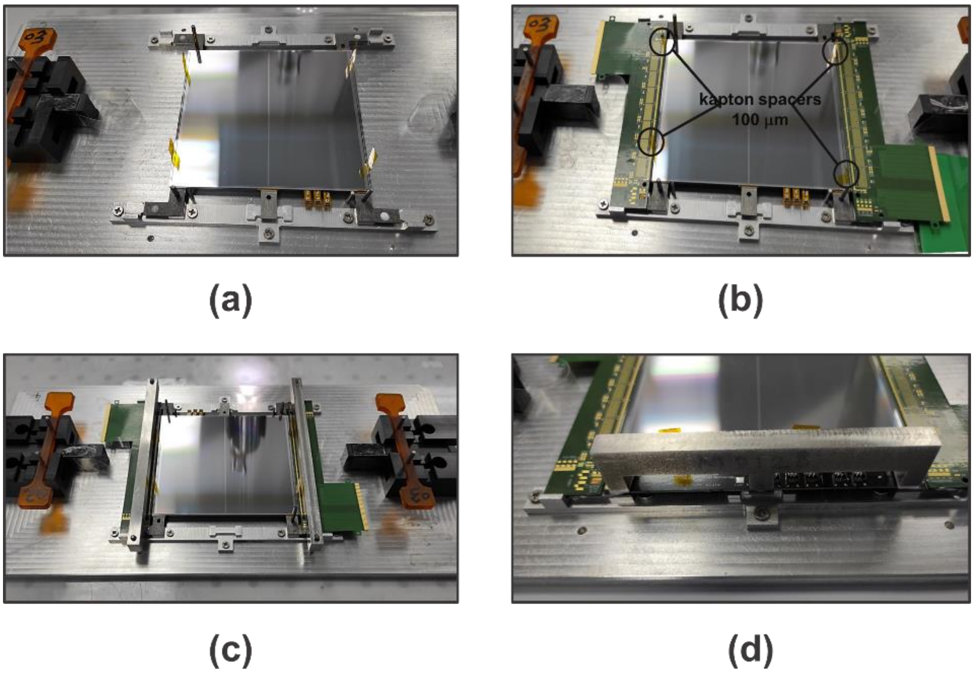

Figure 5.13: Hybrid gluing steps using CERN hybrid gluing Jig variant. (a) Applying glue drops on AlCF bridge corners. (b) Placement of FEH and engaging spring pushers, with 100 μm kapton spacers used between sensor and FEH. (c) Placing weight bars on FEH for proper glue joint. (d) Gluing of SEH, where power plate is used here instead of SEH.

On the other hand, the assembly procedure for the KIT jig is relatively straightforward. All the hybrids are glued to the bare module in a single step. Initially, the hybrid skeleton is constructed on a skeleton jig (Figure 5.14(a)). After applying glue on various points on the bridges, the hybrid skeleton is transferred to the hybrid gluing jig (Figure 5.14(b) and Figure 5.14(c)). A 100 μm gap between the hybrid and the sensor is achieved by adjusting brass bars using small screws. Additionally, different spring pushers are utilized to apply force on the glue joints.

The CERN variant of the hybrid gluing jig was machined and employed during the initial prototyping study at NCP. However, upon reception, it was observed that there was insufficient space to maneuver the hybrid for alignment with the sensor strip. To address this issue, the jig was corrected using dummy hybrids. After receiving the second variant of the jig from KIT,

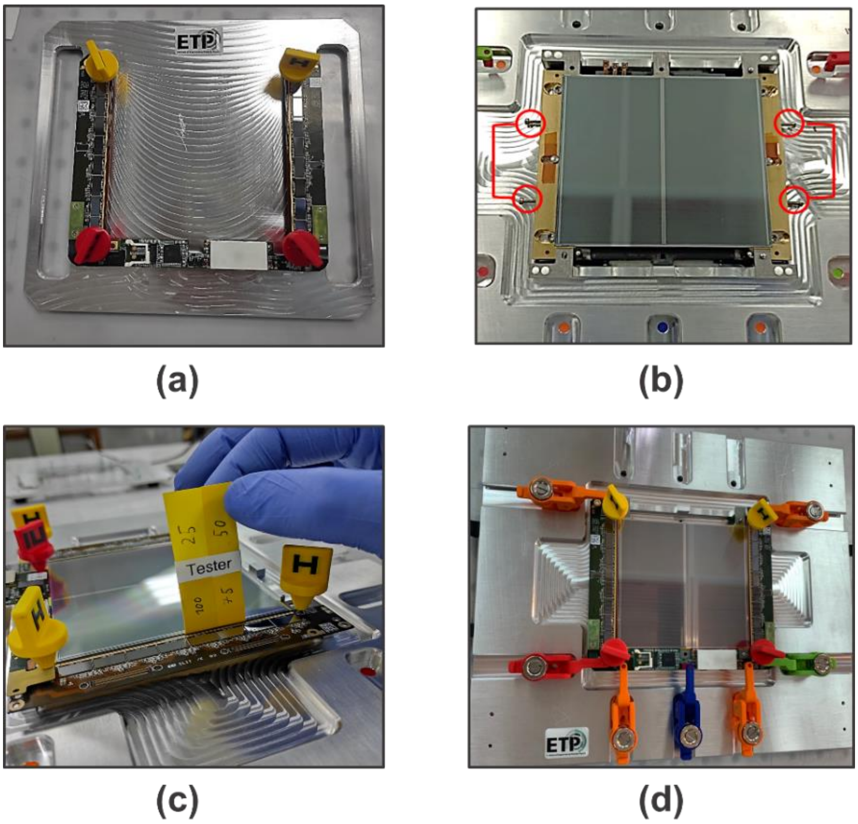

Figure 5.14: Hybrid gluing steps using KIT Jig variant. (a) Hybrid structure on Skeleton Jig. (b) Applying glue drops on AlCF bridge corners. The screw inside red circles are used to vary sensor to hybrid distance. (c) Testing a gap of 100 μm between sensor and FEH. (d) Placing hybrid structure on bare module and applying pressure on glue joint using spring pushers.

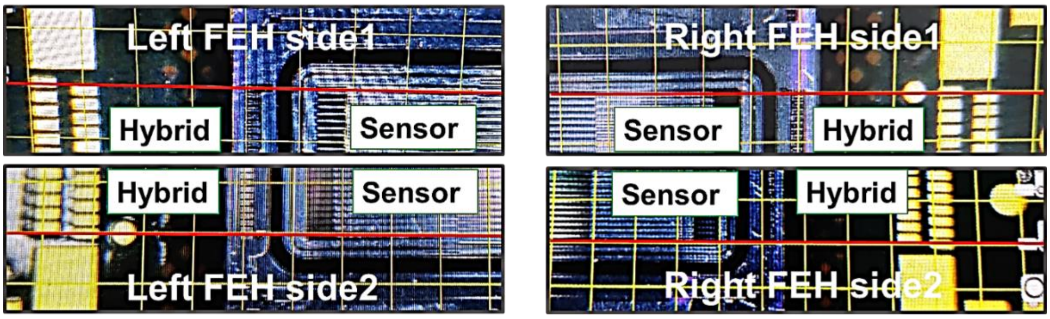

Figure 5.15: Microscopic view of alignment between FEH bond pad (yellow color pads) and sensor strip AC pad (Silver Color on sensor) on extreme ends for both left and right FEH. The alignment on both end of FEH ensures precise alignment of all sensor strips with FEH bond pads.

additional adjustments were made to fine-tune the jig and rectify the minor issues. Subsequently, the KIT jig was utilized for further prototyping studies. Figure 5.15 displays a microscopic image demonstrating the achieved alignment, indicated by the red horizontal line, between the strip AC-pad and the FEH bond-pad.

5.2.6 Sensor-to-FEH Wire-bonding

The sensor-to-hybrid wire-bonding process is executed with the purpose of establishing the electrical connection between each strip of the sensor and a dedicated CBC channel located within the FEH. This process is undertaken to facilitate the readout of the sensors' signals. As discussed in section 4.5.1, the strip sensors in the 2S module consist of 2032 identical strips, segmented into two columns, each with a length of 5 cm. In this configuration, one column comprises 1016 strips from both the top and bottom sensors, connected to a single FEH, either on the right or left side. Consequently, a single CBC chip present on an FEH is responsible for reading 127 strips from each top and bottom sensor, resulting in a total of 254 channels.

The wire-bonding process itself is carried out using a *Delvotec G5 64000* wire-bonder, which utilizes a 25µm diameter Aluminum wire mixed with 1% Si, obtained from Heraeus [102]. During wire-bonding, the bonding tool makes contact with the sensor AC pad (or hybrid pad) surface, exerting a downward force and employing ultrasonic (US) power. This combination of force and vibration initially deforms the wire, and as the temperature rises, the wire is effectively welded to the surface. Once the wire-bonding is completed, a wire-bond pull test is conducted using pull tester, F&S BONDTEC LT – 101 [105], to evaluate the quality of the bonds. The requirements for the wire-bonds in the 2S module stipulate that the wire should break near the heels, and the pull force should exceed 8g. For more detailed insights into the wire-bonding process, comprehensive studies can be found in reference [106].

To facilitate the wire-bonding process, a specialized wire bonding jig, depicted in Figure 5.16(a), is employed. This jig incorporates vacuum suction cups that securely hold the module in place during bonding. Additionally, support bars are present on the jig to provide support to the FEH throughout the bonding procedure. The initial step involves ensuring that the support bars are in the lower position, which can be confirmed by checking the screws below them. Subsequently, the module is carefully positioned on the wire-bonding jig, with the top sensor facing upward, using guiding pins, as illustrated in Figure 5.16(b). The vacuum is then activated, pulling the module down and firmly attaching it to the suction cups. Once the module is securely in place, the support bars are raised, using the screws below them, until they make contact with the hybrids. After completing the wire-bonding between the top sensor and both hybrids, the module is inverted on the jig (Figure 5.16(c)), and the same process is repeated to perform wire-bonding between the bottom sensor and hybrids.

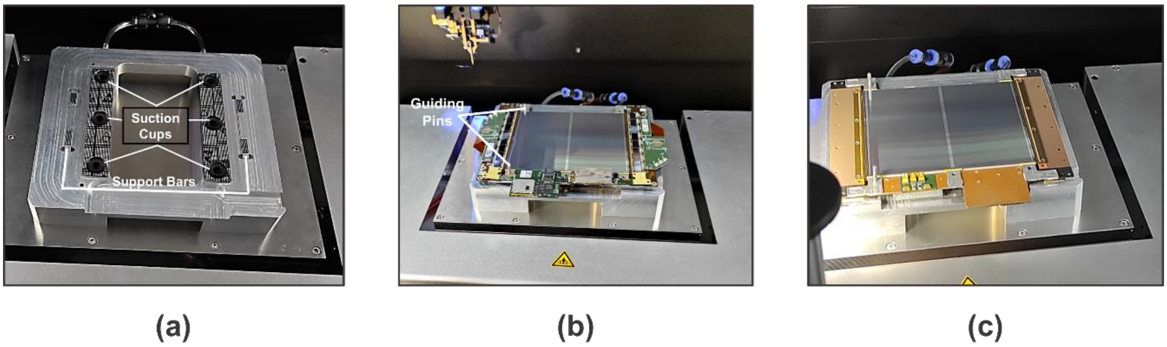

Figure 5.16: (a) Wire bonding Jig, displaying vacuum suction cups and support bars. (b) Top side of the module mounted on the wire-bond jig for bonding. (c) Bottom side of the module mounted on the wire-bond jig for bonding.

Figure 5.17(a) provides a visual representation of the wire-bonding tool in action, creating wire bonds between the sensor and hybrid. Complementing this, Figure 5.17(b) and Figure 5.17(c) present pictures capturing wire-bonds at various locations on the module. These images serve to offer a visual reference for the wire-bonding process. Furthermore, Table 5.2 furnishes valuable information concerning the total number of wire-bonds applied at different locations on the module. In the case of both the top and bottom sides of the module, three wire-bonds are attached between the sensor bias ring and the hybrid ground pad at each of the four corners of the module (Figure 5.17(b)). This arrangement ensures a reliable electrical connection between the sensor and hybrid, promoting optimal performance and signal transmission. Similarly, on each FEH, there are eight antenna pads present, and to ground these pads effectively, two wire-bonds are applied to each pad (Figure 5.17(b)). This meticulous bonding procedure guarantees proper grounding and enhances the overall functionality of the module. Detailed information regarding the wire-bonding process at NCP is beyond the scope this thesis.

In the subsequent step, encapsulation of the wire-bonds is performed to protect them form unwanted damages. The details of the encapsulation process are presented in section 5.3.4 as part of the dispensing studies, where the appropriate methods for protecting the wire-bonds are discussed.

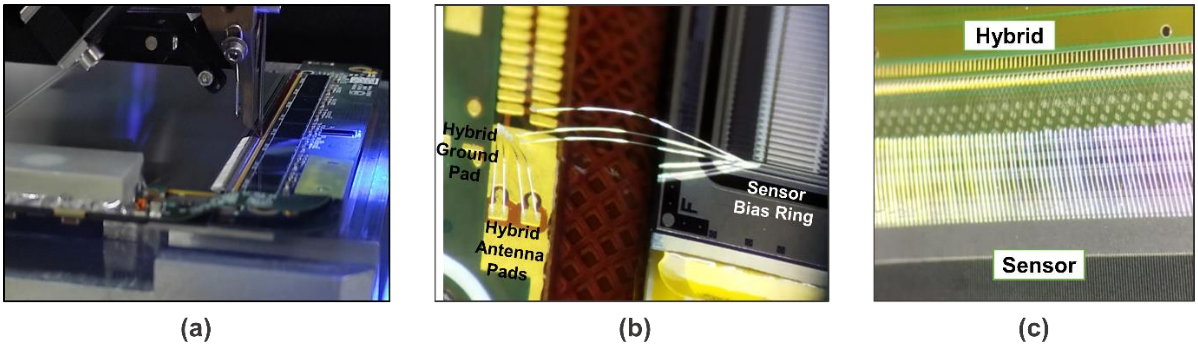

Figure 5.17: (a) Wire-bonding tool applying wire-bonds between the sensor and hybrid. (b) Three wire-bonds are applied between the sensor bias ring and hybrid ground pad, while four wire-bonds are applied between the hybrid antenna and ground pads. (c) Wire-bonds between the sensor AC pads and hybrid bond pads.

5.3 Dispensing Studies for Assembly

In order to ensure optimal performance and functionality, it is crucial to dispense the glue in precise quantities during the PI strip gluing step and the sensor-to-hybrid wire-bond encapsulation process. These steps are very important in the assembly process and require careful attention. A special glue dispensing system is required for these steps. This system consists of a really smart robot and a dispenser that can control the amount of glue very precisely. When they work together, they make sure the glue is applied exactly as needed, with sufficient accuracy and consistency.

Table 5.2: Number of wire bonds applied on different location for a 2S module

Bonds Position	**Number of wire-bonds on top side**	**Number of wire-bonds on bottom side**
Between sensor AC pads & hybrids bond pads	2 x 1016 = 2032	2 x 1016 = 2032
Between sensor bias ring & hybrid ground pad	4 x 3 = 12	4 x 3 = 12
Between hybrid antenna & ground pad	4 x 4 = 16	4 x 4 = 16
Total number of wire-bonds	**2060**	**2060**

5.3.1 Locally Developed Glue Dispensing System

During the initial phase of the project, when a company built (customized) glue dispensing system was not available, a specialized system for dispensing application was developed, comprising a locally designed gantry and dispenser, as illustrated in Figure 5.18. The gantry possesses impressive three-dimensional movement capabilities, enabling precise positioning within a 40 x 40 cm^2 working area. With a remarkable resolution of 100 µm in the x, y, and z dimensions, it ensured meticulous accuracy during operations. The gantry's speed could be conveniently adjusted within a versatile range of 1 mm/s to 5 cm/s, allowing for adaptability to diverse application requirements. Equipped with an Arduino system, the gantry's motion was programmable using G-code, a widely accepted language for controlling automated machines. Detailed specifications of the locally designed gantry system can be found in Table 5.3 offering comprehensive insights into its remarkable features and capabilities.

Simultaneously, the dispenser was meticulously developed utilizing an electro-pneumatic valve, expertly connected to a dedicated access point within the lab's centralized compressed dry air system. This electro-pneumatic valve was ingeniously configured in a normally closed (NC) mode, meaning it would permit the controlled flow of air through its output exclusively when energized. Such a setup enabled precise regulation of the air pressure at the valve's output, a critical factor in ensuring optimal glue dispensing performance. With the energization of the electro-pneumatic valve, the air pressure at its output was skillfully utilized to exert controlled force on the piston of a carefully chosen standard syringe, thus facilitating the precise and consistent dispensation of glue.

To ensure synchronization between the gantry and the pneumatic valve for accurate dispensing, an active pin on the Arduino board of the gantry's control system was ingeniously connected to a 24 V relay. The state of this pin, which could be set to high or low through the intuitive graphical user interface (GUI) of the gantry, effectively governed the operation of the relay. Upon receiving a high signal, the relay would be activated, leading to the energization of the electro-pneumatic valve and the subsequent controlled release of air through its output. Conversely, when the pin was set to a low state, the relay remained inactive, thereby keeping the valve de-energized and preventing the flow of air. This intuitive control mechanism, facilitated through the manipulation of the pin's state via the gantry's GUI, offered precise control over the dispensing time, ensuring consistent and accurate glue application.

It's important to mention that the rate of glue dispensing relied on two main factors: the air pressure in the system (which controls the amount of glue) and the speed of the gantry. These factors played a vital role in determining the flow rate and volume of the dispensed glue, allowing for meticulous fine-tuning and adjustment to suit the specific requirements of the application at hand.

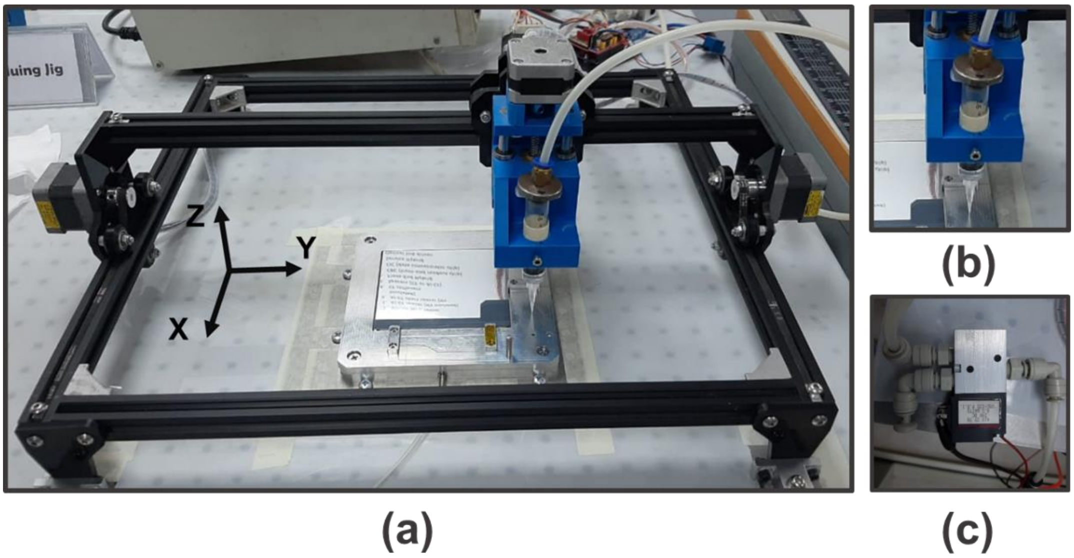

Figure 5.18: (a) Locally developed glue dispensing system featuring a gantry and pneumatic dispenser. (b) Dispensing system equipped with a standard syringe and plastic needle for precise glue application. (c) Crucial role of the pneumatic valve in the dispenser, configured in a normally closed (NC) mode, controlling the air pressure.

Table 5.3: Specifications of locally developed gantry.

Parameter	**Specifications**
Dimensions	45 cm x 45 cm x 20 cm
Working Area	40 cm x 40 cm
Minimum step	100 μm
Speed control	1 mm/s - 5 cm/s
Z-axis limit	6 cm
Control electronics	Arduino
GUI (Coding)	OpenBuilds Control (G-code)

5.3.2 Customized Glue Dispensing System

Following the introduction of a customized glue dispensing system, which included the LH 300 model from the LH series dispenser robot and the state-of-the-art Precifluid [107] volumetric dispensing system (Figure 5.19), a significant improvement in dispensing accuracy and repeatability has been attained. The LH 300 dispenser robot, with its impressive specifications, has revolutionized the gluing process. The details of the LH series dispensing system, derived from the manual, are provided in Appendix A, offering comprehensive insights into its capabilities and features.

The LH 300 dispensing robot functions as the central intelligence of the gluing system, offering a step size of 10 µm and an array of advanced automation capabilities. With exceptional precision and control over its movements, the robot ensures that the dispenser is positioned with utmost accuracy, guaranteeing that the glue is dispensed precisely at the intended locations. Moreover, the LH 300 robot provides various dispensing options such as dispense dot, line dispense, and spiral dispense, catering to specific dispensing requirements. This level of precision is crucial when dealing with delicate components and structures, as it minimizes the risks associated with misalignment or excessive adhesive application.

The Precifluid dispenser, an integral component of the system, facilitates highly accurate dispensing rates through its mechanical design. By precisely controlling the movement of the screw within the dispenser, it exerts force on the syringe piston, regulating the dispensing rate to levels as low as microliters per second (µl/s). This state-of-the-art technology allows for meticulous control over the quantity of glue dispensed, ensuring that each application adheres to the exact specifications outlined for the given task.

The availability of the LH 300 robot and Precifluid dispenser in the gluing system introduces an unparalleled level of control and precision. This dynamic pairing guarantees consistent and repeatable glue dispensing, significantly reducing the chances of errors or inconsistencies that were associated with the previously developed local dispensing system. The integration of these cutting-edge components elevates the overall performance and reliability of the gluing process, paving the way for improved assembly outcomes.

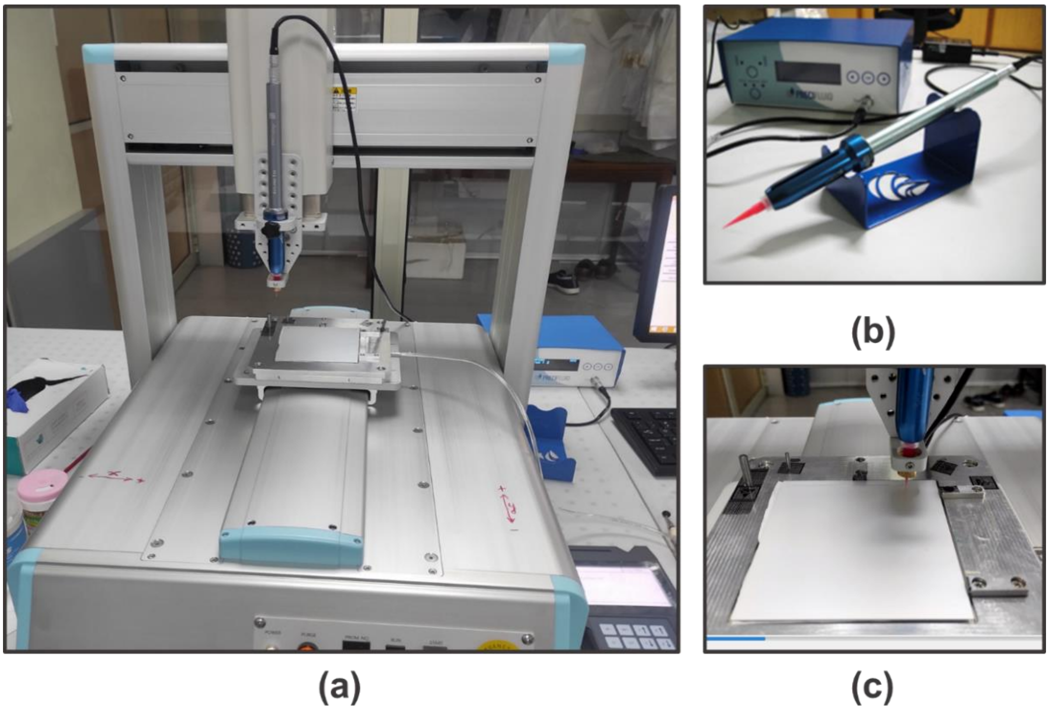

Figure 5.19: (a) Customized glue dispensing system featuring the LH 300 dispensing robot. (b) The advanced Precifluid glue dispenser integrated into the system. (c) Glue dispensing process carried out by the customized glue dispensing system.

5.3.3 Dispensing for PI Strips

As discussed in Section 4.5.4, the Al-CF bridges employed in the system serve the additional purpose of providing cooling to the module during its operation. To ensure effective cooling, it is essential to achieve a high glue coverage beneath the kapton strips, covering at least 95% of the area. This meticulous approach is necessary to maintain consistent thermal conduction since the presence of air within the glue could significantly alter the heat transfer rate. Given the demanding operating conditions of the modules within the tracker, where temperatures can reach as low as -35°C, maintaining optimal heat dissipation becomes paramount.

Moreover, it is crucial to maintain a minimal quantity of glue to achieve a thin glue layer, measuring less than 20 μm, which corresponds to dispensing 22 mg of Polytec LV601 for long strips. Previous research [108] has demonstrated that reducing the glue thickness by every 3 μm below the 20 μm threshold can improve the module's thermal runaway by 0.1 K. This highlights the significance of maintaining an optimum glue layer thickness to enhance the module's thermal performance and stability. Additionally, it is crucial to maintain a low quantity of glue to avoid any potential spill-out, as depicted in Figure 5.20. Spill-out can result in uneven module heights, introducing inconsistencies and potential issues. By carefully controlling the amount of glue used, these concerns can be mitigated, ensuring uniformity and stability in the module structure.

Figure 5.21 (a) illustrates the dispensing patterns of *Polytec LV601* glue accomplished using a locally developed dispensing system for attaching the PI strips. The finalization of the dispensing pattern from the locally developed system involved extensive research and development efforts to achieve the desired dispensing rate and quantity. For the dispensing process, a plastic needle with an inner diameter of 0.21 mm was carefully chosen. However, due to the gantry resolution constraint, it was not possible to select a distance below 100 µm between the needle tip and sensor. Therefore, a distance of 100 µm was chosen for the dispensing process. To attach the long and short PI strips, the dispensing system drew two long lines measuring 87 mm in length and one short line of 28 mm. The dispensing rate was precisely controlled by adjusting the combination of air pressure and gantry speed. Through meticulous experimentation, the optimal dispensing quantities were determined to be 19 mg for the long lines and 6 mg for the short line.

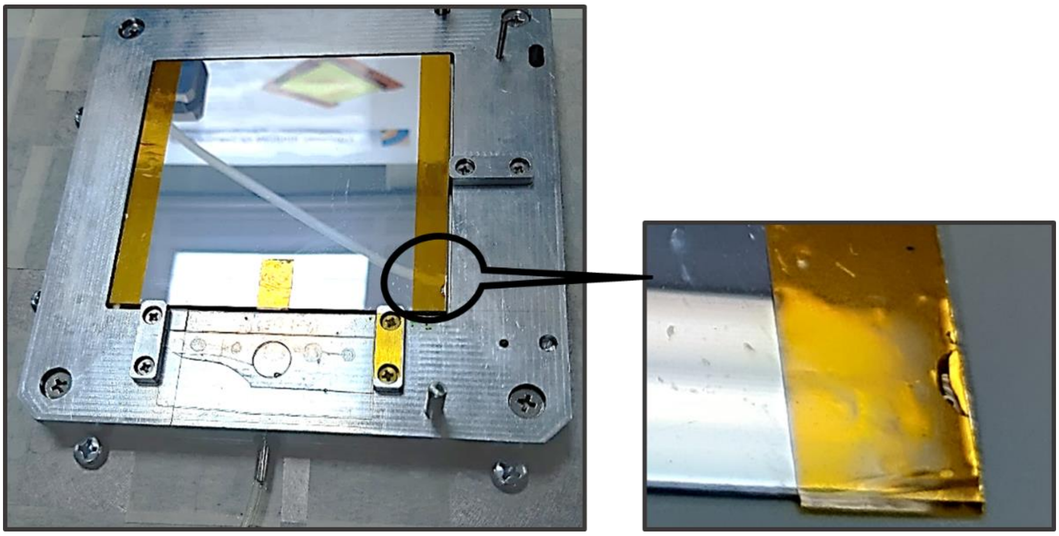

Figure 5.20: Spill-out of glue after attaching PI strips. Maintaining a low dispensing quantity of glue underneath the PI strip helps to prevent such spill-out.

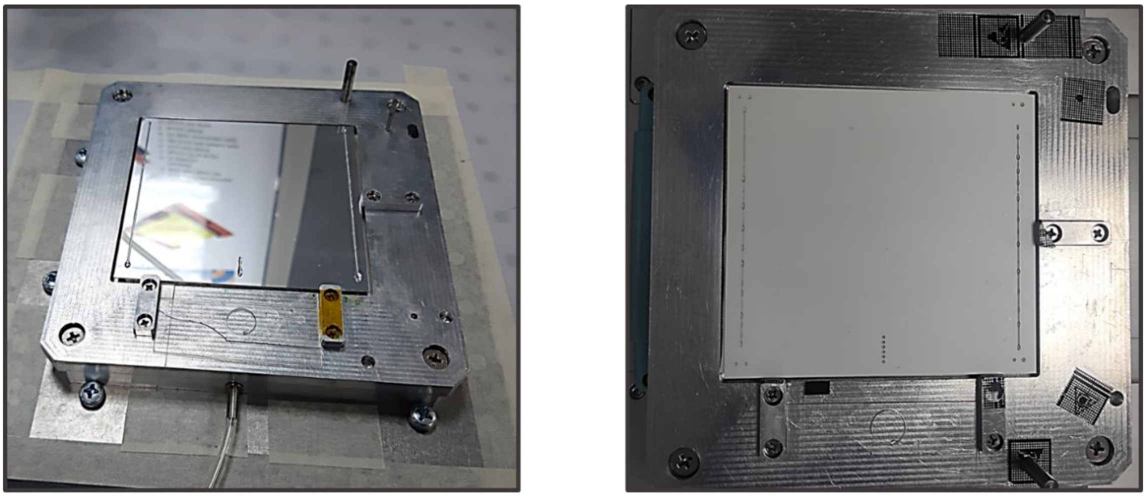

(a) (b)

Figure 5.21: Glue pattern drawn using Polytec LV601 to attach PI strips. (a) Three lines are drawn using the locally developed glue dispensing system. (b) A combination of dispense dot and line dispense is drawn using the customized glue dispensing system consisting of the LH 300 robot and Precifulid glue dispenser.

On the other hand, the use of the customized glue dispensing system made the dispensing process considerably easier. A plastic needle with an inner diameter of 0.25 mm was chosen, and the distance between the sensor and the needle tip was set to 45 μm. A combination of dispense dot and dispense line techniques was employed, as shown in Figure 5.21 (b), to achieve the desired results. Furthermore, a dispensing rate of 0.8225 μl/s was selected from the dispenser to ensure accurate and consistent dispensing of the glue. As a result, the required glue quantities for the long and short strips using the customized glue dispensing system were determined to be 7 mg and 1 mg, respectively. Further details of the glue pattern can be found in Appendix A.

These findings demonstrate the effectiveness of the locally developed and customized glue dispensing system in achieving precise dispensing rates and quantities for attaching the PI glue. This capability allows for accurate and consistent assembly of the long and short PI strips, ensuring the integrity of the module's thermal conduction and overall performance.

5.3.4 Dispensing for Sensor-to-Hybrid Wire-bonds Encapsulation

During the module assembly process, it is necessary to protect the sensor-to-hybrid wire-bonds. To achieve this, the wire-bonds are encapsulated with a silicone elastomer called

Sylgard 186. However, it is crucial to avoid increasing the overall height of the module, so the encapsulation must be done with a precise amount of silicon elastomer. To ensure proper encapsulation of the wire bonds with minimal use of glue, a dispensing pattern that offers more control and precision is required. After detailed experimentation performed in reference [106], it has been found that a spiral pattern provides the best results in terms of complete filling of the bonds using a lesser quantity of glue.

In the locally developed dispensing system, the two wire-bonded sides (right and left FEH) are separately encapsulated for both the top and bottom sides of the module. This means that a single program needs to be calibrated four times for each module to achieve complete encapsulation. A plastic needle with an inner diameter of 1.19 mm is utilized for dispensing the Sylgard, with the tip height set at 1 mm above the height of the wire-bonds. The quantity of Sylgard used to fill the bonds with the spiral pattern has been observed to vary between 540-580 mg for each side.

On the other hand, the customized dispensing system allows the encapsulation of the two wire-bonded sides simultaneously for either the top or bottom side. Consequently, the module only needs to be calibrated twice to achieve complete encapsulation. With this system, the program takes only 5 minutes after calibration to complete the encapsulation of one side of the module. A plastic needle with an inner diameter of 0.41 mm is employed to dispense the Sylgard, and the tip height is selected to be approximately 1.5 mm above the height of the wire-bonds. To achieve precise control of the Sylgard filling quantity, the dispensing rate in the Precifluid dispenser was set to 0.002052 ml/s. This dispenser ensures the accurate control, enabling a consistent filling quantity of 540 mg per side during the encapsulation process.

Figure 5.22 illustrates the precise encapsulation of the sensor-to-hybrid wire-bonds achieved through the precise calibration of both the locally developed and customized dispensing systems. For more information on the specific dispensing patterns employed in this process, please refer to Appendix A, where detailed pattern is provided.

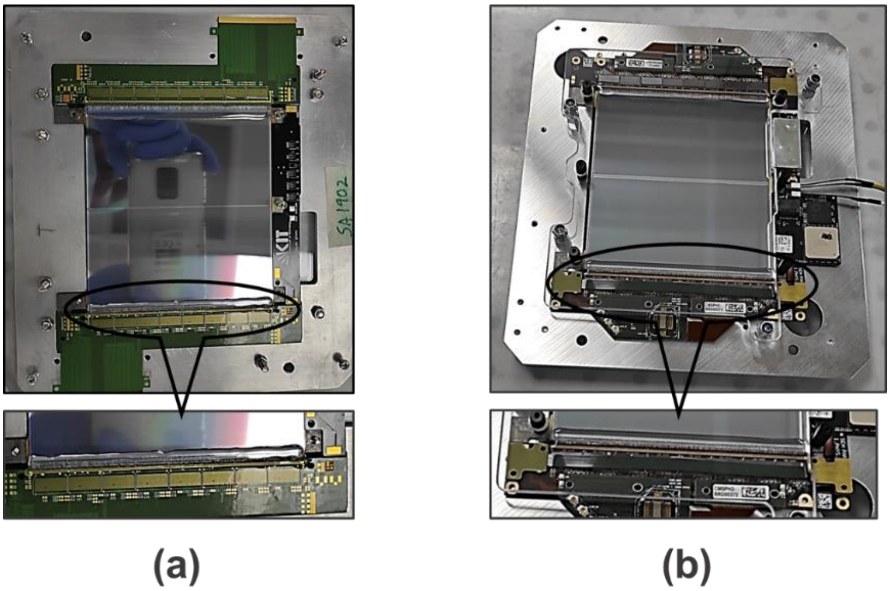

Figure 5.22: Encapsulation of sensor-to-hybrid wire-bonds using (a) locally developed dispensing system and (b) customized dispensing system. The spiral pattern is used for both dispensing. The detailed information about the spiral patterns are shown in Appendix A.

5.4 Module Meteorology Method Development

In section 5.2.4, a crucial aspect that is discussed pertains to the requirement of achieving the necessary misalignment tolerance between two sensors after the assembly of the bare module. This particular topic is thoroughly examined within the same section, where it is revealed that bare module assembly must be adhere to specific tolerance limits. According to the findings, the translation tolerance limits should not exceed 50 μm and 100 μm in the perpendicular and parallel directions to the strip, respectively. Additionally, a rotational tolerance limit of 400 μrad has been established.

To accurately determine the misalignment between the two sensors, the establishment of a common reference point becomes imperative. Assembly centers have recognized this need and have developed three distinct methods for performing bare module metrology. These methods have been compared using a common misaligned bare 2S module, namely SA 1902 [109]. A visual representation of these three methods can be found in Figure 5.23.

The first method (Figure 5.23(a)), known as the "Double sided metrology" [110, 111]. This approach involves the utilization of two cameras simultaneously recording both sensors. A crucial aspect of this method is that the cameras share a common axis of rotation, enabling independent measurements of each sensor.

The second method (Figure 5.23(b)), referred to as the "Laser-based method” [100]. This approach involves the use of a combination of a microscope and a laser system. The laser setup serves as the common reference point from which the distance between the two sensors is measured.

The third method (Figure 5.23(c)), known as the "Needle method” [112]. In this method, four needles are strategically attached to the module carrier jig surrounding the bare module. This arrangement creates a common reference frame for both the top and bottom sensors.

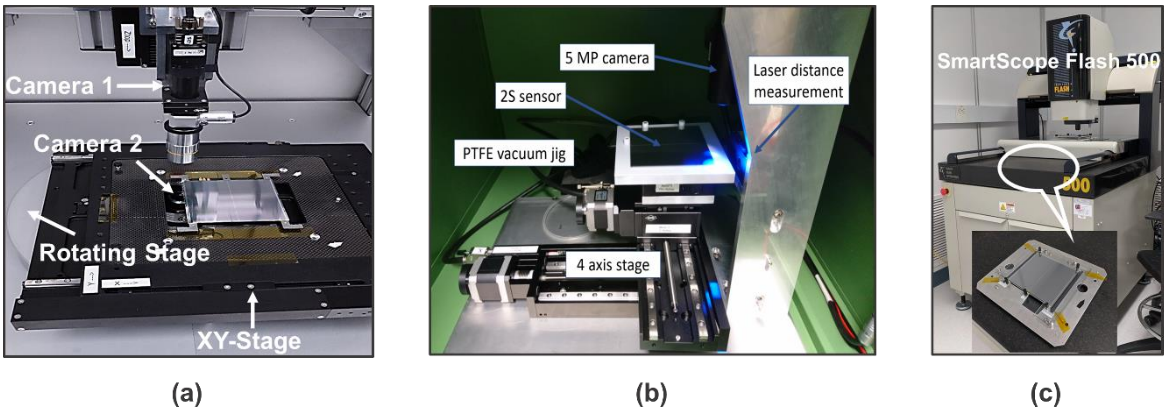

Figure 5.23: Three methods developed for bare module metrology by different assembly centers: (a) Double sided metrology: This approach involves the use of two cameras to measure both sensors independently [110]. (b) Laser-based method: A combination of a laser and a microscope is employed to measure the distance of both sensor edges from the laser [100]. (c) Needle method: A microscope and gantry system are utilized, with four needles attached near the module corners [112].

At NCP assembly center, the needle method has been developed, utilizing the available probe station, *MPI TS2000 - DP* [113] for measurement purposes (Figure 5.24(b)). To commence the process, the bare module is mounted on the module carrier jig with the bottom sensor facing upward. Four needles are strategically attached near the four sensor corners on the jig, as depicted in Figure 5.24(a). This configuration establishes a common reference frame for both sensors during the measurement procedure. The measurements are conducted by placing the module carrier jig on the chuck of the probe station and employing its microscope.

Using the lower left needle as the origin point, as indicated in Figure 5.25, the positions of the four sensors and three needle points (near positions 1, 2, 3, and 4, as mentioned in Figure 5.25) are determined. Once the measurements for the bottom sensor are completed, the jig is flipped upside down, and the same measurement process is repeated for the top sensor.

To analyze and determine the alignment between the two sensors, a Python code has been developedThe code initially fits the measured needle points for both the top and bottom sides using different steps and algorithms. The parameters obtained from this needle fitting process are then applied to the top sensor corners. Finally, the new top sensor coordinates are fitted with bottom sensor coordinates to calculate the misalignment between the two sensors. A detailed description of the steps followed in writing the code to determine the misalignment is provided in Appendix B.

The metrology method itself has been validated by comparing the results for the common misaligned module, SA 1902 [114]. Figure 5.26 provides a graphical view generated by the code after performing the fitting algorithms. The figure illustrates the fitting of the four needle and sensor points, showcasing the accuracy of the fitting process.

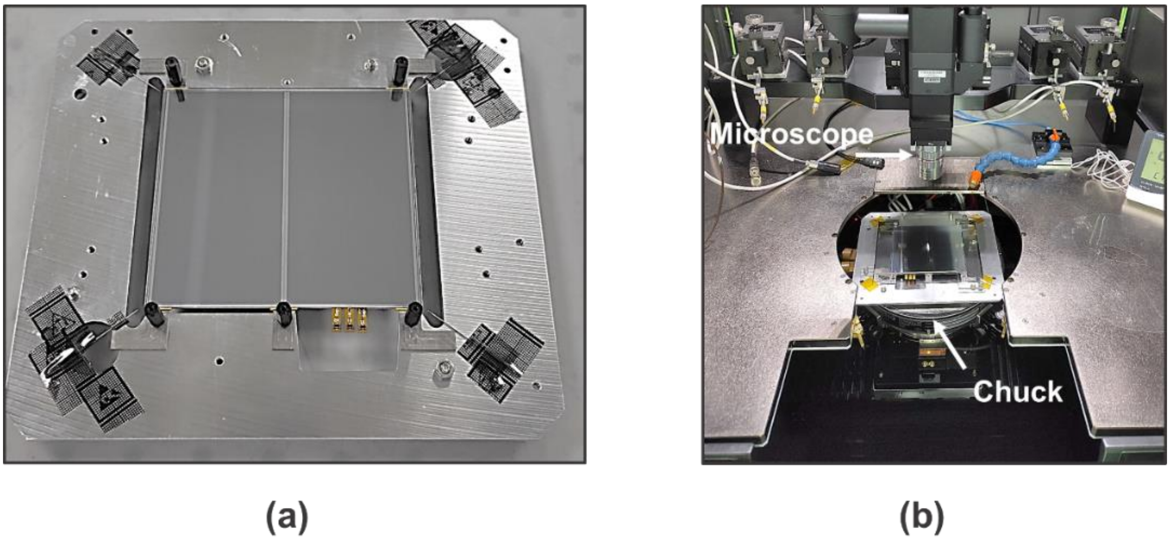

Figure 5.24: (a) The image depicts the bare module mounted in the module carrier jig, with needles attached near the four sensor corners. (b) The carrier jig is placed on the probe station chuck, enabling precise measurements to be taken using the microscope and the movement of the chuck. This setup is utilized for metrology measurements.

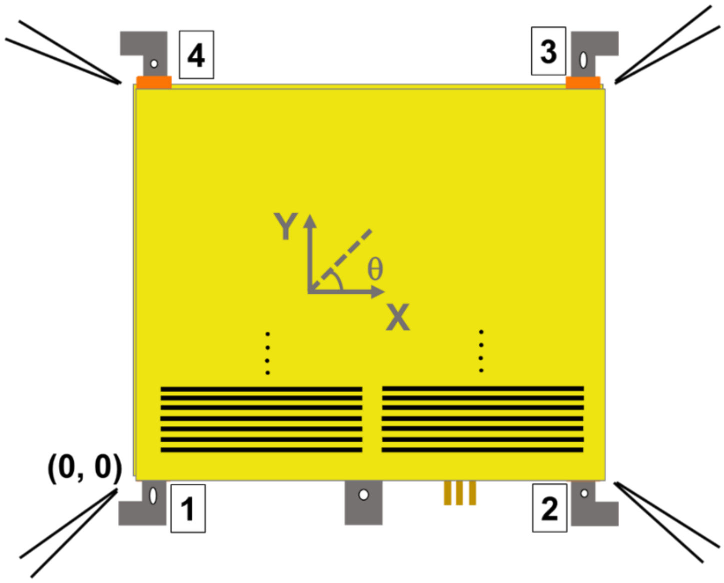

Figure 5.25: The figure shows the convention used for metrology measurements, where the x-axis represents the direction parallel to the strips, the y-axis represents the direction perpendicular to the strips, and θ represents the positive rotation in the anticlockwise direction. The metrology measurements for both the top and bottom sides are performed by measuring the sensor and needle points at positions 1, 2, 3, and 4, with the needle at position 1 serving as the reference point.

Table 5.4 presents the alignment results between the two sensors for one of the assembled functional modules. These results are obtained by considering the measurements for the sensor corners and different alignment marks on the sensor. The results obtained from the sensor corner points includes the inaccuracies introduced due to sensor dicing. Conversely, the results obtained from the three other alignment marks exclude the influence of sensor dicing. The final metrology result is calculated by taking the average of all the measurements, providing a comprehensive evaluation of the alignment between the sensors. The convention followed for the alignment parameters is similar to the description provided in section 5.2.4 and Figure 5.25, where $\Delta\theta$ represents the angular misalignment, Δx represents the misalignment parallel to the strips, and Δy represents the misalignment perpendicular to the strips.

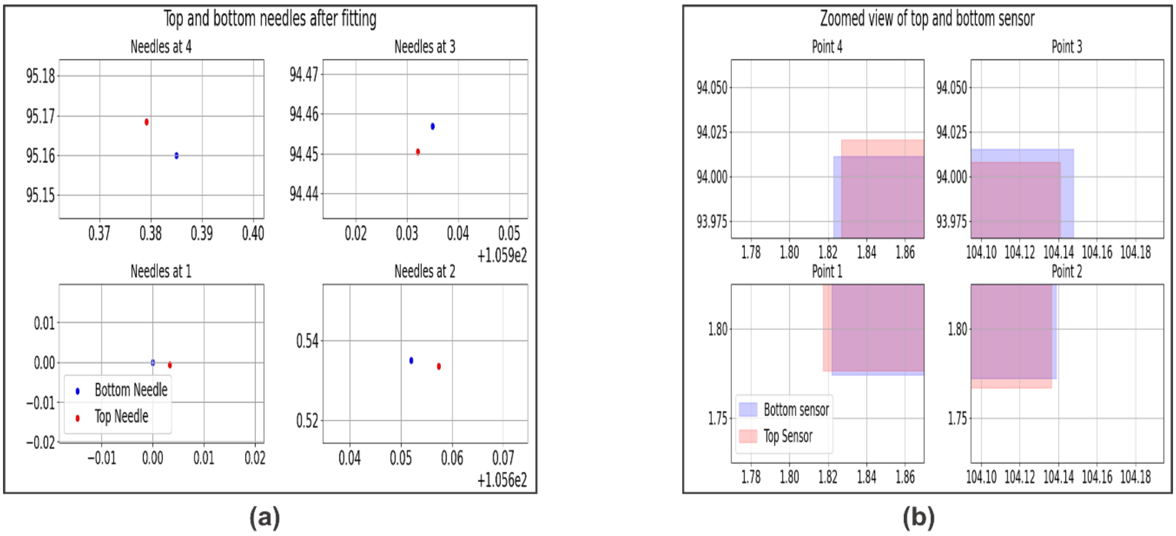

Figure 5.26: Zoom view, after fitting in Python code, of (a) needle points and (b) sensor corners for both top and bottom measurements. The points 1, 2, 3, 4 align with Figure 5.25, and the units on both axes are in millimeters for all subplots.

Table 5.4: Metrology results of a functional module for different alignment marks

Reading #	Δθ (μrad)	Δx (μm)	Δy (μm)	Measurement Mark
1	-17	-12	-4	Sensor Corner
2	-23	-14	-4	
3	-24	-13	-4	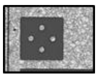
4	-24	-13	-4	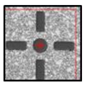
Avg. value	**-22**	**-13**	**-4**	

5.5 Prototyping of Module Testing Procedures

5.5.1 Sensors Leakage Current Measurement Setup

During the prototyping phase, the leakage current of both sensors was measured after each assembly step to assess their condition. This is done by applying sensors' back-plane a negative biasing voltage. The measurements were conducted on the *MPI TS2000 - DP* [113] probe station using a Keithley electrometer [115].

1. For the bare sensors, the probe station chuck was utilized to apply the biasing voltage to the sensor's backside, while the leakage current was measured by placing the probe needle on the sensor bias ring.
2. After gluing the kapton strips to the sensor backside, IV measurements were conducted using a 50 μm thick aluminum foil. This foil was inserted between the probe station chuck and the central area of the sensor backside, which was the region without the kapton strips.
3. The subsequent steps include the assembly of the bare module and hybrid gluing. Once completed, the module was mounted on the module carrier jig, which was then positioned on the probe station chuck. During the bare module assembly, the biasing voltage was supplied through the HV tails using the power plate (Figure 5.27 (a)). However, during the hybrid gluing step, the biasing voltage was provided via the service hybrid (Figure 5.27 (b)). In order to perform IV measurements, the probe needle was placed on the sensor bias ring.
4. After the final two assembly steps of wire-bonding and encapsulation, the IV measurements were performed by directly connecting the Hi and Lo connections of the electrometer to the HV and ground of the LV connectors on the service hybrid, respectively.

To accommodate the series production requirements, a separate HV and IV test setup was constructed, as depicted in Figure 5.28. This specialized test setup not only ensures efficient and accurate IV testing but also supports the high-voltage (HV) test. The HV test will be conducted to qualify each sensor after attaching PI strips to the sensors' backside during series production.

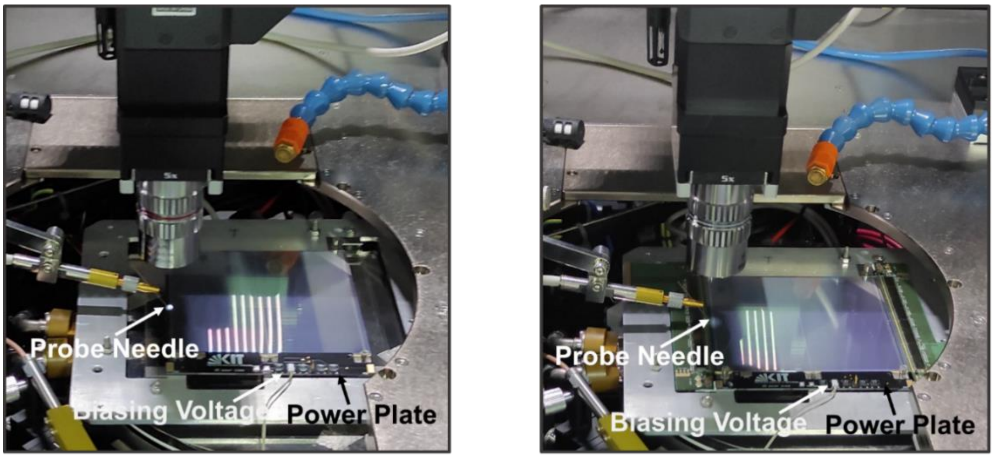

(a) (b)

Figure 5.27: IV measurement on probe station using probe needle. (a) Following bare module the assembly, the module carrier jig was positioned on the probe station chuck, and the power plate was temporarily used to provide HV to the sensors. (b) After the assembly involving hybrid gluing, the module carrier jig was again placed on the probe station chuck, and the HV was provided by the SEH (In the 8CBC2 module, the power plate was utilized instead of the SEH).

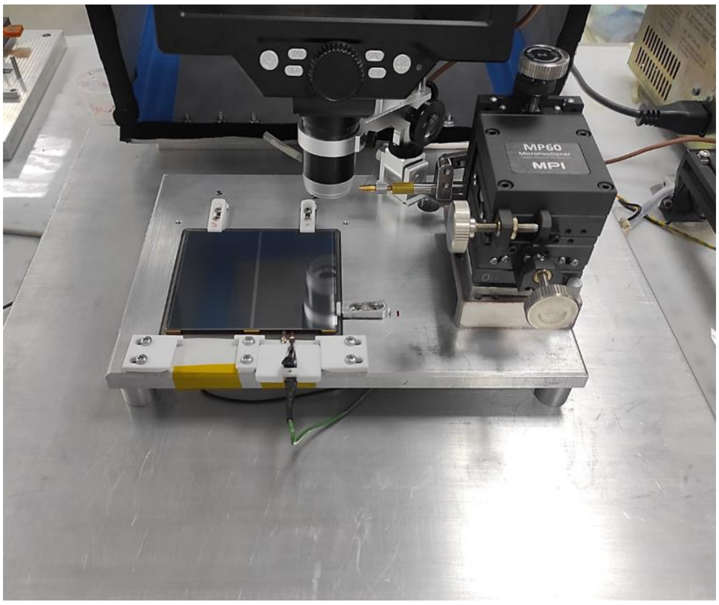

Figure 5.28: HV and IV testing setup[§] built to support the assembly line during the production period.

[§] The setup diagrams are provided by KIT.

5.5.2 Equivalent Noise Charge

Noise in a fully depleted sensor arises due to statistical fluctuations caused by electrons and holes within the sensor. This noise is commonly referred to as Equivalent Noise Charge (ENC) and is an important factor in assessing the performance of a sensor. When an ionizing particle interacts with the sensor, it generates a signal proportional to the amount of charge deposited. However, the presence of noise can interfere with this signal, reducing its accuracy and reliability. Therefore, it is desirable to minimize the noise in order to maximize the signal-to-noise ratio (S/N) of the sensor. The S/N ratio is a key indicator of the quality of a sensor. A higher S/N ratio indicates a better sensor performance because it means that the signal is stronger relative to the noise or the signal can be detected with greater confidence, leading to more accurate measurements.

The noise from different sensor parameters contributes to the total ENC value quadratically, as follows [55]:

$$ENC = \sqrt{ENC_c^2 + ENC_{I_L}^2 + ENC_{R_p}^2 + ENC_{R_s}^2} \tag{5.1}$$

where ENC_{I_L}, ENC_{R_p} and ENC_{R_s} represent the contributions to noise from leakage current, parallel thermal noise from bias resistance, and series thermal noise from metal strip resistance, respectively. These terms typically have minimal impact on the overall noise. The most significant contributing term is the load capacitance ENC_C which can be calculated as follows [55]:

$$ENC_C = a + b.C_{tot} \tag{5.2}$$

$$C_{tot} = C_{int} + C_{back} \tag{5.3}$$

and C_{int} and C_{back} represent the inter-strip and strip-to-backplane capacitance values respectively.

5.5.3 Noise Measurement Setup

The noise measurement of the modules is conducted using the FC7 evaluation board [116]. This board enables the configuration of the CBC register via I2C communication and also facilitates the transmission of trigger and clock signals. To carry out these measurements, the FC7 board is inserted into a μTCA crate or mini μTCA card, as illustrated in Figure 5.29. The operation of the board is controlled by the d19c firmware of the CMS collaboration, which is managed through the Ph2_ACF middleware. This control is established using an Ethernet connection between the computer and the μTCA setup. To operate hybrids and biasing sensors in a module, a low voltage supply and a high voltage supply are respectively utilized. To ensure accurate measurements, a common grounding approach is employed for all the equipment utilized in the testing setup.

As part of this thesis, a dedicated test box, depicted in Figure 5.30, has been developed specifically for the prototyping phase of cold test measurements. The details of this test box will be discussed in the subsequent section. Additionally, the test box serves the purpose of a dark box for performing noise measurements at room temperature. During the prototyping phase, various test setups were developed as the components of functional 2S modules were evolving. The different types of functional 2S modules will be discussed in the next chapter.

For the 8CBC2 functional module, an electrical test setup is implemented using the FC7 board and a mini μTCA card. The FC7 board is connected to an FPGA Mezzanine Card (FMC) that supports electrical connections. A test card, responsible for data transmission with the module, is linked to the FMC card using a VHDCI cable. Furthermore, a four-channel low voltage power supply, Rodge & Schwarz model HMP4040 [117], is connected to the test card to provide the necessary voltages for the operation of the FEH (Front-End Hybrid). Due to the direct connection between the FEH tail of the 8CBC2 hybrid and the test card, only one FEH can be read at a time for noise measurement purposes. To facilitate easy connection and disconnection of the FEH tails, the 8CBC2 modules are placed upside down on the carrier jig, as depicted in Figure 5.30.

The 8CBC3 and fully functional 2S module werre tested using the test setup developed with the FC7 board and μTCA crate. Initially, this setup was configured as an electrical test setup, employing the universal interface board (UIB-2) along with two FMCs that support electrical testing. These arrangements are used to conduct noise measurements on 8CBC3 bare hybrids. After the complete assembly of the 8CBC3 module prototype, the setup is transformed into an 8CBC3 optical test setup. This transformation is achieved by connecting the FMC with an optical connector to the FC7 card. Subsequently, the setup is further updated to enable optical testing of fully functional 2S hybrids and modules. In the case of the 2S module, the noise measurement is performed by connecting the optical link (VTRx+) in the module to the FMC using an optical fiber.

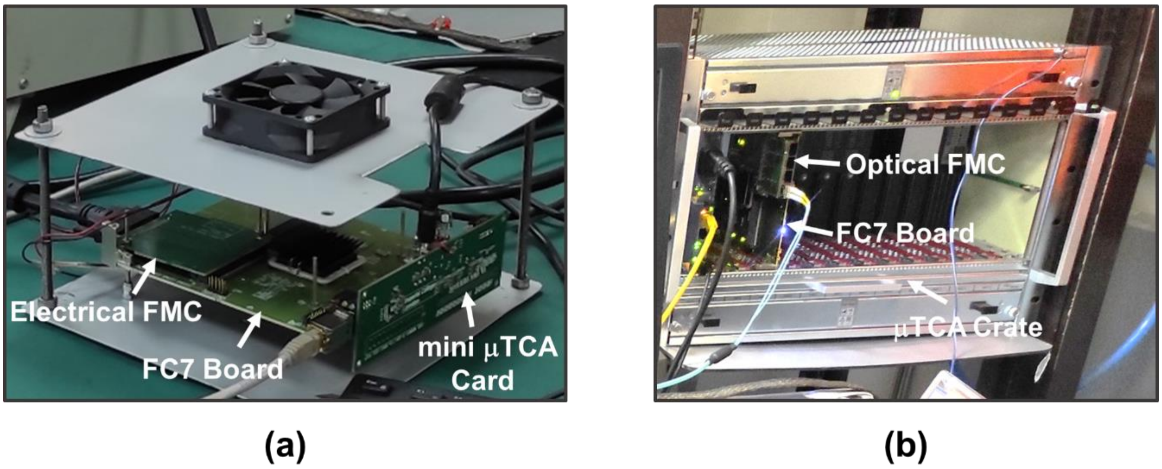

Figure 5.29: Two types of configurations used to attach the FC7 board. (a) Utilizing a mini μTCA card. (b) Utilizing a μTCA crate.

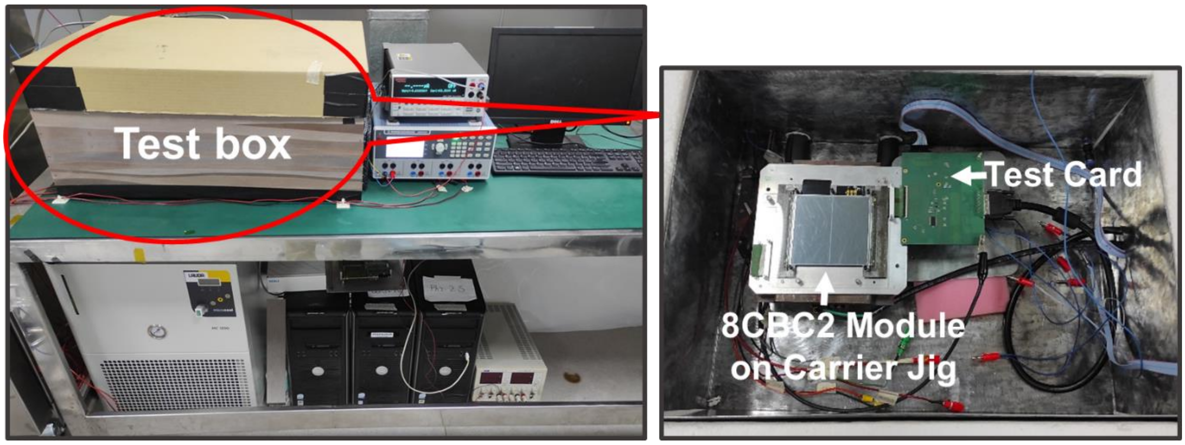

Figure 5.30: Test box utilized as a dark box during noise measurements. The 8CBC2 module is positioned upside down on a carrier jig, and the FEH is connected to the test card. The entire setup is enclosed within the test box for noise measurements.

5.5.4 Nosie Measurement with Ph2_ACF

The noise measurements are performed utilizing the CMS Phase 2 Acquisition and Control Framework (Ph2_ACF) within the test setup. Ph2_ACF is a C++ software implementation that serves as an interface to the modules developed for the CMS Phase-2 Tracker upgrade. The configuration of the hardware components is specified in an XML file, which also contains information regarding data communication, such as the IP address of the readout FC7, clock and trigger sources, and chip settings (e.g., threshold settings for the CBC channels or the latency value). The test setup utilizes specific commands provided by Ph2_ACF for module testing. The "**commissioning**" command is employed to measure noise, latency, and stub latency, while the "**calibration**" command is used for routine calibration procedures.

As described in Section 4.5.2, the channels within the CBC generates a binary output by comparing the incoming signal with a threshold voltage. The threshold voltage, denoted as V_{cth}, is measured in DAC counts. For CBC2, the average conversion factor is approximately 1 V_{cth} unit ≈ 380 e^- [118], whereas for CBC3, 1 V_{cth} unit ≈ 150 e^- [119]. It is important to note that this conversion factor varies from chip to chip. In order to determine the optimal threshold value, a threshold scan is performed. During this scan, the comparator threshold voltages are systematically adjusted in DAC counts (V_{cth} units) while measuring the occupancy, which represents the ratio of the number of hits to the number of triggered readouts. By incrementally lowering the threshold value, the occupancy increases from 0 to 1. It is important to note that higher values in V_{cth} units correspond to lower thresholds in the electronic readout.

The threshold scan results in an S-curve, which provides valuable information such as the pedestal value. The pedestal represents the threshold value at which the occupancy is 50%. In real situation, the S-curve is obtained by temporally integrating the Gaussian-distributed noise pulses due to electronics. The differential distribution of the S-curve reveals the pedestal and the associated smearing caused by electronic noise. The pedestal is determined as the mean value of the differential distribution, while the standard deviation represents the noise level attributed to the electronics. Figure 5.31 illustrates the S-curve obtained from the threshold scan for one of the CBC channels of the 8CBC2 hybrid. From the differential distribution of the S-curve, the pedestal value and electronic noise level are determined to be 118 V_{cth} units and 1.53 V_{cth}, units respectively, for that channel.

The calibration command in Ph2_ACF serves the purpose of achieving a consistent and uniform response behaviour across channels in a CBC. The detailed circuitry of an individual CBC channel can be found in Section 4.5.2 and is depicted in Figure 4.19. The calibration process involves several steps to ensure optimal performance.

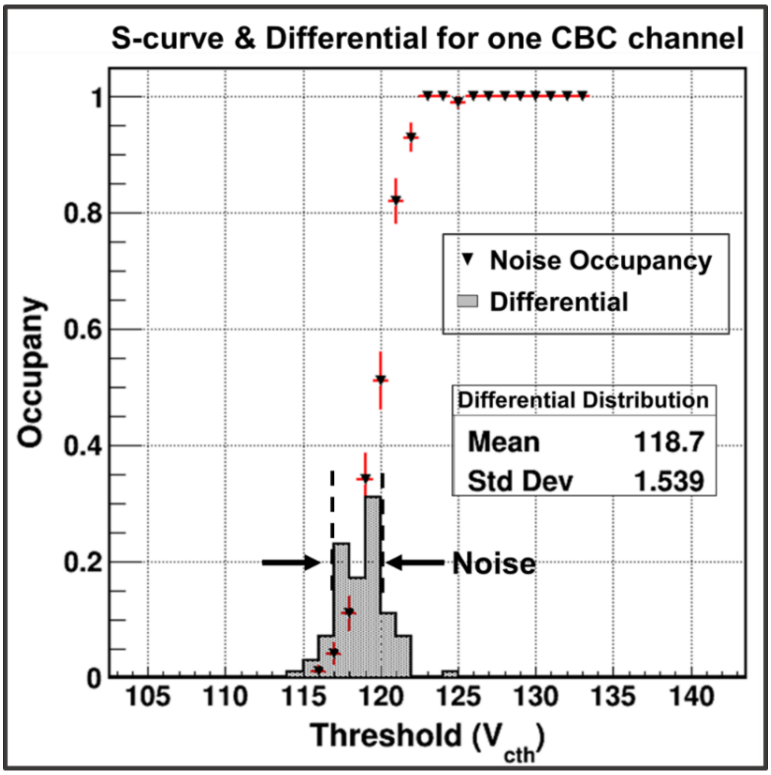

Figure 5.31: Threshold scan of a CBC channel on bare 8CBC2 FEH, yielding the S-curve. The differential of the S-curve generates a distribution, where the mean represents the pedestal and the standard deviation corresponds to the electronic noise value. For this channel, the pedestal is measured at 118 V_{cth} units and the electronic noise level is approximately 1.53 V_{cth} units.

1. Initially, all channels in a CBC are set to a target V_{cth} value.
2. Then, the global VPLUS parameter is adjusted to achieve a 50% occupancy value for all channels.
3. Once the VPLUS value is determined, it is applied to the post-amplifier stage, as shown in Figure 4.19.
4. Each channel is fine-tuned individually by adjusting the Offset Adjustment parameter to achieve a 50% occupancy.
5. After the channel-specific adjustments, the PedeNoise command is executed to perform a threshold scan. During this scan, the software records the S-curve data and computes the noise value for each channel.

5.6 Prototyping of Module Cold Test

As discussed in section 4.6, the modules within the CMS Phase 2 Tracker will be operated at temperatures below -20°C. This temperature control is crucial for minimizing the sensors' leakage current, as a higher value could result in heat dissipation and potentially lead to a thermal runaway situation. To ensure the reliability and performance of the modules, a comprehensive testing at cold temperature will be conducted during series production. The testing process includes subjecting the modules to thermal cycles, exposing them to extreme temperature conditions to assess their stress limits and evaluate their performance. This procedure allows for the identification of any potential issues or weaknesses in the modules that may arise during their operation.

As part of the prototyping studies, a small cold test box has been developed. This specialized test box is designed to evaluate the performance of the modules under various cooling conditions and facilitate thermal cycling during the module prototyping phase. By subjecting the modules to different cooling conditions inside the box, their behavior and performance have been thoroughly analyzed and studied.

5.6.1 Cold Test Box

The cold box has been constructed using the wooden box, depicted as test box in Figure 5.30, as its base. The development of the cold box incorporates the following features:

1. To thermally isolate the internal environment of the box from the external surroundings, polystyrene sheets with a thickness of 5cm are used within the box.
2. Aluminum sheets are placed inside the polystyrene sheets to create a Faraday cage, providing effective electromagnetic shielding for the equipment inside the box.
3. A dry air connection is established to introduce dry air into the box during operation. This helps reduce the dew point at low temperatures by lowering the relative humidity value lower than 10%. Additionally, a humidity monitor is placed inside the box to monitor the relative humidity level.
4. The cooling of the module temperature is achieved using a combination of a Peltier plate, the *LHP 800CP* [120], and a chiller, the *Lauda MC 1200* [121]. Appendix C provides details about these components.

5. Two larger holes are created on one side of the box to allow the coolant connections from the chiller to enter, while three holes are made for electrical cabling. Furthermore, a grounding point is established inside the box to provide grounding for all the equipment. This grounding point is connected to the common grounding point outside the box.
6. A copper plate is designed and machined to serve as a mounting platform for the 2S modules. The copper plate has similar dimensions to the module carrier jig but has been milled down from a 6mm copper plate to 2mm in the central portion. The remaining 2mm thickness in central portion maximizes the transfer of cooling from the Peltier plate to the copper plate. The plate is placed on the Peltier plate, allowing the Peltier plate to cool the copper plate, which in turn cools the module.
7. Temperature monitoring of different points within the box is facilitated by using K-type thermocouples and a thermocouple data logger, the *PicoLogger TC-08* [122].

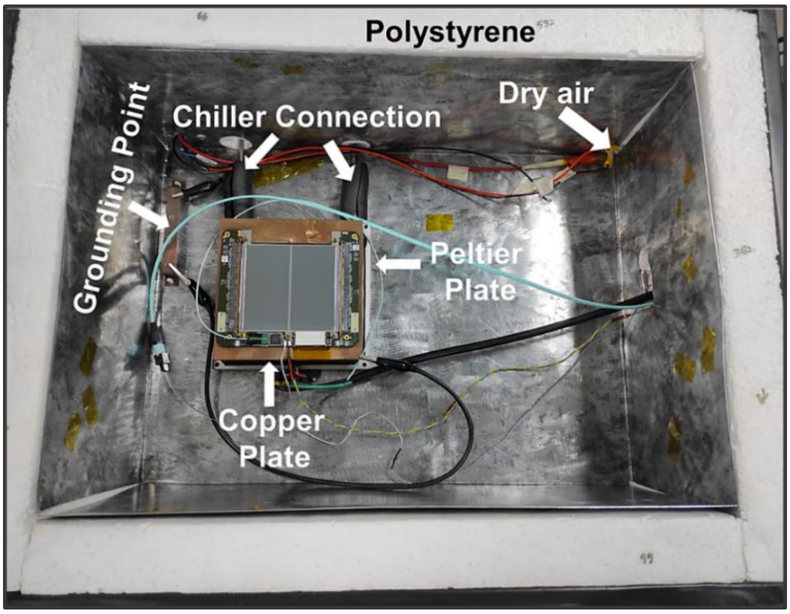

Figure 5.32: Inside view of the cold test box highlighting the chiller connection, grounding point, dry air connection point, and copper plate, designed as a mounting plate for the 2S module, positioned on the Peltier plate.

Figure 5.32 provides a visual representation of the interior of the cold test box, showcasing a module mounted on the copper plate. The cooling process during the cold test operation occurs in two steps. Initially, the chiller is activated to cool the surface of the Peltier plate. Subsequently, the Peltier element is turned on to achieve further cooling.

5.6.2 Temperature Measurements with Cooling System

In the initial stage of the experiment, the cooling measurement focused specifically on the copper plate. Thermocouples were strategically positioned near the module mounting points, as shown in Figure 5.33(a). The temperatures recorded during the operation of the chiller and Peltier plate at these locations are presented in Figure 5.33(b). The plot clearly indicates that the lowest temperature reached on the copper plate was -23.3°C, demonstrating the effectiveness of the cooling system.

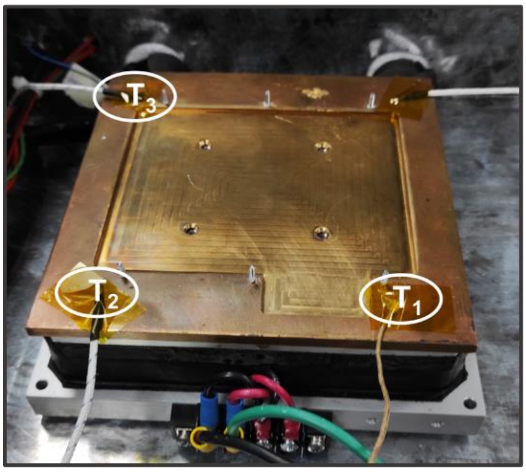

(a)

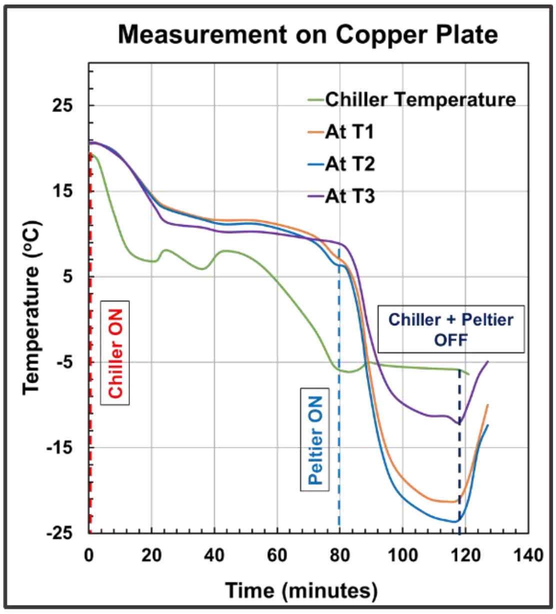

(b)

Figure 5.33: Cold test setup for measuring temperature exclusively on the copper plate. (a) Thermocouples attached to the copper plate at various module mounting positions. (b) Temperature variation at different positions after activating the cooling system, comprising the chiller and Peltier plate [123].

Moving on to the second step, a module was mounted on the copper plate, and the cooling measurements were repeated with the module powered off. Two thermocouples were placed on the module's bridges, while an additional one was positioned on the copper plate, as illustrated in Figure 5.34(a). The temperature variations were monitored after activating the cooling system at different measurement points, as depicted in Figure 5.34(b). The results revealed that the minimum temperature recorded on the copper plate was -18°C, while the temperature on the module's bridges reached -13°C. These measurements demonstrate the ability of the cooling system to efficiently cool both the copper plate and the module itself.

To verify the repeatability of the cooling test, the cooling system was temporarily turned off. Once the temperature of the copper plate rose to +5°C, the cooling system was switched on again. Remarkably, similar minimum temperature values were observed at different positions, as depicted in Figure 5.34(b), validating the consistency and reliability of the cooling system.

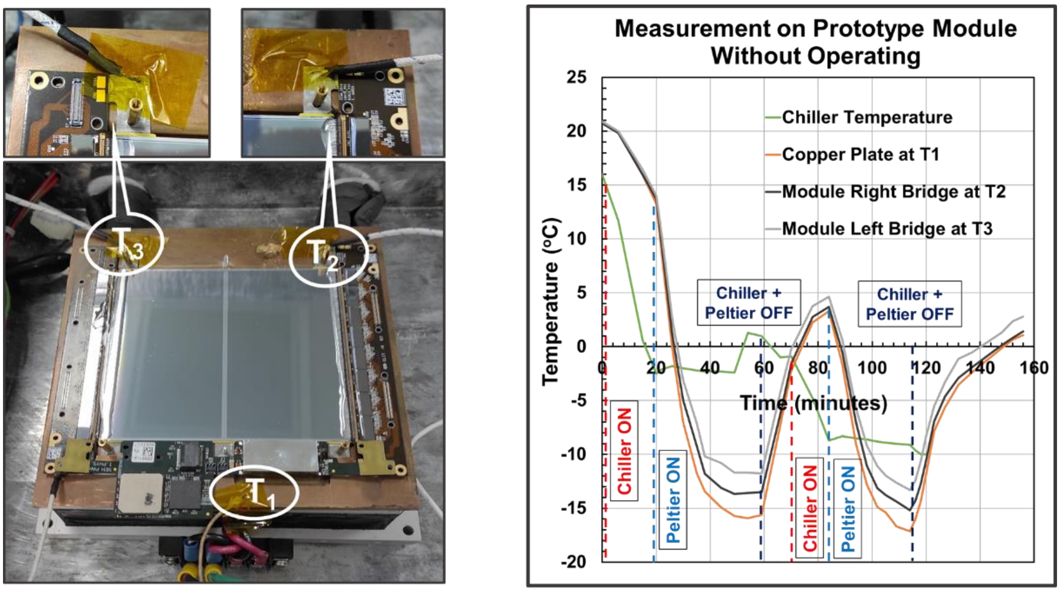

(a) (b)

Figure 5.34: Cold test setup for temperature measurement on a non-operational module mounted on the copper plate. (a) Thermocouples attached to the copper plate and module’s bridges. (b) Temperature variation at copper plate and bridges after activating the cooling system. The cooling system is turned off during measurements and turned on again [123].

In conclusion, the developed cold test box has proven to be a reliable and effective tool for conducting noise measurements and performing thermal cycling on prototype modules. The experiment demonstrated consistent cooling capabilities, as evidenced by the stable and low temperatures achieved on the copper plate and the module's bridges.

6

Results of Functional 2S Modules

In this chapter, the results of the functional modules assembled throughout this study are discussed. Initially, the assembly results are presented to demonstrate the successful development of assembly setups in terms of mechanical tolerances. Subsequently, the IV results of the sensors after each assembly step indicate successful prototyping of the setups for the production assembly line. Furthermore, the noise measurements of assembled functional modules showcase their performance. Lastly, the results from cold tests conducted on the modules provide valuable data on their thermal performance and suitability for operation in extreme environments.

6.1 Module Assembly Results

Three different types of functional modules, depicted in Figure 6.1, were assembled during this study. Each type represents a distinct variant of the FEH, with specific characteristics and testing capabilities. These different types of FEH are discussed in section 4.5.2.

The first type of functional module consists the (Figure 6.1 (a)) 8CBC2 variant of FEH. This variant do not include the CIC chip. Therefore, these hybrids are subjected to the electrical testing where each hybrid is tested individually. The second type of functional module (Figure 6.1 (b)) utilizes 8CBC3 hybrids. These hybrids can undergo both electrical and optical testing. For optical testing, a separate CIC mezzanine card containing the CIC chip is attached to the FEH. This variant allows for comprehensive testing using both electrical and optical readout setups. The third assembled functional module (Figure 6.1 (c)) incorporates 2S hybrid variants.

In this variant, the FEH integrates the CIC chip, providing the complete functionality of the final module. This module can only be tested using optical readout setup.

The first type of functional module (Figure 6.1 (a)) consists of the 8CBC2 variant of the FEH. As this variant lacks the CIC chip, these hybrids undergo individual electrical testing. The second type of functional module (Figure 6.1 (b)) employs 8CBC3 hybrids, allowing for both electrical and optical testing. For optical testing, a separate CIC mezzanine card with the CIC chip is attached to the FEH, enabling comprehensive testing with both setups. The third assembled functional module (Figure 6.1 (c)) integrates final 2S hybrid variants. With the CIC chip included in this variant, the FEH provides complete functionality for the final module, which can only be tested using an optical readout setup.

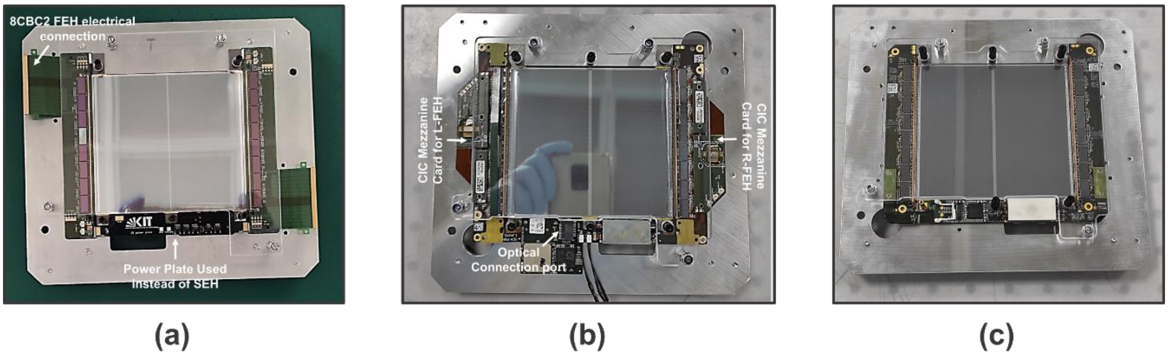

Figure 6.1: Three variants of functional module assembled. (a) Functional module using 8CBC2 FEH variant, could be tested electrically only. (b) Functional module using 8CBC3 FEH variant, capable of electrical and optical readout. (c) Functional module using final 2S hybrids variant (including FEH and SEH), incorporating all functionalities for final modules [124].

6.2 Module Assembly Results

Table 6.1 summarizes the metrology results of the functional bare modules assembled during this study. The metrology method is discussed in section 5.4. It's worth noting that all assembled modules meet the required rotational and translational tolerance limits as discussed in section 5.2.4.

Table 6.1: Meteorology results of different functional modules assembled at NCP [125 - 127]

Module Name	Module Type	**Δx (μm)** *tolerance* *< 100 (μm)*	**Δy (μm)** *tolerance* *< 50 (μm)*	**Δθ (μrad)** *tolerance* *< 400(μrad)*
NCP - F01	8CBC2	54	14	374
NCP - F02	8CBC3	-13	-4	-22
2S_18_5_NCP-00001	2S	-15	-13	-22
2S_18_5_NCP-00002	2S	-1	-9	-31
2S_18_5_NCP-00003	2S	3	3	24
2S_18_5_NCP-00101	2S	-7	-1	51
2S_18_5_NCP-00102	2S	-6	-1	-30

6.3 Sensors Leakage Current Measurement

In section 5.5.1, it is explained that the sensor leakage current is measured after each assembly step to assess sensor health. The IV curves for both top and bottom sensors of the 8CBC2 module are shown in Figure 6.2 after various assembly steps. The presented IV curves are in absolute values of current and voltage. This module utilized thin sensors with a 240 μm thickness from the test sensors badge [88]. The top sensor's IV behavior remained smooth throughout assembly (Figure 6.2 (a)). However, for the top sensor, leakage current varied after each assembly step due to different temperature and humidity conditions during measurements. In contrast, prior to assembly, an early IV breakdown was observed for the bottom sensor at 230 V (Figure 6.2 (b)). The reason for high leakage current is might be the scratches on the sensor's backside. Though partially recovered after the first assembly step, leakage current significantly worsened after wire-bonding, with a sharp increase observed shortly after reaching 30 V.

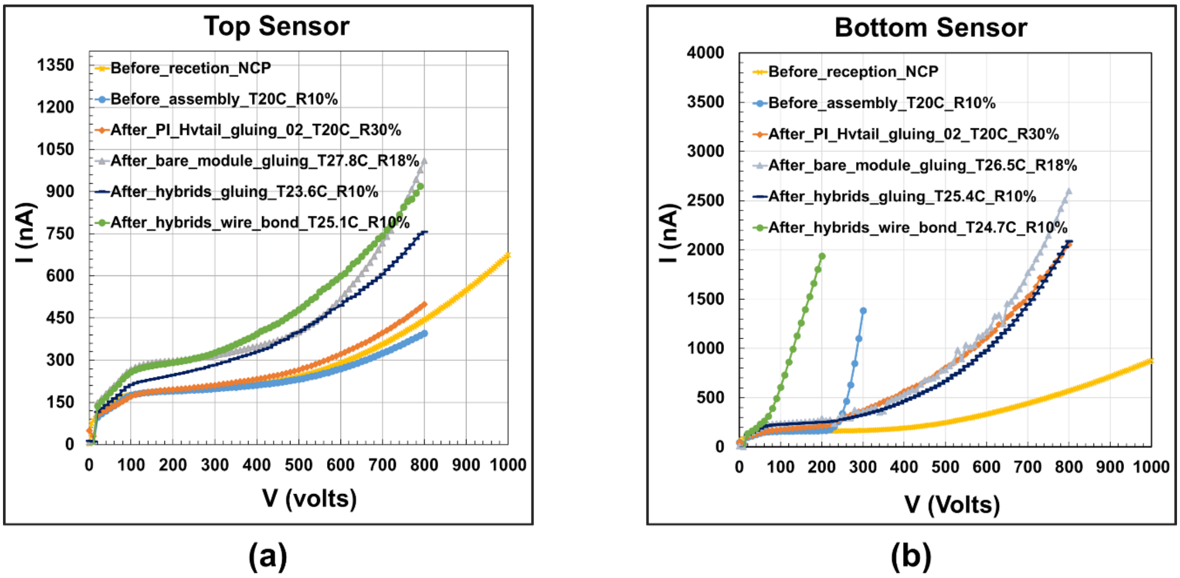

Figure 6.2: IV measurements of both sensors used in the 8CBC2 module conducted after different assembly steps. (a) Measurement results for the top sensor. (b) Measurement results for the bottom sensor [125].

Figure 6.3 illustrates the IV behavior of the sensors in the 8CBC3 module. In this module, sensors with a thickness of 320 μm were used. The leakage current for both sensors exhibited exceptionally low values after completing all the assembly steps. This low leakage current serves as evidence of a successful and seamless assembly process. Furthermore, it is noteworthy that the leakage current of this module was also measured in the DSF clean room facility at CERN, providing a reliable benchmark for measurement comparison.

During the series production of 2S modules, conducting IV performance measurements for both sensors after each assembly step can be challenging and time-consuming. Consequently, it becomes necessary to minimize the number of IV steps to streamline the production process. Therefore, during the assembly of fully functional 2S modules, specifically 2S_18_5_NCP-00001 and 2S_18_5_NCP-00002, IV measurements were carried out only three times throughout the assembly process. These measurements were conducted at the stages of bare sensors, after bonding (after bare module for 2S_18_5_NCP-00002), and after encapsulation. It is important to note that these modules were assembled using production sensors, and sensors on both modules exhibited remarkably low leakage current values, as shown in Figure 6.4.

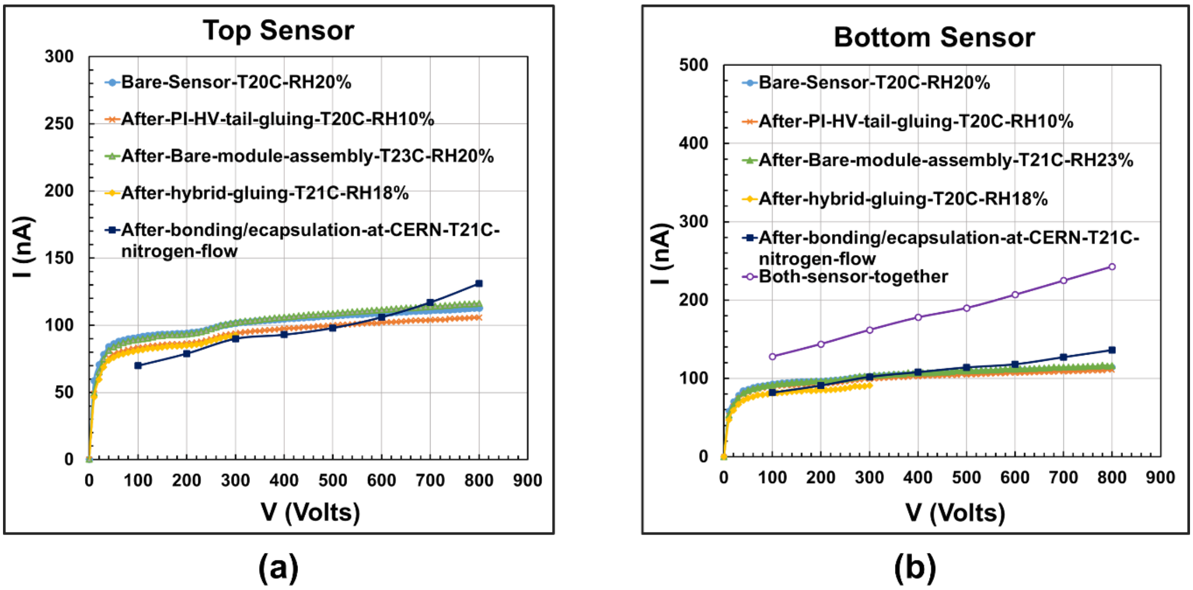

Figure 6.3: IV measurements of both sensors used in the 8CBC3 functional module conducted after different assembly steps. (a) Measurement results for the top sensor. (b) The measurement results for the bottom sensor include the IV measurement outcome when both sensors were operated together [124], [126].

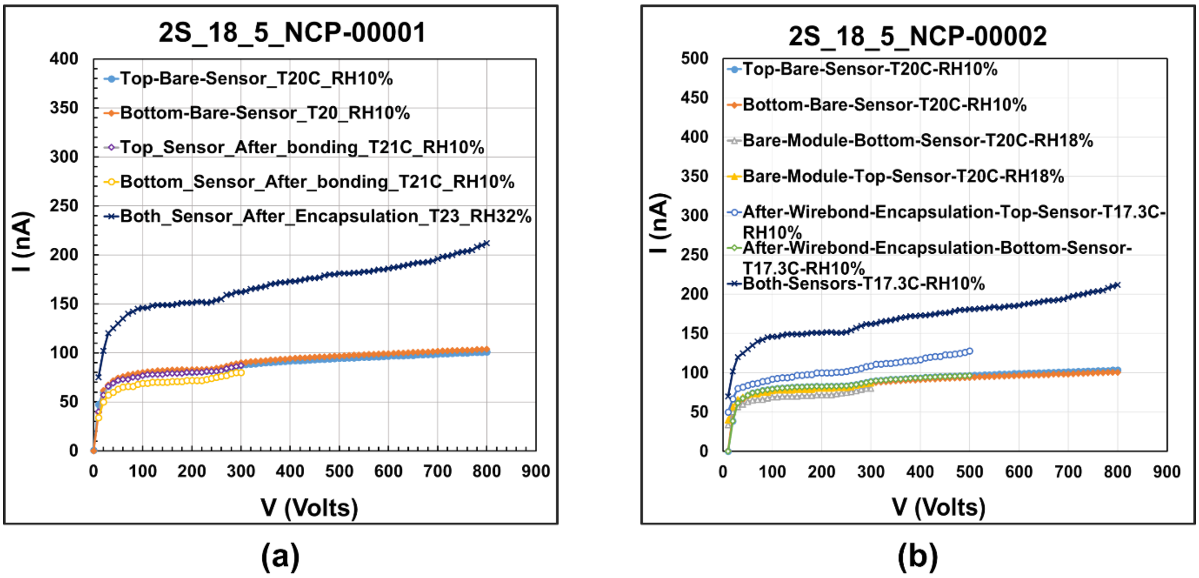

Figure 6.4: IV measurements of fully functional 2S modules. (a) Measurements results for module 2S_18_5_NCP_00001 [127]. (b) Measurements results for module 2S_18_5_NCP_00002.

6.4 Results for Noise Measurements

Noise measurement is an important parameter for assessing the performance of a module. As explained in Section 5.5.2, low noise is always desirable to improve the sensitivity of a detector.

The Ph2_ACF implementation to measure noise level distribution is described in section 5.5.4. Figure 6.5 depicts the S-curve and pedestal distribution for all 254 channels on one of the CBCs of a fully functional 2S module (2S_18_5_NCP-00001). The pedestal distribution of all channels reveals a mean pedestal value of 602.4 V_{cth} units with a standard deviation or noise of 0.89 V_{cth} units.

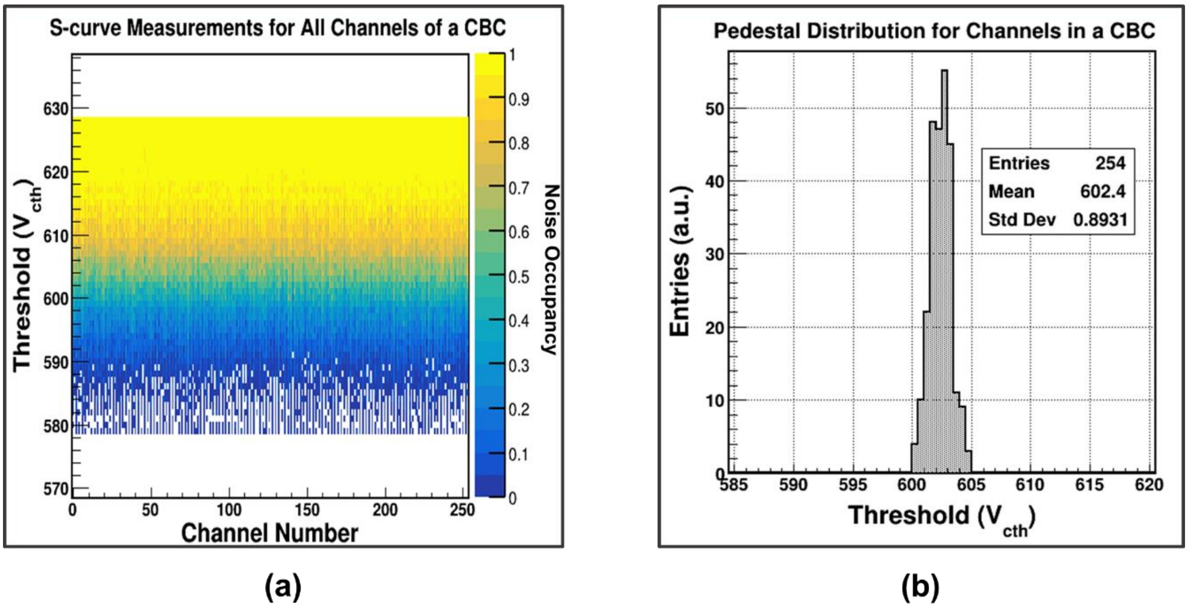

Figure 6.5: Ph2_ACF calibration measurements performed on 2S_18_5_NCP-00001. (a) S-curve showing the threshold scan for all 254 channels of CBC1. (b) Pedestal distribution displaying the Pedestal value in DAC units for all channels of CBC1.

Figure 6.6 presents a comparison of the noise level distribution of channels for both the left and right 8CBC2 hybrids before being glued to the module and after wire-bonding to the sensors in the module. The distribution plot for the bare hybrids, shown in Figure 6.6 (a), indicates noise level values of approximately 1.61 V_{cth} units and 1.67 V_{cth} units for the right and left FEH, respectively. These noise contributions are solely due to the electronics. On the other hand, the noise level distribution of both hybrids in the module increases to 8.13 V_{cth} units and 7.75 V_{cth} units for the right and left FEH, respectively (Figure 6.6 (b)). This increase in noise value is attributed to the addition of sensor capacitance (as described in equations 5.2 and 5.3). It is important to note that the measurements on the module were performed without applying bias voltage to the sensors. Furthermore, in the case of the right FEH, some channels after wire bonding exhibit a low noise value, indicating improper connections to sensors.

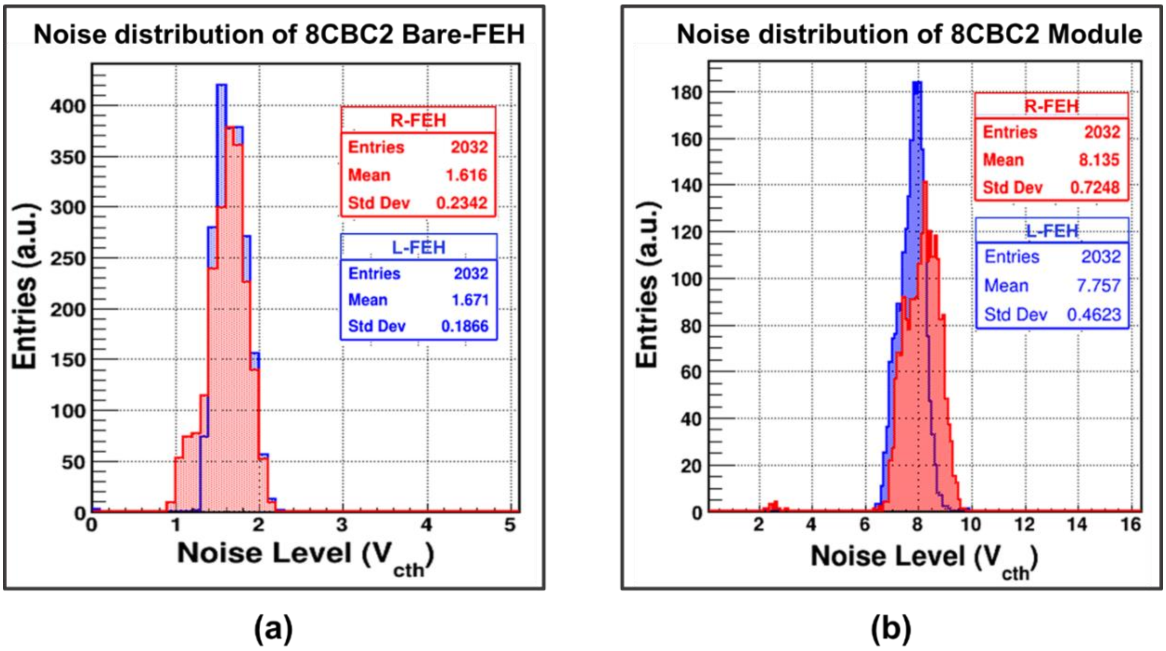

Figure 6.6: Noise level distribution of right (R) and left (L) 8CBC2 FEH. (a) Before gluing to module. (b) After wire bonding to sensors in module. It is important to note that these measurements were performed without applying bias voltages to the sensors [125].

6.4.1 Noise Measurement Test for Wire-Bonding Integrity

Noise measurement is also utilized to assess the integrity of the wire-bonds applied between the CBC channels on the Front-End Hybrid (FEH) and the sensor strips. Hence, the noise measurement test is conducted before the wire-bond encapsulation assembly step. Following wire-bonding, noise values below 3 - 4 V_{cth} units in specific channels may indicate a missing connection between the CBC channel and the sensor strip. For instance, in Figure 6.7 (a), noise measurement for all channels of both hybrids is shown for the fully functional module, 2S_18_5_NCP-00001, after wire-bonding. Notably, two channels in the left hybrid (L-FEH) display noise levels below 3 V_{cth} units. In Figure 6.7 (b), the noise level of channels connected to the top and bottom sensors separately for L-FEH is depicted, with low noise channels identified on the bottom sensor. Visual inspection also reveals two missing wire-bonds on the bottom side of L-FEH, as illustrated in Figure 6.8. Thus, conducting noise measurement immediately after wire-bonding aids in identifying missing wire-bonds, facilitating the resolution of this issue before proceeding with the encapsulation process.

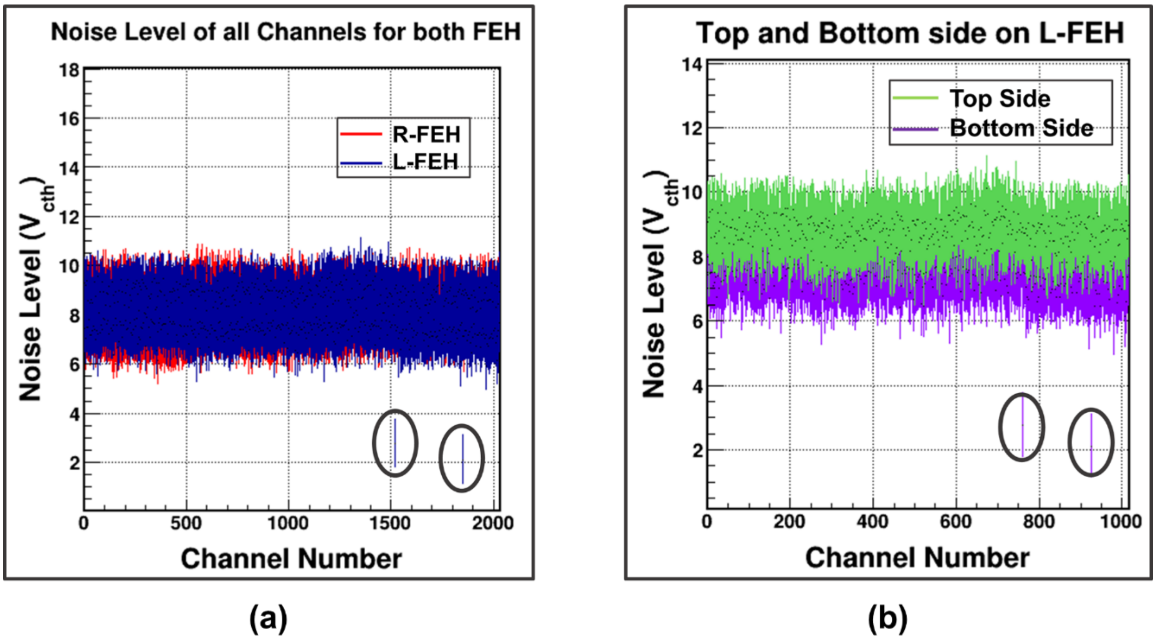

Figure 6.7: Noise level measurements of the fully functional 2S module, 2S_18_5_00001, after wire-bonding, with sensors biased at 300 V. (a) Noise level plot showing noise for all channels on both left and right hybrids. Two channels with noise levels below 3 Vcth units values are observed on the left FEH. (b) Noise level plot indicating noise values for top and bottom channels on L-FEH separately, revealing the presence of low noise channels on the bottom side .

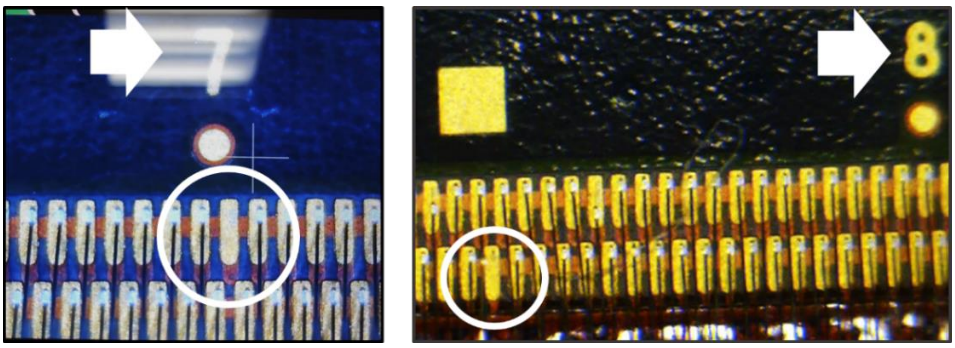

Figure 6.8: Visual inspection of bottom side of left FEH of 2S_18_5_NCP-00001 module reveals two missing wire-bonds. The missing bonds are marked inside white circle where arrow shows there locations [127].

6.4.2 Sensor Biasing Voltage Effect on Noise Level

After sensor-to-hybrid wire-bonding in a module, the increased sensor bulk and inter-strip capacitance contribute to an elevated noise level in the module, as discussed in section 5.5.2. Figure 6.6 demonstrates this effect in a comparison. To achieve a target noise level addition of 1000 e^- [58], it is recommended to set the biasing voltage high enough to fully deplete the sensors. This reduces the bulk capacitance ($C \propto \frac{1}{\sqrt{V}}$) and subsequently decreases the module's noise level while increasing the signal strength.

Figure 6.9 (a) showcases the impact of increasing bias voltage on the noise level for 8CBC2 functional module. In this case, the biasing potential was raised to only 200 V due to increased leakage current observed in the bottom sensor (Figure 6.2 (b)). It can be observed that at a biasing voltage of 150V, the noise level decreases from 8 V_{cth} units to 2.98 V_{cth} units and 3.41 V_{cth} units for the right FEH for the left FEH respectively.

Figure 6.9 (b) illustrates the noise level measurements with increasing bias voltage for the fully functional 2S module, 2S_18_5_NCP-00002. Initially, with sensors biased at 60 V, the noise level is approximately 12 V_{cth}.units As the sensor bias voltage increases up to 300 V, the noise level decreases, indicating that the sensor starts to become fully depleted at 300 V. The noise level stabilizes at approximately 7.57 V_{cth} units and 7.24 V_{cth} units for left FEH and right FEH respectively. It is important to note a higher noise level values, 1154 e^- using conversion factor 150 e^-/ V_{cth}, than target value are observed in case of fully functional 2S module. These measurements were taken after attaching 100 Ω pitch adapters in the HV-tails to reduce noise levels (to be described in the next section).

6.4.3 Higher Noise Level in Fully Functional 2S Module

For the fully functional 2S module, the strip noise plot shows varying noise levels between the top and bottom sides. The noise level, measured above 8Vcth units with a biasing of 320V by different assembly centers, corresponds to approximately 1200 e^- (150 electrons/V_{cth}). This value exceeds the target noise level of 1000 e^- [58].

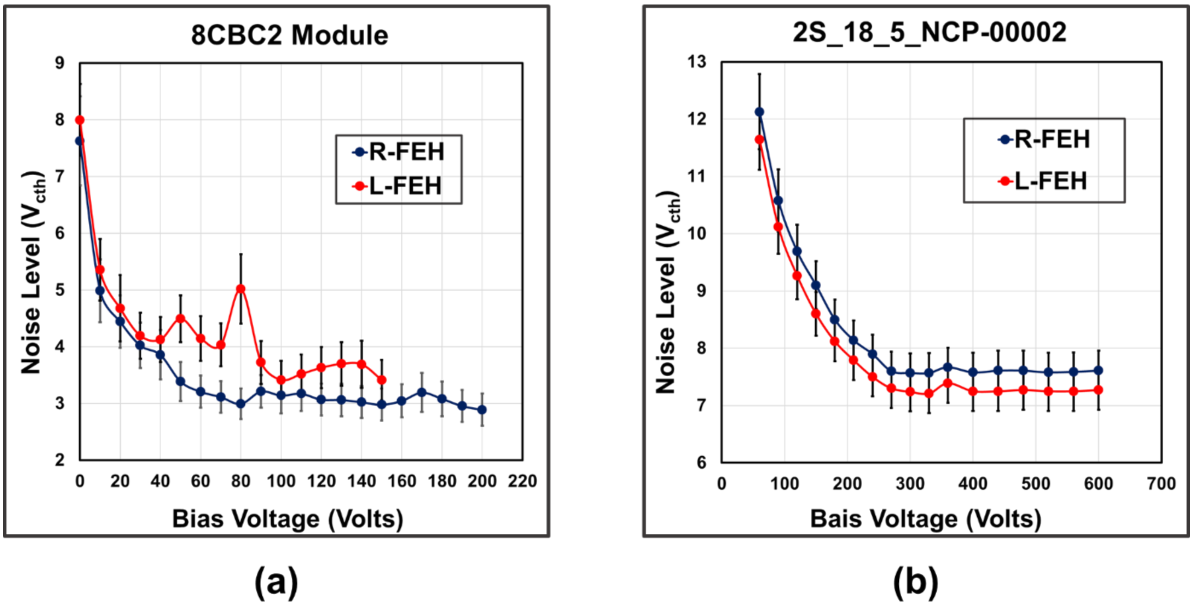

Figure 6.9: Noise level measurements with increasing sensors bias voltages for both FEH. (a) 8CBC2 prototype module. (b) 2S_18_5_NCP-00002 prototype modules. The error-bars on noise level show the standard deviation in noise distribution curve [124].

Figure 6.10 depicts the noise measurement plots of all channels for the right and left FEH of the 2S_18_5_NCP-00002 module. In the case of the L-FEH, Figure 6.10 (a) shows higher noise levels on the top side and lower levels on the bottom side, with the noise being higher for the channels at the far end. Similarly, for the R-FEH shown in Figure 6.10 (b), the noise level is higher on the bottom side and lower on the top side, with lower noise levels observed at the far end. Thus, the noise level exhibits an opposite trend for the top and bottom sides in both R-FEH and L-FEH. Secondly, the module's far end, opposite to the service hybrid, shows a different ground level as the observed noise level is higher at that side for both R-FEH and L-FEH.

To address these issues in the fully functional 2S module, detailed studies have been conducted by the module working group [128]. Two types of changes have been proposed after detailed investigation to mitigate the issue:

1. A 100 Ω resistor is introduced in both HV-tails to support the filter circuit in SEH.
2. A ground balancer flex circuit is introduced at the opposite end to SEH to address the far end grounding issue.

For this purpose, 100 Ω pitch adapters were distributed to the assembly sites to attach them to the HV-tails of the fully functional 2S module for further analysis. Figure 6.11 compares the noise distribution plot before and after attaching the pitch adapter to the 2S_18_5_NCP-00002 module. After introducing 100 Ω resistors to the HV-tails, only one peak in the noise level distribution is observed (Figure 6.11 (b)) instead of multiple peaks for one FEH (Figure 6.11 (a)). This suggests that both the top and bottom sides of a FEH are approximately at the same noise level. Additionally, the noise level of both FEHs is reduced by 0.8 Vcth units. Table 6.2 shows the noise level of different functional modules, assembled at NCP, under different conditions. The noise level of 2S_18_5_NCP-00102, equipped with a ground balancer and a 100 Ω resistor in the HV tail, is the lowest among the measured modules.

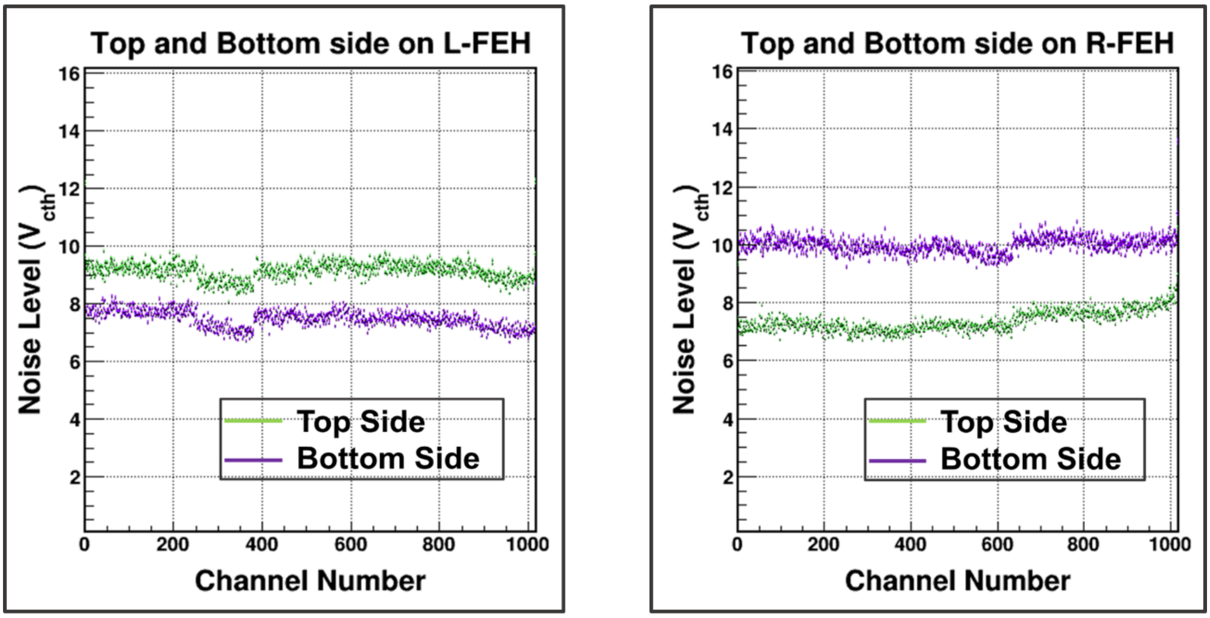

(a) (b)

Figure 6.10: Noise level measurements for 2S_18_5_NCP-00002 module with sensors biased at 300 V. (a) Noise level measurements of top and bottom sides for the left FEH. (b) Noise level measurements of top and bottom sides for the right FEH.

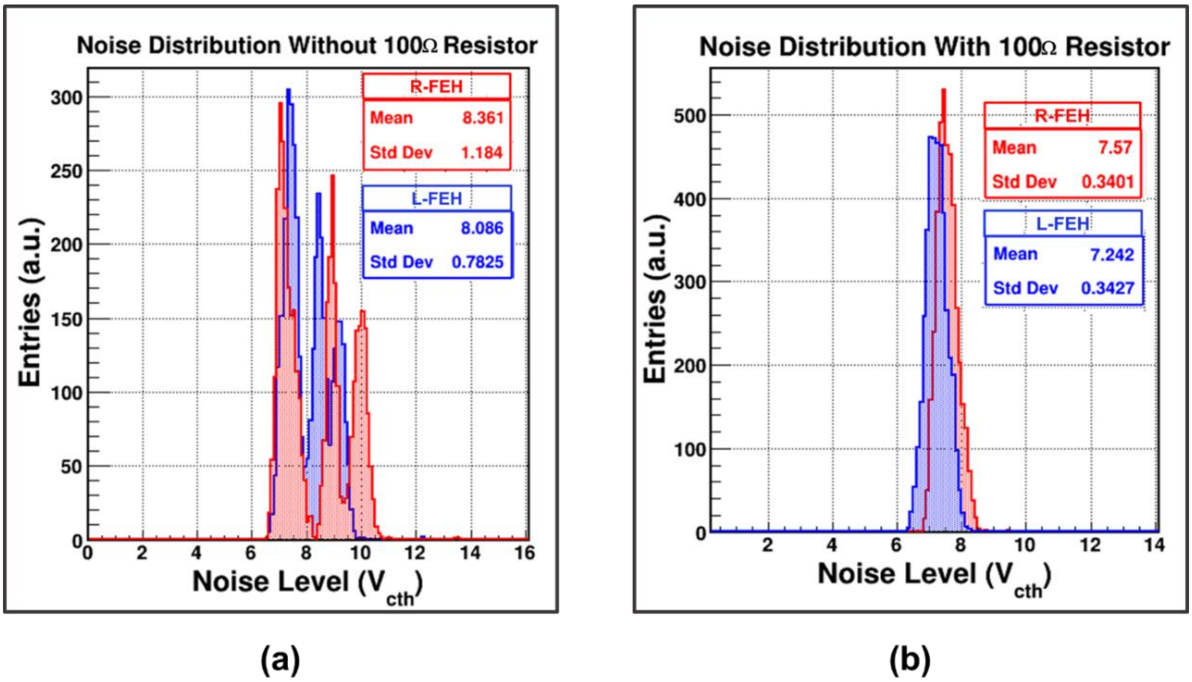

Figure 6.11: Noise level distribution of 2S_18_5_NCP-00002 module with sensors biased at 300 V. (a) Before attaching the 100 Ω pitch adapter to HV-tails. (b) After attaching the 100 Ω pitch adapter to HV-tails [124].

6.5 Noise Measurements inside Cold Box

6.5.1 Noise Measurements at Different Temperatures

Figure 6.12 (a) showcases the different temperature measurement points for a fully functional 2S module mounted on the copper plate in side cold test box as explained in section 5.6. Thermocouples were placed on the R-FEH, copper plate, DC-DC converter, and module's bridges to monitor the temperature variations accurately. The temperature variation at these positions after activating the cooling system is displayed in Figure 6.12 (b). It is worth noting that the module was powered on by enabling the bias voltage and LV supply approximately 30 minutes after initiating the cooling process. Initially, no significant temperature increase was observed at the FEH and module's bridges. However, after 53 minutes, a slight temperature rise of 3°C and 1°C was noticeable at the FEH and module's bridges positions, respectively. This increase can be attributed to the heat generated by the module during the noise measurements.

Table 6.2: Noise level of difunctional modules assembled at NCP under different conditions.

Module Name	Module	L-FEH (Vcth units)	L-FEH (Vcth units)	Measurement Conditions
NCP - F01	8CBC2	3.41 ± 0.35	2.98 ± 0.28	Biasing Voltage: 150 V
2S_18_5_NCP-00001	2S	8.10 ± 0.78	8.11 ± 0.80	Biasing Voltage: 320 V
2S_18_5_NCP-00002	2S	8.78 ± 0.41	9.06 ± 0.71	• Biasing Voltage: 300 V
2S_18_5_NCP-00002	2S	7.57 ± 0.34	7.24 ± 0.34	• Biasing Voltage: 300 V • Attach 100 Ω resistor with HV tails
2S_18_5_NCP-00003	2S	7.95 ± 1.11	7.95 ± 0.55	Biasing Voltage: 300 V
2S_18_5_NCP-00101	2S	6.56 ± 0.43	6.66 ± 0.40	• Biasing Voltage: 300 V • 100 Ω resistor in HV-tails • Common ground SHE
2S_18_5_NCP-00101	2S	12.15 ± 0.95	12.17 ± 0.55	• Biasing Voltage: 300 V • 100 Ω resistor in HV-tails • Split plane SHE
2S_18_5_NCP-00102	2S	10.07 ± 0.61	10.12 ± 0.64	• Biasing Voltage: 300 V • 100 Ω resistor in HV-tails • Common ground SHE
2S_18_5_NCP-00102	2S	6.69 ± 0.32	6.65 ± 0.28	• Biasing Voltage: 300 V • 100 Ω resistor in HV-tails • Common ground SHE
2S_18_5_NCP-00102	2S	6.45 ± 0.31	5.97 ± 0.28	• Biasing Voltage: 300 V • 100 Ω resistor in HV-tails • Common ground SEH • Ground Balancer

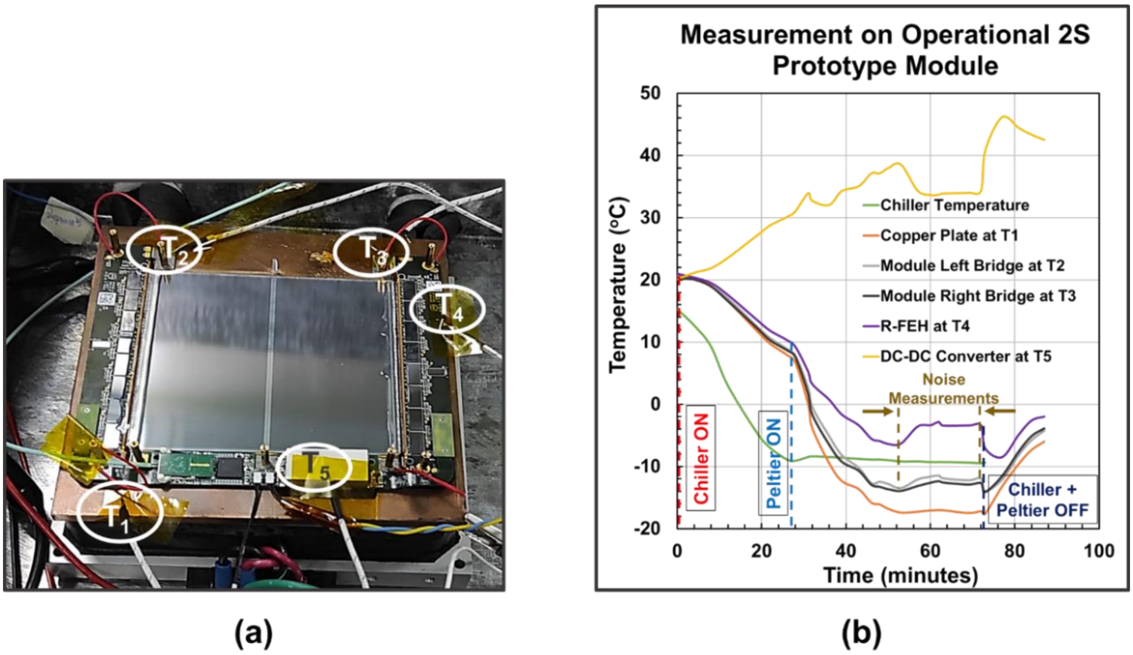

Figure 6.12: Cold test setup for temperature measurement on an operational 2S prototype module mounted on the copper plate. (a) Thermocouples attached to the copper plate, module's bridges, FEH, and DC-DC converter. (b) Temperature variation at different positions after activating the cooling system [123].

To gain insights into the module's noise behavior at cold temperatures, noise measurements were conducted on the 2S_18_5_00002 module before and after attaching the 100 Ω pitch adapter to the HV tails. Initially, the noise level was measured without activating the cooling system. Subsequently, the chiller temperature was gradually adjusted from 15°C to -10°C, decreasing in 5°C steps, and noise measurements were taken once the target temperature was reached for each step. The final measurement was obtained after turning on the Peltier plate and achieving the ultimate cooling temperature. The obtained results were plotted against the temperature of the copper plate.

Figure 6.13 (a) illustrates the noise level measurements taken on the module without attaching the 100 Ω pitch adapter and with the sensors biased at -300V. It can be observed that the noise level decreases by approximately 0.5 V_{cth} for both FEHs with decreasing temperature. In contrast, Figure 6.13 (b) depicts the noise measurements at different temperatures after attaching the 100 Ω pitch adapter and applying a biasing potential of -320V to the sensors. In this case, the noise level of the right FEH decreases by approximately 0.2 V_{cth} units while the left FEH experiences a decrease of about 0.4 V_{cth} units. Comparing the two situations, it's evident that the noise level follows a different decreasing pattern for the two FEHs when the pitch adapter is attached, whereas it shows a similar trend without the adapter. Additionally, after attaching the 100 Ω pitch adapter to the HV tails, the mean noise level and standard deviation values obtained from the noise level distribution plot are lower for both FEHs. Notably, in both cases, the last data point displays a higher noise value, likely due to the magnetic field generated by the current variation in the Peltier elements.

Further studies will be conducted to understand the different behaviors of the noise level for both FEHs under cold conditions after the availability of the ground balancing circuit.

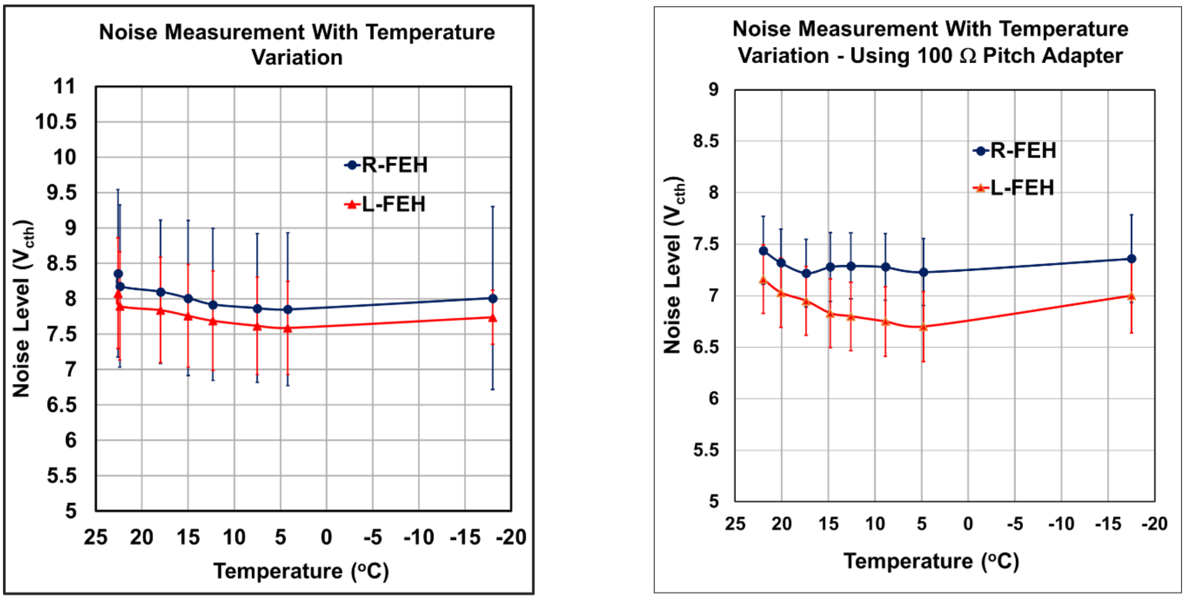

(a) (b)

Figure 6.13: Noise level measurement at different temperatures performed on 2S_18_5_00002. (a) Before attaching the 100 Ω pitch adapter to HV-tails. (b) After attaching the 100 Ω pitch adapter to HV-tails. The error-bars on noise level shows the standard deviation in noise level distribution curve [124].

6.5.2 Module Thermal Cycle

As mentioned earlier, the modules utilized in the CMS Phase-2 tracker are intended to operate at temperatures below -20°C. Once the HL-LHC becomes operational, these modules will be continuously maintained under operational conditions, except during technical stops when they are brought up to +25°C. Therefore, it is essential to subject these modules to thermal cycle testing to ensure their reliability and performance. The cold test box is utilized to subject the modules to extreme temperature conditions to evaluate their stress limits and assess their functionality.

The fully functional 2S module has been subjected to the thermal cycling studies. Figure 6.14 displays the thermal cycles performed on the 2S_18_5_00002 module. The copper plate's temperature was maintained between -18°C and +18°C during the thermal cycles. At each extreme temperature, noise level measurements were taken. It is noteworthy that the noise level remains consistent for both hybrids throughout all cycles, demonstrating the modules' ability to perform reliably under these extreme conditions.

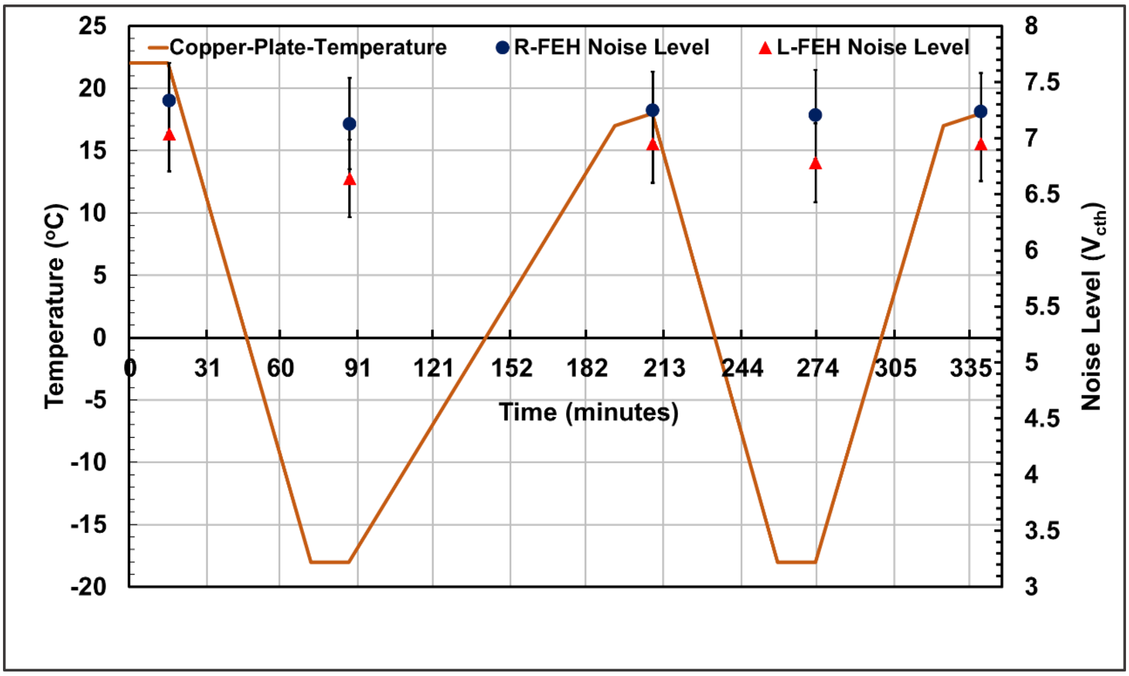

Figure 6.14: Thermal cycle performed on 2S_18_5_00003 module, ranging from +18°C to -18°C. The module remains operational throughout the cycles, and noise measurements are conducted at each extreme temperature

7

Test Beam Analysis of 2S Module

This chapter provides a comprehensive exploration of the test beam data reconstruction and analysis conducted on the functional 2S module. The primary focus lies in utilizing the Corryvreckan reconstruction framework for analyzing the data obtained, for 2S module, during the test beam campaign at DESY.

A detailed description of the setup employed at DESY for the one of the 2S module test beam campaign is presented, offering valuable insights into the instrumentation and experimental conditions utilized during the testing phase. Additionally, this chapter highlights a significant aspect—the comparison study between the analysis results derived from the Corryvreckan framework and the previously generated results using the EUTelescope framework.

7.1 Test Beam Campaigns for 2S Module Prototypes

In the previous chapter, various tests were discussed that can be conducted on 2S modules after their assembly. These tests are typically carried out in a controlled laboratory environment to assess the performance of the modules. However, another crucial aspect of studying module performance involves subjecting these modules to a test beam.

During a test beam, the modules are exposed to a high-energy particle beam, allowing researchers to simulate the conditions in which the modules will operate. To accurately measure and analyse the module's performance, reference telescopes setups are employed. These telescopes serve as a benchmark for comparison and calibration purposes, enabling precise measurements of the module's behaviour.

Large-scale test beam facilities such as CERN, DESY, FNAL etc., are commonly utilized for these experiments. These facilities offer the necessary infrastructure and equipment to generate and control high-energy particle beams, making them ideal for conducting performance studies on prototype 2S modules.

During test beam campaigns, a range of measurements and evaluations are performed on the modules. Some of the key parameters assessed include:

1. **Sensors' Spatial Resolution and Hit Detection Efficiencies:** The precision with which the module's sensors can pinpoint the location of particle interactions, as well as the efficiency of detecting those hits, are crucial factors in assessing the module's overall performance.
2. **Cluster Size:** The cluster size refers to the number of neighboring pixels or strips in the sensor that register hits resulting from a single particle interaction. It is observed that the cluster size increases with the angle of incidence. This measurement is important as it allows for the application of appropriate angular corrections, enabling the accurate reconstruction of particle tracks.
3. **Module Stub Efficiency:** The 2S module demonstrates its ability to pass valid hits by correlating hit data between two sensors, as discussed in Section 3.4. Evaluating the module's stub efficiency provides insights into its capability to effectively contribute to this reconstruction process.
4. **Comparison and Optimization of Different Operational Parameters:** Various operational parameters of the module, such as voltage settings, thresholds, and readout configurations, are systematically adjusted and compared to optimize the module's performance. This iterative process helps identify the most favorable parameter settings.
5. **Modules Integration Test:** Test beam setups often involve mounting and reading multiple modules in parallel, simulating their integration within a larger system. This test verifies the functionality and compatibility of multiple modules working together and provides insights into the overall system performance.

The performance studies of prototype 2S modules have undergone rigorous evaluations through multiple test beam campaigns. The results obtained from these campaigns have provided valuable insights into the modules' performance, allowing for the identification of strengths and areas for improvement. As part of this thesis, the analysis of the 8CBC3 test beam campaign conducted at DESY in November 2019 was carried out using the Corryvreckan test beam reconstruction framework.

7.2 Test Beam Facility at DESY II

Figure 7.1 illustrates three independent test beam facilities, namely T21, T22, and T24, located at DESY II [129]. The beam in the test beam area is generated by employing a two-step process. Initially, the beam in the DESY beam pipe interacts with a primary target consisting of a 25 μm thick carbon fibre. This interaction results in the production of Bremsstrahlung photons. These photons then travel through a tube and subsequently strike a secondary target, which can be in the form of copper wires or aluminium and copper plates. Upon striking the secondary target, the photons generate an electron-positron beam.

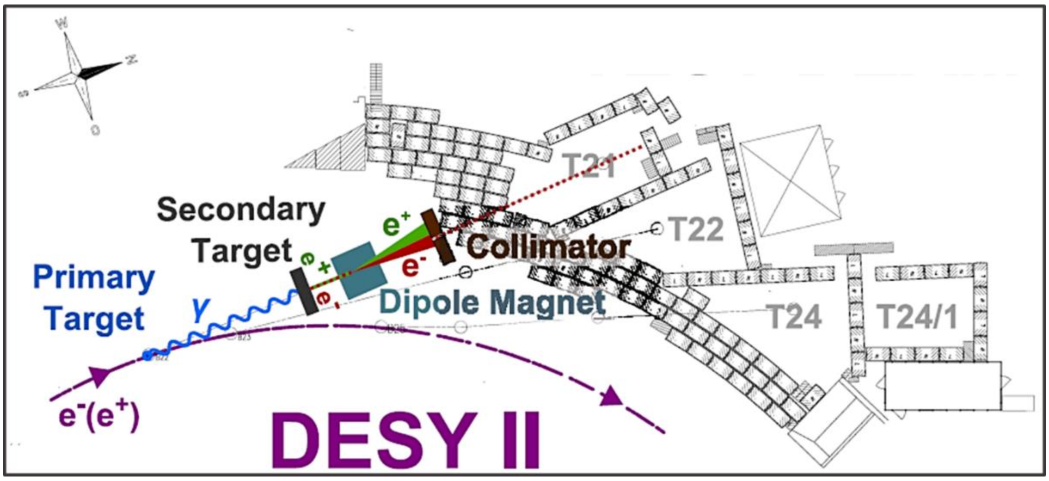

Figure 7.1: Schematic of the production of the secondary beam at DESY II for the test beam setup [129], illustrating a two-step process involving the generation of Bremsstrahlung photons by the primary beam striking the primary target, followed by the production of an electron-positron beam through the interaction of these photons with a secondary target. A dipole magnet and movable collimator are used as the beam selector for controlling and selecting the outgoing particles.

To control the outgoing particles, a dipole magnet is utilized as a beam selector. This magnet allows for the selection and manipulation of the desired beam. Additionally, a movable collimator is employed to further refine the selection of the beam diverted by the magnet. At the end of the collimator, a beam shutter is present. The beam shutter serves the purpose of switching off the beam, allowing safe access to the test beam area when needed.

The particle rate in the test beam area is closely related to the rate of bremsstrahlung photon production, which is directly influenced by the beam intensity in the DESY beamline [129]. In addition to beam intensity, various beamline parameter settings, such as the position of the primary target, momentum selection, and the opening area of the collimator, significantly impact the particle rate. Furthermore, the particle flux in the test beam area exhibits a spread in momentum. Detailed studies on the momentum spread, as documented in reference [129], have demonstrated a strong dependence on the momentum of the particle. Specifically, the momentum spread ranges from 1.5% at 6 GeV to 12.7% at 0.9 GeV. This shows a higher spread at low momentum and vice versa.

7.2.1 DATURA Test Beam Telescope

The DATURA is a pixel beam telescope of the EUDET type [129], installed at the T21 beamline, as depicted in Figure 7.2(a). The telescope consists of two telescope arms, each composed of three planes. The device-under-test (DUT), which is the module or device being tested, is positioned between the two telescope arms. Each of the two telescopic arms in the system is composed of three planes. Three planes located on the arm that the particle beam passes through before reaching the DUT are referred to as the upstream telescope planes. Conversely, the three planes towards which the beam exits the DUT are known as the downstream telescope planes. The configuration of the telescope and DUT can be observed in Figure 7.2(b), providing a visual representation of their spatial layout and the trajectory of the particle beam within the system. This arrangement allows for precise measurements and imaging of the particle beam as it passes through the DUT, enabling detailed analysis of its performance.

i. Telescope Planes

The telescope planes of the system are equipped with MIMOSA26 monolithic active pixel silicon sensors [130]. These sensors consist of an array of pixels arranged in 1152 columns and 576 rows, with each pixel having a pitch of $18.4 \times 18.4\ \mu m^2$, resulting in an active area of 21.2 x 10.6 mm^2. The pixel states of the sensors are sequentially read out in rolling shutter mode, with each pixel row read one after the other. This process is performed with 16 cycles of 80

MHz per row, resulting in a total integration time per MIMOSA26 module of 115.2 μs. The on-chip digitization of the pixel data provides binary information for each pixel.

The MIMOSA26 sensor has a thickness of 50 μm and is shielded from ambient light using a 25 μm Kapton foil. This shielding minimizes the material budget, resulting in optimized track resolution within the energy range of 1-6 GeV/c. The measurements presented in reference [131] demonstrate an intrinsic resolution of (3.24 ± 0.09) μm for the MIMOSA26 sensor.

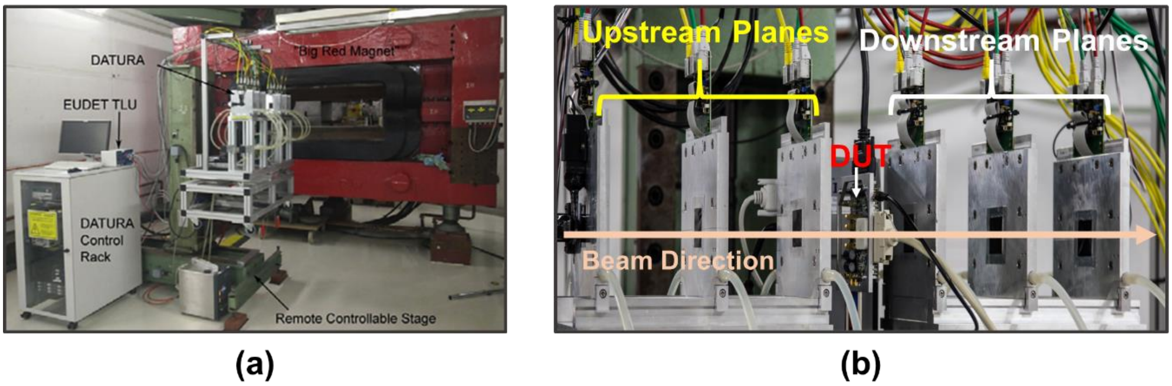

Figure 7.2: (a) T21 test beam setup showing DATURA beam telescope, EUDET TLU, and control rack [129]. (b) The device-under-test (DUT) is mounted between two telescope arms consisting of the MIMOSA26 planes in the upstream and downstream [132]. The direction of the beam follows from the upstream planes to the downstream planes.

ii. DUT (device-under-test) stage

The DUT stage, located between the two telescope arms, offers the capability to move in the x, y, and φ directions with micrometer precision. The movable stage provides a crucial functionality for performing geometrical scans of DUTs that exceed the size of the active area covered by the telescope planes.

iii. Tigger Logic Unit (TLU)

The EUDET trigger logic unit (TLU) [133] is an integral component of the DATURA telescope. The TLU utilizes scintillators with an area of 2 x 1 cm^2, coupled with photomultiplier tubes, as trigger devices. Two trigger devices are positioned in front of the first telescope plane, while another two are placed after the last telescope plane. These trigger devices are responsible for generating trigger signals when particles pass through them.

The data acquisition (DAQ) system of the MIMOSA26 sensors communicates with the TLU in a handshake mode. In this mode, when the TLU generates a trigger signal, the DAQ system of the MIMOSA26 raises a busy signal during the readout of the frame. This handshake mechanism ensures synchronization between the trigger signals and the data acquisition process.

Furthermore, the setup allows for the integration of additional sensors and the device-under-test (DUT) in both handshake and no-handshake modes. In handshake mode, the additional sensors or DUTs can communicate with the TLU and synchronize their operations with the trigger signals. In no-handshake mode, the additional sensors or DUTs simply accept the trigger signals without the need for synchronization.

iv. Data Acquisition Framework

The EUDAQ framework [134] is a comprehensive solution used for data acquisition in experimental setups. It is specifically designed to cater to synchronous systems that operate on the principle of one event per trigger. By integrating the hardware components and merging their data streams into event-based data, EUDAQ facilitates the efficient collection, processing, and analysis of experimental data.

Moreover, the EUDAQ framework is designed to be flexible and customizable. It provides the necessary infrastructure and interfaces to integrate the data acquisition system of the DUT into the overall EUDAQ setup.

7.3 Test Beam Setup for November 2019 Campaign

The majority of the content in this section has been sourced from the reference [135]. The test beam campaign conducted in November 2019 was performed with electron beam of energy 4 GeV on the DATURA telescope at DESY. For this campaign, various 2S prototype modules (8CBC3) were mounted on the telescope using a specially designed box. The schematics of this test beam setup are shown in Figure 7.3, while Figure 7.4 depicts the photograph of the telescope. As mentioned in the previous section the DUT was mounted on a movable stage between two telescope arms, allowing for precise positioning. During the test beam campaign, the power supplies of the movable stages were disabled due to the introduction of noise into the measurements of the DUT. Therefore, the setup configurations were not allowed to change during the test run, and any necessary changes were made in between runs. Additionally, some DUTs were mounted in the available space at the downstream end, following the last plane of the telescope.

7.3.1 Timing Reference Plane

The sampling frequency of the 2S modules is synchronized with the clock scheme of the Large Hadron Collider (LHC), which operates at 40 MHz. This frequency ensures that the data acquisition process aligns with the LHC timing. However, in order to accurately match the tracks recorded by the telescope with the corresponding hits in the DUT, additional timing information is required.

To address this, the ATLAS FE-I4 [136] detector was employed as a timing reference. The FE-I4 detector features a pixel matrix measuring 8 x 336, with each pixel having a size of 50 × 250 μm^2. It was positioned between the fifth and sixth layers of the telescope. By using the FE-I4 as a reference, it was possible to synchronize the 25 ns readout cycle of the DUT with the data acquisition system.

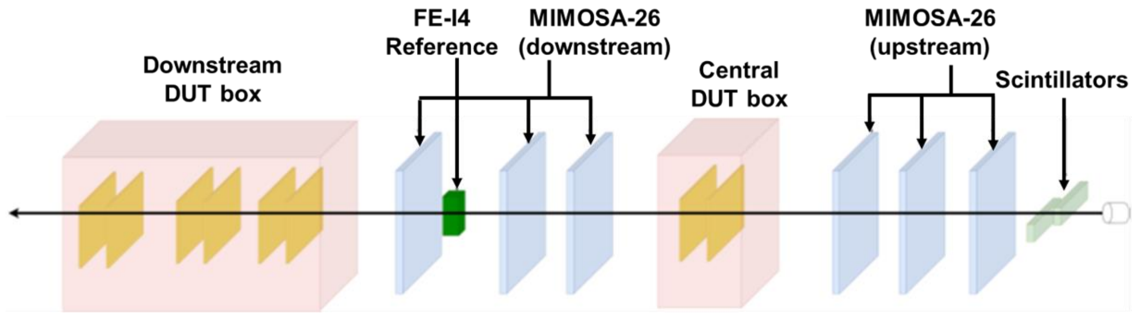

Figure 7.3: Schematics of the setup for the November 2019 test beam, adapted from [135]. The diagram illustrates the two yellow strip sensors of 2S module in the central DUT box, as well as in additional DUT boxes mounted at the end of the telescope. The FE-I4 detector serves as the timing reference plane.

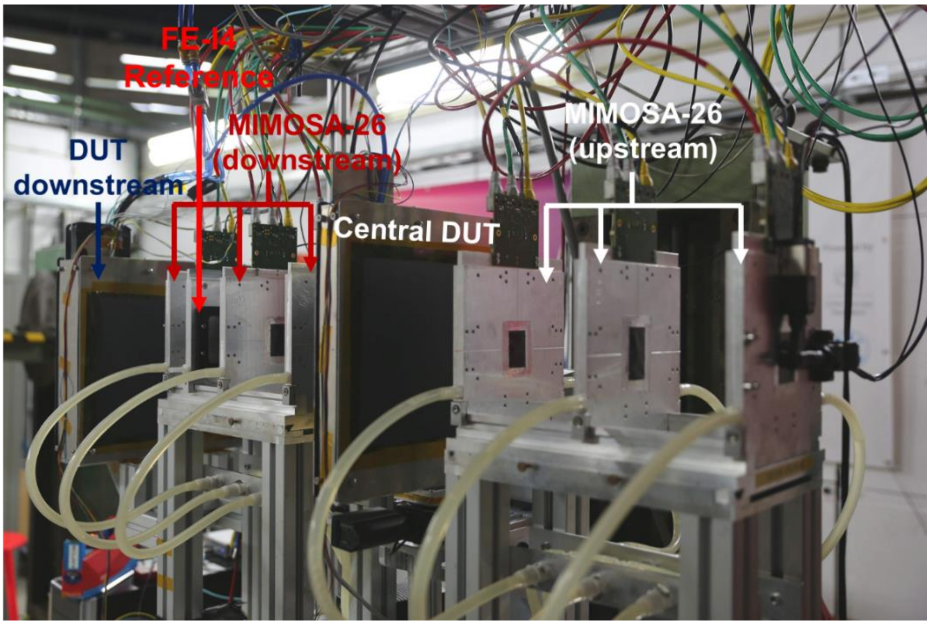

Figure 7.4: Photograph of the DATURA telescope setup for the November 2019 test beam campaign, adapted from [135].

7.3.2 Data Acquisition

Figure 7.5 illustrates the flowchart of the data acquisition system employed during the test beam. In this setup, all the detector planes were connected to their respective back-end Data Acquisition (DAQ) systems. The 2S modules DAQ system were based on FC7 and operated through the Ph2_ACF outer tracker data acquisition framework.

To initiate the data acquisition process, the EUDET TLU triggers when it simultaneously receives signals from the two scintillators mounted upstream, before the first telescope plane. This coincident signal serves as a trigger condition for capturing relevant events. Subsequently, the TLU distributes the trigger signal to the back-end board, which in turn initiates the readout process. At this stage, the TLU awaits feedback from the detector to ascertain if the detector is busy or unavailable for capturing additional events. This feedback mechanism ensures proper synchronization and efficient data acquisition.

Moving forward, the acquired data is processed through each device present in the setup, following their respective procedures. These procedures are controlled by the test beam user through the RunControl system. The RunControl system is responsible for collecting the processed data and storing it in a RawFile, facilitating further analysis.

The subsequent analysis and reconstruction of the acquired data involve the utilization of the EUTelescope framework. Specifically designed to support the EUDET telescope family, it serves the primary purpose of extracting hit clusters and tracks within the telescope from the RawFile, as illustrated in Figure 7.6. Additional comprehensive information on the EUTelescope framework can be found in Reference [137]. The EUTelescope framework provides information in a Root Tree file [138], which is subsequently used for further offline analysis.

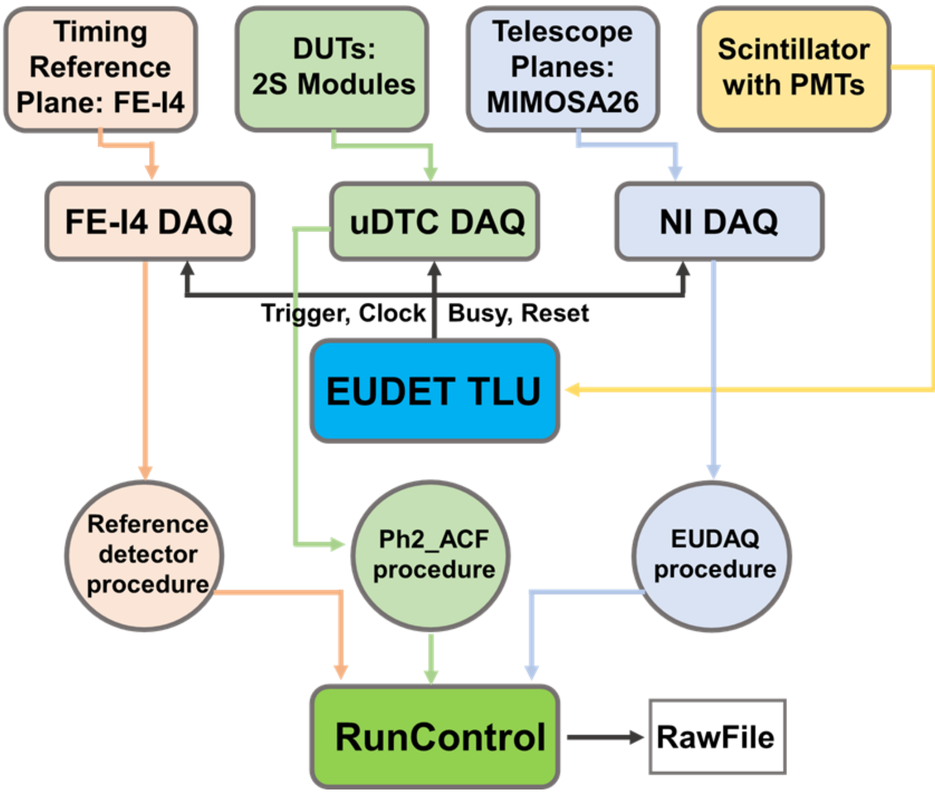

Figure 7.5: EUDAQ data acquisition flowchart illustrating the complete DAQ chain during the November test beam, derived from [135].

i. Time to Digital Converter (TDC) Phase

The TDC phase refers to the temporal relationship between a hit event and the acceptance of an external trigger. Its purpose is to account for any delays that may occur due to the mismatch between the clock of the 2S module and the arrival of the trigger signal. During the test beam, the backend firmware employed a super-sampling technique to accurately capture the arrival time of the trigger signal from the TLU. This super-sampling process involved dividing the time interval into eight bins, with each bin representing a time slice of 3.125

nanoseconds. This configuration was carefully chosen in relation to the system clock frequency of 40MHz. By dividing the arrival time of the trigger signal into these eight bins with precise time slices, the backend firmware ensured a high-resolution representation of the temporal information.

ii. Hit Detection Logic

During the test beam data acquisition in the 2S modules, two out of the four available hit detection modes in CBC3, as shown in Figure 4.21, were specifically configured. These two modes are the fixed pulsed or latched mode and the 40 MHz sampled mode.

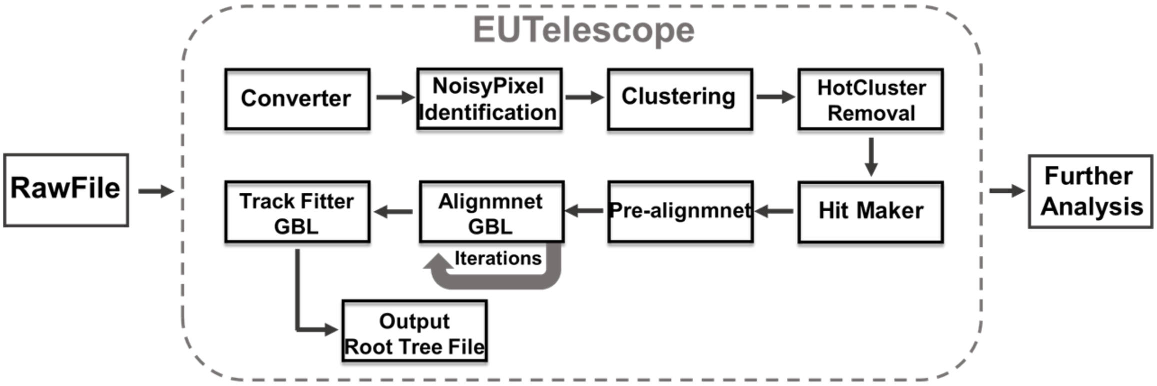

Figure 7.6: Flowchart depicting the reconstruction procedure in EUTelescope, adapted from [137]. The RawFile generated by the EUDAQ framework serves as input for EUTelescope. The output of EUTelescope is a root tree file containing vital information about hits, clusters, and tracks. This output file is then utilized for subsequent analysis and interpretation of the data.

7.4 Corryvreckan: Test Beam Reconstruction and Analysis Framework

In the context of this thesis, the data reconstruction and analysis of the November 2019 test beam data were conducted using the Corryvreckan framework. The primary motivation for this choice was to compare the analysis results obtained using Corryvreckan with those generated by the EUTelescope framework.

The content presented here about Corryvreckan is derived extensively from the referenced material [4], which serves as a valuable resource for the discussion. Corryvreckan is a modular and lightweight framework that has been designed to be fast, with low entry barriers for users.

The key components of the framework include the configuration file, the central event loop, and coordinate transformation. Corryvreckan framework employs individual modules written in C++ that implement specific steps of the reconstruction process. These modules work together and exchange data using a central clipboard storage, enabling efficient communication and coordination between different components. The flexibility of the framework allows for the adaptation of various analysis requirements to the reconstruction chain.

Within the context of this thesis, some key aspects of the Corryvreckan framework are discussed, highlighting their relevance and significance to the research conducted. For more comprehensive information on the implementation and development of Corryvreckan, the framework manual [139] can be consulted which provides detailed insights into the framework's usage and further technical details.

7.4.1 Coordinate Systems

Within the Corryvreckan framework, two types of coordinates are defined: local coordinates and global coordinates. In the right-handed Cartesian coordinate system, local coordinates are established for each individual telescope plane. In this coordinate system, the x and y axis are defined on the sensor's plane, with the origin located at the center of the lower-left pixel grid.

On the other hand, global coordinates are defined for the entire test beam telescope. In this coordinate system, the z-axis represents the beam direction, and there can also be rotation of the sensor about its geometrical center. The transformation between the local and global coordinates is specified in the detector class of the framework core.

7.4.2 Geometry Configuration

The geometry configuration file specifies the positions and orientations of all the detectors, used in the telescope. During the reconstruction process, Corryvreckan only processes the detectors that are present in the geometry file. Each detector plane is described in a separate section, and the name of the section should match the identifier used in the data acquisition (DAQ) system, as it will be referenced in the RawFile (Figure 7.5).

For each detector plane, the corresponding section in the geometry file should include detector properties such as the pixel matrix size and pixel pitch. The “role” parameter specifies the behaviour of the detector plane in the reconstruction process. It can be configured as a “reference” plane, against which the alignment is calculated. The role can also be set as “dut”, indicating that specific modules for DUT analysis. Additionally, the role can be assigned as “auxiliary”, which contributes information to the event building process but does not directly participate in the reconstruction. Figure 7.7(a) presents an example of the parameters for a detector plane in the geometry configuration file, providing insight into the format and structure of the individual detector plane.

7.4.3 Main Configuration File

The main configuration file assumes a vital role in establishing the essential parameters for the reconstruction process in Corryvreckan. It begins with the global configuration parameter "Corryvreckan" and includes the specification of the path to the geometry file. Additionally, the name of the output file should be provided to facilitate the storage of the reconstruction results.

Within the main configuration file, modules are defined using square brackets as section headers, and the corresponding necessary parameters are specified beneath them. The specific parameters utilized by each module can be found in the framework's manual [139]. The modules are executed in the sequence in which they are listed in the main configuration file, ensuring that the reconstruction process follows the desired order and configuration.

Figure 7.7(b) provides an illustrative example of a configuration file, demonstrating the format and structure that is employed in specifying the parameters for the reconstruction process.

```
[MIMOSA26_1]
material_budget = 0.00075
number_of_pixels = 1152, 576
orientation = 0deg,0deg,0deg
orientation_mode = "xyz"
pixel_pitch = 18.4um,18.4um
position = 0um,0um,152mm
spatial_resolution = 4um,4um
time_resolution = 230us
type = "mimosa26"
role = "reference"
```

(a)

```
[Corryvreckan]
log_level = "INFO"
log_format = "DEFAULT"
number_of_events = 50000
detectors_file = "geometries/geometry_file1.geo"
histogram_file = "01-1-correlations.root"

[EventLoaderEUDAQ2]
name = "TLU_0"
file_name = "data/run000979_191207201706.raw"

[EventLoaderEUDAQ2]
type = "MIMOSA26"
file_name = "data/run000979_191207201706.raw"
```

(b)

Figure 7.7: Example of configuration files for the test beam reconstruction process in Corryvreckan. (a) Small part of the geometry configuration file. (b) Small part of the main configuration file.

7.4.4 Test Beam Data Reconstruction and Analysis

The offline analysis reconstruction chain in the Corryvreckan framework is constructed by incorporating modules for individual tasks within a main configuration file. Figure 7.8 visually represents the flowchart of the reconstruction chain process within the main configuration file. The reconstruction process takes as input the geometry configuration file and the data file (RawFile). Each step involved in the reconstruction process is briefly described, providing an overview of the process. For more in-depth information on each step and its implementation, reference [4] could be consulted.

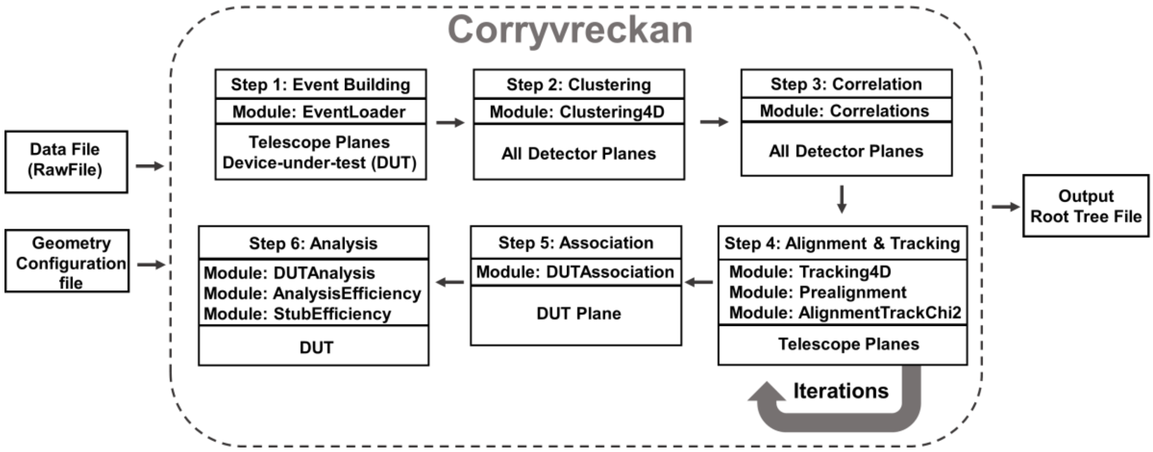

Figure 7.8: Corryvreckan framework reconstruction chain flowchart, adapted from [4]. The input to the reconstruction chain consists of detector-specific or detectors framework-generated data files, along with the geometry configuration files.

Step1: Event Building

The first step in the reconstruction chain is the decoding of pixel or strip hit information from the raw data file. This is accomplished using modules known as *EventLoaders*. In the Corryvreckan framework, *EventLoader* modules are designed to be either detector-specific or framework-associated. Detector-specific *EventLoader* modules directly decode data from the detector file, while framework-associated EventLoader modules decode data from the raw file generated by the framework. For example, *EventLoaderEUDAQ2*, as depicted in the main configuration file in Figure 7.7(b) reads the RawFile generated by the EUDAQ framework to extract information specific to the detector being analysed. In the main configuration file, *EventLoader* modules for all the detectors used in the test setup are created.

The first module in the reconstruction chain defines the time range in which the data chunk is captured. This is done by utilizing the event start and end timestamps or by specifying multiple trigger numbers. Subsequent modules in the reconstruction chain adhere to this event definition and provide matching data for further processing and analysis.

Step2: Clustering and Hit Position

During a single event, after a particle passes through, the charge may spread from one pixel to two or more adjacent pixels due to lateral diffusion, charge sharing, or the creation of electron-hole pairs. These neighbouring pixels together form a cluster. The *Cluster4D* module is utilized in the reconstruction process to form clusters by running a clustering algorithm that groups the pixels or strips together. In the case of strip sensors, strips can be considered as rows of elongated pixels.

Once clusters are formed, the hit position can be calculated in two different ways depending on the available information. If the charge information is available, the charge-weighted center-of-gravity algorithm is used to calculate the hit position. This algorithm takes into account the charge distribution within the cluster. On the other hand, if only binary hit information is available, the arithmetic mean is calculated to determine the hit position.

Step3: Spatial Correlations

The spatial correlation between clusters or pixels of all detector planes is established with respect to a specific reference plane within the *Correlation* module. The choice of the reference plane is arbitrary and can be any of the telescope planes. The *Correlation* module calculates the differences in X and Y coordinates of the clusters (pixels) of each detector plane compared to the reference plane. These differences are then plotted as correlation plots, giving information about the spatial correlation between the planes for each event. The correlation plots are represented by the following equations:

$$X_{correlation} = X_{rp} - X_{op} \tag{7.1}$$

$$Y_{correlation} = Y_{rp} - Y_{op} \tag{7.2}$$

Here, X_{rp} and Y_{rp} represent the cluster (pixel) position at the reference plane, while X_{op} and Y_{op} are the coordinates of the cluster (pixel) on the other detector plane. The correlation plots in early stage of analysis confirms the coherence between the detector planes and is also useful in performing pre-alignment manually in some cases.

Step4: Alignment and Track Fitting

Alignment in Corryvreckan is a two-step process. In the first step, the *Prealignment* module is responsible for constructing a new geometry file based on correlation plots. This involves adjusting the positions of individual detector planes in the global X and Y coordinates to minimize the values of $X_{correlation}$ and $Y_{correlation}$, in Equation 5.1 and 5.2, aiming for them to be close to zero. This pre-alignment step helps bring the detector planes into approximate alignment.

After the pre-alignment, the tracking process takes place using the *Tracking4D* module. This module separates the track finding procedure from the actual fitting of particle tracks. It supports three different track models:

1. **Straight-line track model**, described by a reference position and direction.
2. **Multiplet track model**, which consists of two or more tracklets connected by a single kink.
3. **General Broken Line (GBL) track model** [140], which takes into account the multiple coulomb scattering by all detector planes and the surrounding air.

Based on the selected track model, track candidates are constructed and passed to the track fitting stage. The fitting process is performed by the track objects, and the resulting track parameters are reported back to the tracking module.

In the second alignment step, the *AlignmentTrackChi2* module is responsible for the alignment process. It uses either an iterative approach with Minuit2 [141] or the Millepede-II algorithm [142] to minimize the track χ^2. This step adjusts the positions and orientations of the detector planes to optimize the agreement between the tracks and the observed hits. After each alignment step, an updated geometry file is generated, which incorporates the modifications made during alignment. This updated geometry file is then used for subsequent alignment steps or passed on to the next module in the reconstruction chain.

Step5: Association of DUT Clusters

In Corryvreckan, the association of clusters in the DUT with the reference tracks from the telescope planes is accomplished using the *DUTAssociation* module. Multiple association modules can be utilized for different detectors, each employing different association criteria. There are two methods available for DUT association:

1. Distance Criterion: In this method, the position of the cluster center is compared with the track position at the DUT using a specified distance range. If the distance between the cluster center position and the track position falls within this range, the association between the cluster and the track is established.
2. Closest Distance: This approach focuses on determining the closest distance between the track and any of the pixel hits within the cluster. Instead of comparing the cluster center position, the association decision is based on identifying the track with the closest distance to any of the individual pixel hits within the cluster. If the track is found to have the closest distance to any of the pixel hits, the association is made based on this criterion.

The selection of the appropriate method depends on the specific requirements of the analysis and the characteristics of the DUT.

Step6: Analysis

There are also modules available for the final analysis in Corryvreckan. In the scope of this thesis, two specific analysis modules are used:

1. ***AnalysisDUT***: This module generates histograms that provide information on the spatial and time resolution of the DUT. The spatial resolution is obtained by comparing the coordinates of DUT associated clusters with the tracks from the telescope. It is calculated as the residual difference between the coordinates of the tracks and the associated DUT clusters after performing the DUT software alignment with the telescope.

$$X_{residual} = X_{tracks} - X_{DUT-Cluster} \tag{7.3}$$

$$Y_{residual} = Y_{tracks} - Y_{DUT-Cluster} \tag{7.4}$$

Similarly, the time resolution is defined as the width of the time window between the reference tracks and the associated DUT clusters.

$$t_{residual} = t_{tracks} - t_{UT-Cluster} \tag{7.5}$$

The RMS value of the spatial resolution histogram represents the combined resolution of the telescope and the DUT. If the telescope resolution at the DUT is known, the resolution of the DUT can be calculated using the equation:

$$\sigma^2 = \sigma_t^2 + \sigma_{DUT}^2 \tag{7.6}$$

where σ is the RMS value in residual histogram while σ_t is the telescope resolution at DUT, and σ_{DUT} is the resolution of DUT.

2. ***AnalysisEfficiency***: This module is used to determine the hit detection efficiency of the DUT. It calculates the efficiency using the formula:

$$\epsilon = \frac{N_{DUT}}{N_{total}} \tag{7.7}$$

where N_{DUT} is the number of tracks associated with the DUT and N_{total} is the total number of tracks, including those that are not associated with the DUT.

Other analysis modules are also available in Corryvreckan, such as *AnalysisTelescope* and *AnalysisSensorEdge*. For more details on analysis modules, reference [139] can be consulted. Furthermore, the flexibility of the Corryvreckan framework allows for the addition of new modules in both the local and global branches, tailored to target-specific analysis. In the context of this thesis, an additional module has been added to the local branch of the framework to calculate the 2S module stub efficiency, which will be discussed in section 7.6.3.

Storage File for Reconstruction Data and Results

In Corryvreckan, the reconstructed data, such as detector clusters and tracks, can be saved as data objects in a ROOT TTree format using the *FileWriter* module. This feature allows the data to be stored at any desired point during the reconstruction chain. The stored data can be easily accessed and read back into the framework for further analysis and processing using the *FileReader* module. This capability provides flexibility in handling and analysing the data at different stages of the reconstruction process.

7.5 Data Reconstruction of November 2019 Test Beam

The Corryvreckan framework was specifically configured according to the test beam setup described in section 7.3 for the data reconstruction of the November 2019 test beam campaign, focusing on the 2S module. In this section, a selection of reconstruction results obtained using Corryvreckan are presented, which serve as a testament to the framework's readiness for further analysis. These results demonstrate the capability of Corryvreckan to accurately reconstruct the data from the 2S module.

7.5.1 Raw data and Clustering

The test beam was conducted on the EUDET Telescope and the data acquisition was performed using the EUDAQ framework. Therefore, the *EventLoaderEUDAQ2* module in Corryvreckan was employed to decode the cluster and hit information from the acquired data. The first module in the reconstruction chain is responsible for extracting the trigger information from the EUDET Trigger Logic Unit (TLU) present in the RawFile for a specific run.

Figure 7.9 showcases the hit map generated for the top and bottom sensors of the central DUT (2S Module), as shown in Figure 7.4. The hit map provides a visual representation of the distribution of hits on the sensors. In both Figure 7.9(a) and Figure 7.9(b), the highlighted yellow regions show areas of increased occupancy, indicating the presence of a distinct strip pattern associated with the strip sensors.

Furthermore, Figure 7.10 presents a comparison of the cluster size for different types of detectors present in the beam telescope. The FE-I4 sensor and both sensors of the central DUT (2S module) exhibit single-pixel clusters, while the MIMOSA26 sensor demonstrates cluster size of three pixels. This larger cluster size can be attributed to the measurement process employed for the MIMOSA26, where the signal collection depends on the diffusion process [143].

These reconstruction results provide valuable insights into the hit distribution and cluster characteristics of the detectors used in the test beam campaign. The obtained hit map and cluster size comparison demonstrate the effectiveness of Corryvreckan in accurately processing the acquired data and extracting meaningful information for further analysis and interpretation.

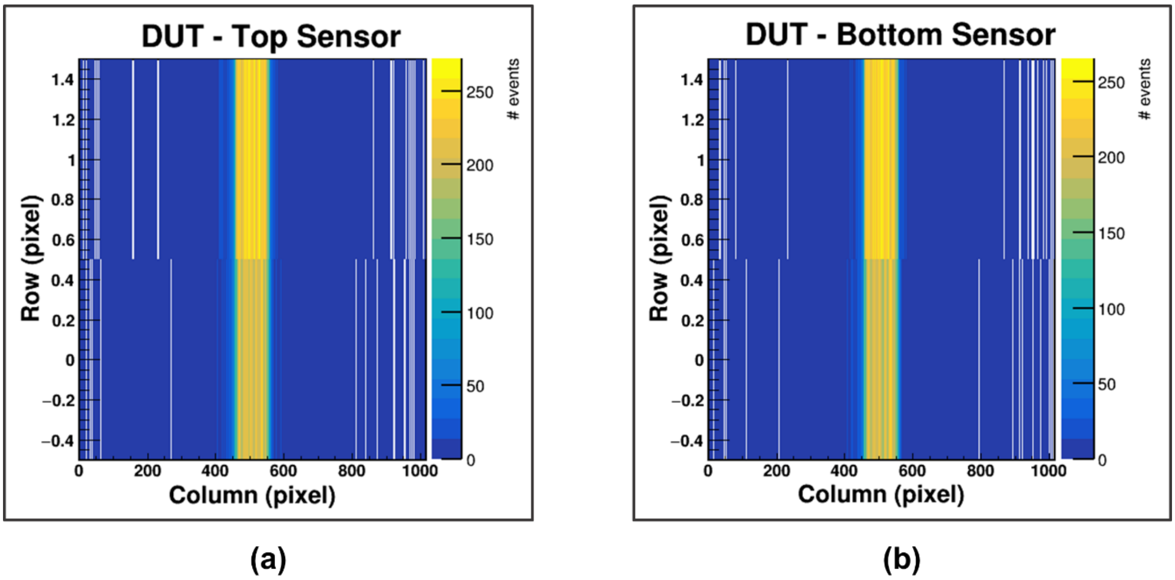

Figure 7.9: Hit maps extracted from the root output file of Corryvreckan for the sensors of the Central DUT shown in Figure 7.4. (a) Hit map for the top sensor. (b) Hit map for the bottom sensor. The yellow area indicates regions of increased occupancy.

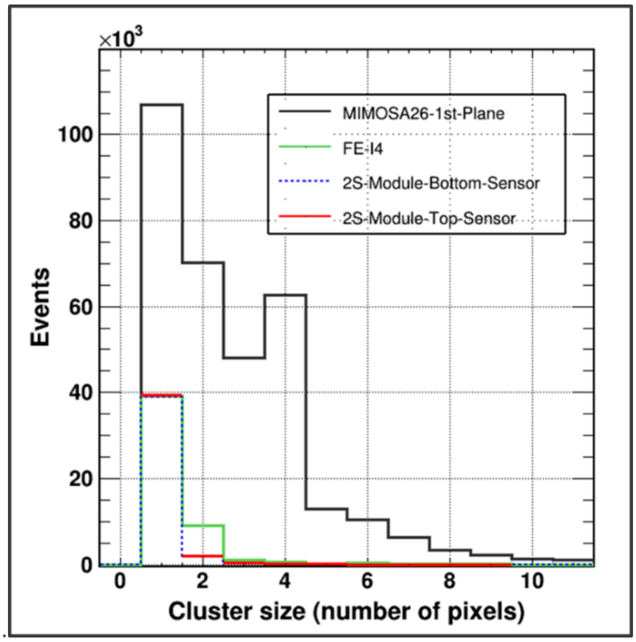

Figure 7.10: Cluster size of different detectors in the beam telescope for a normal run. The top and bottom sensors of the 2S module and the FE-I4 sensor exhibit a cluster size of one pixel, while the MIMOSA26 sensor shows a cluster size of three pixels.

7.5.2 Correlations & Pre-alignment

As described in section 7.4.4, correlation plots are essential for assessing data quality and ensuring synchronization between different detectors. They are particularly useful for evaluating the per-alignment of different detector planes with respect to a chosen reference telescope plane. For the 2S module sensors, the correlation plots are examined only for the strip row side, as the strips column side covers multiple pixels of the telescope reference plane for each strip due to its increased length of 5cm.

Figure 7.11 showcases the correlation plots for both sensors of the central DUT (2S module) obtained during a normal run. These plots depict the correlation between the global *X* coordinate of each DUT sensor and the telescope reference plane, both before and after the pre-alignment process. Notably, in this particular run, the global *X* coordinate is aligned in the strip width direction. Therefore, the correlation analysis is focused along this axis.

Figure 7.12 provides a 2D view of the correlation plots for both DUT sensors after pre-alignment. In the correlation plots, the yellow color indicates regions with an increased number of events observed on both the reference plane and the DUT (top or bottom) planes. Notably, the positions with an increased number of events align closely for both planes, indicating a satisfactory pre-alignment in the first stage of the alignment process.

7.5.3 Tracking and Alignment

The test beam was conducted with electron beam at an energy of 4 GeV (section 7.3). Given the expected presence of multiple scattering along the particle trajectory at this energy, the General Broken Lines (GBL) track model was selected. The *AlignmentTrackChi2* module was employed to align the telescope planes using an iterative approach that minimized the global $\chi 2$ value of the track fit. The alignment process was repeated for all telescope planes until a sub-micron alignment precision was achieved in the residual plots for both the *X* and *Y* global coordinates. Figure 7.13 showcases the distribution of $\chi 2$ values for the tracks over the degrees of freedom obtained from the track fitting procedure for a specific run. The track fitting was performed using the geometry configuration file generated after the final alignment step. The plot shows a nice fit for the detector data, as evidenced by the peak of the distribution being close to one.

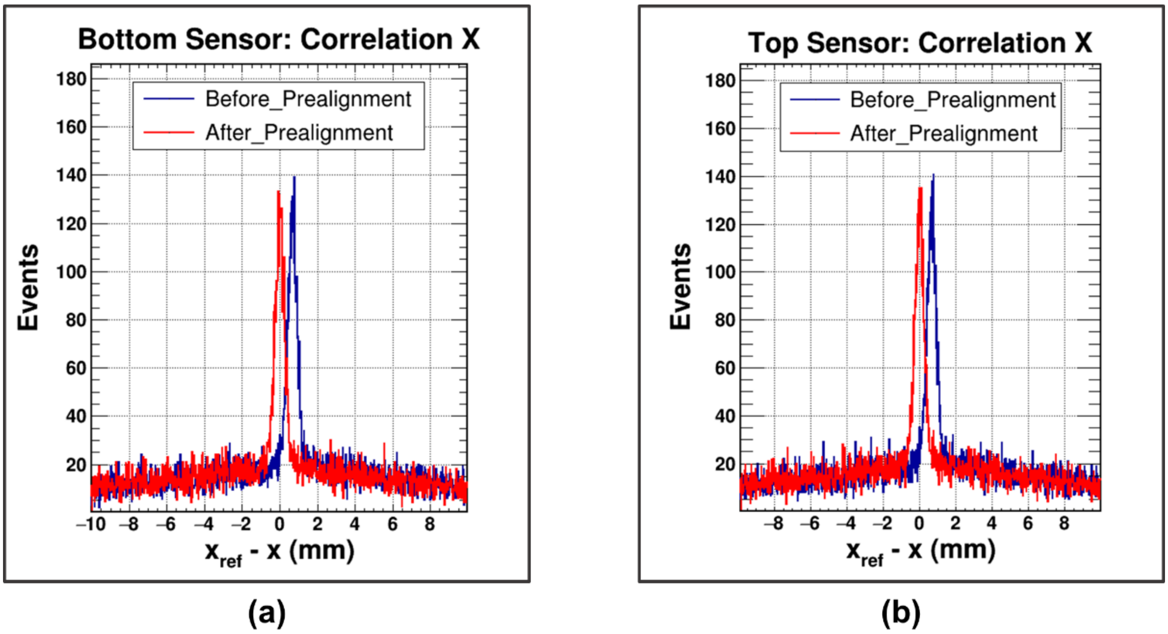

Figure 7.11: Correlation plots showing the correlation between the sensors of the DUT and the reference telescope plane in the global *X* coordinate, both before and after pre-alignment. (a) Correlation plot for the DUT top sensor. (b) Correlation plot for the DUT bottom sensor.

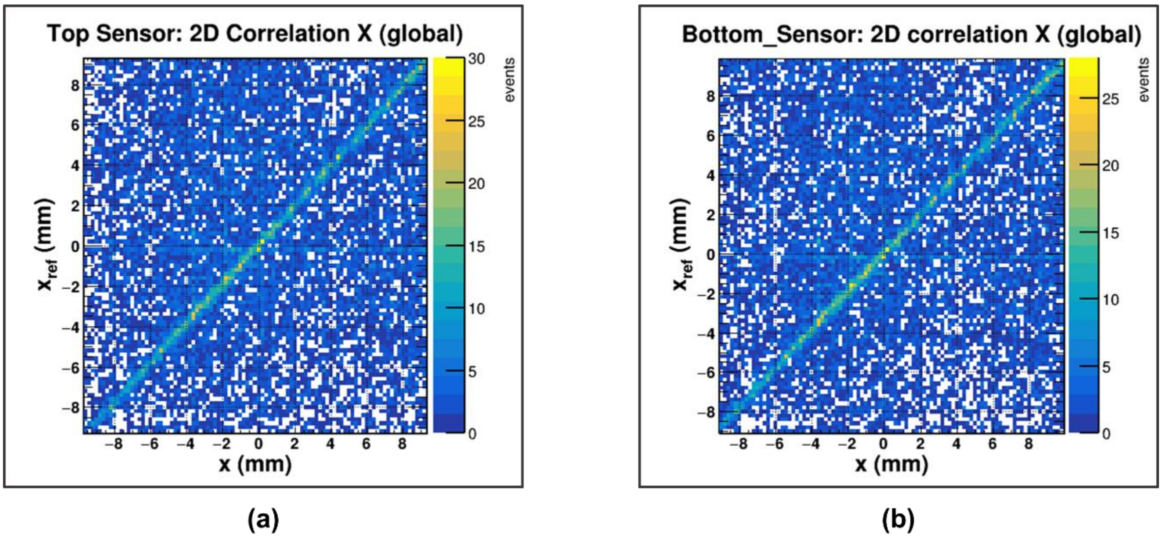

Figure 7.12: 2D view of the correlation plot after the pre-alignment step in the global *X* coordinate, showing that a high number of events are observed at similar positions for both DUT sensors and the telescope reference plane. (a) 2D correlation plot for the DUT top sensor. (b) 2D correlation plot for the DUT bottom sensor.

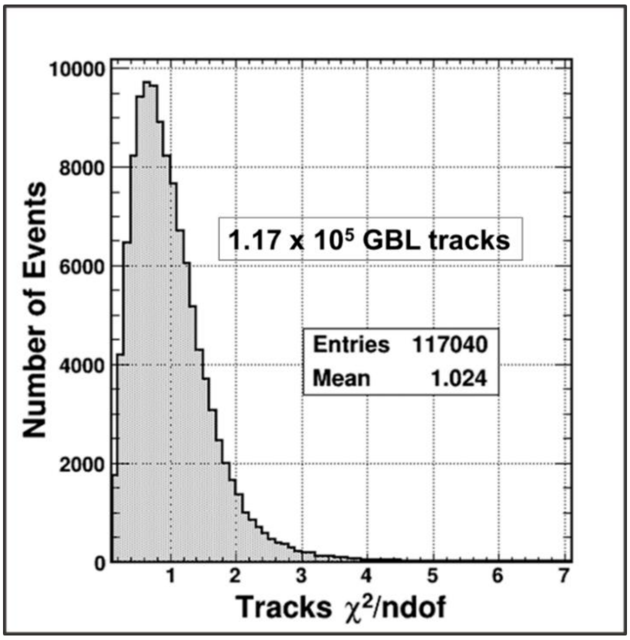

Figure 7.13: The distribution of tracks χ^2 divided by the number of degrees of freedom generated by the *Tracking4D* module using the geometry configuration file produced after the final alignment. The mean of the distribution is close to one indicating a good fit for the detector data.

The hit maps, correlation plots, and alignment plots of all the telescope planes and the timing reference FE-I4 plane for a specific run can be found in Appendix D. The presented plots demonstrate the effectiveness of the alignment procedure and provide confidence in the quality of the reconstructed data for further analysis. The alignment procedure was performed for all the runs that were utilized for the subsequent analysis, which will be presented in the next section.

7.6 Test Beam Analysis Results for 2S module

This section presents the analysis outcomes for the November 2019 test beam data conducted with the Corryvreckan framework. The test beam runs where the module CBCs were operated in sampled mode are chosen for the analysis. Finally, certain results are compared with previously generated EUTelescope framework results to assess the consistency and agreement between the two frameworks.

7.6.1 Sensors Misalignment in Module

The alignment between the top and bottom sensors of a module can be determined after performing the DUT alignment procedure within the analysis framework. The misalignment value in the direction perpendicular to the strip can be calculated by comparing the residual values in the global *X* coordinate of the two sensors. For the module named Ac-M1804, the analysis in the Corryvreckan framework across various runs reveals misalignment values, displayed in Figure 7.14. The calculated mean misalignment and standard deviation are -4.24 ± 1.01 μm, and 3.77 ± 0.71 μm respectively. It is noteworthy that, in laboratory metrology, the misalignment value perpendicular to the strip direction was measured as -5 μm [135].

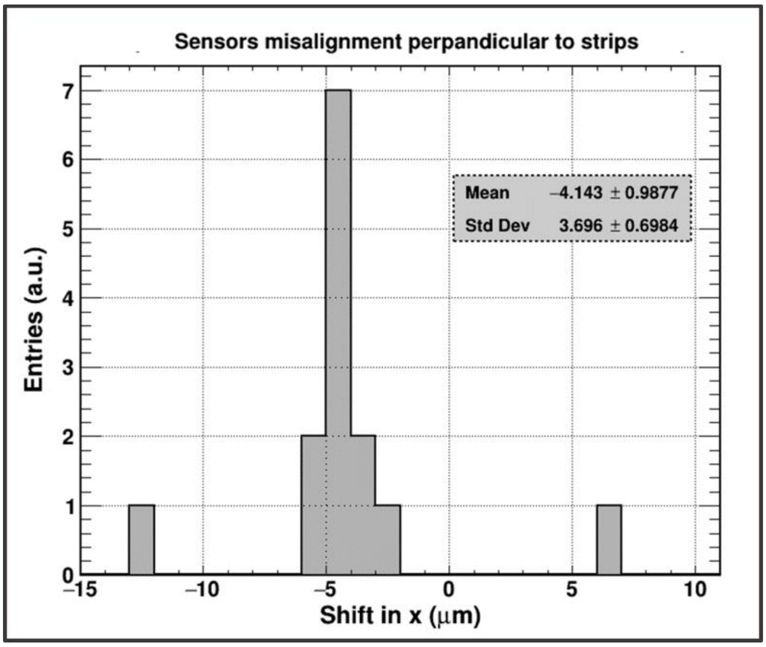

Figure 7.14: Histogram showing the misalignment between the top and bottom sensors, in module Ac-M1804, in the direction perpendicular to the strips. The misalignment values were obtained after performing individual sensor alignment procedure in the Corryvreckan framework.

7.6.2 Spatial Resolution of Top and Bottom Sensors

The spatial resolution of a strip sensor can be calculated by using the relation

$$Sensor\ Resolution = \frac{Sensor\ Pitch}{\sqrt{12}} \tag{7.8}$$

With a strip pitch of 90 μm (described in section 4.4), the spatial resolution of the 2S sensor is found to be approximately 26 μm. As discussed in section 7.4.4, the resolution of the sensor can be determined from the residual distribution plots of the DUT. The standard deviation values in the residual distribution represent the combined resolution of both the DUT sensor and the telescope. By utilizing Equation 5.6, the intrinsic value of the sensor resolution can be calculated.

Figure 7.15 illustrates the residual distribution in global *X* coordinates, generated by the *AnalysisDUT* module within the Corryvreckan framework, for the top and bottom sensors of module Ac-M1804. The standard deviation value for the top sensor are determined as 28.40 ± 0.05 μm, while for the bottom sensor its value is calculated as 28.39 ± 0.05 μm. By considering the telescope resolution at the DUT, 10 μm [123], the intrinsic resolution values are calculated as 26.58 ± 0.05 μm for the top sensor and 26.57 ± 0.05 μm for the bottom sensor. These results closely align with the 2S sensor resolution as calculated using Equation 6.8.

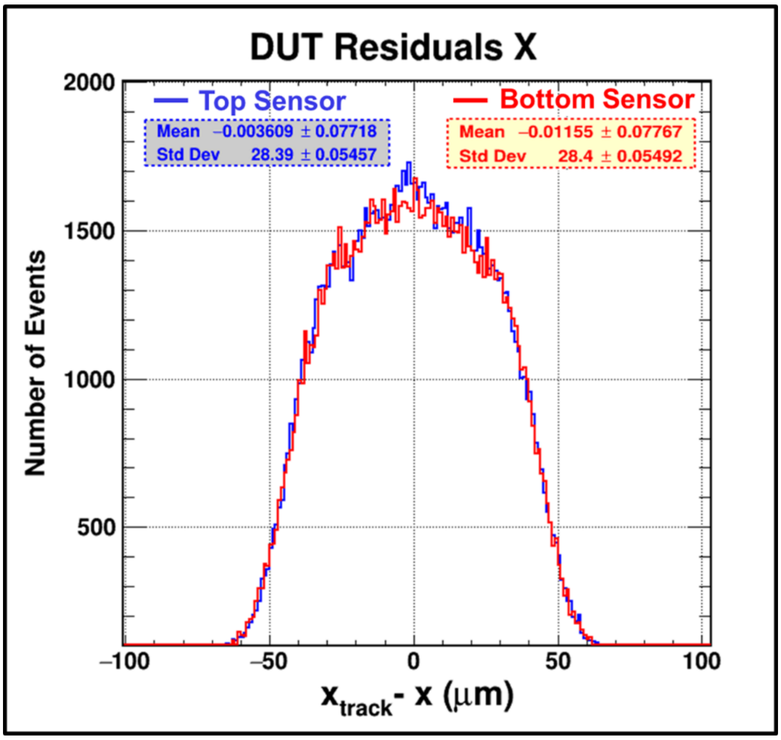

Figure 7.15: Residual distribution in global *X* coordinates for both the top and bottom sensors, of module Ac-M1804. These results are produced by the Corryvreckan framework after performing complete alignment for each sensor.

7.6.3 Module Efficiencies for Analysis

As part of the analysis using the Corryvreckan framework, two crucial efficiencies—the cluster or hit detection efficiency and the module stub detection efficiency—are computed for the 2S module. The definitions of these efficiencies closely follow the description outlined in reference [135].

Hit Detection Efficiency

The module hit detection efficiency is determined within the *AnalysisEfficiency* module. To account for the limited time resolution of the MIMOSA planes, the hit detection efficiency is evaluated by comparing the telescope tracks associated with the DUT to those associated with the reference plane FE-I4. The telescope tracks associated with the reference plane FE-I4, satisfying the conditions $\Delta x \leq 200$ μm and $\Delta y \leq 80$ μm, are defined as $N_{FE\text{-}I4\text{-}associated\ tracks}$. Similarly, the telescope tracks associated with the 2S sensors, within the condition $\Delta x \leq 200$ μm, are defined as $N_{DUT\ associated\ tracks}$. The hit detection efficiency is subsequently calculated using the following formula:

$$\epsilon_{\text{hit}-\text{detection}} = \frac{N_{\text{DUT associated tracks}}}{N_{\text{FE}-\text{I4 associated trcaks}}} \tag{7.9}$$

Stub Efficiency

The Corryvreckan framework offers great flexibility, allowing the addition of modules for target-specific analysis, as discussed in section 7.4.4. In the scope of this thesis, a dedicated module was added to the local branch of Corryvreckan for stub efficiency analysis.

Within this module, the stub efficiency calculation is performed by comparing the telescope tracks associated with both 2S sensors, along with the stub bend information provided by the 2S module, to the telescope tracks associated with the reference FE-I4 plane. Similar to the hit detection efficiency calculation, the telescope tracks associated with the reference plane FE-I4, satisfying the conditions $\Delta x \leq 200$ μm and $\Delta y \leq 80$ μm, are defined as $N_{FE\text{-}I4\ associated\ tracks}$. On the other hand, the telescope tracks associated with the 2S sensors, along with the module bend information, within the condition $\Delta x \leq 200$ μm, are defined as $N_{stub\ associated\ tracks}$. Subsequently, the stub efficiency is calculated using the following formula:

$$\epsilon_{\text{stub}} = \frac{N_{\text{stub associated tracks}}}{N_{\text{FE}-\text{I4 associated trcaks}}} \tag{7.10}$$

This additional module in the local branch of the Corryvreckan framework allows for a thorough analysis of the stub efficiency, providing valuable insights into the module's performance in detecting and reconstructing stubs.

7.6.4 Hit Detection Efficiency vs TDC

As explained in section 7.3.2, the data acquisition process employed a super-sampling technique in the backend firmware. This technique divided the time interval into eight bins of 3.125 ns each to precisely capture the arrival time of the trigger signal from the TLU. Figure 7.16 illustrates the hit detection efficiencies obtained using the Corryvreckan framework for different TDC phases for one specific run, considering both the top and bottom sensors. The average hit detection efficiencies were calculated as 99.2% for the bins [2, 3, 4] and 99.0% for the bins [2, 3, 4, 5] for both top and bottom sensors. The hit detection efficiency analysis was conducted for each run, taking into account the variations in TDC phase. The TDC phases exhibiting the highest hit detection efficiencies were subsequently chosen for further analysis.

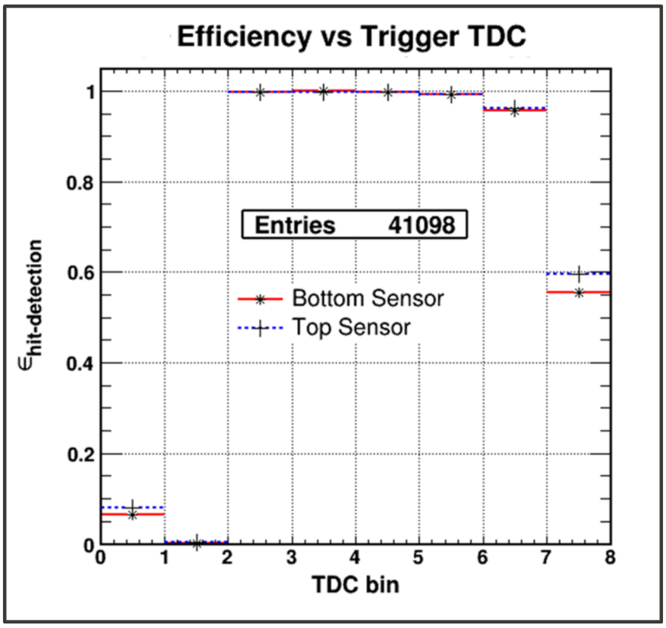

Figure 7.16: Distribution of cluster hit efficiency for both the top sensor and bottom sensor against each TDC phase. The hit detection efficiency is calculated using the Corryvreckan framework.

7.6.5 Threshold Scan

As part of the test beam campaign, a threshold scan was carried out to explore the influence of adjusting the comparator threshold of CBCs on the hit detection efficiency and stub efficiency of the module. The threshold of CBCs was adjusted in DAC counts (V_{cth}).

Module Hit Detection Efficiency

Figure 7.17 depicts the impact of the threshold scan on the hit detection efficiencies of the module. In the zoomed-in view, Corryvreckan calculated an average hit detection efficiency value of 99.7% in the 20 - 60 V_{cth} range. A previous analysis using the EUTelescope reconstruction framework, as documented in reference [144], revealed an average hit detection efficiency of 99.5% within the same threshold value range.

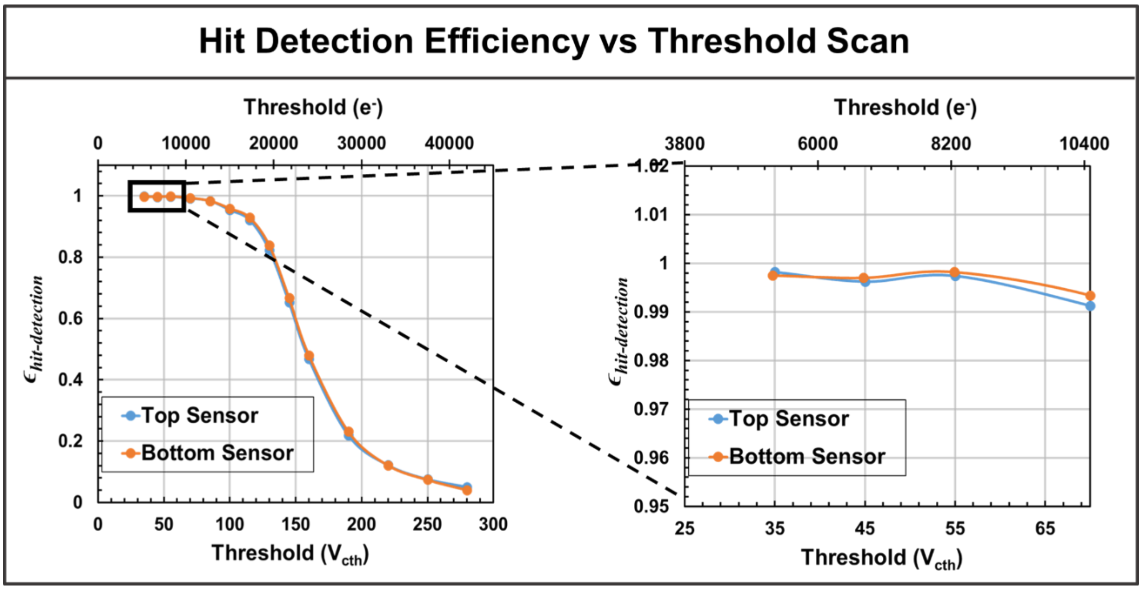

Figure 7.17: Variation in module hit detection efficiency with CBC threshold values in DAC counts (V_{cth}). The efficiency analysis for each run is performed in the Corryvreckan reconstruction framework.

Module Stub Efficiency

The impact of varying the threshold value on module stub efficiency is depicted in Figure 7.18. The average stub efficiency values, calculated by Corryvreckan, within the threshold voltage range of 20 - 60 V_{cth}, as displayed in the figure's zoomed plot, are found to be 99.5%. Comparatively, the average stub efficiency value within this range was greater than 99% using the EUTelescope reconstruction framework [144]. Consequently, the results from the threshold scan analysis, conducted with the Corryvreckan reconstruction framework, align well with the results obtained using the established EUTelescope framework.

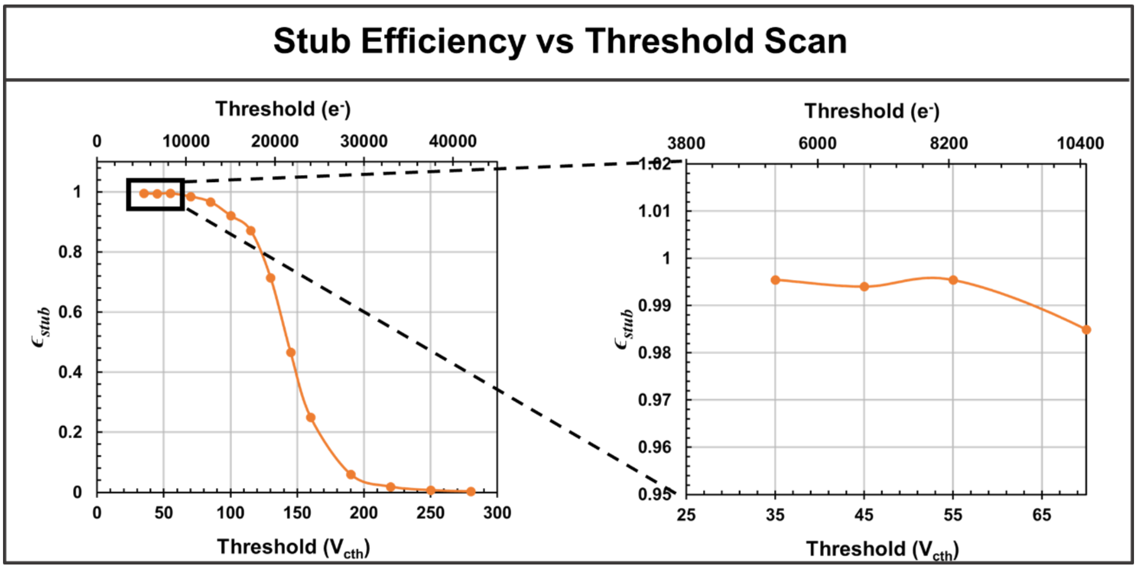

Figure 7.18: Variation in module stub efficiency with CBC threshold values in DAC counts (V_{cth}). The efficiency analysis for each run is performed in the Corryvreckan framework.

7.6.6 Angular Scan

Cluster Size

The cluster size denotes the accumulation of the charge cloud on the strip surface of the sensor. As outlined in reference [145], the cluster size is impacted by the incident angle (θ) of the beam on an ideal point-like strip. This association is described by the following equation:

$$s(\theta) = s_0 + \frac{d_0}{p} . |\tan(\theta - \theta_0)| \tag{7.11}$$

In this equation, s_o refers to the cluster size at zero incident angle, d_o and p represents the sensor's thickness and pitch, and θ_o denotes the offset angle between the incident beam and the rotation stage setting on the telescope.

Figure 7.19 illustrates the cluster size dependence on angle within the range of 0° to 37.5°, focusing on a threshold value of 545 V_{cth} unit, for both top and bottom sensor. Remarkably, the cluster size distributions obtained exhibit a high degree of similarity with the reconstructed cluster sizes at various angles when utilizing the EUTelescope framework, as referenced in [135].

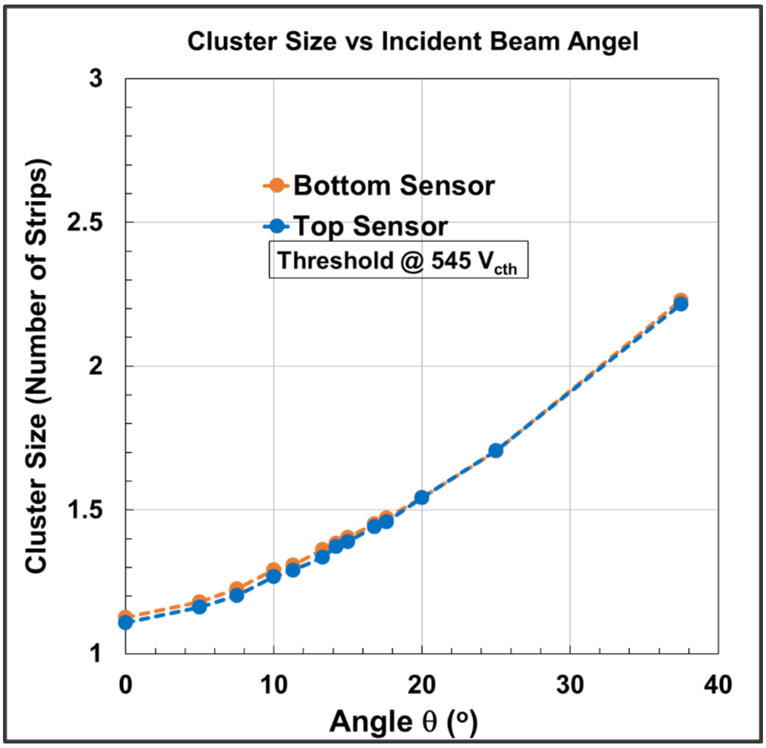

Figure 7.19: Cluster size dependence on incident beam angle from 0° to 37.5° for a threshold value of 545 V_{cth} unit, reconstructed using the Corryvreckan framework.

Module Stub Efficiency

During the test beam campaign, an angular scan was performed by adjusting the DUT stage to different angles, causing the beam to approach the module at various angles around the strip axis. For this scan, the stub window size in the module was set as ±5 strips. With this stub window size for a 1.8 mm module, the anticipated turn-on angle (θ), which is the angle at which the stub efficiency drops to zero as depicted in Figure 7.20, was calculated to be approximately 14° as

$$\theta = \tan^{-1}\left(\frac{5 \times 90}{1.8}\right) \approx 14° \tag{7.12}$$

Figure 7.21 showcases the module stub efficiency variation from 0° to 37.5° reconstructed using the Corryvreckan framework. The stub efficiency maintains an average of 99.2% up to 15° and decreases to 2.8% at larger angles, demonstrating comparability with the calculated turn-on angle. In contrast, the EUTelescope analysis reported nearly 100% efficiency up to 15°, decreasing to 2.5% at larger angles, as documented in reference [135].

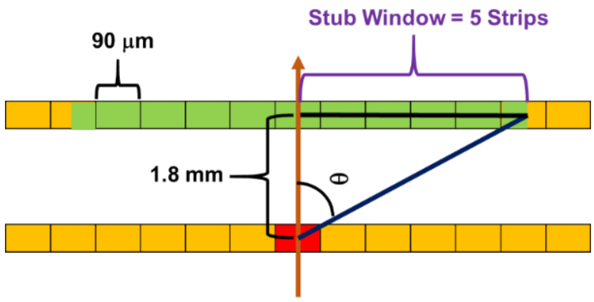

Figure 7.20: The figure illustrates the schematic for calculating the maximum stub angle 'θ' for a 1.8 mm module with a stub window size of ±5 strips.

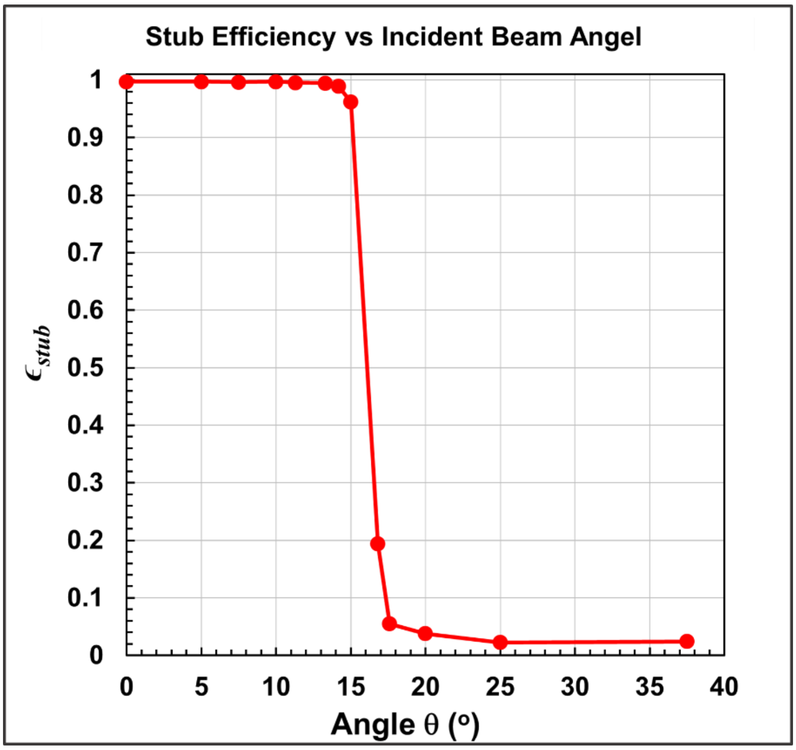

Figure 7.21: Analysis of module stub efficiency variation for different beam incident angles around the strip axis using Corryvreckan framework.

Performance of Transverse Momentum Discrimination

The incident angle (θ) can be transformed into emulated transverse momentum at the first ladder position (71.5 cm) corresponding to the CMS magnetic field (3.8 T) using the relation described in reference [146]:

$$p_T(GeV) = \frac{0.40755}{Sin(\theta)} \quad (7.13)$$

Figure 7.22 presents the results of the stub efficiency versus transverse momentum (p_T) and reveals a turn-on transverse momentum of 1.48 GeV.

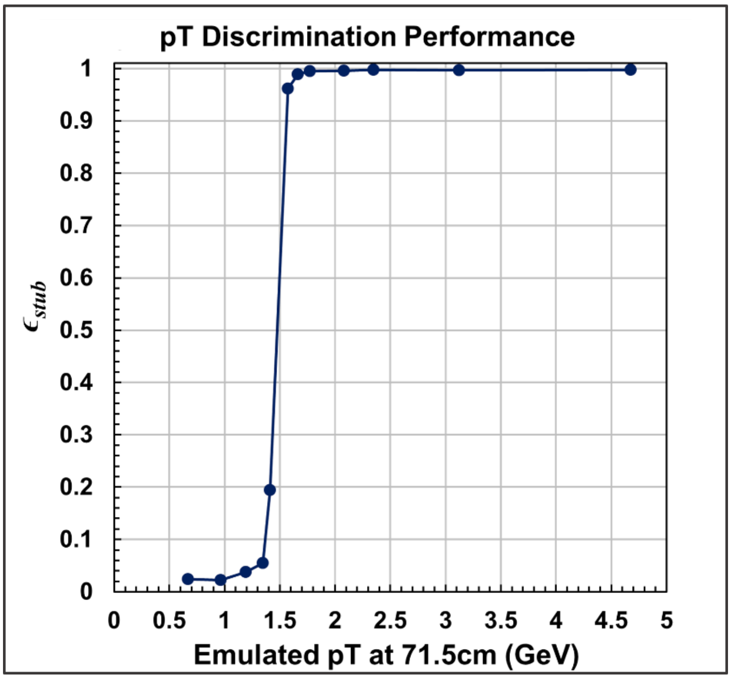

Figure 7.22: The module stub efficiency plotted against the emulated transverse momentum at 71.5 cm and the turn-on momentum is 1.48 GeV.

7.7 Corryvreckan Analysis Comparison Summary

Table 7.1 presents a detailed comparison of parameter values between the Corryvreckan and EUTelescope frameworks. The comparison encompasses module-level analysis, including hit detection efficiency and module stub efficiency for CBC threshold scans, as well as angular scan analysis, which involve studying cluster size and module stub efficiency at various incident angles. Remarkably, all these analysis exhibit an agreement within 1% between the two frameworks. This comprehensive comparison underscores the robustness and effectiveness of the Corryvreckan framework for future test beam analysis of 2S modules.

Table 7.1: Comparison between EUTelescope and Corryvreckan framework results.

Parameter	**Corryvreckan framework**	**EUTelescope framework**	**Results Comparison**
Hit detection efficiency vs CBC threshold in 10000e$^-$ threshold value range	99.7%	99.5%	Agreement within 1%
Module stub efficiency vs CBC threshold in 10000e$^-$ threshold value range	99.5%	> 99%	Agreement within 1%
Cluster Size with angle at threshold 545 V_{cth} unit	~1.1 strips at 0^o and ~2.2 strips 37.5^o	~1.1 strips at 0^o and ~2.2 strips 37.5^o	Agreement within 1%
Module stub efficiency vs angle around strip axis	Averages 99.2% up-to 15^o and 2.8% for large angles	~ 100% up-to 15^o and ~ 2.5% for large angles	Agreement within 1%

8

Summary and Outlook

The CMS detector will undergo a Phase-2 upgrade to cope with the higher luminosity during the HL-LHC. This thesis primarily concentrated on establishing the assembly and testing facilities for the Strip-Strip (2S) module, an essential part of the CMS Outer Tracker Phase-2 upgrade. Furthermore, this thesis delved into the test beam analysis for the 2S module utilizing the user-friendly offline reconstruction framework Corryvreckan.

The development of an assembly and testing site for 2S modules has progressed through several phases. This includes a detailed study involving the assembly of various mechanical modules to correct assembly jigs, which are used to assemble different components such as kapton strips and sensor placement. Correcting the assembly jigs has enabled to achieve assembly of components within tolerance limits. The study of kapton strips' placement on the sensor backplane, on various glass and silicon sensors, demonstrates placement well within the tolerance limits of ±150 µm and ±200 µm in parallel and perpendicular to the strip direction, respectively. Corrections made to the sensor gluing jig resulted in sensor-to-sensor alignment within rotational and translation tolerances in bare mechanical modules. Similarly, adequate alignment between sensor strips and FEH bond-pads for both dummy and functional modules has been achieved. During the prototyping phase, detailed studies on glue dispensing were conducted to ensure controlled application of glue during assembly. This study involved the development of an automated glue dispensing system initially and the use of a company built system for final production. A needle-based metrology method was developed to check sensor-to-sensor misalignment in bare modules, utilizing measurements performed using a probe station and Python code for evaluation. The bar module metrology of the available test modules of different levels of functionality, the 8CBC2, 8CBC3, and the fully functional 2S, revealed rotational misalignment values of 374 µrad, -22 µrad, and -31 µrad, respectively, were found well within the mechanical tolerance limits [124].

The voltage-current (IV) measurements were conducted after each assembly step to verify the sensors' quality, showing a current of 150nA at 800V, confirming good assembly follow-through for functional modules. A separate HV/IV testing setup was developed as part of the module assembly line during series production. Electrical and optical test setups were developed to measure the noise levels for functional modules, including 8CBC2, 8CBC3, and fully functional 2S. The recorded noise measurements showed noise levels of 980 e^- and 920 e^- for 8CBC2 and fully functional 2S modules [124], respectively, which are very close to the target value of 1000 e^-.

A test box, incorporating a chiller and Peltier plate, was designed and constructed to perform noise measurements under cold temperatures and to conduct thermal cycles on modules during the prototyping phase. The module noise level remains consistent with varying temperatures, including extreme conditions between +18 °C and -18°C, demonstrating the module's stability. Beginning from scratch, this research work has resulted in the creation of an effective assembly and testing site for silicon modules. Seven functional 2S modules were assembled well within the metrology tolerance limits and exhibited fully functional electrical performance.

A user-friendly Corryvreckan test beam reconstruction framework environment has been established to analyze the test beam data of 2S modules for hit detection and stub efficiencies. The analysis results reveal a resolution of 26.5 µm for the 2S sensor. The calculated translation displacement between two sensors, perpendicular to strips in a module, is found to be -4 µm, close to the metrology value measured in the laboratory. Threshold scans demonstrate hit detection efficiency and stub efficiency, while angular scans show cluster size and stub efficiency. The results obtained demonstrate agreement within 1% with the EUTelescope framework [124], highlighting Corryvreckan's promising potential for 2S module analysis in future test beams.

A. Glue Dispensing

A.1 LH Series Dispensing System Specification

(Models)	LH-200T	LH-300T	LH-400T	LH-500T
Working RangeX/Y/Z(mm)	200 / 200 / 100	300 / 300 / 100	400/400/100	500/500/100
Load Y-AXIS / Z-AXIS	5kg/8kg	10kg / 15kg		
X&Y / Z (mm/sec)	0.1~200 / 200	0.1~200 / 200		
Resolution	0.01 mm/Axis			
SingleRepetitive Positioning Accuracy	+/- 0.02 mm/ Axis			
Program Capacity	100Programs、4000 points/Program			
Program Display	Teach Pendant LCD and PC			
Motor System	High resolution stepping motor			
Control Method	PTP & PC			
Interpolation Function	3 axis			
Programming Method	Teach Pandent / PC			
I/O Signals Port	10 Inputs / 10 Outputs			
External Control Interface	Ethernet			
Power Supply	AC100 ~ 240V 600W			
Working Temperature	-10—50 ℃			
Working Relative Humidity	20—90% no condensation			
Dimensions (WxDxH mm)	405/505/735	495/600/750	595/700/750	695/800/750
Robot Weight (kg)	40 kg	45 kg	50 kg	55 kg

A.2 Dispensing Pattern Coordinates

The coordinates used for dispensing in both the locally developed and customized dispensing systems are documented and available for reference. These coordinates provide essential guidance during the dispensing process, ensuring precise and accurate glue placement. They consider the specific positions and movements required by the dispensing system to achieve desired patterns and quantities. By following these coordinates, operators can consistently replicate the dispensing process and maintain consistent glue application across multiple instances.

A.2.1 Coordinates for PI-Strips

Locally Developed Dispensing System

The table presented provides a comprehensive display of the specific set of coordinates utilized in the graphical user interface (GUI) of the local dispensing system. These coordinates are instrumental in creating a precise glue pattern intended for attaching PI (Polyimide) strips. The figure situated on the right side of the table complements the information by visually presenting the resulting dispensing pattern originating from the designated reference point.

Air Pressure = 0.25 bar
Line Speed = 41 mm/s

Point Number	Position		Dispense Pattern
	X (mm)	Y (mm)	
1	5.2	89.5	Line start
2	5.2	4.5	Line stop
3	50.3	3.5	Line start
4	50.3	12.4	Line stop
5	97.5	89.5	Line start
6	97.5	4.5	Line stop

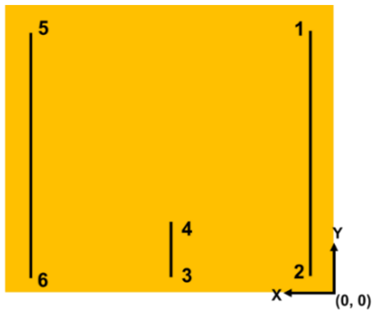

Figure A.1: Coordinate values and dispensing pattern used in the local dispensing system.

Customized Dispensing System

The table presented illustrates the specific set of coordinates used in the graphical user interface (GUI) of the customized dispensing system. These coordinates are employed to draw a glue pattern specifically designed for attaching PI (Polyimide) strips. The figure on the right side serves as a complementary visual representation, showcasing the resulting dispensing pattern originating from the designated reference point.

Dispensing rate = 0.8225 µl/s
Dispense dot time = 0.30 s
Line dispense speed = 12.40 mm/s

Point Number	Position		Dispense Pattern
	X (mm)	Y (mm)	
1	4.0	90.2	Dot
2	7.2	90.2	Dot
3	5.6	87.0	Line start
4	5.6	7.0	Line stop
5	4.0	4.0	Dot
6	7.2	4.0	Dot
7	51.3	4.0	Dot
8	51.3	5.8	Dot
9	51.3	7.6	Dot
10	51.3	9.4	Dot
11	51.3	11.2	Dot
12	51.3	13.0	Dot
13	95.5	4.0	Dot
14	98.7	4.0	Dot
15	97.1	7.0	Line start
16	97.1	87.0	Line stop
17	95.5	90.2	Dot
18	98.7	90.2	Dot

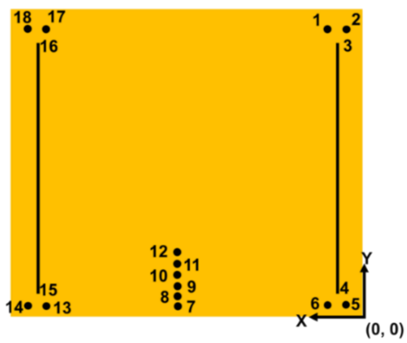

Figure A.2: Coordinate values and dispensing pattern used in the customized dispensing system.

A.3 Coordinates for Wire-bonds Encapsulation

A.3.1 Locally Developed Dispensing System

The table presented provides an overview of the set of coordinates utilized for encapsulation in the GUI of a local dispensing system. These coordinates play a crucial role in guiding the precise placement of materials during the encapsulation process. The figure accompanying the table serves as a complementary visual representation, showcasing the dispensing pattern that originates from a designated reference point.

Air Pressure = 0.25 bar
Line Speed = 5 mm/s

Point Number	Position		Dispense Pattern
	X (mm)	Y (mm)	
1	0	0	Line Start
2	0	94.5	Line passing
3	4.4	94.5	Line passing
4	4.4	0	Line passing
5	1.0	0	Line passing
6	1.0	93.5	Line passing
7	3.4	93.5	Line passing
8	3.4	1.0	Line passing
9	2.0	1.0	Line passing
10	2.0	92.5	Line stop

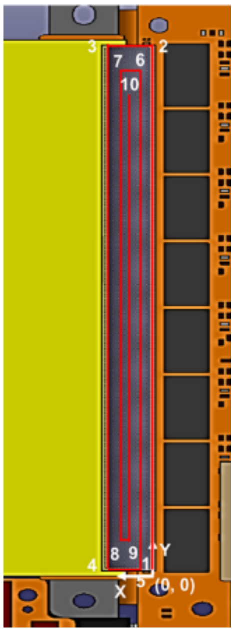

Figure A.3: Coordinate values and dispensing pattern for encapsulation used in the local dispensing system

A.3.2 Customized Dispensing System

The table provided showcases the set of coordinates utilized in the GUI of a customized dispensing system for encapsulation purposes. These coordinates play a vital role in guiding the precise positioning of materials during the encapsulation process. Both FEH are encapsulated in single program. Complementing the table, the accompanying figure visually displays the resulting dispensing pattern originating from a designated reference point.

Dispensing rate = 2.052 μl/s
Line dispense speed = 6.0 mm/s

Point Number	Position		Dispense Pattern
	X (mm)	Y (mm)	
1	-2.8	0.4	Line Start
2	-2.8	93.9	Line passing
3	1.4	93.9	Line passing
4	1.4	0.4	Line passing
5	-2.1	0.4	Line passing
6	-2.1	93.2	Line passing
7	0.7	93.2	Line passing
8	0.7	1.1	Line passing
9	-1.4	1.1	Line passing
10	-1.4	92.5	Line passing
11	0.0	92.5	Line passing
12	0.0	1.8	Line stop
13	105.5	0.4	Line start
14	105.5	93.9	Line passing
15	101.3	93.9	Line passing
16	101.3	0.4	Line passing
17	104.8	0.4	Line passing
18	104.8	93.2	Line passing
19	102.0	93.2	Line passing
20	102.0	1.1	Line passing
21	104.1	1.1	Line passing
22	104.1	92.5	Line passing
23	102.7	92.5	Line passing
24	102.7	1.8	Line stop

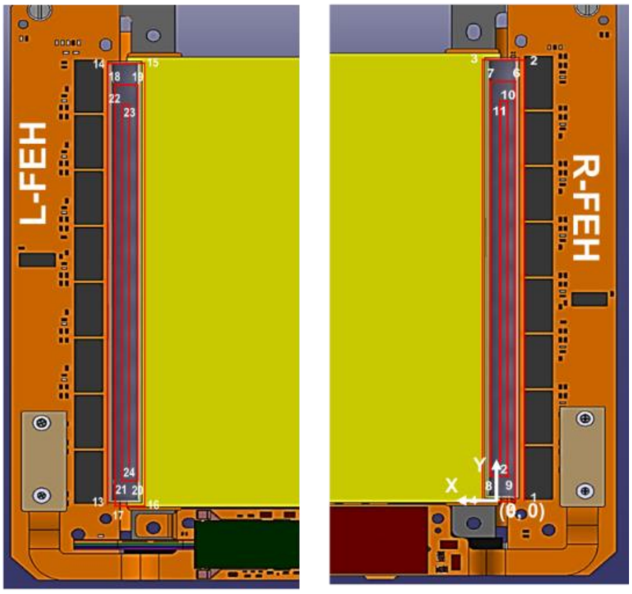

Figure A.4: Coordinate values and dispensing pattern for encapsulation used in the customized dispensing system.

B. Module Metrology Steps for Python Code

The code developed in Python is utilized to determine the misalignment results of the sensors by processing the measured metrology points. The code follows a series of fundamental steps to calculate the misalignment values. These steps are explained pictorially in the following context.

B.1 Polygon construction

In the first step, polygons are created using the measured points for both the needles and the alignment marks of the top and bottom sensors.

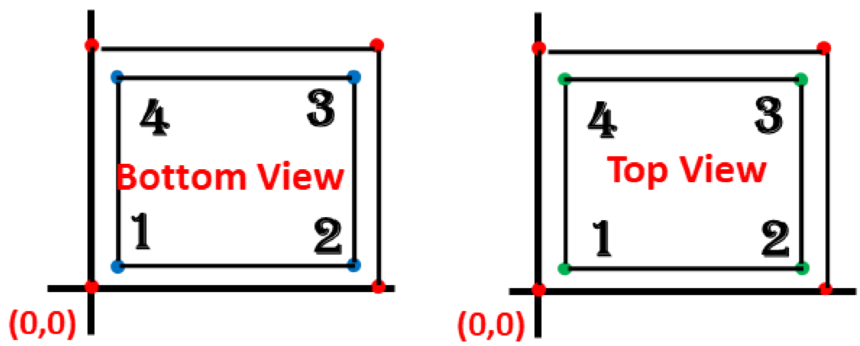

Figure B.1: Construction of polygons from measurement points.

B.2 Needle Points Fitting

First, the needle frames of both the top and bottom measured points are aligned by fitting them on top of each other, establishing them as the reference frame. This alignment is based on the assumption that the polygons for both views have similar values, ensuring consistency between the two frames.

B.2.1. Reflection

To achieve needle point fitting, the code initially performs a reflection operation on all the measured points of the top needle frame. This reflection is carried out about the axis passing through points 1 and 4. It is crucial to apply the reflection to the side of the frame whose measurements are obtained after the physical rotation of the jig.

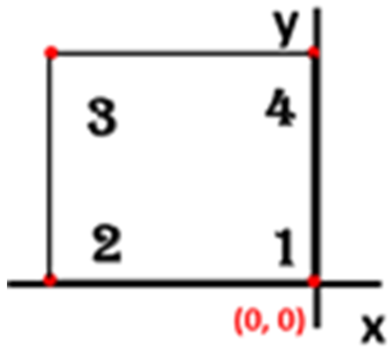

Figure B.2: Reflection operation on top measured values around axis passing points 1 and 4.

B.2.2 Geometrical Center (GC)

The next step involves calculating the geometric center (GC) for both the bottom needle frame and the reflected top needle frame. This calculation is performed to determine the central position or average location of the measured points within each frame.

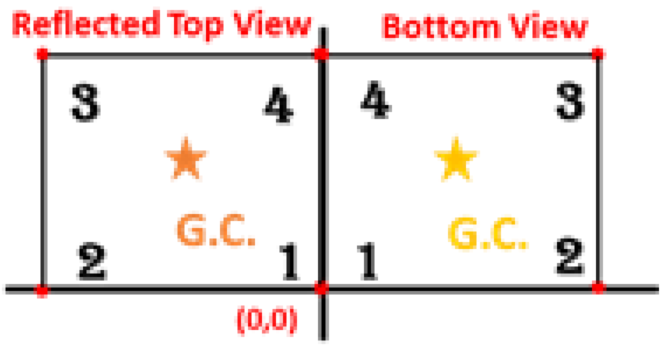

Figure B.3: Calculation of Geometric Center (GC) for bottom and reflected top needle frames.

B.2.3 Translation

The subsequent step involves calculating the distance between the geometric centers of the two frames. This distance is then used to translate all the points of the reflected top needle frame by the same amount as the difference in GC positions. This translation ensures alignment between the frames for further comparison.

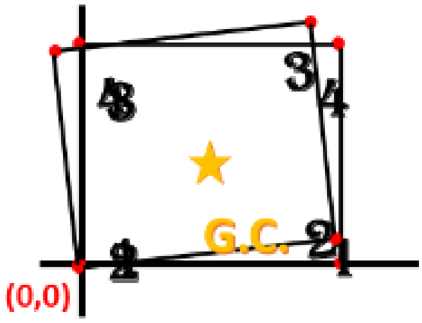

Figure B.4: Translation of reflected top needle frame points based on GC difference value.

B.2.4 Rotation

The next step involves calculating the angles between the rays extending from the geometric center (GC) to the same point in both the top (reflected and translated) and bottom frames. After obtaining the four angles, they are averaged. Subsequently, the top reflected and translated frame is rotated around the GC by the average angle. This rotation ensures complete alignment between the bottom and reflected top view of needle points.

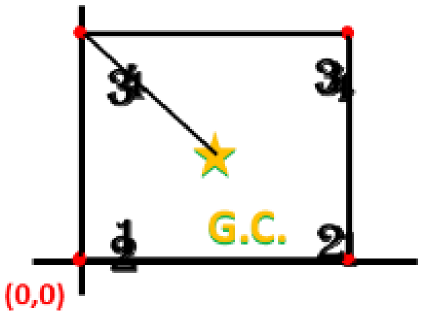

Figure B.5: Alignment of reflected and translated top frame by rotation around GC.

B.3 Sensor Points Fitting

B.3.1 Reflection, Translation and Rotation

The subsequent step involves applying the same values of reflection, translation, and rotation that were calculated for the needle frame to the sensor alignment marks. These values, obtained through the previous alignment process, are utilized to ensure that the alignment marks of the sensors undergo the same transformations as the needle frame. By applying these consistent transformations, the misalignment values between the sensors are maintained, allowing for accurate analysis and evaluation.

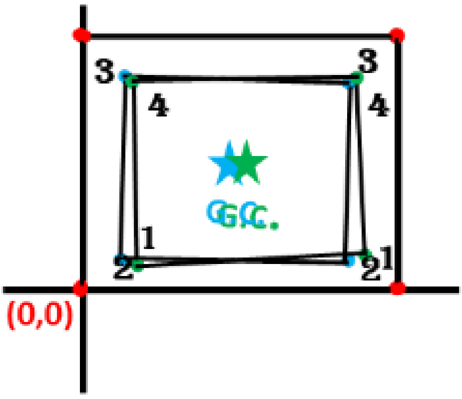

Figure B.6: Application of transformation values to sensor alignment marks

B.3.2 Δx, Δy and Δθ calculation

The final step involves applying the operations of reflection, translation and rotation specifically to the sensor alignment marks. This yields the values of the misalignment values Δx, Δy and Δθ between two sensors in directions as referenced in Figure X.

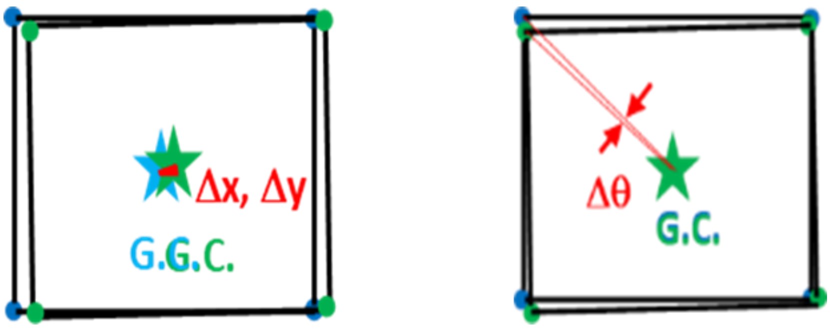

Figure B.7: Calculating sensors' misalignment values after application of translation and rotation operations to sensor alignment marks.

C. Chiller and Thermoelectric Plate

C.1 Chiller, Laudu MC 1200

The specifications of the Laudu MC1200 chiller, as extracted from the manual, are presented in table below. The chiller utilizes glycerol as the cooling liquid.

Technical Attributes	Microcool MC 1200
Working temperature min.	-10 °C
Working temperature max.	40 °C
Ambient temperature min.	5 °C
Ambient temperature max.	40 °C
Temperature stability	0.5 ±K
Filling volume min.	7 L
Filling volume max.	14 L
Cooling output at 20°C measured with ethanol	1.20 kW
Cooling output at 10°C measured with ethanol	1.05 kW
Cooling output at 0°C measured with ethanol	0.75 kW
Cooling output at -10°C measured with ethanol	0.40 kW
Power consumption	1.15 kW
Interface(s)	RS-232
Noise level	59 dB(A)
Display resolution	0.1 °C

Figure C.1: Specifications and picture of Laudu MC1200 Chiller.

C.2 Peltier Plate, LHP-800CP

The specification of the LHC-800CP thermoelectric plate, along with the performance curve, is obtained from the manual. In the performance curve, the "differential temperature" refers to the temperature difference between the hot and cold sides of the plate.

SPECIFICATIONS LHP-800CP

MODEL	PART NUMBER	NOTES	PERFORMANCE RATING BTU/HR	VOLTAGE VDC	CURRENT AMPS.	WEIGHT LBS. (KG)	MIN FLOW GPM	OPERATING AMBIENT °C	HEAT VOLTAGE
LHP-800CP	3-5095-0-000	Heat/Cool *	700-830	24	14	5.2 (2.3)	0.3	0/+70	24 VDC

* Heating via reverse polarity to thermoelectrics

Figure C.2: Specifications of LHP-800CP thermoelectric plate.

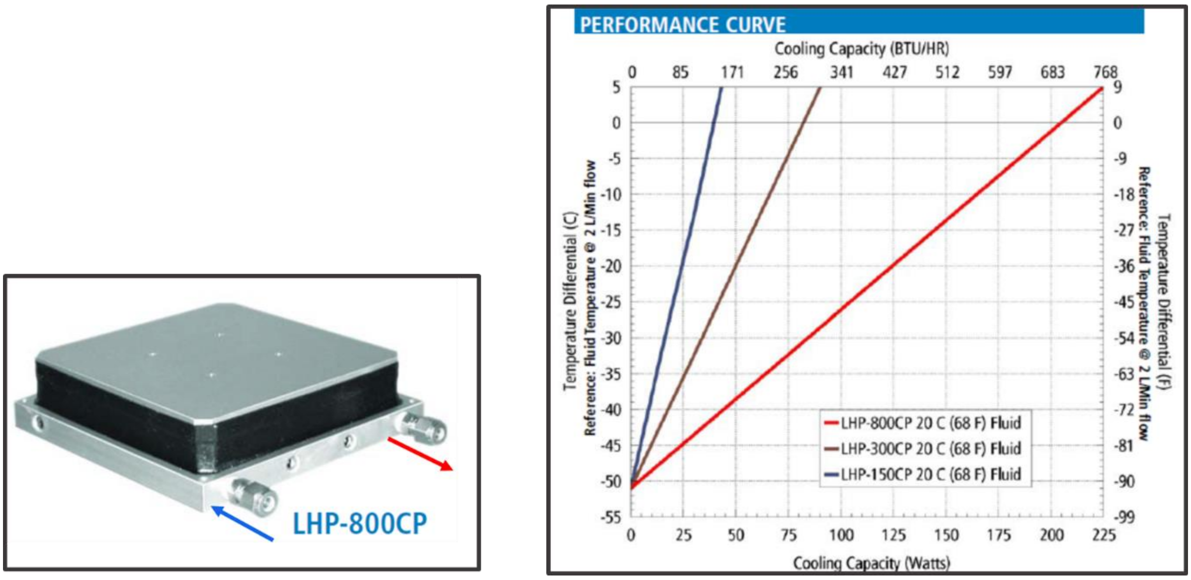

Figure C.3: The LH-800CP is shown on left side while its performance curve is shown on right side.

D. Beam Telescope Alignment Plots

D.1 FE-I4 Reference Plane Hit Map

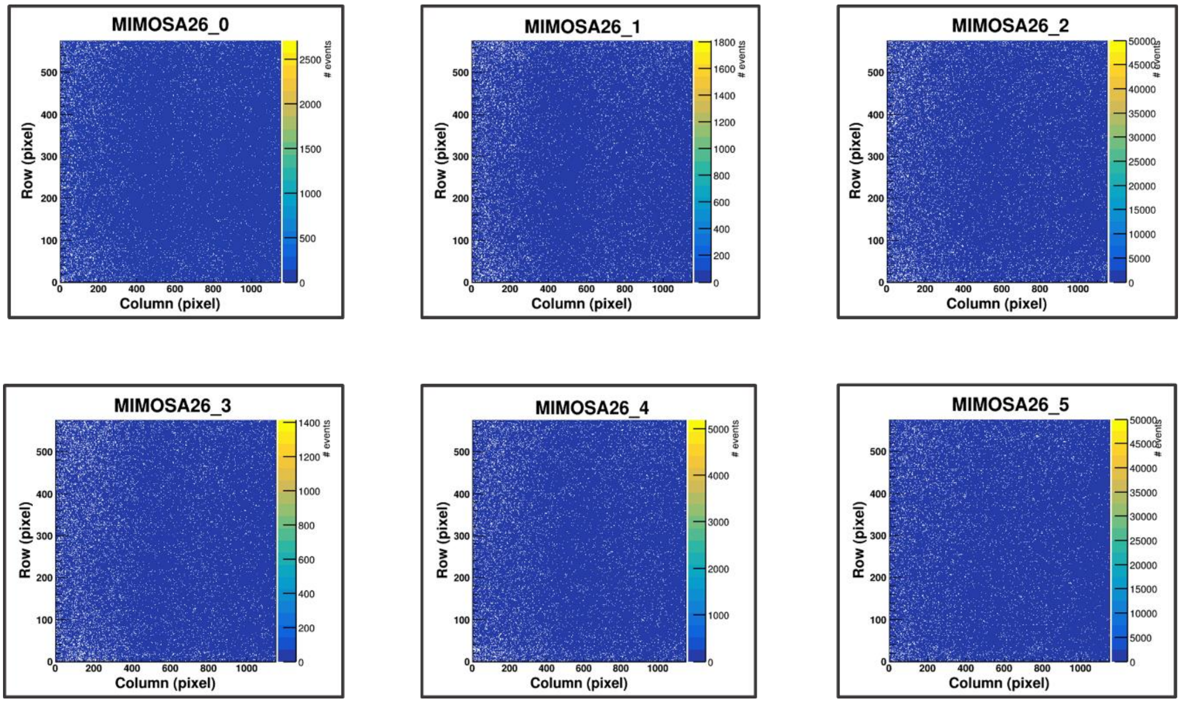

Figure D.1: Hit maps of all telescope planes (MIMOSA26).

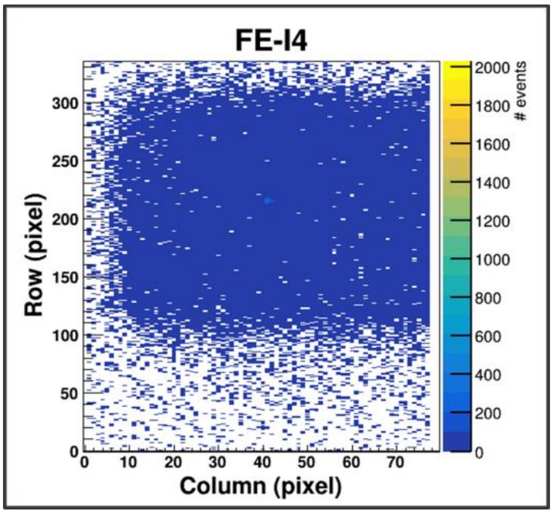

Figure D.2: Hit map of timing reference plane (FE-I4).

D.3 Pre-alignment Plots

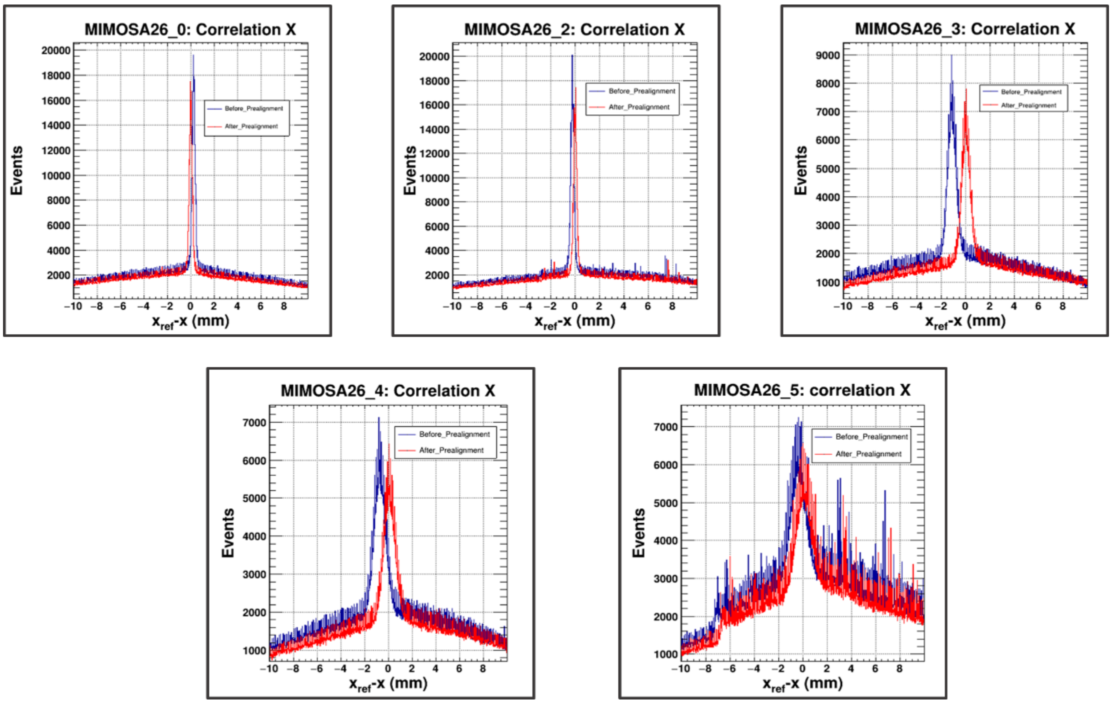

Figure D.3: *X*-Correlation plots before and after pre-alignment for all telescope planes with respect to MIMOSA26_1.

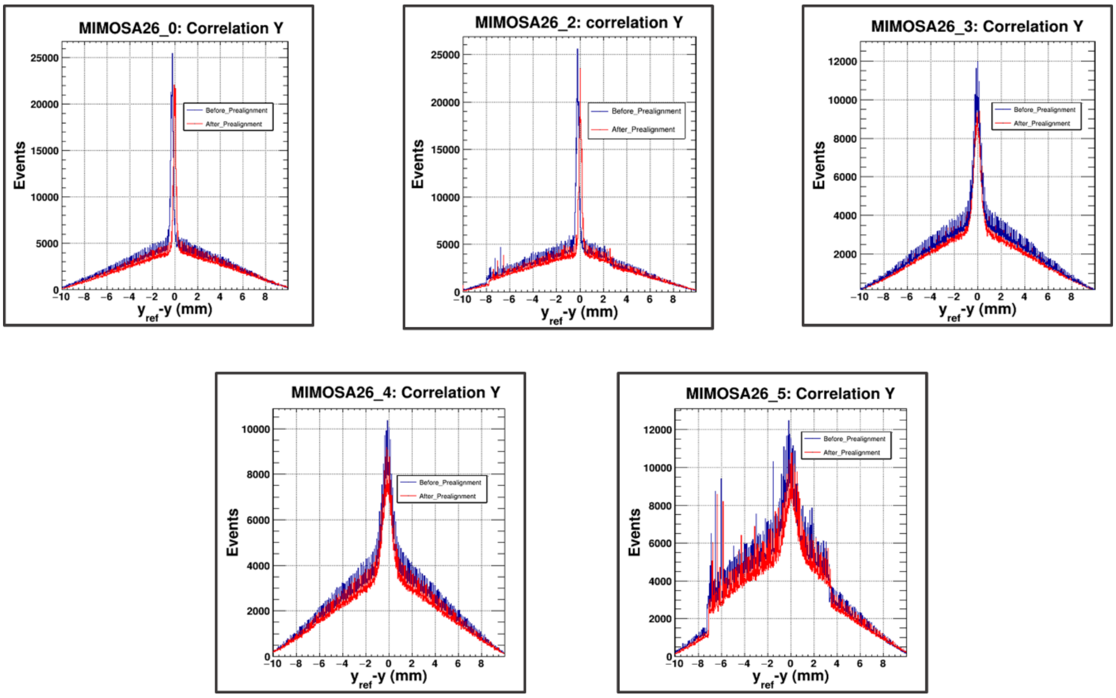

Figure D.4: *Y*-Correlation plots before and after pre-alignment for all telescope planes with respect to MIMOSA26_1.

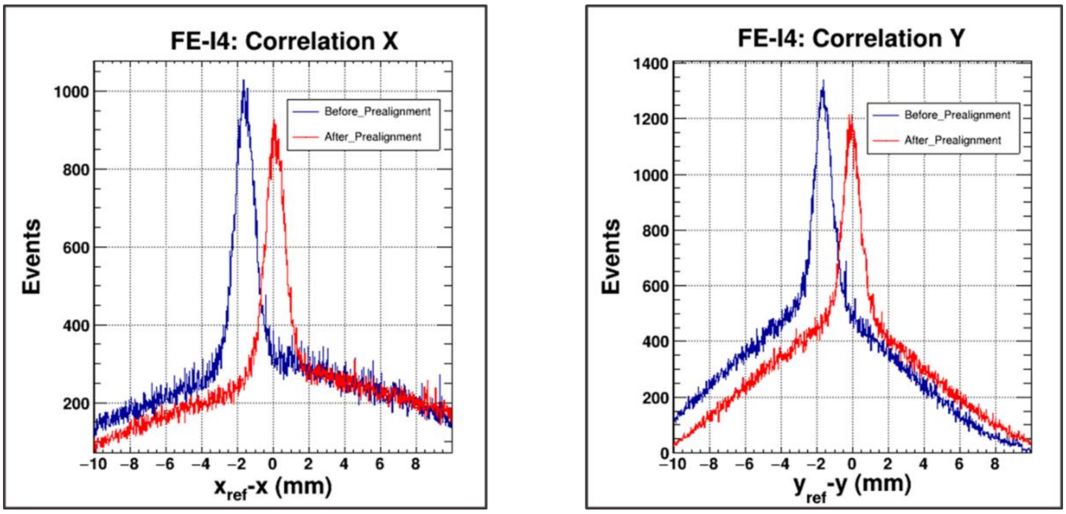

Figure D.5: *X*- and *Y*-Correlation plots before and after pre-alignment for timing reference plane (FE-I4) with respect to MIMOSA26_1.

D.4 Alignment Plots

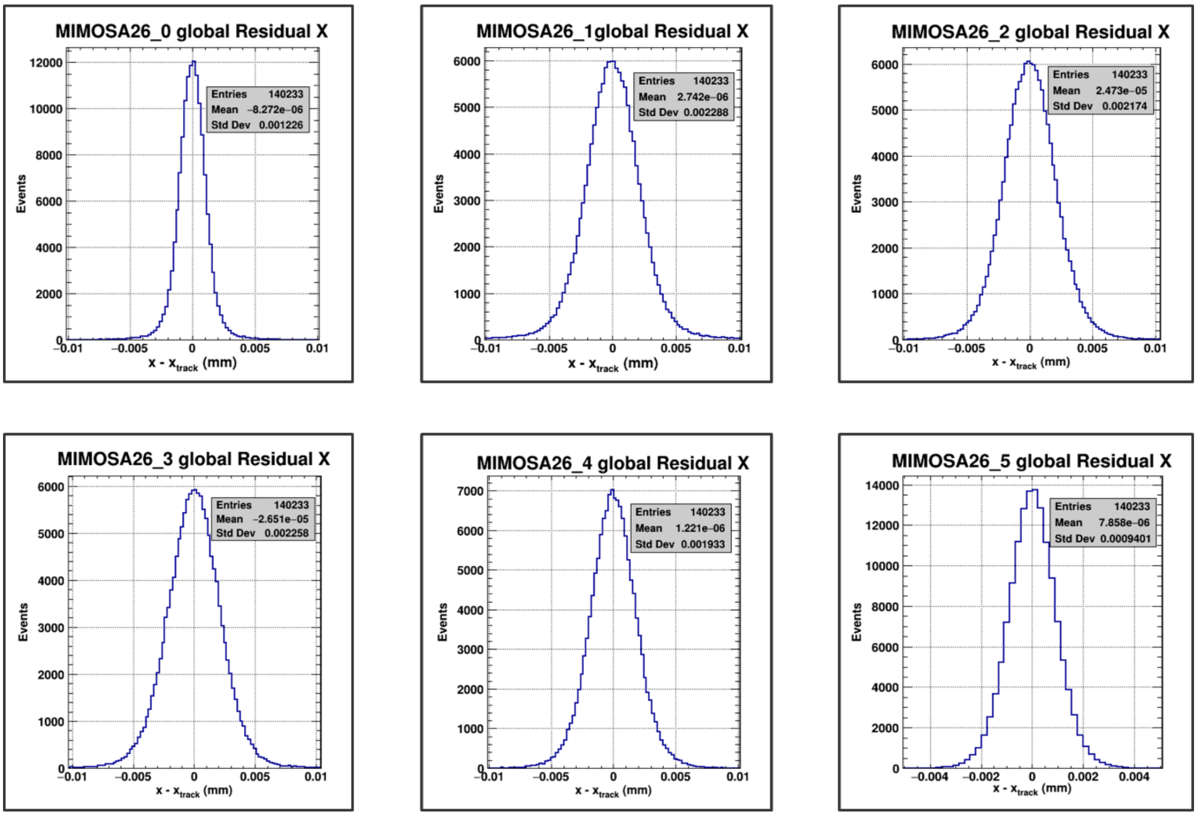

Figure D.6: The residual plots of all telescope planes after complete alignment in global *X*-Coordinates.

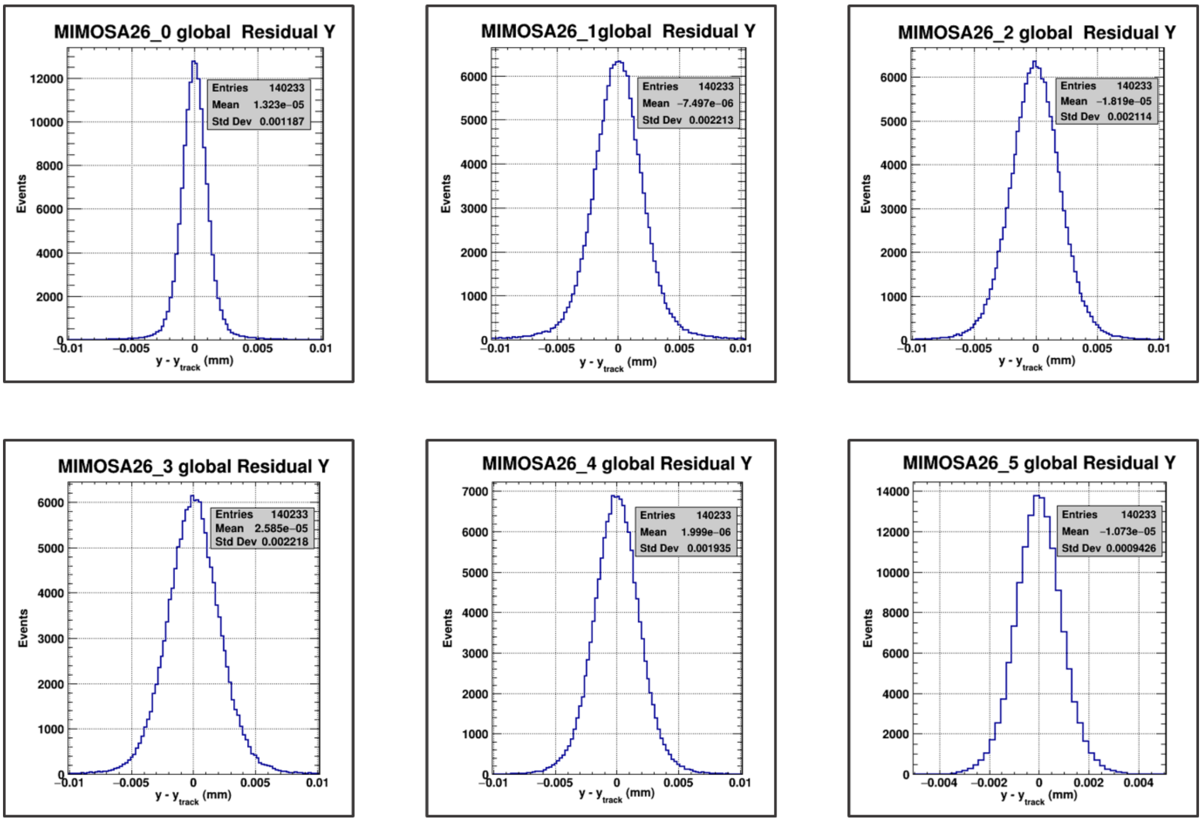

Figure D.7: The residual plots of all telescope planes after complete alignment in global *Y*-Coordinates.

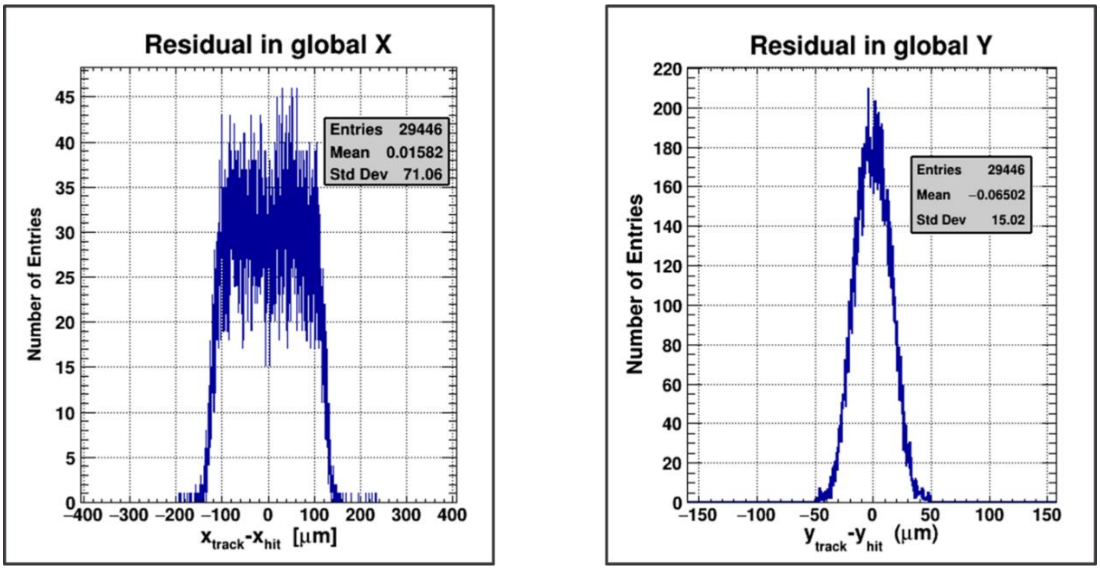

Figure D.8: The residual plots of timing reference plane (FE-I4) in global *X*- and *Y*-Coordinates after complete alignment.

Bibliography

[1] G. Apollinari, Béjar Alonso I, Brüning O, Lamont M, and Rossi L, 'High-Luminosity Large Hadron Collider (HL-LHC) Preliminary Design Report', 2015, doi: 10.5170/CERN-2015-005.

[2] The CMS Collaboration, 'Technical Proposal for the Phase-II Upgrade of the CMS Detector Tech. Rep. CERNLHCC-2015-010. LHCC-P-008', CMS-TDR-15-02, 2015.

[3] C. Foudas, A. Rose, J. Jones, and G. Hall, 'A Study for a Tracking Trigger at First Level for CMS at SLHC'. arXiv, Oct. 25, 2005. Accessed: May 05, 2023. [Online]. Available: http://arxiv.org/abs/physics/0510227

[4] D. Dannheim *et al.*, 'Corryvreckan: a modular 4D track reconstruction and analysis software for test beam data', *J. Instrum.*, vol. 16, no. 03, p. P03008, Mar. 2021, doi: 10.1088/1748-0221/16/03/P03008.

[5] L. Evans and P. Bryant, 'LHC Machine', *J. Instrum.*, vol. 3, no. 08, pp. S08001–S08001, Aug. 2008, doi: 10.1088/1748-0221/3/08/S08001.

[6] The CMS Collaboration *et al.*, 'The CMS experiment at the CERN LHC', *J. Instrum.*, vol. 3, no. 08, pp. S08004–S08004, Aug. 2008, doi: 10.1088/1748-0221/3/08/S08004.

[7] S. Weinberg, 'A Model of Leptons', *Phys. Rev. Lett.*, vol. 19, no. 21, pp. 1264–1266, Nov. 1967, doi: 10.1103/PhysRevLett.19.1264.

[8] A. Salam and J. C. Ward, 'Weak and electromagnetic interactions', *Il Nuovo Cimento*, vol. 11, no. 4, pp. 568–577, Feb. 1959, doi: 10.1007/BF02726525.

[9] S. L. Glashow, 'Partial-symmetries of weak interactions', *Nucl. Phys.*, vol. 22, no. 4, pp. 579–588, Feb. 1961, doi: 10.1016/0029-5582(61)90469-2.

[10] G. 't Hooft and M. Veltman, 'Regularization and renormalization of gauge fields', *Nucl. Phys. B*, vol. 44, no. 1, pp. 189–213, Jul. 1972, doi: 10.1016/0550-3213(72)90279-9.

[11] M. Gell-Mann, 'THE EIGHTFOLD WAY: A THEORY OF STRONG INTERACTION SYMMETRY', TID-12608, CTSL-20, 4008239, Mar. 1961. doi: 10.2172/4008239.

[12] G. Zweig, 'An SU$_3$ model for strong interaction symmetry and its breaking', 2002, doi: 10.17181/CERN-TH-412.

[13] M. Thomson, *Modern particle physics*. Cambridge, United Kingdom ; New York: Cambridge University Press, 2013.

[14] F. Halzen and A. D. Martin, *Quarks and leptons: an introductory course in modern particle physics*. New York: Wiley, 1984.

[15] M. E. Peskin, *An Introduction To Quantum Field Theory*, 0 ed. CRC Press, 2018. doi: 10.1201/9780429503559.

[16] E. Noether, 'Invariant variation problems', *Transp. Theory Stat. Phys.*, vol. 1, no. 3, pp. 186–207, Jan. 1971, doi: 10.1080/00411457108231446.

[17] P. W. Higgs, 'Broken symmetries, massless particles and gauge fields', *Phys. Lett.*, vol. 12, no. 2, pp. 132–133, Sep. 1964, doi: 10.1016/0031-9163(64)91136-9.

[18] P. W. Higgs, 'Broken Symmetries and the Masses of Gauge Bosons', *Phys. Rev. Lett.*, vol. 13, no. 16, pp. 508–509, Oct. 1964, doi: 10.1103/PhysRevLett.13.508.

[19] J. J. Thomson, 'XL. *Cathode Rays*', *Lond. Edinb. Dublin Philos. Mag. J. Sci.*, vol. 44, no. 269, pp. 293–316, Oct. 1897, doi: 10.1080/14786449708621070.

[20] A. Einstein, 'Über einen die Erzeugung und Verwandlung des Lichtes betreffenden heuristischen Gesichtspunkt', *Ann. Phys.*, vol. 322, no. 6, pp. 132–148, 1905, doi: 10.1002/andp.19053220607.

[21] S. H. Neddermeyer and C. D. Anderson, 'Note on the Nature of Cosmic-Ray Particles', *Phys. Rev.*, vol. 51, no. 10, pp. 884–886, May 1937, doi: 10.1103/PhysRev.51.884.

[22] F. Reines and C. L. Cowan, 'Detection of the Free Neutrino', *Phys. Rev.*, vol. 92, no. 3, pp. 830–831, Nov. 1953, doi: 10.1103/PhysRev.92.830.

[23] G. Danby *et al.*, 'Observation of High-Energy Neutrino Reactions and the Existence of Two Kinds of Neutrinos', *Phys. Rev. Lett.*, vol. 9, no. 1, pp. 36–44, Jul. 1962, doi: 10.1103/PhysRevLett.9.36.

[24] E. D. Bloom *et al.*, 'High-Energy Inelastic e − p Scattering at 6° and 10°', *Phys. Rev. Lett.*, vol. 23, no. 16, pp. 930–934, Oct. 1969, doi: 10.1103/PhysRevLett.23.930.

[25] M. Breidenbach *et al.*, 'Observed Behavior of Highly Inelastic Electron-Proton Scattering', *Phys. Rev. Lett.*, vol. 23, no. 16, pp. 935–939, Oct. 1969, doi: 10.1103/PhysRevLett.23.935.

[26] J.-E. Augustin *et al.*, 'Discovery of a Narrow Resonance in e + e − Annihilation', *Phys. Rev. Lett.*, vol. 33, no. 23, pp. 1406–1408, Dec. 1974, doi: 10.1103/PhysRevLett.33.1406.

[27] J. J. Aubert *et al.*, 'Experimental Observation of a Heavy Particle J', *Phys. Rev. Lett.*, vol. 33, no. 23, pp. 1404–1406, Dec. 1974, doi: 10.1103/PhysRevLett.33.1404.

[28] M. L. Perl *et al.*, 'Evidence for Anomalous Lepton Production in e + − e − Annihilation', *Phys. Rev. Lett.*, vol. 35, no. 22, pp. 1489–1492, Dec. 1975, doi: 10.1103/PhysRevLett.35.1489.

[29] S. W. Herb *et al.*, 'Observation of a Dimuon Resonance at 9.5 GeV in 400-GeV Proton-Nucleus Collisions', *Phys. Rev. Lett.*, vol. 39, no. 5, pp. 252–255, Aug. 1977, doi: 10.1103/PhysRevLett.39.252.

[30] Ch. Berger *et al.*, 'Evidence for gluon bremsstrahlung in e+e− annihilations at high energies', *Phys. Lett. B*, vol. 86, no. 3–4, pp. 418–425, Oct. 1979, doi: 10.1016/0370-2693(79)90869-4.

[31] R. Brandelik *et al.*, 'Evidence for planar events in e+e− annihilation at high energies', *Phys. Lett. B*, vol. 86, no. 2, pp. 243–249, Sep. 1979, doi: 10.1016/0370-2693(79)90830-X.

[32] G. Arnison *et al.*, 'Experimental observation of isolated large transverse energy electrons with associated missing energy at', *Phys. Lett. B*, vol. 122, no. 1, pp. 103–116, Feb. 1983, doi: 10.1016/0370-2693(83)91177-2.

[33] M. Banner *et al.*, ‘Observation of single isolated electrons of high transverse momentum in events with missing transverse energy at the CERN p collider’, *Phys. Lett. B*, vol. 122, no. 5–6, pp. 476–485, Mar. 1983, doi: 10.1016/0370-2693(83)91605-2.

[34] G. Arnison *et al.*, ‘Experimental observation of lepton pairs of invariant mass around 95 GeV/c2 at the CERN SPS collider’, *Phys. Lett. B*, vol. 126, no. 5, pp. 398–410, Jul. 1983, doi: 10.1016/0370-2693(83)90188-0.

[35] P. Bagnaia *et al.*, ‘Evidence for Z0→e+e− at the CERN p collider’, *Phys. Lett. B*, vol. 129, no. 1–2, pp. 130–140, Sep. 1983, doi: 10.1016/0370-2693(83)90744-X.

[36] F. Abe *et al.*, ‘Observation of Top Quark Production in p ‾ p Collisions with the Collider Detector at Fermilab’, *Phys. Rev. Lett.*, vol. 74, no. 14, pp. 2626–2631, Apr. 1995, doi: 10.1103/PhysRevLett.74.2626.

[37] S. Abachi *et al.*, ‘Observation of the Top Quark’, *Phys. Rev. Lett.*, vol. 74, no. 14, pp. 2632–2637, Apr. 1995, doi: 10.1103/PhysRevLett.74.2632.

[38] K. Kodama *et al.*, ‘Observation of tau neutrino interactions’, *Phys. Lett. B*, vol. 504, no. 3, pp. 218–224, Apr. 2001, doi: 10.1016/S0370-2693(01)00307-0.

[39] The CMS Collaboration *et al.*, ‘Observation of a new boson at a mass of 125 GeV with the CMS experiment at the LHC’, *Phys. Lett. B*, vol. 716, no. 1, pp. 30–61, Sep. 2012, doi: 10.1016/j.physletb.2012.08.021.

[40] The ATLAS Collaboration *et al.*, ‘Observation of a new particle in the search for the Standard Model Higgs boson with the ATLAS detector at the LHC’, *Phys. Lett. B*, vol. 716, no. 1, pp. 1–29, Sep. 2012, doi: 10.1016/j.physletb.2012.08.020.

[41] The ATLAS Collaboration *et al.*, ‘The ATLAS Experiment at the CERN Large Hadron Collider’, *J. Instrum.*, vol. 3, no. 08, pp. S08003–S08003, Aug. 2008, doi: 10.1088/1748-0221/3/08/S08003.

[42] The LHCb Collaboration *et al.*, ‘The LHCb Detector at the LHC’, *J. Instrum.*, vol. 3, no. 08, pp. S08005–S08005, Aug. 2008, doi: 10.1088/1748-0221/3/08/S08005.

[43] The ALICE Collaboration *et al.*, ‘The ALICE experiment at the CERN LHC’, *J. Instrum.*, vol. 3, no. 08, pp. S08002–S08002, Aug. 2008, doi: 10.1088/1748-0221/3/08/S08002.

[44] T. Sakuma and T. McCauley, ‘Detector and Event Visualization with SketchUp at the CMS Experiment’, *J. Phys. Conf. Ser.*, vol. 513, no. 2, p. 022032, Jun. 2014, doi: 10.1088/1742-6596/513/2/022032.

[45] The CMS Collaboration, ‘The CMS tracker system project: Technical Design Report No. CERN/LHCC 98-6’. CMS-TDR-005, 1997.

[46] The CMS Collaboration, ‘The electromagnetic calorimeter technical design report No. CERN/LHCC 97-033’. CMS-TDR-4, 1997.

[47] The CMS Collaboration, ‘The hadron calorimeter technical design report’. CERN/LHCC 97, 031, 1997.

[48] The CMS Collaboration, ‘Interactive Slice of the CMS detector’. CMS-OUTREACH-2016-027, 2016.

[49] The CMS Collaboration, ‘CMS TriDAS project: Technical Design Report, Volume 1: The Trigger Systems. No. CERN-LHCC-2000-038’. CMS-TDR-006-1, 2000.

[50] The CMS Collaboration, ‘The TriDAS Project: Technical Design Report, Volume 2: Data Acquisition and High-Level Trigger. No. CERN-LHCC-2002-026’. CMS-TDR-006, 2002.

[51] D. K. Schroder, *Semiconductor Material and Device Characterization*, 1st ed. Wiley, 2005. doi: 10.1002/0471749095.

[52] ‘Frontmatter’, in *Physics of Semiconductor Devices*, Hoboken, NJ, USA: John Wiley & Sons, Inc., 2006, pp. i–x. doi: 10.1002/9780470068328.fmatter.

[53] G. Lutz, *Semiconductor Radiation Detectors*. Berlin, Heidelberg: Springer Berlin Heidelberg, 2007. doi: 10.1007/978-3-540-71679-2.

[54] N. D. Arora, J. R. Hauser, and D. J. Roulston, ‘Electron and hole mobilities in silicon as a function of concentration and temperature’, *IEEE Trans. Electron Devices*, vol. 29, no. 2, pp. 292–295, Feb. 1982, doi: 10.1109/T-ED.1982.20698.

[55] F. Hartmann, *Evolution of Silicon Sensor Technology in Particle Physics*, vol. 275. in Springer Tracts in Modern Physics, vol. 275. Cham: Springer International Publishing, 2017. doi: 10.1007/978-3-319-64436-3.

[56] W. Shockley, ‘Currents to Conductors Induced by a Moving Point Charge’, *J. Appl. Phys.*, vol. 9, no. 10, pp. 635–636, Oct. 1938, doi: 10.1063/1.1710367.

[57] R. L. Gluckstern, ‘Uncertainties in track momentum and direction, due to multiple scattering and measurement errors’, *Nucl. Instrum. Methods*, vol. 24, pp. 381–389, Jul. 1963, doi: 10.1016/0029-554X(63)90347-1.

[58] The CMS Collaboration, ‘The Phase-2 Upgrade of the CMS Tracker Tech. Rep. CERN-LHCC-2017-009’, CMS-TDR-014, 2017.

[59] L. Caminada, ‘Performance and operation of the CMS Phase 1 pixel detector’, *Nucl. Instrum. Methods Phys. Res. Sect. Accel. Spectrometers Detect. Assoc. Equip.*, vol. 936, pp. 688–690, Aug. 2019, doi: 10.1016/j.nima.2018.10.084.

[60] The CMS Collaboration, ‘Silicon Strip Tracker Performance results 2018’. CMS-DP-2018-052, 2018. [Online]. Available: https://cds. cern. ch/record/2638062

[61] The CMS Collaboration, ‘CMS technical design report for the pixel detector upgrade, CERN. Tech. Rep. CERN-LHCC-2012-016’. CMS-TDR-011, 2012.

[62] The CMS Collaboration, ‘CMS Tracking POG Performance Plots For 2017 with PhaseI pixel detector’. 2017.

[63] M. Moll, ‘Radiation Damage in Silicon Particle Detectors’, PhD Thesis, Universität Hamburg, 1999. [Online]. Available: https ://mmoll.web. cern . ch/mmoll/thesis/pdf/moll - thesis.pdf

[64] F. Hoenniger, ‘Radiation damage in silicon : Defect analysis and detector properties’, Deutsches Elektronen-Synchrotron, DESY, Hamburg, 2008. doi: 10.3204/DESY-THESIS-2008-002.

[65] A. Junkes, ‘Influence of radiation induced defect clusters on silicon particle detectors’, PhD Thesis, Universität Hamburg, 2011. [Online]. Available: https://inspirehep.net/literature/ 940715

[66] A. M. Sirunyan *et al.*, 'Observation of the Higgs boson decay to a pair of τ leptons with the CMS detector', *Phys. Lett. B*, vol. 779, pp. 283–316, Apr. 2018, doi: 10.1016/j.physletb.2018.02.004.

[67] M. Aaboud *et al.*, 'Cross-section measurements of the Higgs boson decaying into a pair of τ -leptons in proton-proton collisions at s = 13 TeV with the ATLAS detector', *Phys. Rev. D*, vol. 99, no. 7, p. 072001, Apr. 2019, doi: 10.1103/PhysRevD.99.072001.

[68] A. M. Sirunyan *et al.*, 'Observation of Higgs Boson Decay to Bottom Quarks', *Phys. Rev. Lett.*, vol. 121, no. 12, p. 121801, Sep. 2018, doi: 10.1103/PhysRevLett.121.121801.

[69] ATLAS Collaboration, 'Observation of $H \rightarrow b\bar{b}$ decays and VH production with the ATLAS detector', 2018, doi: 10.48550/ARXIV.1808.08238.

[70] CERN. Geneva. The LHC Experiments Committee, D. Contardo, M. Klute, J. Mans, L. Silvestris, and J. Butler, 'Technical Proposal for the Phase-II Upgrade of the CMS Detector', 2015, doi: 10.17181/CERN.VU8I.D59J.

[71] CERN, 'CERN Yellow Reports: Monographs, Vol 4 (2017): High-Luminosity Large Hadron Collider (HL-LHC) Technical Design Report V. 0.1', p. 29.94 MB, Sep. 2017, doi: 10.23731/CYRM-2017-004.

[72] K. Hanke *et al.*, 'The LHC Injectors Upgrade (LIU) Project at CERN: Proton Injector Chain', *Proc. 8th Int Part. Accel. Conf*, vol. IPAC2017, p. 4 pages, 0.737 MB, 2017, doi: 10.18429/JACOW-IPAC2017-WEPVA036.

[73] B. Schmidt, 'The High-Luminosity upgrade of the LHC: Physics and Technology Challenges for the Accelerator and the Experiments', *J. Phys. Conf. Ser.*, vol. 706, p. 022002, Apr. 2016, doi: 10.1088/1742-6596/706/2/022002.

[74] The CMS Collaboration, 'A MIP Timing Detector for the CMS Phase-2 Upgrade, Technical Design Report, CERN-LHCC-2019-003', CMS-TDR-020, 2019.

[75] The CMS Collaboration, 'The Phase-2 Upgrade of the CMS Barrel Calorimeters, Technical Design Report, CERN-LHCC-2017-011', CMS-TDR-015, 2017.

[76] The CMS Collaboration, 'The Phase-2 Upgrade of the CMS endcap calorimeter, Technical Design Report, CERN-LHCC-2017-023', CMS-TDR-019, 2018.

[77] The CMS Collaboration, 'The Phase-2 Upgrade of the CMS Muon Detectors, Technical Design Report, CERN-LHCC-2017-012', CMS-TDR-016, 2017.

[78] S. Orfanelli, 'The CMS Inner Tracker electronics system development', *J. Instrum.*, vol. 17, no. 08, p. C08003, Aug. 2022, doi: 10.1088/1748-0221/17/08/C08003.

[79] M. Meschini *et al.*, 'Radiation resistant innovative 3D pixel sensors for the CMS upgrade at the High Luminosity LHC', *Nucl. Instrum. Methods Phys. Res. Sect. Accel. Spectrometers Detect. Assoc. Equip.*, vol. 978, p. 164429, Oct. 2020, doi: 10.1016/j.nima.2020.164429.

[80] N. Demaria *et al.*, 'Recent progress of RD53 Collaboration towards next generation Pixel Read-Out Chip for HL-LHC', *J. Instrum.*, vol. 11, no. 12, pp. C12058–C12058, Dec. 2016, doi: 10.1088/1748-0221/11/12/C12058.

[81] T. T. Böhlen *et al.*, 'The FLUKA Code: Developments and Challenges for High Energy and Medical Applications', *Nucl. Data Sheets*, vol. 120, pp. 211–214, Jun. 2014, doi: 10.1016/j.nds.2014.07.049.

[82] A. Ferrari, P. R. Sala, A. Fasso, and J. Ranft, 'FLUKA: A Multi-Particle Transport Code', SLAC-R-773, 877507, Dec. 2005. doi: 10.2172/877507.

[83] D. Ceresa *et al.*, 'Macro Pixel ASIC (MPA): the readout ASIC for the pixel-strip (PS) module of the CMS outer tracker at HL-LHC', *J. Instrum.*, vol. 9, no. 11, pp. C11012–C11012, Nov. 2014, doi: 10.1088/1748-0221/9/11/C11012.

[84] A. Caratelli *et al.*, 'Short-Strip ASIC (SSA): A 65nm Silicon-Strip Readout ASIC for the Pixel-Strip (PS) Module of the CMS Outer Tracker Detector Upgrade at HL-LHC', in *Proceedings of Topical Workshop on Electronics for Particle Physics — PoS(TWEPP-17)*, Santa Cruz, California: Sissa Medialab, Mar. 2018, p. 031. doi: 10.22323/1.313.0031.

[85] M. Raymond *et al.*, 'The CMS binary chip for microstrip tracker readout at the SLHC', *J. Instrum.*, vol. 7, no. 01, pp. C01033–C01033, Jan. 2012, doi: 10.1088/1748-0221/7/01/C01033.

[86] A. Dierlamm, 'CMS HPK sensor characterisation', in *Proceedings of The 21st International Workshop on Vertex Detectors — PoS(Vertex 2012)*, Jeju, Korea: Sissa Medialab, Jul. 2013, p. 016. doi: 10.22323/1.167.0016.

[87] K.-H. Hoffmann, 'Development of new sensor designs and investigations on radiation hard silicon strip sensors for CMS at the Large Hadron Collider during the high luminosity phase', 2013, doi: 10.5445/IR/1000034517.

[88] W. Adam *et al.*, 'Selection of the silicon sensor thickness for the Phase-2 upgrade of the CMS Outer Tracker', *J. Instrum.*, vol. 16, no. 11, p. P11028, Nov. 2021, doi: 10.1088/1748-0221/16/11/P11028.

[89] G. Blanchot, D. Braga, A. Honma, M. Kovacs, and M. Raymond, 'Hybrid circuit prototypes for the CMS Tracker upgrade front-end electronics', *J. Instrum.*, vol. 8, no. 12, pp. C12033–C12033, Dec. 2013, doi: 10.1088/1748-0221/8/12/C12033.

[90] T. Gadek, G. Blanchot, A. Honma, M. Kovacs, M. Raymond, and P. Rose, 'Testing of the front-end hybrid circuits for the CMS Tracker upgrade', *J. Instrum.*, vol. 12, no. 01, pp. C01010–C01010, Jan. 2017, doi: 10.1088/1748-0221/12/01/C01010.

[91] K. Uchida *et al.*, 'Results from the CBC3 readout ASIC for CMS 2S-modules', *Nucl. Instrum. Methods Phys. Res. Sect. Accel. Spectrometers Detect. Assoc. Equip.*, vol. 924, pp. 175–180, Apr. 2019, doi: 10.1016/j.nima.2018.09.051.

[92] Imperia College, 'CBC 3.1 User Manual, V1.4'. 2019. [Online]. Available: http://www.hep.ph.ic.ac.uk/ASIC/CBC_documentation/CBC3p1_User_Manual_V1p4.pdf

[93] B. Nodari, L. Caponetto, G. C. Galbit, S. Viret, and S. Scarfi, 'A 65 nm Data Concentration ASIC for the CMS Outer Tracker Detector Upgrade at HL-LHC', in *Proceedings of Topical Workshop on Electronics for Particle Physics — PoS(TWEPP2018)*, Antwerp, Belgium: Sissa Medialab, May 2019, p. 099. doi: 10.22323/1.343.0099.

[94] S. Viret *et al.*, ‘CIC2: a radiation tolerant 65 nm data aggregation ASIC for the future CMS tracker’, *J. Instrum.*, vol. 17, no. 05, p. C05016, May 2022, doi: 10.1088/1748-0221/17/05/C05016.

[95] K. Klein *et al.*, ‘Service hybrids for the silicon strip modules of the CMS Phase-2 Outer Tracker upgrade’, in *Proceedings of Topical Workshop on Electronics for Particle Physics — PoS(TWEPP2018)*, Antwerp, Belgium: Sissa Medialab, May 2019, p. 127. doi: 10.22323/1.343.0127.

[96] A. Zografos, G. Blanchot, I. M. Dominguez, A. E. Hollos, M. I. Kovacs, and N. Rasevic, ‘Power, readout and service hybrids for the CMS phase-2 upgrade’, *J. Instrum.*, vol. 17, no. 03, p. C03034, Mar. 2022, doi: 10.1088/1748-0221/17/03/C03034.

[97] Paulo Moreira on On behalf of the lpGBT team, ‘The lpGBT: a radiation tolerant ASIC for Data, Timing, Trigger and Control Applications in HL-LHC’, presented at the Topical Workshop on Electronics for Particle Physics, 2019. [Online]. Available: https://indico.cern.ch/event/799025/contributions/3486153/attachments/1901196/3138449/lpGBT20190903.pdf

[98] J. Troska *et al.*, ‘The VTRx+, an Optical Link Module for Data Transmission at HL-LHC’, in *Proceedings of Topical Workshop on Electronics for Particle Physics — PoS(TWEPP-17)*, Santa Cruz, California: Sissa Medialab, Mar. 2018, p. 048. doi: 10.22323/1.313.0048.

[99] G. Ripamonti *et al.*, ‘A 2.5V Step-Down DC-DC Converter for Two-Stages Power Distribution Systems’, in *Proceedings of Topical Workshop on Electronics for Particle Physics — PoS(TWEPP-17)*, Santa Cruz, California: Sissa Medialab, Mar. 2018, p. 059. doi: 10.22323/1.313.0059.

[100] Stefan Maier, ‘Assembly and qualification procedures of 2S modules and high rate tests of the CMS Binary Chip for the Phase 2 Upgrade of the CMS Outer Tracker’, PhD Thesis, karlsruhe institute of technology, 2019. [Online]. Available: https://cds.cern.ch/record/2725964/files/Maier.pdf

[101] ‘Polytec LV 601 glue, http://old.polytec.com/fileadmin/user_uploads/Polytec_EP_601-LV_engl.pdf’. [Online]. Available: https://www.polytecstore.fr/polytec_images/documents/FT_PT/ep/polytec-ep-601-lv_en.pdf

[102] ‘Heraeus, Bonding Wires for Semiconductor Technology’. [Online]. Available: www.heraeus.com/media/media/het/doc_het/products_and_solutions_het_documents/bonding_wires_documents/Brochure_Bonding_Wire.pdf

[103] ‘Sylgard 186’. [Online]. Available: https://www.dow.com/documents/en-us/productdatasheet/11/11-12/11-1253-sylgard-186-silicone-elastomer.pdf

[104] ‘Polytec TC 437 glue’. [Online]. Available: https://www.polytec-pt.com/fileadmin/user_uploads_Polytec-PT/home/documents/Polytec_Klebstoffe_ENG/Polytec_TC_437_engl.pdf

[105] ‘F&S Pull Tester’. [Online]. Available: https://www.fsbondtec.at/wp-content/uploads/2018/12/LT-101_ENG.pdf

[106] Tim Ziemons, ‘Wire Bonding on 2S Modules of the Phase-2 CMS Detector’, Faculty of Mathematics, Computer Science and Natural Sciences at the RWTH-Aachen, 2017. [Online]. Available: https://cds.cern.ch/record/2292301?ln=en

[107] ‘Precifluid volumetric dispenser’. [Online]. Available: https://precifluid.com/wp-content/uploads/2014/08/FT_PRECIFLUID_EN.pdf

[108] N. M. Röwert, ‘Assembly and Characterization of a First Functional 2S Module for the CMS Phase-2 Upgrade at LHC’, Master, RWTH Aachen, 2018. [Online]. Available: https://cds.cern.ch/record/2671895/files/

[109] M. Lipinski, ‘2S Module Metrology’, [Online]. Available: https://indico.cern.ch/event/962296/contributions/4048256/attachments/2132947/3592079/2020_10_29_ML_Metrology.pdf

[110] M. Lipinski, ‘Metrology at RWTH Aachen University’, [Online]. Available: https://indico.cern.ch/event/924612/contributions/3885463/attachments/2053283/3443302/Metrology_RWTH_2020_06_09.pdf

[111] The PETTL Collaboration, ‘Enabling Technologies for Silicon Microstrip Tracking Detectors at the HL-LHC’, PETTL Project Report, 2018.

[112] Michel Lukasik et al., ‘2S Meterology’, [Online]. Available: https://indico.cern.ch/event/924612/contributions/3885463/attachments/2053283/3442193/2S_Metrology_UH_updated_2.pdf

[113] ‘MPI TS2000 - DP probe station’. [Online]. Available: https://www.mpi-corporation.com/wp-content/uploads/ASTPDF/MPI-TS2000-Automated-Probe-System-Data-Sheet.pdf

[114] Muhammad Ahmad, ‘Metrology of SA 1902 Module at NCP, Pakistan’, [Online]. Available: https://indico.cern.ch/event/991716/contributions/4248056/attachments/2196205/3713372/metrology_TrackerGroup.pdf

[115] ‘Keithley electrometer 6517B’. [Online]. Available: https://smt.at/wp-content/uploads/smt-handbuch-keithley-6517b- englisch.pdf

[116] M. Pesaresi *et al.*, ‘The FC7 AMC for generic DAQ & control applications in CMS’, *J. Instrum.*, vol. 10, no. 03, pp. C03036–C03036, Mar. 2015, doi: 10.1088/1748-0221/10/03/C03036.

[117] ‘Rodge & Schwarz HMP4040’. [Online]. Available: https://scdn.rohde-schwarz.com/ur/pws/dl_downloads/dl_common_library/dl_manuals/gb_1/h/hmp_serie/HMPSeries_UserManual_en_02.pdf

[118] Davide Braga, ‘Development of the Readout Electronics for the High Luminosity Upgrade of the CMS Outer Strip Tracker’, High Energy Physics Group Department of Physics Blackett Laboratory Imperial College London, 2016.

[119] Nikkie Deelen, ‘Characterizing detector modules for the Upgrade of the Silicon Tracker of the Compact Muon Solenoid experiment’, PhD Thesis, Karlsruher Institue for Technologies (KIT), 2019. [Online]. Available: https://cds.cern.ch/record/2707148/

[120] ‘Thermoelectric Plate, LHP 800CP’. [Online]. Available: https://www.thermoelectric.com/cold-plates/general-use-liquid-cooled/lhp-800cp-series/

[121] 'Chiller, Lauda MC 1200'. [Online]. Available: https://www.manualslib.com/manual/1295584/Lauda-Mc-250.html#product-MC%201200

[122] 'Pico Theologies, TC-08'. [Online]. Available: https://www.picotech.com/download/datasheets/usb-tc-08-thermocouple-data-logger-data-sheet.pdf

[123] Ali Awais et al., 'Cold Test Measurements & Experience with Corryvreckan Test Beam Analysis Package', [Online]. Available: https://indico.cern.ch/event/1199129/contributions/5084127/attachments/2523520/4339683/20221006_system_test_meeting.pdf

[124] Ali Awais on behalf of CMS Outer Tracker, 'Assembly and Testing of 2S Module Prototypes for the CMS Phase-2 Outer Tracker Upgrade', presented at the 13th Position Sensitive Detectors conference, Oxford, UK, Sep. 03, 2023. [Online]. Available: https://indico.cern.ch/event/1230837/contributions/5518165/

[125] Ali Awais et al., '1st Functional Module of NCP', [Online]. Available: https://indico.cern.ch/event/991721/contributions/4353095/attachments/2239502/3796733/Ali-20210505_CERN_meeting.pdf

[126] Ali Awais et al., '8CBC3 Module Assembly at NCP', [Online]. Available: https://indico.cern.ch/event/1043643/contributions/4560980/attachments/2323558/3957389/20211005_CERN_meeting.pdf

[127] Ali Awais et al., 'Module Assembly Update from NCP', [Online]. Available: https://indico.cern.ch/event/1108595/contributions/4707943/attachments/2388437/4082318/20220209_CERN_meeting.pdf

[128] Stefan Maier, 'KIT 2S Module Noise Studies', Jul. 14, 2022. [Online]. Available: https://indico.cern.ch/event/1178556/contributions/4950935/attachments/2480113/4257435/220714%20System%20Test%20Meeting%20-%20Update%20on%202S%20Noise%20Investigations.pdf

[129] R. Diener *et al.*, 'The DESY II test beam facility', *Nucl. Instrum. Methods Phys. Res. Sect. Accel. Spectrometers Detect. Assoc. Equip.*, vol. 922, pp. 265–286, Apr. 2019, doi: 10.1016/j.nima.2018.11.133.

[130] C. Hu-Guo *et al.*, 'First reticule size MAPS with digital output and integrated zero suppression for the EUDET-JRA1 beam telescope', *Nucl. Instrum. Methods Phys. Res. Sect. Accel. Spectrometers Detect. Assoc. Equip.*, vol. 623, no. 1, pp. 480–482, Nov. 2010, doi: 10.1016/j.nima.2010.03.043.

[131] H. Jansen *et al.*, 'Performance of the EUDET-type beam telescopes', *EPJ Tech. Instrum.*, vol. 3, no. 1, p. 7, Dec. 2016, doi: 10.1140/epjti/s40485-016-0033-2.

[132] Adrian Herkert, 'Status Report on the The DESY II Test Beam Facility and the EUDET/AIDA Beam Telescopes', presented at the 9th BTTB Workshop, Lecce, Italy, Feb. 2021. [Online]. Available: https://indico.cern.ch/event/945675/contributions/4181051/

[133] D. Cussans, 'Description of the JRA1 Trigger Logic Unit (TLU), v0.2c'. 2009. [Online]. Available: https://www.eudet.org/e26/e28/e42441/e57298/EUDET-MEMO-2009-04.pdf

[134] H. Perrey, ‘EUDAQ and EUTelescope: Software Frameworks for Test Beam Data Acquisition and Analysis’, in *Proceedings of Technology and Instrumentation in Particle Physics 2014 — PoS(TIPP2014)*, Amsterdam, the Netherlands: Sissa Medialab, Jul. 2015, p. 353. doi: 10.22323/1.213.0353.

[135] Tim Ziemons, ‘Assembly and Test of Prototype 2S Modules for the Phase-2 Upgrade of the CMS Outer Tracker’, PhD Thesis, RWTH Aachen University, 2022. [Online]. Available: https://cds.cern.ch/record/2836729

[136] M. Garcia-Sciveres *et al.*, ‘The FE-I4 pixel readout integrated circuit’, *Nucl. Instrum. Methods Phys. Res. Sect. Accel. Spectrometers Detect. Assoc. Equip.*, vol. 636, no. 1, pp. S155–S159, Apr. 2011, doi: 10.1016/j.nima.2010.04.101.

[137] T. Bisanz *et al.*, ‘EUTelescope: A modular reconstruction framework for beam telescope data’, *J. Instrum.*, vol. 15, no. 09, pp. P09020–P09020, Sep. 2020, doi: 10.1088/1748-0221/15/09/P09020.

[138] ‘ROOT: analyzing petabytes of data, scientifically.’ [Online]. Available: https://root.cern/

[139] Morag Williams, Simon Spannagel, Jens Kröger, ‘Corryvreckan User Manual’. [Online]. Available: https://cern.ch/corryvreckan/usermanual/corryvreckan-manual.pdf

[140] C. Kleinwort, ‘General broken lines as advanced track fitting method’, *Nucl. Instrum. Methods Phys. Res. Sect. Accel. Spectrometers Detect. Assoc. Equip.*, vol. 673, pp. 107–110, May 2012, doi: 10.1016/j.nima.2012.01.024.

[141] F. James and M. Roos, ‘Minuit - a system for function minimization and analysis of the parameter errors and correlations’, *Comput. Phys. Commun.*, vol. 10, no. 6, pp. 343–367, Dec. 1975, doi: 10.1016/0010-4655(75)90039-9.

[142] V. Blobel, ‘Software alignment for tracking detectors’, *Nucl. Instrum. Methods Phys. Res. Sect. Accel. Spectrometers Detect. Assoc. Equip.*, vol. 566, no. 1, pp. 5–13, Oct. 2006, doi: 10.1016/j.nima.2006.05.157.

[143] I. Rubinskiy, ‘An EUDET/AIDA Pixel Beam Telescope for Detector Development’, *Phys. Procedia*, vol. 37, pp. 923–931, 2012, doi: 10.1016/j.phpro.2012.02.434.

[144] Roland Koppenhöfer, ‘Comparison of Testbeam Results for Unirradiated and Irradiated Sensors’, Feb. 04, 2021. [Online]. Available: https://indico.cern.ch/event/1000257/contributions/4217318/attachments/2184375/3690535/Irrad-Unirrad-Comparison.pdf

[145] Mykyta Haranko, ‘Development of a test DAQ system for the CMS Phase-2 outer tracker upgrade’, Department of Physics of the University of Hamburg, 2019. [Online]. Available: https://cds.cern.ch/record/2711873?ln=en

[146] W. Adam *et al.*, ‘Test beam demonstration of silicon microstrip modules with transverse momentum discrimination for the future CMS tracking detector’, *J. Instrum.*, vol. 13, no. 03, pp. P03003–P03003, Mar. 2018, doi: 10.1088/1748-0221/13/03/P03003.